UNIVERSITÉ PARIS-SUD

THÈSE

pour obtenir le grade de

DOCTEUR de l'Université Paris-Sud

Spécialité : **Physique Nucléaire**

préparée au laboratoire **Centre de Spectrométrie Nucléaire et de Spectrométrie de Masse**

dans le cadre de l'École Doctorale **MIPEGE (Modélisation et Instrumentation en Physique, Énergies, Géosciences, et Environnement)**

présentée et soutenue publiquement
par

SOTTY Christophe

le 22 Mars 2013 - 22nd March 2013

Titre (Title):

Etude de la Structure Nucléaire loin de la Stabilité: Excitation Coulombienne des Isotopes de Rb riches en neutrons autour de N=60; Production de Faisceaux au Spin Nucléaire Polarisé via la Technique des "Feuilles Orientées"

—

Study of the Nuclear Structure far from Stability: Coulomb Excitation of Neutron-rich Rb Isotopes around N=60; Production of Nuclear Spin Polarized Beams using the Tilted Foils Technique.

Directeur de thèse (Thesis advisor): **GEORGIEV Georgi** ***(CSNSM, Orsay, France)***

Jury

Dr. SCARPACI Jean Antoine *(CSNSM, Orsay, France)*,	Président du Jury (Jury President)
Dr. REDON Nadine *(IPNL, Lyon, France)*,	Rapporteur (Referee)
Pr. GÖRGEN Andreas *(University of Oslo, Oslo, Norway)*,	Rapporteur (Referee)
Dr. SULIGNANO Barbara *(CEA/IRFU, Saclay, France)*,	Examinateur (Advisor)
Dr. GEORGIEV Georgi *(CSNSM, Orsay, France)*,	Directeur de thèse (Thesis advisor)

A mon grand père Louis Cantat,
dont le souvenir guide chacun de mes pas.

Acknowledgement/Remerciements

Une thèse représente beaucoup d'efforts et son aboutissement est parfois difficile, mais il faut toujours garder à l'esprit que c'est surtout pour autrui qu'on la fait. Cela ne représente qu'une modeste contribution à cette quête de la connaissance, qui nous fait espérer arriver vers de meilleurs rivages ... Cela représente beaucoup de travail et d'investissement personnel, mais on ne peut la réduire au travail d'une seule personne. La réalisation de travaux scientifiques et notamment expérimentaux, n'est possible que grâce à la contribution de nombreuses personnes et pas seulement venant du milieu académique (chercheurs, thésards, post-docs, techniciens, secrétaires, ...). Je tiens à remercier toutes personnes ayant soutenues de près ou de loin ces travaux, ainsi que la rédaction de ce manuscrit.

Premièrement, je tiens à remercier mon directeur de thèse Georgi Georgiev, qui m'a donné l'opportunité de réaliser ces recherches au CSNSM (Centre de Spectométrie Nucléaire et de Spectrométrie de Masse), mais aussi à Nadine Redon qui m'introduisit à l'époque auprès de mon directeur de thèse. Je ne réalisais pas alors ce que la recherche experimentale impliquait. Grâce à de nombreuses expériences à travers l'Europe j'ai découvert et appris de nombreuses techniques. Ayant été basé au CERN (Centre Européen pour la Recherche Nucléaire), j'ai eu la chance d'être dans un environnement propice à l'émulation scientifique. Cela facilita également la résolution des innombrables problèmes techniques rencontrés lors de la création du dispositif "β-NMR + TFT".

J'aimerais remercier les membres du jury d'examination de mes travaux de thèse, Dr. Nadine Redon, Dr. Barbara Sulignano, Dr. Georgi Georgiev, Pr. Andreas Gorgen et le président du jury Dr. Jean-Antoine Scarpaci.
Après avoir passé six mois au sein de l'IPNL (Institut de Physique Nucléaire de Lyon) dans le cadre de mon stage de seconde année de master, sous la direction de Nadine, j'ai pris goût à la physique nucléaire et voulu continuer dans cette branche de la physique. On ne peut pas résister au professionnalisme, la droiture et la gentillesse de Nadine. Après la fin de la thèse, le choix de Nadine comme membre du jury s'est imposé de lui-même. Ce fut en quelque sorte, la boucle qui se refermait.

Comme je l'ai déjà mentionné, aucun travail expérimental n'est possible seul, et si tant est que certain puisse croire le contraire, j'ose espérer qu'un jour ils se rendront compte de leur méprise. Je souhaiterai saluer le travail et l'aide de collaborateurs que je n'ai pas encore eu l'occasion de mentionner (très souvent ami(e)s). Je vais débuter par les personnes ayant contribuées principalement aux travaux de polarisation et je poursuivrais avec ceux dont la contribution se porta plus sur les travaux d'excitation Coulombienne.
Hans Törnqvist (alias maître Jedi du C++), mon compaire du CERN, avec lequel nous avons passé des jours et des nuits et préparé, réparé le dispositif "β-NMR + TFT", mais également pour nos nombreuses et passionnantes discussions (même si il fallait retenir son souffle pour ne pas casser les feuilles de carbone) ; Fredrick Wenander, qui a toujours soutenu notre projet contre vents et tempêtes, supervisant nos travaux au CERN ; Pr. Zeitz, sans lequel la réalisation de ces travaux n'auraient pu être possible ; Magdalena Kowalska, qui devint la superviseur de Hans à la fin de son séjour au CERN, et qui amena un gros boost à la collaboration (alias the woman who is speaking faster than the speed of light) ; Dimiter Balabanski, pour son aide tout au long de mon parcours de thèse (polarisation, Coulex, noyaux déformés ...), je lui dois également un gros panier d'orange ; Michael Hass, Yigal Sachar et Gedalia Perelman, pour le travail qu'ils ont réalisé sur le dispositif "TFT", mais aussi pour la gentillesse de leur accueil, lors de mes séjours en Israël ; Andrew Stuchberry, Alexander Gottberg, Monika Stachura, Imai Nobuaki, Deyan Yordanov et Hakan T. Johansson, pour leurs aides durant l'expérience de polarisation ; Magda Zielinska, pour son travail et son aide durant l'analyse des résultats avec GOSIA ; Liam Gaffney, pour son aide lors des expériences d'excitation Coulombienne ; Nigel Warr, pour son importante contribution à MINIBALL, mais aussi pour avoir été le seul à rester jusqu'à la fin de l'expérience d'excitation Coulombienne ; Karl Johnston, pour nous avoir toujours aidé lorsqu'on avait besoin de son aide, notamment la fourniture de sources fraîchement implantées ; Janne Pakarinen, Lili Atasanova, Jean-Michel Daugas et bien entendu tous les membres, opérateurs et techniciens d'ISOLDE : Fredrick Wenander, Stefano Marzari, Miguel Lozano Benito, Emiliano Piselli, Didier Voulot, Pascal Fernier, Erwin Siesling, Alexander Herlert, Yorick Blumenfeld, Jenny Weterings, Ermano Barbero,

Julien Para-Lopez, ... pour avoir toujours répondu présent lorsqu'il le fallait.
Je voulais remercier également les personnes qui ont contribué à la rédaction de ce manuscrit. Catherine Thibault, qui a eu la difficile tâche de relire mon manuscrit, pour ses conseils avisés et sa gentillesse ; Georges Audi (very good Asli ! ! !) pour sa sagesse, la justesse de ses argumentations mais surtout pour sa ferveur en la connaissance et aux hommes qui l'enrichissent ; Stéphanie Roccia (qui restera notre éternelle jeune thésarde), pour sa bonne humeur et qui a essuyé les premières lectures du manuscrit ; Alain Goasduff (qui devra en répondre "This is yours ?"), qui m'a aidé à la fois moralement et techniquement lors du dénouement de ma thèse ; Asli Kusoglu, pour avoir partagé à mes côtés les moments les plus heureux mais aussi les plus difficiles ; Joa Ljunvall pour sa gentillesse et son aide ; Carole Gaulard qui me fit confiance pour cadrer les enseignements de travaux pratiques de physique nucléaire ; Asénath Etile, qui a mis du peps dans la salle des thésards, et dont j'espère que sa thèse se dénouera avec moins d'embuches ; Cédric Bareille et Cédric Baumier, pour leur aide et leur amitié ; Samia Habbas (alias la plus mieux des mieux) qui m'a toujours soutenue.

Finalement, je voudrais adresser mes pensées les plus chaleureuses à ceux qui ont toujours été là, ma famille et particulièrement ma mère (ti cliques, ti cliques ! ! !), mon père (1 datte = 3 repas, Frison Roche), mon frère (Raymond la Science), mon oncle ("Non !, mais il faut garder le bon vieux sens paysans !", alias Gros le premier du nom) qui est maintenant par-delà l'océan atlantique et mes grand-parents.

Contents

List of Figures

53figure.caption.57

List of Tables

Abstract

The underlying structure in the region A∼100, N∼60 has been under intensive and extensive investigation, mainly by β-decay and γ-ray spectroscopy from fission processes. Around N∼60, by adding just few neutrons, protons a rapid shape change occurs from spherical-like to well deformed g.s. shape. Shape coexistence has been observed in the Sr and Zr nuclei, and is expected to take place in the whole region.
The mechanisms involved in the appearance of the deformation is not well understood. The interplay between down-sloping and up-sloping neutron Nilsson orbital is evoked as one of the main reasons for the sudden shape change. However, a clear identification of the active proton and neutron orbitals was still on-going. For that purpose, the neutron rich ^{93,95,97,99}Rb isotopes have been studied by Coulomb excitation at CERN (ISOLDE) using the REX-ISOLDE post-accelerator and the MINIBALL setup.
The completely unknown structures of ^{97,99}Rb have been populated and observed. Prompt γ-ray coincidences of low-lying states have been observed and time correlated to build level schemes. The associated transition strengths have been extracted with the GOSIA code. The observed matrix elements of the electromagnetic operator constituted new inputs of further theoretical calculations giving new insight on the involved orbitals.
The sensitivity of such experiment can be increased using nuclear spin polarized RIB. For that purpose the Tilted Foils Technique (TFT) of polarization has been investigated at CERN. A new TFT polarizer with a β-NMR setup have been created and installed after REX-ISOLDE. The uncomplete knowledge of the polarization process associated to the technique needs to be investigated. Conclusive preliminary tests have been performed on ^{8}Li in order to determine the potential of the present setup.

Résumé

La structure sous-jacente dans la zone A∼100, N∼60 a été étudiée intensivement et extensivement, principalement par décroissance β et spectroscopie γ suite à des réactions de fission. Autour de N∼60, en ajoutant juste quelques neutrons, protons un changement de forme rapide des états fondamentaux se produit, allant de sphérique à bien déformé. La coexistence de forme observée dans les noyaux de Sr et Zr est supposée avoir lieu dans toute la région.
Les mécanismes impliqués dans l'apparition de la déformation n'était pas clairement identifiés. L'interaction entre les orbitales de Nilsson montantes et descendantes est évoquée comme l'une des principales raisons du changement de forme. Cependant, une identification claire des orbitales proton et neutron en jeu était nécessaire. A cet effet, l'étude des isotopes ^{93,95,97,99}Rb rich en neutrons a été réalisée par excitation Coulombienne au CERN (ISOLDE) en utilisant le post-accélérateur REX-ISOLDE et le dispositif MINIBALL.
Les structures excitées encore inconnues des isotopes ^{97,99}Rb ont été peuplées et observées. Les coïncidences de transitions γ des états de basse énergie ont été observées et leur corrélations ont permis la construction de schémas de niveaux. Les probabilités de transitions associées ont été extraites grâce au code Gosia. Les éléments de matrice de l'opérateur électromagnétique observés constituent de nouveaux apports afin d'effectuer de nouveaux calculs théoriques permettant de statuer sur les orbitales impliquées.
La sensibilité des expériences de ce type peut être accrue en utilisant des faisceaux radioactifs d'ions dont le spin nucléaire est polarisé. La technique de polarisation des feuilles orientées (TFT) fut étudiée dans ce but au CERN. Un nouveau polariseur TFT et un dispositif β-NMR ont être créés et installés après REX-ISOLDE. La connaissance du processus de polarisation associé à la technique reste incomplète à ce jour et de plus amples études sont nécessaires. Des tests préliminaires prometteurs ont été effectués sur le noyau de ^{8}Li afin de déterminer le potentiel du dispositif actuel.

Mots clés: structure nucléaire; spectroscopie γ; excitation Coulombienne; excitation multiple; modèle rotationnel; déformation; feuilles orientées; polarisation nucléaire; β-RMN;

Key words: nuclear structure; γ-ray spectroscopy; Coulomb excitation; multi-step excitation; rotational model; deformation; tilted foils; nuclear polarization; β-NMR;

Discipline/Matter: Constituants élémentaires/Elementary constituents

Centre de Spectrmétrie Nucléaire et de Spectrométrie de Masse
Bât. 104-108 - 91405 Orsay Campus (Cedex)

Synthèse

Durant les dernières décennies, la région autour de N~60, A~100 riche en neutrons a été sujette à des études intensives et extensives. La structure nucléaire sous-jacente de la région fut principalement étudiée par décroissance β et spectroscopie γ grâce à des réactions de fissions induites via des protons de haute énergie ou des neutrons thermiques et des réactions de fission spontanée.
Dans cette partie de la charte nucléaire, le développement de déformation le plus soudain est observé. En ajoutant juste quelques neutrons/protons, une transition de forme rapide se produit, allant d'une forme sphérique à une forme bien déformée pour les états fondamentaux autour de N~60.
Généralement, l'observation de transitions de forme est accompagnée par le phénomène de coexistence de formes. Observé dans les noyaux de Sr et Zr, elle est supposée être présente dans l'ensemble de la région. Bien que les états fondamentaux déformés ont été clairement observés autour de N~60, entre les chaînes isotopiques de Mo et de Rb incluses, il n'est pas aisé de déterminer une limite stricte au développement de déformation. Les dernières mesures de masses et de rayons de charge indiquent l'absence d'apparition soudaine de déformation pour la chaîne isotopique du Kr (Z=36). Les mesures systématiques des moments dipolaires électriques et quadrupolaires magnétiques mettent en exergue le fait que les isotopes de Rb sont les premiers à présenter l'apparition soudaine de déformation pour les faibles numéros atomiques de la région.

Les mécanismes impliqués dans ce développement de déformation sont peu compris. Dans une première approche, les calculs de modèles théoriques pointaient l'interaction proton/neutron résiduelle des partenaires spin-orbite $\pi g_{9/2}$ et $\nu g_{7/2}$ comme responsable du développement de déformation. Cependant, de plus amples calculs prenant en compte un espace de valence plus large remirent en question cette hypothèse en obtenant un meilleur accord avec les données expérimentales (notamment pour les isotopes de Mo). L'interaction entre les orbitales de Nilsson neutron montantes et descendantes est évoquée comme l'une des principales raisons du soudain changement de forme. Cependant, jusqu'à aujourd'hui peu d'expériences avaient été proposées pour établir l'importance relative des ces orbitales.

Des bandes rotationnelles ont déjà été identifiées à N~60 pour les numéros atomiques les plus élevés de la région, exhibant une déformation des noyaux dans leurs états fondamentaux. Une claire identification des spins de tête de bandes, des déformations en présence et des orbitales de Nilsson sur lesquelles sont construites les bandes rotationnelles, devrait constituer une source suffisante de nouvelles informations afin de déterminer les mécanismes responsables du développement de déformation. La nature de la plupart des nucléides de la région fait de leur étude expérimentale un challenge; par exemple, étant situé loin de la vallée de stabilité, ils possèdent de faibles durées de vie, de surcroît, leurs natures chimiques très différentes des nucléides en présence, offrent plus ou moins de difficulté pour les produire.
Les récents développements effectués dans le domaine des faisceaux radioactifs d'ions (RIB) permirent l'étude de la région via d'autres mécanismes de réaction. La collaboration établie autour du spectromètre MINIBALL situé au CERN envisagea l'étude extensive de

la région par excitation Coulombienne afin de clarifier la situation.

L'excitation Coulombienne est gouvernée par différentes règles de sélection que les réactions précédemment utilisées pour peupler les états excités. Elle consiste en la collision de deux noyaux à une énergie proche de la barrière Coulombienne. Si l'excitation relève uniquement d'une interaction purement électromagnétique, les seules propriétés nucléaires en jeu sont décrites par les éléments de matrice de l'opérateur multipolaire électromagnétique. Nous nous restreindrons à ce cas, communément appelé excitation Coulombienne "sûre" pour lequel l'interaction forte est négligeable et peut être traitée à un ordre perturbatif.
De part leur collision, les noyaux peuvent subir une transition d'un état nucléaire initial à un état nucléaire final. Cet état final excité décroît principalement par émission de transition γ ou d'électrons de conversion.
Les intensités de transitions γ observées ainsi que les différents rapports d'embranchement sont directement reliés aux éléments de matrice de l'opérateur multipolaire. Ils décrivent les processus d'excitation et de dés-excitation caractéristiques de la structure nucléaire. Par exemple, les éléments de matrice diagonaux décrivent la déformation via les moments quadrupolaires. Les probabilités de transitions B(E2) découlant des éléments de matrice constituent des ingrédients essentiels pour évaluer la collectivité proche des nombres magiques et des transitions de formes.
L'atout principal de cet technique est de pouvoir extraire des informations sur la structure nucléaire sans dépendance à un modèle quelconque.

Concernant la chaîne isotopique du Kr, le développement de déformation n'était pas observé en terme de mesures de masse et de rayon, mais il se pourrait que ce changement s'opère graduellement. Afin d'évaluer cette hypothèse, une étude par excitation Coulombienne des isotopes ^{94,96}Kr a été effectuée dans le cadre de la même collaboration (MINIBALL).
Les systématiques présentes dans ces isotopes pair-pair, pour les énergies $E(2_1^+)$, $E(4_1^+)$, leur ratio $R_{4/2}$ et probabilité de transition $B(E2, 2_1^+ \rightarrow 0_1^+)$ indiquent un faible développement de déformation. Ce constat confirme que la chaîne isotopique des Rb est la première présentant un développement soudain de déformation. Placé à la frontière du changement rapide de forme, son étude constitue un ingrédient clé pour comprendre les mécanismes en présence.

Dans la chaîne isotopique des Rb, les états fondamentaux présentent un rapide développement de déformation à N=60 pour le noyau ^{97}Rb. Auparavant, il n'était pas possible d'étudier leurs structures nucléaires du fait de leurs exotismes. Les récents développements dans le domaine des faisceaux radioactifs permettent maintenant leur étude . L'existence de bandes rotationnelles pouvait être raisonnablement envisagée dans les isotopes de rubidium riches en neutron de masse impaire à $N \gtrsim 60$. L'identification des configurations de particule célibataire sur lesquelles sont basées les bandes rotationnelles constituerait une étape essentielle quant à la compréhension des mécanismes de déformation. De plus, l'arrangement des orbitales proton pour $N \gtrsim 60$ n'est pas connu. L'étude de la structure nucléaire de basse énergie par excitation Coulombienne des isotopes de ^{93,95,97,99}Rb constituait la meilleure option afin d'identifier les orbitales proton actives.

Etant au niveau d'une transition de forme, l'observation du phénomène de coexistence de formes dans les isotopes de Rb étudiés peut être raisonnablement envisagée. De plus,

des calculs théoriques basés sur le modèle QPRM ont prédit l'existence d'isomères de forme à basse énergie. Cependant, compte tenu de leurs longues durées de vie et de leurs basses énergies, il sera difficile de les observer par les dispositifs expérimentaux d'excitation Coulombienne.

Des études par excitation Coulombienne similaires à l'expérience proposée ont d'ors et déjà démontré la performance du dispositif expérimental MINIBALL avec REX-ISOLDE au CERN. Nous pouvons citer à titre d'exemple l'étude des isotopes de Cu de masse impaire. Cette dernière apporta la confirmation qu'un tel type d'expérience apportait un gain d'informations conséquent à la fois sur les états collectifs et de particule célibataire des noyaux exotiques.

Lors d'une expérience d'excitation Coulombienne, les noyaux d'intérêt doivent être produit de façon à former un faisceau d'ions radioactifs (RIB) correspondant aux spécifications d'intensité, de pureté et d'énergie requises. Ce faisceau radioactif est ensuite conduit à une cible secondaire où l'excitation Coulombienne prend place.
L'utilisation de faisceaux radioactifs implique de dépasser plusieurs obstacles techniques provenant de la nature instable du faisceau et généralement de leurs faibles sections efficaces de production. Du fait que ceux-ci sont produits avec de faibles intensités dans un environnement très radioactif, ils doivent être extraits et transportés loin de leur source de production afin d'améliorer le rapport signal/bruit. L'efficacité la plus haute dans les phases de production, de préparation et de transport du faisceau doit être atteinte.
Le temps de vie des noyaux d'intérêt impose de réduire au maximum le temps de chacun des processus allant de la production au dispositif expérimental chargé de faire l'étude.
De plus, la plupart des faisceaux produits contiennent des contaminants qui peuvent être considérablement plus abondants que les noyaux d'intérêt. Ces contaminants doivent être réduit au maximum pour permettre l'identification des noyaux étudiés. Leur présence peut engendrer des dommages aux détecteurs d'un point de vue balistique, mais aussi des temps morts additionnels dans les systèmes d'acquisition. Du fait de sa nature radioactive, le faisceau ne peut être stoppé. Donc, il est crucial d'avoir la plus précise des sélections afin de réaliser l'étude expérimentale avec la meilleure efficacité et dans des conditions de sûreté effective.

Les noyaux d'intérêt ont été produits par la technique ISOL (Isotopic Separation On-Line). Elle consiste au bombardement par un faisceau primaire (par exemple: protons, deuterons ou ions lourds) avec une cible suffisamment épaisse pour stopper les projectiles. Les atomes produits dans la cible sont stoppés dans un élément de "recueil", quelques fois comme à ISOLDE celui-ci est la cible elle-même. Les atomes alors diffusent/effusent hors de la cible et passent à travers une ligne de transfert. Afin de limiter le temps de transfert, la cible est portée à haute température (>2000°C) tout comme la ligne de transfert. Les atomes entrent alors dans une source d'ions qui ionise et permet l'accélèration de ceux-ci. L'intensité finale dépend grandement de la nature chimique des noyaux étudiés. En effet, la diffusion et effusion des noyaux sont gouvernées par les processus chimiques. Le principal avantage de cette technique vient du découplage en un faisceau primaire et secondaire. Le découplage permet d'atteindre une qualité optique de faisceau optimum. Cependant, les processus de diffusion/effusion/ionisation restreignent l'usage de la méthode à des noyaux dont le temps de vie est de plus de quelques millisecondes.
ISOLDE bénéficie du complexe d'accélérateurs du CERN. Le faisceau de protons utilisé pour produire les noyaux radioactifs est fourni par le PS-Booster. Il est pulsé avec un

temps de répétition de 1.2 s. Le PS-Booster est composé de quatre synchrotrons couplés qui délivre à ISOLDE des faisceaux de protons de 1.4 GeV jusqu'à 4 μA. Le faisceau de protons impactant une cible de $^{238}UC_x$ produit jusqu'à 10^{13} produits de fission par seconde. La cible est relativement épaisse $\sim$ 50mg/cm^2. Les isotopes de Rb ont un potentiel d'ionisation de $\sim$ 4.2eV relativement faible, ce qui va limiter la quantité de contaminants. Dans notre cas, les atomes sont ionisés via la technique d'ionisation de surface.
Après extraction de la source d'ions, les isotopes de plusieurs éléments sont présents dans le faisceau. Afin de sélectionner les ions radioactifs d'intérêt, le faisceau (RIB) passe au travers d'un séparateur de masses, dans notre cas le HRS (High Resolution Separator). Un dispositif "RFQ Cooler" améliore ensuite l'espace de phase du faisceau, en réduisant la dispersion axiale, radiale et en énergie.
Le faisceau provenant de la source d'ions à 60 keV est injecté dans un piège de Penning, appelé REXTRAP. Le faisceau est capturé dans le piège par des champs électromagnétiques. Ce dernier est rempli de gaz (généralement un gaz noble). Les collisions des ions avec le gaz réduisent la "température" du faisceau, le faisant décélérer de 60 keV à quelques eV, lui conférant une meilleure émittance transversale. Les ions sont alors concentrés en une collection compacte. Ils sont extraits du piège en décroissant le seuil du potentiel piégeant.
L'étape suivante consiste à accroître l'état de charge des ions afin de pouvoir post-accélérer le faisceau au travers d'un LINAC (LINear ACcelerator), en utilisant le processus d'impact d'électrons (EBIS). Les ions sont bombardés par un faisceau d'électrons mono-énergétique arrachant les électrons externes. REX-TRAP et REX-EBIS sont synchronisés afin d'extraire et d'injecter le faisceau proprement selon les collections d'ions. Donc, le temps de piégeage et le temps d'accroissement de la charge sont identiques.
Le gaz résiduel ainsi que certains contaminants ayant des A/q proches des noyaux d'intérêt sont également ionisés et extrait d'EBIS. En considérant la faible intensité du faisceau radioactif, il apparaît essentiel de purifier celui-ci. Un spectromètre de Nier à été installé dans ce but entre REX-EBIS et le LINAC. Ce dernier est composé de différents dispositifs d'accélération, notamment des cavités accélératrices. Il post-accélère le faisceau de quelques 5 keV/u à 2.83 MeV/u. Finalement, le faisceau est délivré au dispositif expérimental MINIBALL par un aimant de distribution.

L'excitation Coulombienne étant un processus de réaction laissant les noyaux émetteur en mouvement, l'application de corrections Doppler est requise pour recouvrer l'énergie photopic. Le dispositif MINIBALL a été designé dans ce but, avec une haute efficacité et une importante granularité, qui est nécessaire pour déterminer précisément l'angle d'émission des transitions γ. Le spectromètre MINIBALL consiste en un ensemble de détecteurs HPGE (High Pure Germanium) de haute résolution, disposer en géométrie rapprochée. Les détecteurs Germanium sont segmentés afin d'augmenter la granularité du dispositif. Celui-ci est composé de 8 groupes de détecteurs. Chaque groupe consiste en 3 cristaux de Germanium encapsulés dans une enceinte d'Aluminium. Les cristaux sont électriquement séparés en 6 segments le long de la direction radiale et autour d'une électrode de collection (appelée "core"). Les groupes de détecteurs sont placés à environ 11 cm de la cible secondaire, autour de la chambre d'excitation.
Sept différents signaux peuvent être extraits indépendamment pour chaque cristal: les énergies collectées par les segments et l'énergie collectée par l'électrode centrale de collection. La résolution intrinsèque des segments et "cores" sont différentes, respectivement $\sim$ 2.8 keV et $\sim$ 2.3keV.

Un système d'acquisition spécifique à été mise en œuvre afin de mettre en forme et

d'intégrer le plus efficacement et précisément les signaux d'énergie des transitions γ. Des pré-amplificateurs associés à des modules DGF (Digital Gamma Finder) réalisent respectivement l'amplification des signaux d'énergie brutes, leurs mises en forme et leurs intégrations. Les modules DGF possèdent quatre chaînes spectroscopiques complètes chacun. Ils ont une horloge interne rapide de 40 MHz. Afin d'éviter les décalages en temps de chaque module, ceux-ci sont synchronisés.
Le point d'interaction des transitions γ est défini comme le point d'impact (dépôt d'énergie) où la plus haute énergie à été détectée. L'énergie collectée par l'électrode centrale est assimilée à l'énergie totale.

Durant l'excitation Coulombienne les noyaux de recul et éjectiles sont collectés par un détecteur de silicium segmenté double face (DSSSD: double-sided silicon strip detector), appelé détecteur CD. Le détecteur de particules consiste en 4 différents quadrants. La face avant du détecteur est composée de 16 jonctions p^+n annulaires de 1.9 mm de largeur. La face arrière possède 24 secteurs n^+n angulaires (dépendance en ϕ) de type ohmique d'une ouverture de 3.4°. La couverture angulaire de diffusion dans le référenciel du laboratoire est 16.2°-53.3°, et la couverture azimutale représente 83% de l'espace azimutal total. Le détecteur de particules fut positionné à $\sim$ 29.5 mm de la cible secondaire.
Les signaux correspondant aux dépôts d'énergie produits par l'impact des particules dans le détecteur CD, sont préamplifiés par des cartes RAL-108 charge-sensible. Le signal résultant est mise en forme et discriminé à l'aide de cartes RAL-109, fournissant une chaîne électronique analogique complète pour chacun des éléments de détection du détecteur CD. Les signaux finaux des particules sont convertis au sein de module MADC-32. Ces derniers possèdent une horloge interne similaire au DGF de 40 MHz.
Comme décrit, le choix du système d'acquisition et de ses modules électroniques associés a été entièrement pensé afin d'optimiser la détection des coïncidences $\gamma - particule$ (haute granularité, échantillonnage court, haute efficacité, ...).

Le faisceau arrivant sur la cible secondaire n'est généralement pas complètement pur, et d'autres composantes que les noyaux d'intérêts peuvent être présents. Les composantes indésirables constituent une source de temps mort et peuvent endommager les détecteurs si le taux de comptage devient trop élevé.
De plus, dans le cadre de notre étude nous avons envisagé de normaliser les éléments de matrice de l'opérateur multipolaire par un élément de matrice connu. Dans notre cas, nous souhaitions réaliser la normalisation en prenant comme référence le(s) élément(s) de matrice de la cible. On comprend aisément que si la proportion de contaminants est importante alors l'excitation de la cible que nous observons est non seulement due aux noyaux d'étude mais également aux noyaux contaminants.
Les principales sources de contaminants proviennent de la cible primaire (contaminant isobarique avec leur nombre de masse similaire) et de REX-TRAP par l'extraction du piège du gaz de confinement. Afin de déterminer précisément la composition du faisceau une chambre d'ionisation est utilisée à la fin de la ligne de faisceau dédiée au dispositif MINIBALL.
La chambre d'ionisation consiste en un télescope de détection ΔE-E. Le détecteur ΔE est une chambre remplie de gaz CF4. Le détecteur E correspond à un détecteur silicium.
Lorsque les particules entrent dans la chambre, elles passent au travers du gaz et déposent une partie de leur énergie en ionisant les particules de gaz voisines. La différence de potentiel entre des électrodes placées dans la chambre transporte et collecte les charges. L'énergie restante est déposée dans le détecteur de silicium.

L'analyse des données s'est effectuée selon plusieurs étapes clés que nous allons décrire brièvement. Cependant, il est important de préciser que dans ce genre d'étude, il est courant de réaliser plusieurs fois la chaîne d'analyse afin de raffiner les résultats. En effet, l'obtention des différents paramètres permettant l'analyse provient en majorité de processus de minimisation.

Le système d'acquisition enregistre les données selon un format similaire aux systèmes MBS, nommé medfile (.med). Le code d'extraction des données brutes a été réalisé en langage C/C++ par Hans Törnqvist et moi-même. Il se base sur le code standard d'analyse on-line des expériences d'excitation Coulombienne de la collaboration MINIBALL. Les données brutes se présentent comme une collection de valeurs ordonnées en temps et modules, cependant aucune corrélation n'exite entre elles. Lors de l'extraction, les données sont structurées selon des arbres contenant seulement les corrélations particule-γ. Afin de rendre le processus plus rapide, une partie du bruit de fond est exclu du traitement; par exemple, un seuil de traitement des données a été fixé aux détecteurs de particules pour lesquels d'important bruits de fond sont observés à basse énergie.

La calibration en énergie des détecteurs germanium de MINIBALL a été réalisée en utilisant des sources de ^{152}Eu et ^{138}Ba dont on connaît précisément les énergies et rapports d'embranchement des transitions les plus intenses. Afin de déterminer l'efficacité absolue des détecteurs de germanium, une source additionnelle de ^{60}Co, dont on connaît l'activité, a été employée. L'efficacité absolue, sur la large gamme d'énergie balayée par les sources, est obtenue en normalisant les efficacités relatives par l'efficacité absolue trouvée pour la source de ^{60}Co.
Comme nous l'avons déjà mentionné lors de l'excitation Coulombienne, la plupart des transitions γ sont émises en vol. De ce fait, des corrections Doppler sont nécessaires.
Afin de réaliser celles-ci dans de bonnes conditions, la connaissance précise de la position des détecteurs germanium et silicium est requise. Les détecteurs germanium sont montés sur des bras amovibles permettant un changement des angles (θ,ϕ,α). Le couple (θ,ϕ) dénote la position de l'axe central du groupe de détecteurs, l'angle α correspond à la rotation de l'ensemble du groupe autour de son axe de symétrie. Grâce aux graduations présentent sur les bras amovibles, la position des détecteurs est approximativement connue. Mais afin d'obtenir un positionnement plus fin, la réaction de transfert $^2H(^{22}Ne,^{23}Ne)p$ a été utilisée. Durant la réaction de transfert l'état $1/2^+$ de 1017 keV du noyau ^{23}Ne peut être peuplé. Sa courte durée de vie lui permet de se désexciter en vol. L'optimisation de la position est faite grâce à la minimisation de la largeur des pics photoélectriques pour lesquels la correction Doppler doit être optimisée. L'optimisation des largeurs Doppler est un processus itératif. Notons que dans le cas présent la position du détecteur de particules est supposée connue. Si un raffinement de la position du détecteur CD est nécessaire alors le processus de positionnement des détecteurs germanium doit être réitéré, et inversement.

La calibration en énergie des détecteurs de particules s'effectue en plusieurs étapes. Une pré-calibration est réalisée à l'aide de sources d'alpha d'une énergie d'environ 5 – 6MeV. Etant donné que l'énergie de notre faisceau est de l'ordre de $\sim$ 270MeV, on devra beaucoup extrapoler et cela donnera des résultats médiocres mais suffisant pour commencer un raffinement de la calibration.
Dans une seconde approche nous avons réalisé une calibration à l'aide de la diffusion Rutherford d'un faisceau cocktail en provenance de REX-EBIS sur une cible de ^{196}Pt. La diffusion Rutherford étant bien connue, nous pouvons déterminer l'énergie attendue pour

un angle θ donné. La calibration fut améliorée, mais sa qualité était toujours insuffisante pour l'obtention de corrections Doppler satisfaisantes.
Finalement, en se basant sur les données de calibration obtenues via le faisceau cocktail, la calibration a été raffinée en utilisant les données avec faisceau de Rb.
La calibration obtenue correspond à une énergie de faisceau incident d'environ 180 – 200MeV, ce qui est significativement plus bas que l'énergie de faisceau utilisée d'environ ~270 MeV. Considérée dans un premier temps comme erronée de plus amples tests ont été réalisés; ils convergèrent sur une énergie incidente plus faible.
Les processus d'excitation et de des-excitation ont des échelles de temps différentes. En effet, l'excitation est un processus rapide de l'ordre de 10^{-20}s et la des-excitation de l'ordre de 10^{-12}s. Donc, même si l'excitation se produit dans la cible, le temps de désexcitation est suffisamment long pour que le noyau excité parcourt l'ensemble de la cible avant d'émettre une transition γ. Lors de son parcours, le noyau perd de l'énergie ce qui explique pourquoi une plus faible énergie incidente de faisceau est trouvée.
Afin d'améliorer les corrections Doppler le positionnement précis du détecteur de particules à également été réalisé.

Après une première calibration de l'ensemble des détecteurs, les spectres de transitions γ simples (correspondant à une coïncidence particule-γ) peuvent être obtenus. Afin d'obtenir l'intensité correcte des transitions, nous sélectionnons les événements (particule-γ) prompts par le biais de la différence en temps, entre la détection de la particule et de la transition γ. A ces événements prompts, nous soustrayons des événements aléatoires provenant de coïncidences fortuites. La largeur en temps des composantes aléatoires et prompts doit être équivalente. D'autres corrections doivent être également apportées comme l'efficacité et les coefficients de conversion électronique.

L'investigation de structures excitées totalement inconnues requiert l'utilisation d'outils spécifiques, afin d'identifier et construire les différentes cascades de transitions γ. Si durant le processus de des-excitation, les transitions γ d'une même cascade sont détectées dans des détecteurs différents au même instant, alors elles sont qualifiées de transitions coïncidentes. La fenêtre de coïncidence temporelle doit être aussi courte que possible en optimisant le ratio $N^{\gamma}_{vrai\ coinc.}/N^{\gamma}_{alatoire\ coinc.}$. Elle a été obtenue en étudiant l'évolution du nombre de coïncidences en fonction de la largeur de la fenêtre de coïncidence. Après un certain temps, l'accroissement du nombre de coïncidences se stabilise. Cela correspond au temps après lequel la grande majorité des coïncidences sont fortuites.
Grâce à l'identification des événements coïncidants, nous avons construit une matrice $\gamma - \gamma$ des événements coïncidants (E^{γ}_1 vs E^{γ}_2). Les projections de ces matrices assurent l'identification des transitions γ coïncidantes.
La diffusion Compton impacte directement sur l'identification des énergies de transitions γ, créant des événements avec des énergies plus basses que l'énergie photopic. L'ensemble de détection MINIBALL n'a pas de détecteurs visant à identifier les événements Compton. Cependant, selon la formule énoncée par Klein et Nishina, une couverture angulaire minimisant la probabilité d'avoir des événements Compton peut être définie. Dans notre cas nous avons rejeté l'ensemble des événements coïncidants ayant un angle de 40 degrés entre eux.

Comme mentionné précédemment, l'analyse d'une expérience d'excitation Coulombienne "sûre" à pour but l'extraction des éléments de matrice d'une manière modèle indépendant. Le code GOSIA a été utilisé dans ce but. Celui-ci réalise une minimisation de moindre carré des taux de transition expérimentaux et théoriques en utilisant des calculs d'équations couplées dans la limite des considérations semi-classiques.

En d'autres termes, GOSIA ajuste chaque élément de matrice par minimisation du χ^2 afin de reproduire les intensités de transitions γ observées en fonction de l'angle de diffusion. Cette minimisation prend en compte l'ensemble des données spectroscopiques connues.

Ces expériences d'excitation Coulombienne des isotopes de Rb avec une cible de ^{60}Ni permirent l'identification de nouvelles transitions et structures excitées. L'analyse de ces excitations Coulombiennes par le code GOSIA a fourni de nombreux éléments de matrice transitionnels et diagonaux. Cependant, le nombre d'observables et leurs précisions ne sont pas suffisantes pour contraindre fermement les éléments de matrice.
Les éléments de matrice transitionnels peuvent être traduits en transitions de probabilité réduites et les éléments de matrice diagonaux en moments quadrupolaires statiques.

A l'issue de cette expérience, de nouvelles transitions de basse énergie d'excitation ont été identifiées dans les isotopes ^{93,95}Rb. Ces derniers présentent des structures excitées de type particule-célibataire similaires. A la fermeture de sous-couche à N=56, l'inversion des configurations de spins des états fondamentaux entre les isotopes ^{91}Rb(N = 54,3/2$^-$) et ^{93}Rb(N = 54,3/2$^-$) peut être expliquée par une force tenseur entre les partenaires spin-orbite $\nu g_{7/2}$ et $\pi g_{9/2}$.
Ayant des structures similaires, ils sont susceptibles d'avoir des configurations similaires et donc des transitions de probabilité proches. En effet, cela est le cas pour les transitions de probabilité B(E2). Cependant, la faible sensibilité de la technique par rapport au caractère M1 ne nous permet pas de déduire plus d'informations sur leurs propriétés physiques.

Cette étude expérimentale permit la première observation des structures excitées des isotopes ^{97,99}Rb. Ces derniers présentent tous les deux des bandes rotationnelles très similaires. L'observation de bandes rotationnelles constitue une preuve directe de la non-sphéricité de leurs états fondamentaux.
Entre la réalisation de l'expérience présente et son analyse, deux expériences réalisées à l'ILL (Grenoble) et RIKEN (Japan) prouvèrent la présence d'une transition d'environ 76.5 keV provenant d'un état isomérique de ~5-7 μs. Deux différents assignements ont été supposés pour cet état isomérique, l'un basé sur l'orbitale 3/2$^-$[312] déformée oblate, et l'autre sur l'orbite sphérique $f_{5/2}$. Du fait de sa nature, cette transition n'a pas été identifiée dans notre expérience.
Lors de notre expérience une transition de 275keV a été observée en coïncidence avec certaines transitions de la bande rotationnelle de l'état fondamental. Celle-ci pourrait correspondre à une autre configuration que celle de l'état fondamental et de l'état isomérique de 76.5 keV.
La présence d'une quantité importante de Kr stable dans le faisceau de ^{99}Rb, ainsi que la très faible excitation de la cible n'ont pu permettre la normalisation des éléments de matrice pour cet isotope.

Concernant le noyau ^{97}Rb, des calculs du modèle Quasi-particule + Rotor ont été réalisés par G. Simpson. Ceux-ci reproduisent parfaitement les données expérimentales et prédisent l'existence de deux états nucléaires de configurations différentes à 600 keV (1/2$^+$[440] et 5/2$^+$[422]). D'autres calculs théoriques réalisés par F. Kondev ont été confrontés aux résultats expérimentaux afin d'identifier l'orbitale déformée sur laquelle la bande rotationelle est construite. Le modèle à quasi-particules consiste en l'utilisation du potentiel de Yukawa et de la théorie BCS. Les rapports d'embranchements, de probabilités de transitions B(M1)/B(E2), ainsi que $|g_K - g_R|$ et $|\delta|$ ont été calculés pour les configurations possibles de part les mesures de moments dipolaires magnétiques: 3/2$^+$[431], 3/2$^-$[312] et 3/2$^-$[301]. La configuration 3/2$^-$[312] est complètement exclue, ne reproduisant pas

les résultats expérimentaux pour chacune des variables citées plus haut. La configuration $3/2^+[431]$ est la plus favorisée étant en très bon accord avec les résultats expérimentaux. La dernière configuration est peu favorable du fait d'une déviation significative comparée à l'expérience.
La présence d'un effet d'oscillation de la constante rotationelle ($A=\hbar^2/(2I)$) en fonction du spin nucléaire à été mise à jour. Le moment d'inertie est presque constant sans compter la présence de séparation de signatures. Le découplage des signatures pourrait être dû à une importante force de Coriolis ou à la perturbation appliquée par une autre bande avec un nombre quantique K différent.

La technique de l'excitation Coulombienne constituant d'ors et déjà un outil très performant pour l'étude de la structure nucléaire pourrait être améliorée dans le cas d'une utilisation de faisceaux radioactifs polarisés. On peut vraisemblablement envisager de possibles effets dans les distributions angulaires, ce qui pourrait aider à déterminer la nature des transitions (M1, E2, ...).
Nous nous proposons d'étudier la possibilité de polariser des faisceaux radioactifs via la technique dite des feuilles orientées (TFT) au CERN. Le projet de polarisation au CERN débuta il y a de nombreuses années avec la plate-forme haute tension. Le but ultime de ce projet serait d'offrir la possibilité de délivrer des faisceaux radioactifs polarisés que l'on puisse post-accélérer.

Plusieurs techniques existent déjà pour produire des ensembles de noyaux orientés. L'orientation peut être obtenue par des mécanismes de réaction où le noyau étudié est produit, ou, par l'interaction de la collection de noyaux avec son environnement. La plus ancienne technique employée pour produire des ensembles polarisés est l'orientation nucléaire à basse température (Low Temperature Nuclear Orientation: LTNO). Les noyaux sont généralement implantés dans un échantillon ferromagnétique à très basse température ($\sim$ mK) et un champ magnétique intense d'environ quelques Tesla est appliqué à l'ensemble. Les spins nucléaires s'orientent dans la direction préférentielle du champ. Le taux de polarisation résultant est de l'ordre de 10-100%.
Nous pouvons citer un autre processus de polarisation, le pompage optique. On peut obtenir une polarisation quasi totale des ensembles nucléaires, cependant le degré de polarisation dépend grandement de la structure atomique.

La technique des feuilles orientées consiste à faire passer le faisceau au travers de fines feuilles de carbone ayant un angle avec l'axe du faisceau. Durant son passage dans la feuille, la polarisation atomique et nucléaire sont considérées comme complètement découplées. A la surface de sortie de la feuille, les états électroniques des ions sont polarisés par asymétrie de charge créée par l'angle d'orientation.
Après la feuille, l'ion est atomiquement polarisé. Le transfert de la polarisation atomique à la polarisation nucléaire se produit en vol par interaction hyperfine. Dans ce cas, F est un bon nombre quantique et se conserve, il résulte du couplage du spin nucléaire I et du spin atomique. Afin de réaliser ce transfert, le système doit avoir suffisamment de temps pour précesser un nombre important de fois ($\omega t \gg 1$), afin de moyenner le spin nucléaire qui aura tendance à pointer dans la direction de F.
Afin d'obtenir un haut degré de polarisation, le faisceau peut traverser un certain nombre de feuilles. La polarisation atomique sera affectée par la feuille suivante alors que le spin nucléaire sera supposé non affecté.

Un polariseur contenant jusqu'à 10 feuilles orientées a été conçu afin d'étudier les différents impacts de la technique sur le degré de polarisation résultant. Afin de mesurer

l'asymétrie des distributions de particules β, un dispositif β-NMR à été installé dans la continuité du polariseur. Une expérience test a été réalisée récemment en juillet 2012 afin d'évaluer le potentiel du nouveau polariseur. Les résultats préliminaires indiquent l'obtention d'une asymétrie d'environ 1%.

L'expérience de préparation a prouvé que le dispositif créé à ISOLDE était prêt pour de plus amples investigations de la technique, exemples: dépendance en énergie du faisceau, nombre de feuilles, angle des feuilles, la fermeture des couches atomiques après polarisation etc.

La prochaine étape consistera en l'étude de la post-accélération de faisceaux radioactifs polarisés.
Le dispositif de polarisation est d'ors et déjà l'objet d'une proposition d'expérience visant à mesurer le moment magnétique des isotopes d'indium.

Introduction

During the last decades, the neutron rich A∼100 N∼60 region has been under intensive and extensive investigations. The underlying structure in the region has been mainly studied by β-decays and γ-ray spectroscopy from induced fission via high energy protons or thermal neutrons and spontaneous fissions.
In this part of the nuclear chart, the most sudden development of deformation has been observed. By adding just few neutrons/protons, a rapid shape transition occurs from spherical to well deformed ground state shape around N∼60. Shape coexistence has been expected and observed in the Sr and Zr nuclei.
Deformed ground states are clearly observed around N∼60 between the Mo and Rb isotopes, it is not straightforward to determine a strict limit of this onset of deformation. The last mass and charge radii measurements indicates the lack of sudden onset of deformation for the lowest atomic Kr isotopes (Z=36).

The mechanisms involved in the development of deformation are not well understood. The interplay between down-sloping and up-sloping neutron Nilsson orbitals is evoked as one of the main reasons for the sudden shape change. However, until now no experimental evidence has been forthcoming that establishes the relative importance of these orbitals. A clear identification of the active proton and neutron orbitals was still ongoing, and more experimental data were requested on low-lying excited structure.

The recent development of Radioactive Ion Beam (RIB) allowed to study the region via other reaction mechanisms. The collaboration around the γ-ray array MINIBALL at CERN envisaged to study extensively the A∼100 mass region by Coulomb excitation in order to clarify the situation. The Coulomb excitation is governed by different selection rules than the previous reactions used to populate excited states. Its strong potential to improve our knowledge on single particle-like and collective states in the exotic nuclei has been illustrated many times, e.g. in the odd-A and odd-odd Cu isotopes. Recently, Coulomb excitation studies of ^{94,96}Kr isotopes corroborated the mass and charge radii measurements. Positioned between the Kr and Sr isotopic chains, the Rb isotopes are the first exhibiting deformed ground states. Thus, placed at the corner of the shape transition, they are of great interest to understand the underlying nuclear structure as well on the proton side as on the neutron side.

The Coulomb excitation studies of the neutron rich ^{93,95,97,99}Rb isotopes reported here aim at identifying the active orbitals in low lying states. A number of excited states have been already identified in ^{93,95}Rb from previous β-decay and isomeric studies. On contrary, the excited states of ^{97,99}Rb were completely unknown. Far from stability, the study of such short lived and high mass beam requests a high purity, selectivity and intensity. The nuclei of interest have been produced at ISOLDE (CERN), purified and post-accelerated up to 2.85 MeV/u by REX-ISOLDE and delivered to the MINIBALL setup, where they are Coulomb excited impinging in a secondary target.
Prompt γ-ray coincidences of low-lying states have been observed and time correlated to build partial level scheme. The associated transition strengths have been extracted with the code GOSIA. The observed matrix elements of the electromagnetic operator constitutes new inputs of further theoretical calculations giving new insight on the involved orbitals.

In order to increase the sensitivity of the odd mass Rb Coulomb excitation, it has been envisaged to use radioactive nuclear spin polarized beams with the Tilted Foils Technique (TFT). This technique presents different advantages such as the possibility to polarize any nuclei with an atomic/nuclear spin different from zero. Designed as a compact setup to be easily introduced in existing beam lines, it can constitute a powerful tool for future experiments. Some models have been developed to describe and reproduce the experimental data, trying to explain the polarization mechanism in presence. However, more experimental data are requested to establish the relative impact of the technical parameters on the obtained beam polarization, such as the foils angle of the incoming beam energy.
A β-NMR setup has been developed at CERN to clarify the situation and to investigate the possibility to use polarized post-accelerated RIB. The development phase and the first tests on ^{8}Li are presented here. They constitute an important step for further investigations.

The study realized on the Coulomb excitation of odd-mass Rb isotopes and the experimental setup to

polarize radioactive beams using the Tilted Foils Technique are discussed in two distinct parts.

In the Coulomb excitation part, an effort has been made to introduce some basic concepts and models in nuclear physics. The physics motivations supporting such study will be argued, describing the problematic of the region A∼100 N∼60. A special attention will be made to understand why the study of neutron rich Rb isotopes is a keystone. Afterwards, the production and experimental setup will be described in details as well as the analysis tools developed and used for the present study. At the end, the different results extracted from the collected data will be discussed and interpreted.

The second part is dedicated to the nuclear spin polarization using the specific tilted foils technique. A complete presentation of the β-NMR experimental setup and different issues of the development will be described. The last chapter treats about the preliminary results obtained during the first successful test performed in July 2012.

Finally, a conclusion on the present studies and the possibility to combine them will be drawn. Some outlooks will be put into perspectives in order to give clues for further studies.

Part I

Study of Odd-Mass Neutron-Rich Rubidium Isotopes by Coulomb Excitation

Chapter 1

Generalities on the Nuclear Structure

1 Introduction: The atomic nucleus

The study of the atomic nuclei is a piece of the puzzle constituting our knowledge of some aspects of the Nature. The mass of matter is essentially concentrated in the nucleus. Basically, the mass and charge of the atoms determine most of the physical and chemical properties of the matter. The knowledge of the atomic nucleus is important to probe the forces governing this many body system, but it also impacts other domains such as the astrophysics helping to understand the nucleosynthesis processes.

The evolution of the nuclear shell structure far from stability is one of the fundamental and still opened questions in nuclear physics. Many models exist to reproduce the experimental observables. All of them are based on a representation of the nuclear matter. Each model leads to some simplifications or approximations of certain aspects of the nucleus. By virtue to the nucleus, some of the models are more appropriate than the other, describing in a better way some of its behaviours under specific conditions.

The atomic nucleus is constituted by two types of fermions - the neutrons and protons - with opposite isospin. The nucleus forms a bound system where the neutron and proton are in strong interaction to maintain the cohesion of the system. The strong interaction can not been treated as a perturbation problem. In addition, the approach of statistical physics can not be applied for such small system.

The nuclear shape is intrinsically linked to its tendency to minimize the energy inside a constant volume. The perfect minimization for an isotropic system would correspond to a uniform distribution of nucleons as a sphere. Browsing the nuclei chart it appears clearly that the tendency to roll away the spherical form is the most common case. Taking into account the degrees of freedom related to the deformation, the experimental observables such as the level schemes or the transition strengths could be reproduced.

1.1 Interactions and cohesion in the atomic nucleus

1.1.1 Stability and radioactivity

Firstly, to unearth the stable or unstable (N, Z) combinations, we have to understand the principle of the total relativistic energy. For example in case of unstable/metastable (N, Z) combinations, in order to minimize the total energy, a decay can occur and thus create a new (N, Z) combination more stable.

Those radioactive processes are governed by several laws such as the conservation of the total number of nucleons (conservation of the baryon number). If we consider a collection of unstable nuclei searching to minimize their total relativistic energy by decay, they will emit particles (α, β^+, β^-, ...) in order to find a more stable (N, Z) combination. The experimental observation led to a characteristic down-sloping exponential, proportional to the number of nuclei (N(t)) at a given time t. The radioactivity law is written as:

$$\frac{dN(t)}{dt} = -\lambda N(t) \tag{1.1}$$

Resolving this differential equation, one obtains: $N(t) = N_0(t)e^{-\lambda t}$: nuclei number at a given time t, N_0 the initial number of nuclei, λ : decay constant.

One defined the lifetime as : $\tau = \frac{1}{\lambda}$ and the half-life as : $T_{1/2} = \frac{ln(2)}{\lambda} \cong \frac{0.693}{\lambda}$.

1.1.2 Forces and cohesion in the microscopic world

A nucleus is so small that the macroscopic and mesoscopic physics "rules" are not relevant anymore, their order of magnitude are staggered. At the scale of a nucleus (femtometer = 10^{-15} m), the only in-play macroscopic forces are the repulsive Coulomb force acting between the protons and the attractive gravitation force. However, the gravitation can be neglected due to the simple reason that at such range the Coulomb interaction is several order of magnitude higher. The nucleus is constituted of neutrons (neutral) and positively charged protons, which should be repulsed under the effect of the Coulomb interaction. Thus, how the cohesion of nucleons is possible?

An interaction from other origins was needed to restore the cohesion of the nucleus: the strong nuclear interaction. This one acts as a strong attraction in a really reduced range of distances, explaining its none observation in the macroscopic world.

Another interaction called the weak interaction plays an important role, its intensity is several orders of magnitude lower than the strong interaction. For example, the electrons being not sensitive to the strong interaction can feel intensively the weak interaction. The β-decays are one of the expression of the presence of weak interaction.

One of the primordial principle administering the infinitesimally small world, is the Pauli principle [1]. According to their fermionic nature the protons and neutrons obey to the Pauli principle. They have antisymmetric wave functions, this character results in the impossibility for fermions to possess the same quantum numbers. In quantum physics, the corrections associated to this principle are called exchange corrections, see Ref. [2] for application.
This principle is necessary to restore the over-stability observed experiementally for specific protons/neutrons numbers, commonly called "magic" numbers, see Ref. [3]. We could roughly explain the building of level scheme by the way that nucleons should have different quantum states, which are pushed higher in energy under the effect of the Pauli principle.

At high energy the strong interaction is more or less understood, but at low energy the problem is far to be completely solved. In order to study the fundamental strong interaction, it is also important to study the many-body problem that constitutes the atomic nucleus. The two-body problem would not provide the same informations than the many body interactions.

The experimental observables can be explained by nuclear potentials with different forms. Note that the intrinsic interaction between the free nucleons are more important than between the nucleons bound inside the nucleus. This effect is mostly explained by the Pauli principle, taking into account quantumly the presence of more than one particle. The structure of nuclei is essential to understand the forces in presence.

Due to a unaccomplished portrait of the strong interaction, it remains difficult to create a unified theory permitting to reproduce the N-body problem that constituted the nucleus. Therefore, the simplest models have been investigated, passing through the liquid drop model to the more complicated model such as the Nilsson model. Each model stresses on a particular characteristic of the nuclear matter reproducing the nuclear structure locally.

1.2 Distribution of matter in the nucleus

The nuclear matter can be represented with an average density function ρ(r), see Fig. 1.1, called the Fermi function, defined as:

$$\rho(r) = \frac{\rho_0}{1 + e^{(\frac{r-R}{a})}} \tag{1.2}$$

with: R$\approx$R$_0\cdot$A$^{1/3}$ [fm] is the nuclear radius, a$\simeq$ 0.55-0.60 [fm] is the diffuseness constant, ρ_0 is the initial density found at the center.

This density is almost constant in the inner part of the nucleus and a surrounded density takes place with a relatively high gradient to reach zero. It also agrees with the simple representation of the nucleus as an inert core surrounded by a valence space which confers most of the properties of the nucleus.

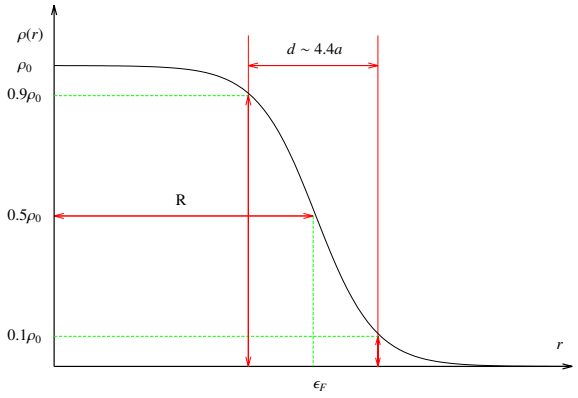

Figure 1.1: Average radial distribution of the nuclear matter density. ϵ_F is the Fermi energy, defined as the energy of the highest occupied state in a fermion particle system. d~ $(4 \cdot \ln(3))$a [fm] is the skin thickness of the nucleus [1].

One of the most common experimental observables used to probe the distribution of matter in the nucleus is the root mean square charge radius. The average square radius of the charged particle distribution (ρ_c(r)) is defined as:

$$< r_c^2 >= \frac{\int r^2 \rho_c(r)\, d^3r}{\int \rho_c(r)\, d^3r} \tag{1.3}$$

In order to get informations on the nuclear proton distribution, the probe needs to have a wavelength smaller than the object of the analysis. The electrons were the most appropriated particles available to evaluate the nuclear radius, thanks to the well known Coulomb interaction, see Fig. 1.2. Note that the discovery of the atomic nucleus has been done in 1903 by Rutherford [4] with impinging α-particle on an Al target (Au target had been used after).

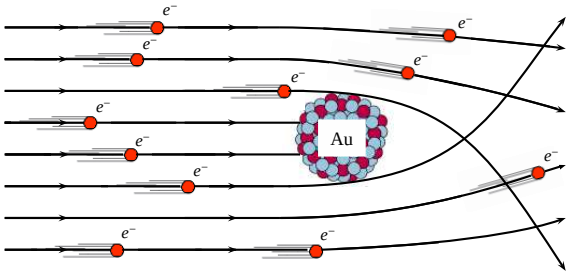

Figure 1.2: Electron scattering from the Coulomb attraction of the nuclear charge. This experiment is similar to the discovery of nucleus in 1903 by Rutherford and Soddy [4].

2 Nuclear Structure and deformation

2.1 Introduction: nuclear structure

In a simple representation, the nucleus can be regarded as a sphere whose the neutrons and protons distribution would be isotropic. We retrieve such spherical form for a few nuclei and particularly in the case of magic nucleus with totally occupied nuclear shells (8, 20, 28, 50, 82 ...) according to the standard shell model. Nevertheless, most of nuclei deviate from the sphere and acquire deformed shapes in order to minimize their potential energies, allowing them to be more stable. A nucleus is considered as deformed if its shape deviates from the sphere.

In an appropriate quantum description, the nucleons occupy specific orbits. By analogy, classically, static charge and current distributions generate fields. If they vary sinusoidally with an angular frequency (ω), a

radiation field is produced. It can be described as a development in electric/magnetic multipole moments for a point at a distance R from the z-axis.

$$V(R) = \frac{1}{R}\int \rho(r)dr + \frac{1}{R^2}\int z\rho(r)dr + \frac{1}{R^3}\int (3z^2 - r^2)\rho(r)dr + ... \tag{1.4}$$

For most of the cases, the nucleus can get an elongated shape that can be approximated as an ellipsoid with axial symmetry. In such a case, the monopole and quadrupole terms can describe the nuclear shape.

2.2 Parametrization of the deformation

The nuclear shape can be expressed through the following parametrization of the nuclear radius as seen in Subsec. 1.2. Usually the nuclear radius is expanded in spherical coordinates:

$$R(\theta,\phi) = R_0\left[1 + \sum_{\lambda=1}^{\infty}\sum_{\mu=-\lambda}^{\lambda}\alpha_{\lambda\mu}Y_{\lambda\mu}(\theta,\phi)\right] \tag{1.5}$$

with: $R(\theta,\phi) \in \mathbb{R}$, i.e. $R(\theta,\phi) = R^*(\theta,\phi)$, R_0: sphere radius of the same volume.
The spherical harmonics $Y_{\lambda\mu}(\theta,\phi)$ have the standard characteristics:

$$Y^*_{\lambda\mu}(\theta,\phi) = (-1)^{\mu}\, Y_{\lambda-\mu}(\theta,\phi) \tag{1.6}$$

and

$$\int Y^*_{\lambda\mu}Y_{\lambda\mu'}d\Omega = \delta_{\lambda\lambda'}\delta_{\mu\mu'} \tag{1.7}$$

The parameters $\alpha_{\lambda\mu}$ represent the shape deformation.The equation 1.6 leads to:

$$\alpha^*_{\lambda\mu}(\theta,\phi) = (-1)^{\mu}\,\alpha_{\lambda-\mu}(\theta,\phi) \tag{1.8}$$

with: λ the deformation mode (or degree) and μ the order:

$$\begin{cases} \lambda = 0: & \text{monopole deformation (volumic variation)} \\ \lambda = 1: & \text{dipolar deformation} \\ \lambda = 2: & \text{quadrupolar deformation (axially symmetric deformation: prolate, oblate)} \\ \lambda = 3: & \text{octupolar deformation} \\ \lambda = 4: & \text{hexadecapolar deformation} \end{cases}$$

After a transformation in the body-fixed frame described by the Euler angles, the symmetry properties impose the disappearance of the $\alpha_{\lambda\mu}$ coefficients except α_{2-2}, α_{22} with $\alpha_{2-2} = \alpha_{22}$. The two intrinsic variables of the deformation α_{20} and α_{22} can be re-expressed with the β and γ deformation parameters formulated by Hill and Wheeler [5]:

$$\begin{cases} \alpha_{20} &= \beta\cos\gamma \\ \alpha_{22} &= \dfrac{1}{\sqrt{2}}\beta\sin\gamma \end{cases} \tag{1.9}$$

For small oscillations of the ellipsoid, introducing the Hill and Wheeler deformation parameters, the radius is found to be:

$$R = R_0\left(1 + \beta\sqrt{\frac{5}{16\pi}}\cos\gamma(3\cos^2\theta - 1) + \sqrt{\frac{15}{16\pi}}\sin\gamma\sin^2\theta\cos(2\phi)\right) \tag{1.10}$$

The extreme deformation modes are found to be:

$$\begin{cases} \text{If } \gamma \bmod 60° \neq 0 & : & \text{the nucleus has a triaxial shape.} \\ \text{If } \gamma = 0°, 120° \text{and } 240° & : & \text{the ellipsoid has a stretched shape called prolate shape.} \\ \text{If } \gamma = 60°, 180° \text{and } 300° & : & \text{the ellipsoid has a flatten shape called oblate shape.} \end{cases}$$

A summary of the different possible configurations in the (β,γ) plane are shown on the Fig. 1.3.

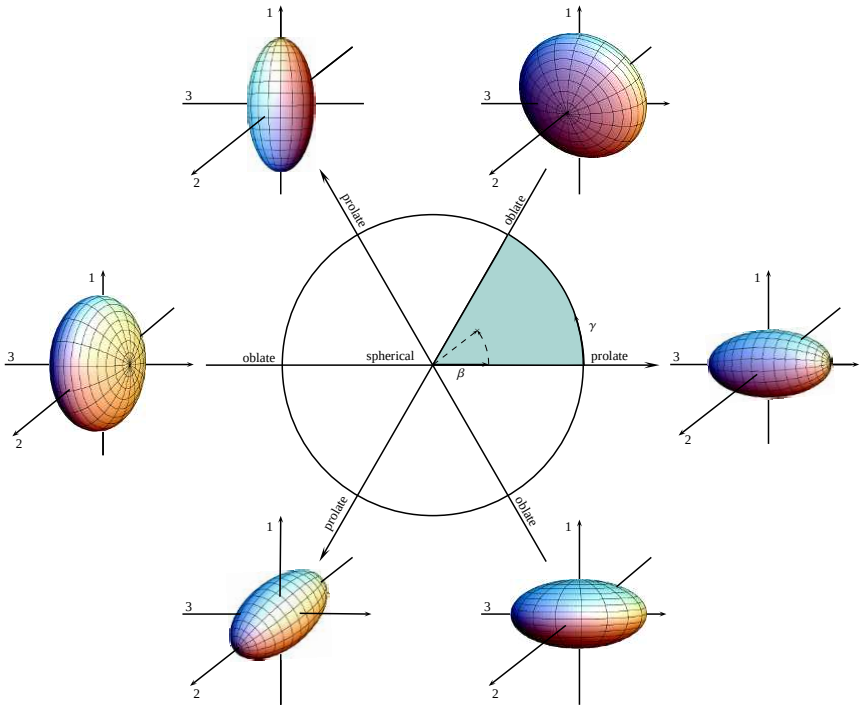

Figure 1.3: Deformation parametrization of Hill and Wheller, see Ref. [5].

3 Nuclear Models

Most of the nuclear models are often used locally in order to describe a specific region of the chart. For light nuclei, the relatively small amount of nucleons gives the possibility to use the two-body interaction to reproduce the nuclear behaviours, e.g. in ab-initio calculations, see Ref. [6], see Fig. 1.4. However going to heavier nuclei, the amount of correlations impedes an analytic solution treated via the two-body interaction. Usually called N-body problem, it exists different approach to reduce the number of correlations, e.g. the nucleons can be separated in an inert core and a valence space assumed responsible of the nuclear properties. An effective two body interaction of the nucleon-nucleon force can be considered and a nuclear mean field can be generated in a self consistent way. Each nucleons constituting the nucleus feels a mean potential corresponding the sum up of all interactions. Those calculations are usually called mean field theory calculations. Other models exists, among them, the nuclear "shell model" calculations considering as inert the inner shells. In the following, some of the precursor and more recent models representing the nucleus are briefly described in order to present some concepts and formalisms.

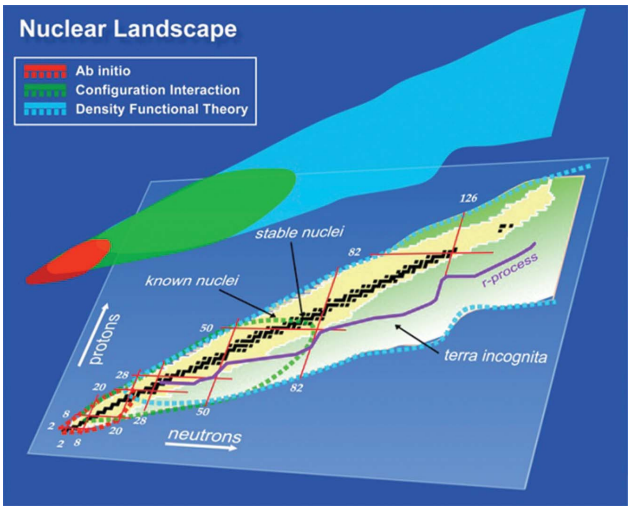

Figure 1.4: Different types of calculations used in the nuclear chart. The current ab-initio calculations are restricted to light nuclei with limited nucleon-nucleon correlations. The Unified Nuclear Energy Density Functional technique can potentially be applied on the whole nuclear chart excepted the light nuclei. The blue sector is sufficient to describe the nuclear deformation. From Ref. [7].

3.1 Liquid Drop Model

In 1932, Chadwick [8] discovered the neutron and gave rise to a new field in physics, the nuclear structure study. Actually, the same year, Heisenberg developed a theoretical model representing the nucleus based on a combination of neutrons and protons. In the following years, several experiments showed a characteristic feature: the binding energy has a saturation level for the binding energy per nucleon ($\left(\frac{B(N,Z)}{A}\right)_{max} \approx 8.8$ MeV), see Fig. 1.5. In 1935, Weizsäeker [9] published a model of the binding energy making the analogy between the nucleus and a liquid drop. The nucleus is assimilated to a quantum fluid of nucleons confined by strong interaction in a finite volume. In fact, for a liquid drop the evaporation energy is proportional to the number of evaporated atoms; concerning the nuclei, the binding energy is roughly proportional to the nucleon number.

As a result, the Weizsäeker-Bethe-Bloch formula has been established:

$$B(N,Z) = \underbrace{a_v A}_{\text{Volume term}} + \underbrace{a_s A^{2/3}}_{\text{Surface term}} + \underbrace{a_c \frac{Z^2}{A^{2/3}}}_{\text{Coulomb term}} + \underbrace{a_a \frac{(N-Z)^2}{A}}_{\text{Asymmetry term}} - \underbrace{\delta(A)}_{\text{Pairing term}} \tag{1.11}$$

with:
- $a_v A$: $a_v \approx +16$ MeV, proportional to the volume ($\propto A$), called volume term, it represents the evaporation energy of one nucleon in an infinite space.
- $a_s A^{2/3}$: $a_s \approx -18.56$ MeV, proportional to the surface of the nucleus ($\propto A^{2/3}$), is called surface term. It describes the lower strength felt by the nucleons on the boundary surface of the nucleus.
- $a_c \frac{Z^2}{A^{2/3}}$: $a_c \approx -0.7$ MeV, this term called Coulomb term represents the repulsion due to the Coulomb interaction ($\propto Z^2$) acting between protons.
- $a_a \frac{(N-Z)^2}{A}$: $a_a \approx -25$ - -30 MeV, called the asymmetry term, it describes the difference in energy created by a none equal numbers of neutrons and protons (minimal for $N = Z$).
- $\delta(A) \approx$ $\begin{cases} +34A^{-3/4}, & \text{if (N:odd, Z:odd)} \\ 0, & \text{if (N:even, Z:odd) or(N:odd, Z:even)} \\ -34A^{-3/4}, & \end{cases}$

The binding energy per nucleon increases rapidly along the mass number and reaches at $A \sim 15$ a value of ~ 8 MeV, see Fig. 1.5. The volumic term is predominant for low masses, the surface energy starts to become the dominant term of the semi-empirical mass formula, see Eq. 1.11 on the facing page. The largest value is obtained for the ^{56}Fe which is logically the last nucleus produced in the stars. For higher masses the Coulomb repulsion deflects the binding energy curve giving less cohesion of the nuclear structure.

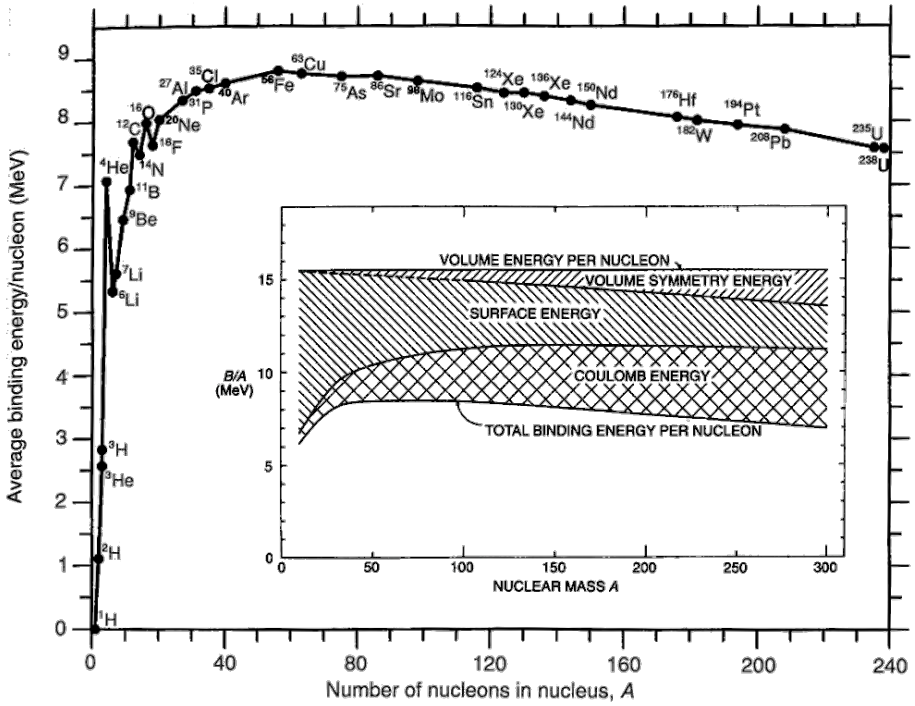

Figure 1.5: Relative binding energy. The Coulomb, surface, volumic contribution are represented qualitatively on the inner graphic. $^{62}_{28}$Ni, $^{58}_{26}$Fe, $^{56}_{26}$Ni are the most tightly bound isotopes with a 8.8 MeV binding energy per nucleon. Elements heavier than iron can yield energy by nuclear fission. From Ref. [10].

An "asymmetric term" has been added to correct the effect of the isospin dependence of the surface and of the volume terms, see Ref. [11, 12]. A slightly different effect occurs if the neutron/proton number is even or odd. A pair of same isospin lowers the binding energy leading to a more stable nucleus.
The even-even nuclei are more stable than the odd-odd one, and the $\delta(A)$ term describes this effect, called pairing effect (Pauli principle).

Defining different parameters helps to describe the pairing effect:

$$\begin{cases} \Delta_n &= \text{E(odd−N)} - \text{E(even−even)} \\ \Delta_p &= \text{E(odd−Z)} - \text{E(even−even)} \\ \Delta_p + \Delta_n - E_{np} &= \text{E(odd−odd)} - \text{E(even−even)} \end{cases} \tag{1.12}$$

with E_{np} representing the coupling energy associated to unpaired neutron/proton.
The relative mass excess, see Fig. 1.6, in the (odd-Z,odd-N) nuclei implied $\Delta_n \sim \Delta_p$. For (odd,odd) and (even,even), extra coupling between neutrons and protons impacts the binding energy in a non-negligible proportion.

The neutron and proton separation energy are written:

$$\begin{cases} S_n &= B(A,Z) - B(A-1,Z) \\ S_p &= B(A,Z) - B(A-1,Z-1) \end{cases} \tag{1.13}$$

The two neutrons and protons separation energy are written:

$$\begin{cases} S_{2n} &= B(A,Z) - B(A-2,Z) \\ S_{2p} &= B(A,Z) - B(A-2,Z-2) \end{cases} \tag{1.14}$$

The liquid drop model is useful to describe the macroscopic behaviour of the nucleus. It cannot explain the presence of magic nuclei but permit the highlighting of substructure inside the nucleus: the nuclear shells, see Subsec. 3.2.1.

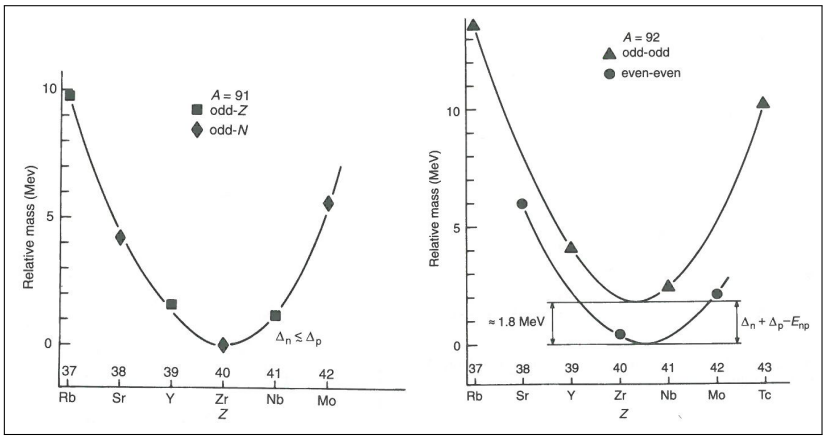

Figure 1.6: Relative Mass Excess shown for nuclei close to onset of deformation. Almost no pairing is present for odd-Z and odd-N nuclei. On contrary, a pairing gap is observed between the odd-odd and even-even nuclei characterized by two different parabola. From Ref. [10].

3.2 Single Particle Model

3.2.1 Nuclear Shell Model

Noble gas atoms He, Ne, Ar, Kr, and Rn are chemically stable and inert. In order to explain such behaviour, the introduction of quantum treatment was necessary. The quantum numbers thereby created form electronic shells and their full filling confers to the noble gas their chemical stability, see Fig. 1.7. With the same philosophy, D. Ivanenko and E. Gapon [13] transposed this framework onto the atomic nucleus for the first time in 1932, in order to explain the "over-stability" observed for certain numbers of neutrons (N) and protons (Z).

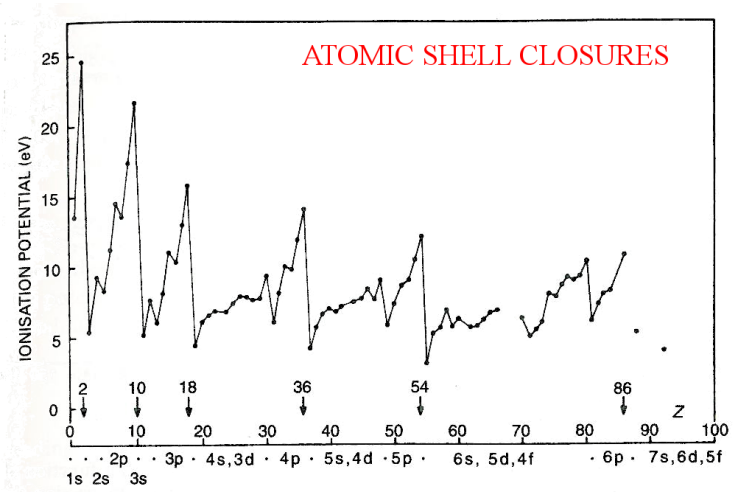

Figure 1.7: Atomic shell effect observed via the ionization potential where the atomic magic numbers 2, 10, 18, 36, 54, 86 are observed. Modified from Ref. [10].

The Fig. 1.8 shows the differences between the measured nuclear masses and the semi-empirical mass formula of Myers and Swiatecki [11]. Characteristic substructure appears in the residues for specific neutron number except for the very light nuclei. The hypothesis of the viability of the atomic formalism into the nuclear framework was correct, however all the shell closures were not reproduced. M. Goeppert-Mayer and H. Jensen worked on a mathematical model and formalism associated to this idea and introduced corrections associated to the spin-orbit coupling. They shared the Physics Nobel Price in 1963 [14] for their work in the field.

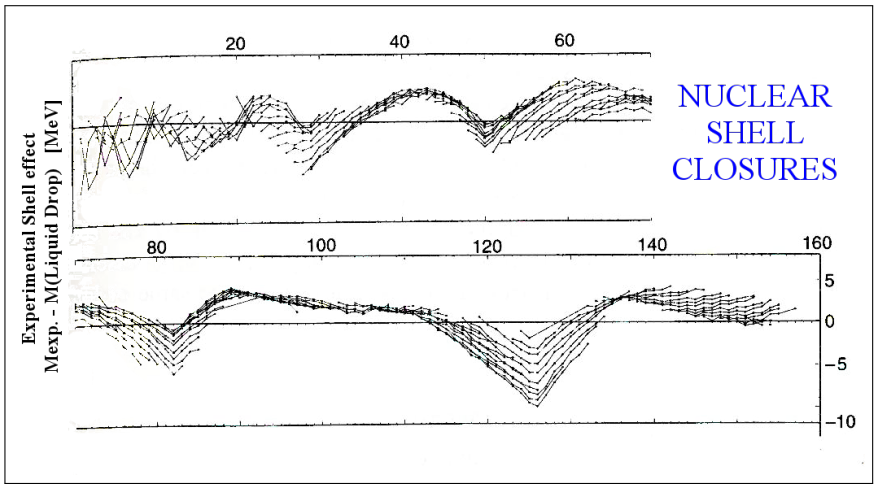

Figure 1.8: Differences between the measured nuclear masses and the semi-empirical mass formulae of Myers-Swiatecki, see Ref. [11]. The "magic numbers" corresponding to the effect of shell closures appears clearly at N=28, 50, 82, and 126.

The established "magic numbers" are:

$$\begin{array}{lcl} \mathrm{N} & = & 2, 8, 20, 28, 50, 82, 126 \\ \mathrm{Z} & = & 2, 8, 20, 28, 50, 82 \end{array} \tag{1.15}$$

3.2.2 Formalism and magic numbers

The Hamiltonian describing the motion of a particle in a spherical symmetric potential can be expressed in two main parts: the radial and angular degrees of freedom. The number of nodes appearing in the radial wave-function is denoted n, the angular momentum l and its projection m_l. Taking into account the independence of the eigenvalues from the m_l, the total degeneracy is $(2s+1)(2l+1) = 2(2l+1)$ [1]. If spin-dependent forces are present this degeneracy is broken. Usually the sub-shell associated to the angular momentum quantum number l is denoted as in atomic physics: s(l=0), p(l=1), d(l=2), f(l=3), g(l=4), h(l=5), etc.

countries. Soustenu par son colleague Hahn, elle échangea épistolairement avec celui-ci lui permettant de poursuivre ses travaux dans le domaine. The community attributed the understanding of the extra energy lacking from the intrinsic masses of products as the cohesion energy that Einstein mentioned in his works. Indeed, the history told us that during a discussion with her nephew on vacation, she refused to understand the results of Hahn as an error of manipulation, considering the brillant and cleaver scientific "démarche" of her colleague Hahn. Her "obstination" were "prolific" and she realized the fact that the energy lacking from the experiments such as Hahn experiments corresponded to the cohesion energy.

3.2.3 Mean Field Models

Instead of describing the nucleon-nucleon interaction and extrapolating the nuclear behavior from this basis, the nucleon can be considered as immersed in a mean field potential created by all the nucleons, and each nucleon feels the potential independently. Several mean field potentials exist and we will cite some of them.

Potentials To describe the nucleus the Hamiltonian problem described by the time-independent Schrödinger equation, Eq. 1.16, has to be solved.

$$H\psi = -\frac{\hbar^2}{2M}\Delta + V(r)\psi \tag{1.16}$$

with $V(r)$ the nuclear one-body potential. In spherical coordinates, the Hamiltonian could be rewritten:

$$H = -\frac{\hbar^2}{2M}\frac{1}{r}\frac{\partial^2}{\partial r^2}r + \frac{l^2(\theta,\phi)}{2Mr^2} + V(r) \tag{1.17}$$

1. $m_s = -\frac{1}{2}, +\frac{1}{2}$

In the spherical framework one could separate the wave-function in two parts: ψ =R_{nl}(r).$Y_{lm_l}(\theta,\phi)$.

$$l^2 Y_{lm_l}(\theta,\phi) = \hbar^2 l(l+1) Y_{lm_l}(\theta,\phi) \tag{1.18}$$

The radial part can be written:

$$\left(-\frac{\hbar^2}{2M}\frac{1}{r}\frac{d^2}{dr^2}r + \frac{\hbar^2 l(l+1)}{2Mr^2} + V(r) - E\right)R(r) = 0 \tag{1.19}$$

The Wood-Saxon potential is the most famous among the modified potentials. This refined potential takes into account the aspect of the infinite square potential and the harmonic oscillator potential:

$$\text{Harmonic Oscillator: } V_{H.O.} = \frac{M\omega_0^2 r^2}{2} \tag{1.20}$$

$$\text{Infinite Square Well: } V_{inf.squ.} = \begin{cases} -V_O & \text{if } r \leqslant R \\ +\infty & \text{if } r > R \end{cases} \tag{1.21}$$

For the harmonic oscillator potential, one extracts the main quantum number N and the energy such as:

$$N = 2n + l \tag{1.22}$$

$$E = \hbar\omega_0\left(2n + l + \frac{3}{2}\right) = \hbar\omega_0\left(N + \frac{3}{2}\right) \tag{1.23}$$

For the energy degeneracy of each N-value one finds $\sum_l^N (2l+1)$, and the degeneracy of each energy is (N+1)(N+2).

From the harmonic oscillator and the infinite square potentials one can reproduce some of the magic numbers, see Tab. 1.1 and Tab. 1.2.

N	$E/\hbar\omega_0$	States $(n+1)l$	Degeneracy	"Magic Number" Sum	Magic or not?
0	3/2	1s	2	2	yes
1	1 + 3/2	1p	6	8	yes
2	2 + 3/2	2s, 1d	12	20	yes
3	3 + 3/2	2p, 1f	20	40	no
4	4 + 3/2	3s, 2d, 1g	30	70	no
5	5 + 3/2	3p, 2f, 1h	42	112	no

Table 1.1: Closed shells of the spherical harmonic oscillator potentials. The "Magic Numbers" are well reproduced until N/Z=20.

Woods-Saxon The Wood-Saxon potential, see Ref. [15], considers the nucleus as a sphere. The nuclear potential could be on a first approach considered as radial:

$$V_r(r) = \frac{V_0}{1 + exp\left[\dfrac{(r - R_0)}{d}\right]} \tag{1.24}$$

with: $\begin{cases} V_0 \approx [-60, -50] \text{ MeV} : \text{well potential deep, independent from the nucleon number,} \\ R_0 : \text{mean radius of the nucleus,} \\ d : \text{diffuseness parameter.} \end{cases}$

With such potential the internal nucleons (Core) and the external (Valence) ones don't feel the same potential. The core nucleons ($r < R_0$) feel an almost constant potential V_0. In this state, the Wood-Saxon potential cannot reproduce the magic numbers.

The harmonic oscillator potential leads to an extra degeneracy due to the spherical symmetry. And, in the infinite potential, the degeneracy of l is removed. A centrifugal potential is necessary to restore the experimental ordering of the nuclear states:

$$V(r) = V_r(r) + \frac{\hbar^2}{2Mr^2} l(l+1) \tag{1.25}$$

l	n	State	$E\left[\frac{\hbar^2}{2MR^2}\right]$	Degeneracy	"Magic number" Sum	Magic or not?
0	1	1s	3.14	2	2	yes
1	1	1p	4.49	6	8	yes
2	1	1d	5.76	10	18	no
0	2	2s	6.28	2	20	yes
3	1	1f	6.99	14	34	no
1	2	2p	7.73	6	40	no
4	1	1g	8.18	18	58	no
2	2	2d	9.10	10	68	no
5	1	1h	9.35	22	90	no
0	3	3s	9.43	2	92	no
3	2	2f	10.42	14	106	no
6	1	li	10.51	26	132	no
1	3	3p	10.90	6	128	no

Table 1.2: Closed shells obtained with the square well potential. The "Magic Numbers" are well reproduced until N/Z=8.

The same result can be obtained with the following formalism:

$$V_{centrifugal} = -\mu' \hbar\omega_0 l(l+1) \tag{1.26}$$

A spin-orbit and a Coulomb term were added by M. Goeppert-Mayer, H. Jensen, O. Haxel,J. Hans and H.E. Süss, see Ref. [16, 17, 18, 19]. The magic number N/Z=50 was not reproduced at that time and a quantum treatment was needed.

Finally, the Wood Saxon potential takes the form:

$$V_{W-S}(r) = V_r(r) + V_{LS}(r) + V_{Coul}(r) \tag{1.27}$$

with: $\begin{cases} V_{LS}(r) = \lambda \frac{1}{r}\frac{dV_r}{dr}\vec{l}.\vec{s}: \text{ spin-orbit coupling correction term,} \\ V_r : \text{nuclear radial potential,} \\ \lambda : \text{the coupling strength.} \end{cases}$

A Coulomb term is added to describe the presence of protons subject to Coulomb repulsion:

$$V_{Coul}(r) = \begin{cases} \frac{Ze^2}{R_0}\frac{1}{2}\left[3 - \left(\frac{r}{R_0}\right)^2\right], & \text{for } r \leq R_0 \\ \frac{Ze^2}{r}, & \text{for } r \geq R_0 \end{cases} \tag{1.28}$$

The Wood Saxon potential cannot be used analytically in the calculations. Nilsson and Gustafsson created the modified oscillator in order to apply calculations, see Ref. [20, 21].

Modified Oscillator The Modified Oscillator can reproduce the results obtained with the Wood Saxon potential, it falls between the infinite and the harmonic oscillator potentials, see Fig. 1.9, 1.10, and Tab. 1.4. The "Nilsson" anisotropic harmonic oscillator associated to the single particle model of deformed nuclei is discussed separately, see Appendix 205.

$$V_{M-O} = \frac{1}{2}\hbar\omega_0\rho^2 - \kappa\hbar\omega_0\left[2\vec{l}\cdot\vec{s} + \mu\left(l^2 - < l^2 >_N\right)\right] \tag{1.29}$$

with: $\begin{cases} < l^2 >_N = \frac{N(N+3)}{2}, \\ \rho = \left(\frac{M\omega_0}{\hbar}\right)^{\frac{1}{2}} r \end{cases}$

In order to reduced the compression effect of the l^2 term the average value over neutron shells is subtracted.

The model is governed by three major parameterizing terms: κ, μ and ω_0.
ω_0 is employed to determine the radius of the matter distribution. For high mass number, the stable nuclei

have more neutrons than protons subjected to the Coulomb repulsion, such as in the Fermi gas model. The Pauli principle needs also to be considered. Those phenomenon can be included in the potential via the parameter ω_0 declined in two terms [2] associated to neutrons (N) and protons (Z):

$$\begin{cases} \omega_0^N &= \omega_0\left(1+\gamma\dfrac{N-Z}{A}\right) \\ \omega_0^Z &= \omega_0\left(1-\gamma\dfrac{N-Z}{A}\right) \end{cases} \tag{1.30}$$

The condition $< r^2 >_N \simeq < r^2 >_Z$ leads to $\gamma \simeq \frac{1}{3}$.
κ and μ' [3] are obtained generally by fitting the level spectra for nuclei around the doubly-magic cases.The energy can be expressed as:

$$E(Nlj) = \begin{cases} \hbar\omega_0\left[N+\dfrac{3}{2}-\kappa l-\mu'\left(l(l+1)-\dfrac{N(N+3)}{2}\right)\right], & \text{if } j = l+\frac{1}{2} \\ \hbar\omega_0\left[N+\dfrac{3}{2}+\kappa(l+1)-\mu'\left(l(l+1)-\dfrac{N(N+3)}{2}\right)\right], & \text{if } j = l-\frac{1}{2} \end{cases} \tag{1.31}$$

where N denotes the equivalent shell number of the harmonic oscillator.
The parameters change according to the part of the chart studied, in some case to reproduce the behaviour of nuclei in a specific part of the chart one uses the same κ and μ' values or different values for different shells. Some examples of values are given in Tab. 1.3.

	Protons		Neutrons	
N	κ	μ	κ	μ
0	0.120	0.00	0.120	0.00
1	0.120	0.00	0.120	0.00
2	0.105	0.00	0.105	0.00
3	0.090	0.30	0.090	0.25
4	0.065	0.57	0.070	0.39
5	0.060	0.65	0.062	0.43
6	0.054	0.69	0.062	0.34
7	0.054	0.69	0.062	0.26
8	0.054	0.60	0.062	0.26

Table 1.3: κ and μ values obtained for the Modified Oscillator by Bengtsson and Ragnarsson [22]. N denotes the equivalent shell number of the harmonic oscillator.

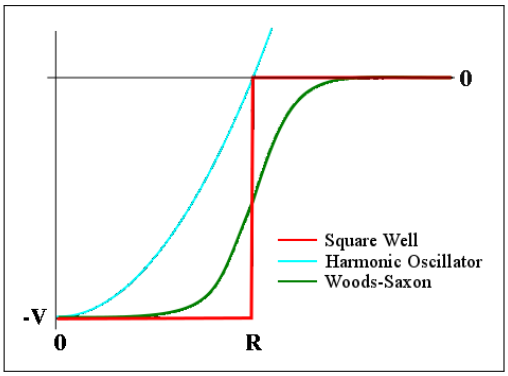

Figure 1.9: Shape of different potentials. The Woods-Saxon potential falls between the infinite and the harmonic oscillator potentials.

Actually, if the potential shape is mathematically well defined, the final work consists in the fitting of relevant parametrization reproducing the considered nuclei. Generally, specific parameters are allocated to a given region of the nuclear chart. A "universal parametrization" can be obtained by fitting on the nuclear chart. Nazarewicz et al. described the process to obtained such parametrization, see Ref. [23].

Finally the modified-oscillator describing the spherical nuclei can be written as:

$$H_{\text{Sph. Single Part.}} = -\frac{\hbar^2}{2M}\Delta + \frac{1}{2}M\omega_0^2 r^2 - C\vec{l}\cdot\vec{s} - D\left(\vec{l}^2 - < \vec{l}^2 >_N\right) \tag{1.32}$$

where: $\begin{cases} < \vec{l}^2 >_N = N(N+3)/2 \\ C = 2\kappa\hbar\omega_0 \\ D = \mu'\hbar\omega_0 \\ \mu' = \kappa\mu \end{cases}$

The different discussed potentials are shown on the Fig. 1.9.

Further solution: the Yukawa potential In the mean field theory, another famous potential similar to the Wood Saxon potential use different parametrization for example the Yukawa potential created by Hideki Yukawa, see Ref. [24].

2. In the same philosophy than for the Fermi gas model, the separated treatment of neutrons and protons is effective.
3. μ' is defined as $\mu' = \kappa \cdot \mu$

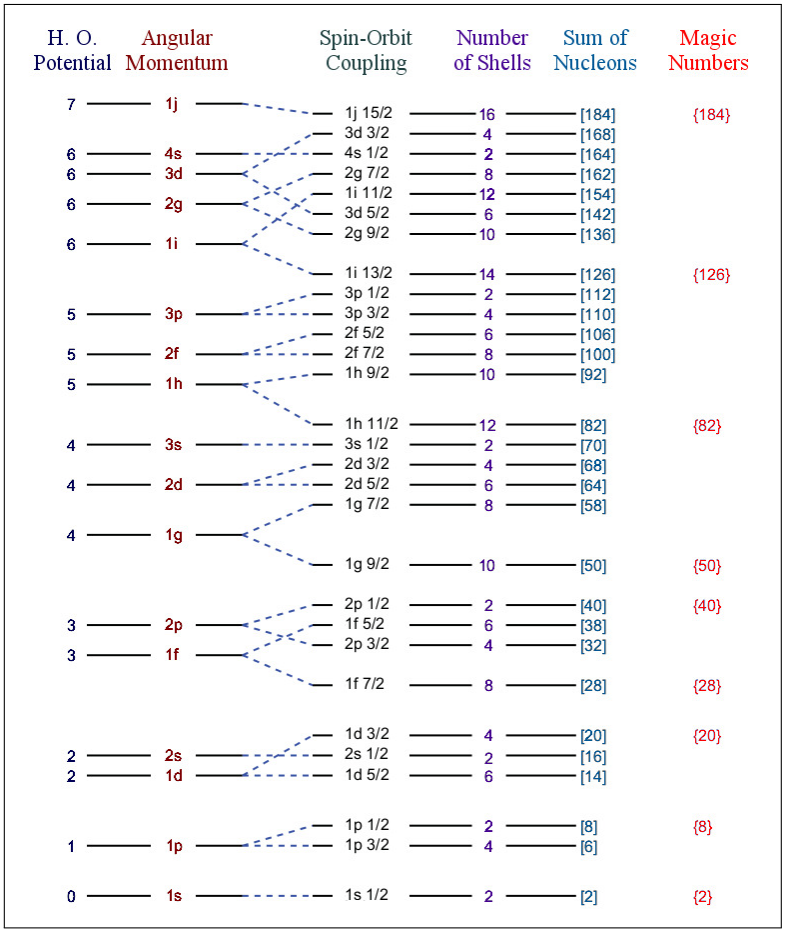

Figure 1.10: Nuclear Shell Model. A single-particle shell model with a harmonic oscillator (H.O.) potential including angular momentum and with spin-orbit interaction. The fourth column indicates the level degeneracy, the number of nucleons per shell. The resulting magic numbers are shown in the last column, representing shell closures.

States	Degeneracy	Magic number Sum	Magic or not?
$1s_{1/2}$	2	2	yes
$1p_{3/2}$, $1p_{1/2}$	4, 2	8	yes
$1d_{5/2}$, $2s_{1/2}$, $1d_{3/2}$	5, 2, 4	20	yes
$1f_{7/2}$	8	28	yes
$2p_{3/2}$, $1f_{5/2}$, $2p_{1/2}$ $1g_{9/2}$	4, 6, 2, 10	50	yes
$1g_{7/2}$, $2d_{5/2}$, $2d_{3/2}$, $3s_{1/2}$, $1h_{11/2}$	8, 6, 4, 2, 10	82	yes
$1h_{9/2}$, $2f_{7/2}$, $2f_{5/2}$, $3p_{3/2}$, $3p_{1/2}$, $1i_{13/2}$	10, 8, 6, 4, 2, 14	126	yes

Table 1.4: Closed shells obtained with the Modified Oscillator. The "Magic Numbers" are well reproduced.

4 Unified Nuclear Model

The nuclear ground state can be considered as an equilibrium state of the nucleon assembly. The perturbation of the ground state caused by a diffusion probe might lead to collective motions of the nucleons. They can be vibrational or rotational, depending on the shape of the equilibrium state. Indeed, generally if the ground state is spherical then the collective motion is vibrational, and if the ground state is ellipsoidal the motion is generally rotational.

Nuclei in the vicinity of "magic numbers", with few particles/holes, are usually spherical at equilibrium (ground state) and their lowest excited states exhibit generally collective vibration. In the present work, one focuses on the deformed nuclei, thus the vibrational nuclei will not be described. Adding particles/holes, the residual interaction from the valence space enforces the nucleus to adopt a deformed shape in order to minimize its energy. Such nuclei present an ellipsoidal shape easily subject to a rotation. The valence space deforming the shape confers collective character to the nucleus, such as large quadrupole moments (Q_0) and high transition strengths (B(E2)). This coherent motion exhibits characteristic excited structure called rotational bands. The observation of such bands in the nuclear level scheme is a direct proof of its non-sphericity.

4.1 Rotational models

4.1.1 The Rotor

In case of a deformed shape, one can define orientation of the nucleus in space. The separation of nucleons in an intrinsic and a collective motion leads to consider the nucleus as constituted with a core and a valence space. The nuclear feature is thus described as resulting from the intrinsic motion of the valence nucleons in the deformed potential, and from the collective rotation of the whole nucleus. The easiest deformation adopted by the nucleus consists in an elongation along an axis. In our studies, we would consider only axially symmetric nuclei. The axial deformation breaks the least possible the spherical symmetry. In order to determine the nuclear orientation, one needs 3 Euler angles and 3 quantum numbers to describe the motion along this direction, see Fig. 1.11.

The Hamiltonian considered as rotational invariant leads naturally to a specific parametrization. A possible set of quantum numbers describing the nuclear state is constituted by the total angular moment $\vec{I}$, its projection **M** on the **z-axis** of the laboratory frame and its projection **K** on the **3-axis** of nucleus frame. The total angular momentum is the sum of the angular momentum related to the intrinsic motion of valence nucleons $\vec{J}$ with its projection on the nuclear frame Ω, and the angular momentum related to the collective motion $\vec{R}$:

$$\vec{I} = \vec{R} + \vec{J} \tag{1.33}$$

The intrinsic angular momentum **J** does not constitute a "good" quantum number, instead of its projection Ω along the symmetry axis which can be considered as such.

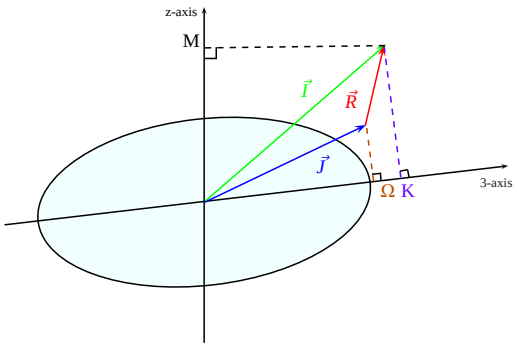

Figure 1.11: Coupling between the core and the valence nucleons.

In terms of nuclear wave function, the rotation in the laboratory frame (x, y, z) can be expressed as a

function of the rotating coordinates (1, 2, 3):

$$\Psi^I_M = \sum_K \mathcal{D}^I_{M,K}(\theta_{Euler})\Psi^I_K \tag{1.34}$$

with: $\mathcal{D}^I_{MK}(\theta_{Euler})$ is the rotational matrix.

As a consequence of the time-reversal invariance the nuclear state $|I{+}KM>$ and $|I{-}KM>$ should have the same energy. Finally, considering that the time reversal invariance is equivalent to the rotational invariance, the intrinsic states ψ_K is found as [25]:

$$\Psi^I_{M,K} = \sqrt{\frac{2I+1}{16\pi^2}}\left\{\mathcal{D}^I_{M,K}(\theta_{Euler})\,\psi_K + (-1)^{I+K}\,\mathcal{D}^I_{M,-K}(\theta_{Euler})\,\psi_{-K}\right\} \tag{1.35}$$

The intrinsic states can be expressed in the parametrization $|\alpha J\Omega>$ diagonalizing the operators $\vec{J}^2$ and $J_3(=\Omega)$:

$$|\psi_\Omega>=\sum_{\alpha J} C^{\alpha J}_\Omega |\alpha J\Omega> \tag{1.36}$$

or the basis diagonalizing the operators $\vec{l}^2$, $l_3(=\Lambda)$, s^2 and $s_3(=\Sigma)$:

$$|\psi_\Omega>=\textstyle\sum_{\alpha l\Lambda} a_{\alpha l\Lambda}|\alpha l\Lambda\Sigma> \qquad \text{with: } \Lambda+\Sigma=\Omega>0 \tag{1.37}$$

with: Σ the projection of the intrinsic spin on the **3-axis** and Λ the projection of the orbital momentum. α is used to substitute the rest of quantum number to identify the nuclear state, see Fig. 1.12. Usually the Nilsson notation is used to express the nuclear state as a function of the asymptotic quantum numbers [20]:

$$\Omega^\pi\,[Nn_3\Lambda] \tag{1.38}$$

with:
- N is the principal quantum number (i.e. the total number of oscillator quanta),
- Ω is the projection of the angular moment on the **3-axis**,
- $\pi=(-1)^N$ is the parity of the nuclear state,
- Λ and Σ are respectively the projection of the orbital and intrinsic spins on the **3-axis**

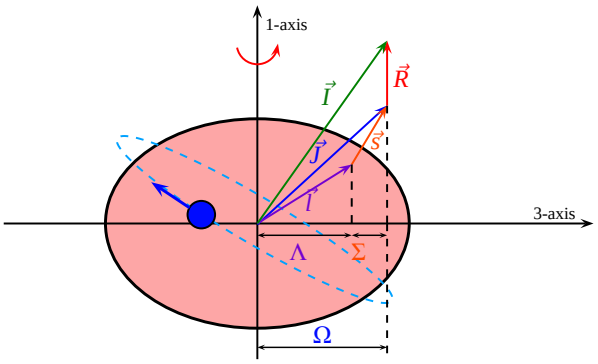

Figure 1.12: Coupling of the angular moment $\vec{J}=\vec{l}+\vec{s}$ of the valence nucleons and the collective rotation $\vec{I}=\vec{R}+\vec{J}$, for axially symmetric nucleus. Ω, Λ and Σ are the respective projections of $\vec{J}$, $\vec{l}$ and $\vec{s}$.

The introduction of the deformation parameter removes the J degeneracy (2J+1) compared to a spherical nucleus.

4.1.2 Particle + Rotor Model

For an axially symmetric nucleus, the Hamiltonian can be described as a rigid rotor at the first order with the form:

$$H_{core} = H_{rotor} = \frac{\hbar^2(R_1^2+R_2^2)}{2\mathcal{J}} = \frac{\hbar^2\vec{R}^2}{2\mathcal{J}} \tag{1.39}$$

with $\mathcal{J}$ the inertia momentum with respect to the rotation axis.

If the rotation is purely collective: $\vec{I} = \vec{R}$ and the excited state energies follow the rule:

$$E_I = \frac{\hbar^2 I(I+1)}{2\mathcal{J}} \tag{1.40}$$

Only the deformed nuclei have rotational spectra and it constitutes a manner to identify them. However, the pure rotor conditions (e.g. see Eq.1.40) are never fulfilled due to the influence of the valence particle on the whole nuclear feature. For spherical-like nuclei, the valence particle(s) determines the ground state angular momentum. Similar non-collective effects occur in deformed nuclei. The low energy nuclear structure results from the mixing of single-particle and rotational collective components.

Let us take the case of odd nuclei, as in our study, for which the valence nucleon determines the ground state and the main energy structure. The valence nucleon is more or less coupled with the core, producing numerous effects. This model developed in the 1950s has been unified and describe by A. Bohr and B.R. Mottelson [25] to create a proper formalism associated.
This model proved its utility by the good reproduction of rotational bands notably in odd nuclei. It implies also a better description of high spin states. The coupling between the valence nucleon and the core is assumed adiabatic: the motion of the single nucleon is supposed rapid and not affected by the core motion. In this frame, the valence nucleon turns around the core giving specific properties to the nucleus. In this representation, the Hamiltonian is separated in two different parts:

$$H = H_{core} + H_{valence} \tag{1.41}$$

The spin of the nucleus is built from the two contributions: $\vec{I} = \vec{R} + \vec{J}_{valence}$ with $\vec{J}_{valence} = \sum_i \vec{j}_i$ (for one valence nucleon $\vec{J}_{valence} = \vec{j}$), see Fig. 1.13. For ground state and low energy states only the non-paired nucleons are summed up and contribute to the angular momentum of the intrinsic motion ($\vec{J}$).

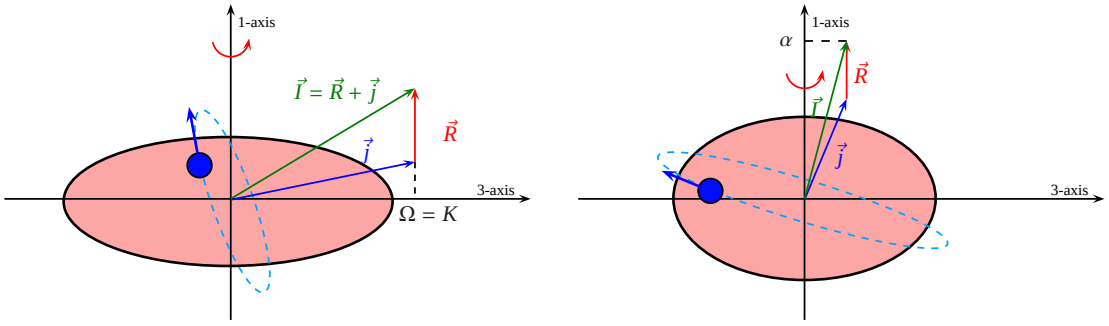

(a) Deformation aligned. (b) Rotation aligned.

Figure 1.13: Coupling between the core and the single nucleon (single particle) of axially symmetric nuclei. Two cases are presented the strong coupling (a) (or coupling to the deformation) at the left and the coupling to the rotation (b) at the right.

According to the Eq. 1.33, $\vec{R} = \vec{I} - \vec{J}$, we can re-express the rotor Hamiltonian as:

$$H_{rotor} = \frac{\hbar^2}{2\mathcal{J}}\left(\vec{I}^2 + \vec{j}^2 - 2\vec{I}\cdot\vec{j}\right) \tag{1.42}$$

From the Eq. 1.42 and using the standard quantum mechanics operators X^+, X^- the Hamiltonian can be separated in three components:

$$H_{rotor} = \frac{\hbar^2}{2\mathcal{J}}\left(\underbrace{\vec{I}^2 - I_3^2}_{\text{Core Rotation}} + \underbrace{\vec{j}^2 - j_3^2}_{\text{Single Nucleon(s) Rotation}} - \underbrace{(I^+ j^- + I^- j^+)}_{\text{"Coriolis Effect"}}\right) \tag{1.43}$$

The "Core Rotation" term is the angular momentum of the core. The second term describes the characteristics of the single nucleon. The last term describes the coupling between the core (with a collective rotation) and the valence part, it has been called Coriolis effect due to its strong similarity with the classical

Coriolis effect, see Ref. [1]. In this framework, the valence nucleon(s) is in motion inside the rotating frame of the nuclei (the rotor). Sometimes the Coriolis effect is defined as:

$$\text{Coriolis term} = \frac{\vec{I}\vec{j}}{\mathcal{J}} \tag{1.44}$$

$\left\{ \begin{array}{l} \text{- For high } \vec{j} \text{ value the Coriolis effect is important, and the projection of } \Omega \text{ is small. On the contrary if} \\ \vec{j} \text{ is small and } \Omega \text{ high the Coriolis effect is negligible.} \\ \text{- The Coriolis effect grows as the importance of the nuclear angular momentum.} \\ \text{- The Coriolis effect is directly affected by the deformation via the moment of inertia value.} \end{array} \right.$

Moment of Inertia Assuming that the nucleus can be considered as a rigid rotor or an hydrodynamic fluid, the moment of inertia is found as [10, 26] with the body-fixed axis k:

$$\begin{aligned} \mathcal{J}_k^{Rigid} &= \frac{2}{5} mAR_0^2 \left(1 - \sqrt{\frac{5}{4\pi}}\beta \cos\left(\gamma - \frac{2\pi}{3}k\right)\right) \quad , \quad \text{k=1, 2, 3,} \\ \mathcal{J}_k^{Hydrodynamic} &= \frac{2}{5} mAR_0^2 \beta^2 \sin^2\left(\gamma - \frac{2\pi}{3}k\right) \quad , \quad \text{k=1, 2, 3.} \end{aligned} \tag{1.45}$$

For a purely prolate nuclei $\gamma = 0$, and one obtains $\mathcal{J}_{Rigid} = \frac{2}{5} mAR_0^2(1 + 0.315\beta)$ and $\mathcal{J}^{Hydrodynamic} = 0.258 mAR_0^2\beta^2$.
The moment of inertia can be determined from the experimental data as:

$$\frac{2\mathcal{J}}{\hbar^2} = \left(\frac{dE}{dI(I+1)}\right)^{-1} \simeq \left(\frac{E_I - E_{I-2}}{4I - 2}\right)^{-1} \tag{1.46}$$

The nuclear rotation can be evaluated from the frequency, defined as $\omega = \frac{\partial H}{\partial I}$ which can be determined from the experimental data as:

$$\hbar\omega = \frac{E_I - E_{I-2}}{[I(I+1)]^{\frac{1}{2}} - [(I-2)(I-1)]^{\frac{1}{2}}} \tag{1.47}$$

4.2 Coupling Mode

4.2.1 Strong Coupling or Coupling to the deformation

The strong coupling conditions are fulfilled if the Coriolis effect is negligible compared to the individual particle energies, see Ref. [25]. The strong coupling case is shown on the Fig. 1.13(a).
The intrinsic motion of the single particle is assumed decorrelated from the rotational motion of the core [4]. The Coriolis interaction characterizing the influence of the core rotation on the intrinsic motion of the single particle can be treated in first order perturbation theory of the rotor. Thanks to the axially symmetric hypothesis, the nucleus is expected turning along a perpendicular axis to the 3-axis ($\vec{R}$ perpendicular to the **3-axis**, thus Ω =K), in this condition K can be approximately considered as a good quantum number. Finally, the nuclear state is written $|IKM>$. The Hamiltonian used to evaluate the collective energy would correspond to the Eq. 1.43:

$$H_{rot} = \frac{\hbar^2}{2\mathcal{J}}\left[\vec{I}^2 + \vec{j}^2 - (I_+ j_- + I_- j_+) - 2K^2\right] \tag{1.48}$$

If $\Omega = K$ (coupling to the deformation), the matrix elements of the operators are found as:

$$\left\{ \begin{array}{l} < j\Omega\,|j^{\pm}|\,j\Omega \mp 1 >= \sqrt{(j \pm K)(j \mp \Omega + 1)}, \\ < IK\,|I^{\pm}|\,IK \pm 1 >= \sqrt{(I \mp K)(I \pm K + 1)}. \end{array} \right. \tag{1.49}$$

with: $\left\{ \begin{array}{l} 2\vec{I}\vec{J} = (I^+ j^- + I^- j^+) + 2K^2 \text{ and,} \\ I^{\pm} = I_1 \pm iI_2,\ j_{\pm} = j_1 \pm ij_2 \end{array} \right.$

4. It is the adiabatic condition

The selection rules of j^+ and j^- impose that only $\Delta\Omega = \pm 1$ eigenstates can be coupled. For large value of K or large deformation, the K^2 term dominates and the Coriolis effect is reduced. Grodzins [27] found for the even-even nuclei the phenomenological relation $\frac{\hbar}{2\mathcal{J}} = \frac{204}{A^{7/3}\beta}$. It confirms the Coriolis reduction at large deformation. Each orbital is degenerated according to the two signs of the Ω quantum number. In such conditions, for the odd nuclei, the diagonal matrix elements of the "Coriolis effect" term, see Eq. 1.43, are different from zero if $\Omega = \pm\frac{1}{2}$ (two signatures).

For high deformation, the orbitals of the same shell with different $\Omega = \pm\frac{1}{2}$, $\Omega = \pm\frac{3}{2}$, ... are splitted in energy [5].
Far in energy from each other, those orbitals can be coupled together. However, the orbitals from different shells, crossing with the increase of the deformation, can also be coupled, see Fig. 1.16.

Applying that on the Coriolis Hamiltonian $H_{Coriolis} = -\frac{\hbar^2}{2\mathcal{J}}(I^+J^- + I^-J^+)$, for K= $\frac{1}{2}$:

$$< IKM|H_{Coriolis}|IKM >= \frac{\hbar^2}{2\mathcal{J}} a(-1)^{I+\frac{1}{2}}\left(I+\frac{1}{2}\right) \tag{1.50}$$

If the intrinsic decoupling parameter, defined as $a_{intr.} = -(\phi_{K=\frac{1}{2}} j^+ \phi_{K=-\frac{1}{2}})$, is null, the two signature partner bands of the Nilsson state are in strong coupling. This matrix element can be expressed in the spherical basis:

$$a_{intr.} = \sum_j (-1)^{(j-\frac{1}{2})}\left(j+\frac{1}{2}\right) C^2_{j\Omega=\frac{1}{2}} \tag{1.51}$$

The energies of the rotational bands are found as:

$$E_{IK} = E_K + \frac{\hbar^2}{2\mathcal{J}}\left\{I(I+1) - K^2 + \delta_{K,\frac{1}{2}} a(-1)^{I+\frac{1}{2}}\left(I+\frac{1}{2}\right)\right\} \tag{1.52}$$

The Coriolis effect increases when the nuclear spin I increases and for high spins, the situation can change and the Coriolis term can predominate.

4.2.2 Coupling to the rotation

In the 1970, F.S. Stephens [28, 29] showed for the first time the existence of another important coupling to the rotation motion. Previously, one treated the case of nuclear deformation and rotational motion completely uncoupled. The rotational motion was not high enough to break this coupling.
The coupling to the rotation case is represented on the Fig. 1.13(b). The total Hamiltonian can still be written as: $H = H_{s.p.} + H_{rot} = H_{s.p.} + \frac{\hbar^2}{2\mathcal{J}}\left(I^2 + j^2 - 2\vec{I}\vec{j}\right)$. If j is pure the orbitals are splitted according to, see Ref. [10]:

$$e_\Omega = e_0 + \frac{1}{6}\epsilon M\omega_0^2 < r^2 > \frac{3\Omega^2 - j(j+1)}{j(j+1)} \quad , \quad \text{with: } < r^2 >= \left(N+\frac{3}{2}\right)\frac{\hbar}{M\omega_0} \tag{1.53}$$

For the extreme case the orbitals can be quantized along the 1-axis. If the nuclear momentum I is high and K is small, the $(I^+j^- + I^-j^+)$ term will predominate and the eigenvalues of the total Hamiltonian would correspond to the ones diagonalizing H_{rot}. In such condition, K is not a "good" quantum number; however, the projection of j along the rotation axis (α) is as such.
The rotation energies for such coupling can be estimated for $I \gg K$, $j \gg K$ and j close to a "good" quantum number ($j \approx \alpha$) as:

$$E_{rot} = \frac{\hbar^2}{2\mathcal{J}}[I(I+1) + j(j+1) - 2I\alpha] = \frac{\hbar^2}{2\mathcal{J}}[(I-\alpha)(I-\alpha+1) + 2\alpha] = \frac{\hbar^2}{2\mathcal{J}}R(R+1) + C^{ste} \tag{1.54}$$

with: R=I−α. The structure of the energy states corresponding to R=0, 2, ... constitutes a rotational band (usually qualified as decoupled) built on the rotational aligned Nilsson state is equivalent than in the neighboring even nuclei. Such decoupled band can also be exhibited for $K = \frac{1}{2}$ due to the diagonal matrix elements of the Coriolis term.

5. The orbitals go away from each other if the deformation increases.

4.2.3 Weak Coupling

The two extreme cases have been treated but the intermediate situations exist in the Nature, see Ref. [30, 31, 32].

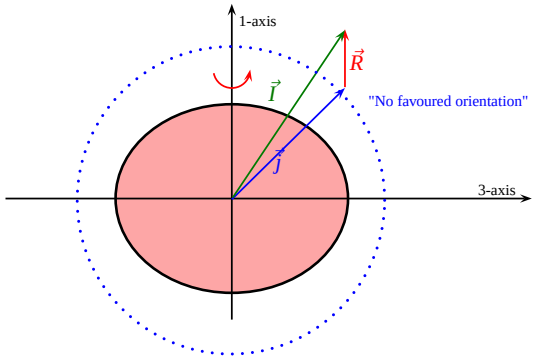

Figure 1.14: Weak coupling between the core and the single nucleon (single particle).

If the deformation is small, the nuclear shape is close to a sphere. The eigenstates are close to the spherical states. The angular moment of the single particle is independent of the core rotation. All the values of the nuclear spin $| R - j | \leqslant I \leqslant | R + j |$ are degenerated. This configuration is called weak coupling, see Fig. 1.14 The spin of the intrinsic motion of the valence nucleon (conserved) cannot be oriented in a specific direction. For a given total angular momentum, the nucleus searches to be in the lowest energy state, the Coriolis effect plays an important role promoting the gain of momentum of inertia.

4.2.4 Rotor + 2 particles Model

Considering the nuclear system with two valence particles in the rotational model. The resulting Hamiltonian is found as:

$$H_{Total} = H_{Rotor} + H_{s.p.1} + H_{s.p.2} + W_{s.p.12} \tag{1.55}$$

with: $\begin{cases} \mathrm{H}_{Rotor}\text{: the rotor Hamiltonian treated previously,} \\ \mathrm{H}_{s.p.1} \text{ and } H_{s.p.2}\text{: the single particle Hamiltonians,} \\ \mathrm{W}_{s.p.12}\text{: Interaction between the two particles.} \end{cases}$

The intrinsic Hamiltonian combines now the two valence particles, such as $\vec{j} = \vec{j}_1 + \vec{j}_2$. The projection of $\vec{j}$ on the symmetry axis (z-axis) is noted K, with: $K = K_{s.p.1} \pm K_{s;p;2}$.

Consider two paired nucleons with one reverse in time compared to the other one. The Coriolis interaction drives the nucleons to be aligned along the rotational axis (x-axis). If the Coriolis effect is strong, the pair can be broken, this situation is called "back-bending", see Fig. 1.15. The alignment of the pair is followed by an increase of the moment of inertia and a reduction of the rotational frequency. Note that the back-bending effect is usually observed for high nuclear spins.

Rotor Plus Particle(s) Model As the Eq. 1.41 implies the total energy is the sum of the rotational energy and the energies of the constituents of the individual valence particles.

$$H_{valence}\psi_{valence,\Omega} = E_{valence,\Omega}\psi_{valence,\Omega} \tag{1.56}$$

The Rotor + Particle(s) model has been treated to describe systems with rotational nucleus with relatively low spins. For high spins, the rotation and the Coriolis effect affect the nucleus [6].
Another model is commonly used to describe high rotational nuclei: the "Cranked Shell Model". Introduced by D.R. Inglis in 1954, see Ref. [33], the "Cranking" model considers the nucleus in the coordinates system fixed to the nucleus with a constant rotation around the rotational-axis [7]. The collective rotation is taken into account due to the treatment of the nucleons inside a mean field potential in rotation.

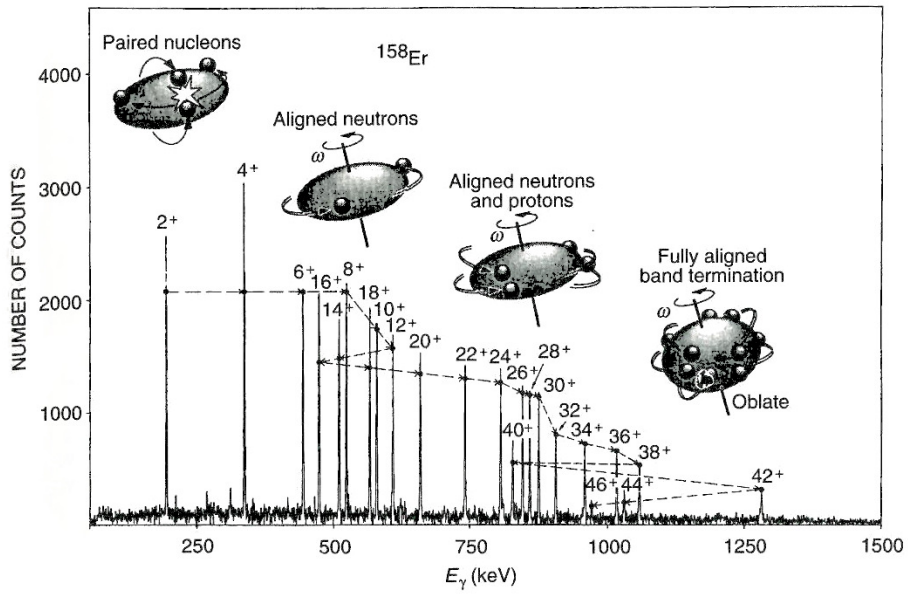

Figure 1.15: Backbending: Pairing and Alignment of nucleons. Following the configuration of the nucleons, one can observe different kind of γ-rays energies, for example on this figure for ^{158}Er. Initially the nucleons are coupled and adding rotation, the nucleon pair breaks. The two single particle aligns along the rotational and are part of the core corpus turning with it (their spins contributes to the rotation). The alignment of the pair is followed by an increase of the moment of inertia and a reduction of the rotational frequency. When the nucleons are paired, they don't contribute to the moment of inertia. If the pair is broken, the two nucleons contribute to the total moment of inertia. From Ref. [10]

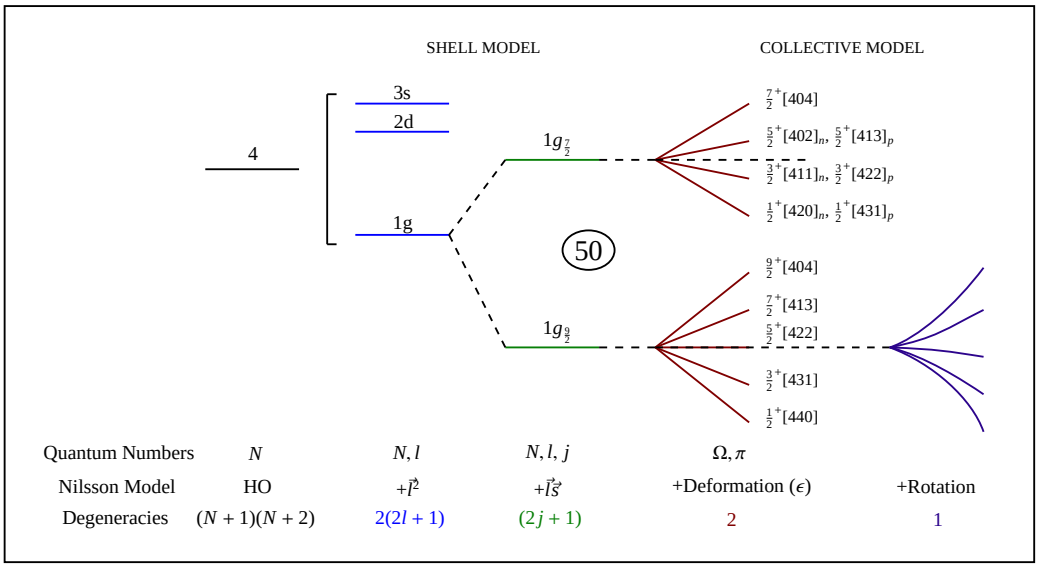

Figure 1.16: Shell Model, Collective Model and degeneracies. The successive introduction of corrections leads to a total breaking of the degeneracies.

4.2.5 From the models, a description of the nuclei

The introduction of the different corrections from the shell to the collective models led to remove totally the degeneracies. The introduction of the different ingredients in the Nilsson model is summarized in the Fig. 1.16 for some of the neutron orbitals discussed in the present study.

6. The rotation is not adiabatic and the non-diagonal matrix elements cannot be treated as perturbations.
7. Considering the axial symmetric nuclei, the rotational axis corresponds to the 1-axis on Fig. 1.13

The simple Particle + Rotor model constitute a good approximation in a first approach for the present study where one populated low-lying states. However, more sophisticated model has been used to reproduce and discuss the results of the present experiments. For example, an iterative process using the Wood Saxon potential and the BCS model was employed. A brief description of such process is done on the Appendix 207.

5 Conclusion

In this first chapter, the different theoretical models which can be used to describe the nuclear structure of the studied nuclei have been presented. They constitute theoretical elements helping to understand the nuclear structure going from the liquid drop model to the single particle models and the collective models. The pairing interaction has been mentioned and described in the liquid drop model. However, more information on the pairing is present in the Appendix 207.

The nuclear matter is usually described locally with a specific model. Few models try to describe the nuclear structure of whole chart such as models based on energy density functionals. Most of the theoretical models arose from the investigation of a specific property/feature of the nuclear matter. The reciprocal emulation coming from theory and experimental results is a key ingredient in nuclear structure studies.

Chapter 2

Physics Motivation

1 Introduction: Overview of the region A~100, N~60

In 1965, the work of S.A.E. Johansson [34] reported the existence of a new region of stable deformation in the neutron-rich side of the nuclear chart around A=100. Actually, it is one of the most sudden and intense development of deformation observed in the nuclear chart. The shape change is so abrupt that it has been qualified as a "phase transition". The presence of strong similarities between the A=100 mass region and the rare earths region, which was already considered as a "deformed" region, gave hints of deformation. They both present rotational-like spectra in the emission of γ-rays.

Since then considerable efforts have been made to understand the properties of the region, see Ref. [35, 36, 37]. The mass and charge measurements are of great importance to describe the rough behavior in the whole tendency of the region. Firstly, accessible by fission in the study of S.A.E. Johansson [34], the region has been studied later on by mass and charge radii measurements, highlighting the presence of deformation at N~60. The mass and charge radii measurements in the region are presented in the Sec. 2 on the following page.

A few decades ago, the mass 100 region has been mainly investigated by studying the β-decays of mass separated fragments from induced and spontaneous fissions. It provided the identification of the lowest levels of rotational bands (mainly for even-even nuclei) characterizing the presence of deformed structures with the increase of the neutron number, see Ref. [38, 39, 40, 41, 42, 43, 44, 45, 46] as examples.

Most of the electric quadrupole moments of the ground states or first excited states of nuclei in the region have been already determined, highlighting the shape transition, see Ref. [47]. Across the years, it has been demonstrated that many nuclei in the region are characterized by a strong prolate deformation ($\beta_2 \simeq$ 0.3-0.4).The energies of the first 2_1^+ states E(2_1^+) of the even-even nuclei and the E(4_1^+)/E(2_1^+) ratios can be used as a tool to reveal the deformation trend, see Sec. 3 on page 43.

The Sr and Zr isotopic chains show the strongest development of deformation at N~60. The shape transition is disappearing for the Kr isotopes. The deformation increases from Z=36 until Z=38-40, and then decreases until the Mo isotopic chain, for which the transition is smoother. This feature has been explained in many articles by a possible triaxiality; the triaxiality in Z>37 nuclei is discussed in the following publications, see Ref. [48, 49, 50, 51]. Transitional structures have been observed for intermediate cases.
The study of Rodriguez et *al.* [51] suggests a too low degree of triaxiality in the rubidium isotopes to be taken into account. The latter can be considered as axially symmetric nuclei. The shape coexistence at low excitation energy has been highlighted in the region notably for the N=59 isotones for the ^{96}Rb, ^{97}Sr, ^{98}Y and ^{99}Zr, see Ref. [37, 52, 53, 54, 55, 56, 57], see Sec. 5 on page 47.

The dramatic change appearing at N=60 could be assigned to the filling of specific orbitals. The identification of the driving mechanism(s) of the deformation constitutes the main motivation of the present experimental study of odd-mass rubidium isotopes. Nilsson diagrams, calculated for protons and neutrons numbers of the region, are shown on the Fig. 2.1.

Using the spherical shell model, the deformation due to the iso-vector interaction between the $\pi g_{9/2}$ and $\nu h_{11/2}$ particles for the Zr isotopes has been considered of great importance according to Federman et *al.* [58, 59]. Extensive calculations by Etchegoyen et *al.* [60] emphasized the importance of this interaction. However, they consider of low importance the influence of the $\nu h_{11/2}$ intruder orbitals at the onset of deformation, as claimed for the Zr and Mo isotopes [60]. The $\nu h_{11/2}$ orbit plays an dominant role for larger

neutron number than the ones found at the shape transition.

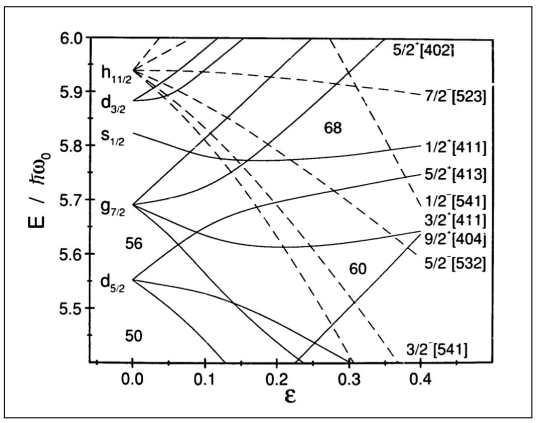

(a) For neutrons in the N=60 region . The energies were calculated using the potential parameters κ = 0.066 and μ = 0.35.

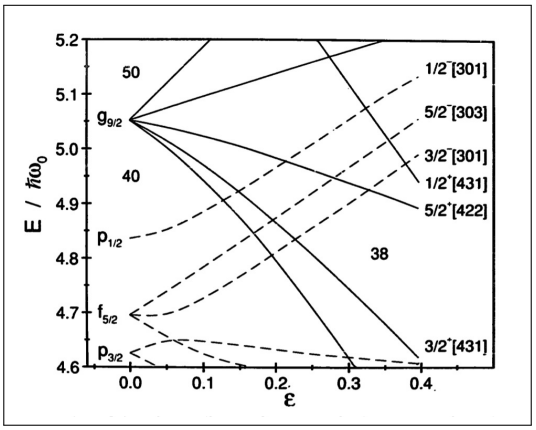

(b) For protons in the Z=40 region. The energies were calculated using the potential parameters κ =0.07 and μ =0.40.

Figure 2.1: Expanded portion of the Nilsson diagrams for neutrons (a) and protons (b). From Ref. [35, 44].

According to deformed mean field calculations [49, 61, 62, 63], the deformation driving components of the $\nu h_{11/2}$ intruder orbit lie below the Fermi level at N∼60. The low-Ω orbital from the $\nu h_{11/2}$ are in this picture preferably occupied compared to the $\nu g_{7/2}$ orbitals.
By analogy with the rare earth isotopes, the intruder orbitals are expected to stabilize the deformation, as done in the rare earth nuclei by the intruder orbitals arising from the $\nu i_{13/2}$ orbit.

Even if the presence of deformation for N$\gtrsim$60 is well known, its origins are not clearly determined. The energies of the low lying states and the transition strengths can be used to distinguish the nature of the collectivity.

After an overview of the problematics of the region, we will show, in the following section, the most relevant parameters highlighting the onset of deformation, and present several theoretical calculation performed along the years. Moreover, we will emphasize the different spectroscopic properties known before this experiment and the ones necessary to complete our knowledge.

2 Mass and Charge Radii Measurements

The mass measurements, constituting a qualitative and quantitative observation of the deformation, are corroborated by the charge radii measurements. The latter confirmed in a clear way the presence of an onset of deformation for nuclei in their ground states.

2.1 Mass Measurements

The region is of great interests and fences other observations such as the sub-shell closure at N=56 observed between Z=37-42 and the N=50 shell closure. The decrease in separation energies describes the ease to pull out the nucleons from a nucleus. The proton sub-shell closure occurring at Z=40 can also be observed looking on the two proton separation energies S_{2p}, see Fig. 2.2.

Passing from spherical to well deformed shape at N=60, the two-neutron separation S_{2n} should increase, see Fig. 2.2, see Ref. [1, 26, 64]. The jump in S_{2n} at N∼60 indicates an increase of the binding energy due to the appearance of the deformation.

The mass informations presented in this document are reported from the Atomic-Mass Evaluation collaboration AME2012 under the coordination of G. Audi, see Ref. [65].

From the mass measurements, one can deduce that the most important deformation is observed for the Zr, Y and Sr cases. Furthermore, in all the cases there is a sudden increase of the deformation at N∼60, but it

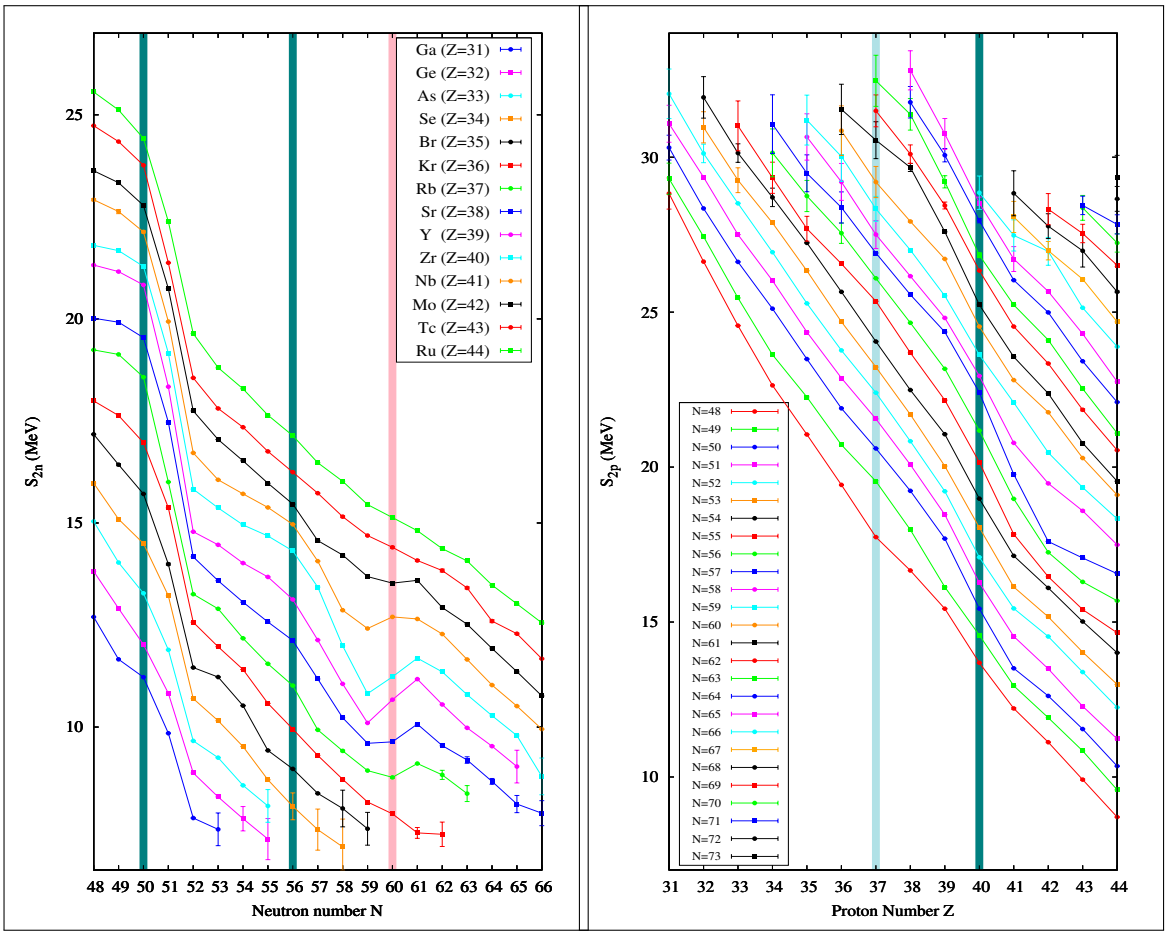

(a) Two-neutron separation energies *vs* neutron number.

(b) Two-proton separation energies *vs* proton number.

Figure 2.2: S_{2n} (a) and S_{2p} (b) values over neutron number around A∼100, N∼60 from tabulated values of AME2012 [65] and the Ref. [66, 67, 68, 69, 70, 71, 72]. The dark blue bands highlight the shell closure at N=50, Z=40 and sub-shell closure at N=56. The light blue band indicates the rubidium isotopes. The red band corresponds to the development of deformation at N∼60.

continues along neutron number until N≳62. The molybdenum isotopic chain is considered as the upper limit of the shape transition region where a rather continuous trend takes place instead of a jump. However, the limits of the shape transition region are not clear and the determination of its boundaries should help to understand the responsible processes of the development of deformation. The krypton isotopic chain is placed at the border of the shape transition region and raised interest in the community. According to microscopic calculations, we should observe the same deformation for ^{96}Kr, ^{98}Sr, and ^{100}Zr, see Ref. [52, 58, 73, 74]. Some other calculations, such as HFB-17 using the Skyrme force or HFB based on the Gogny energy density functional with two parametrization D1S and D1M, predicted a strong and sudden development of deformation, see Ref. [51, 74, 75]. The status of the Kr isotopic chain has been clarified firstly by the Penning-trap measurements of S. Naimi et *al.* [66], showing that the deformation development should be gradual or absent. The results for ^{94,96}Kr isotopes are presented on the S_{2n} of the Fig. 2.2, exhibiting no sudden change at N=60; which is in sharp contrast with the heavier isotopic chains.

The differential variation of the two-neutron separation energy dS_{2n}(Z,N) which is defined as a function of the neutron number, see Fig. 2.3 and Ref. [76], as:

$$dS_{2n}(Z,N) = \frac{S_{2n}(Z,N+2) - S_{2n}(Z,N)}{2} \tag{2.1}$$

This parameter is more difficult to interpret than the two-neutron separation for example, since it involves three different masses. The dS_{2n}(Z,N) is expected to be negative at the neutron "magic number" (shell closure, sub-shell closure) and positive at the increase of binding energy indicating the presence of deformation.

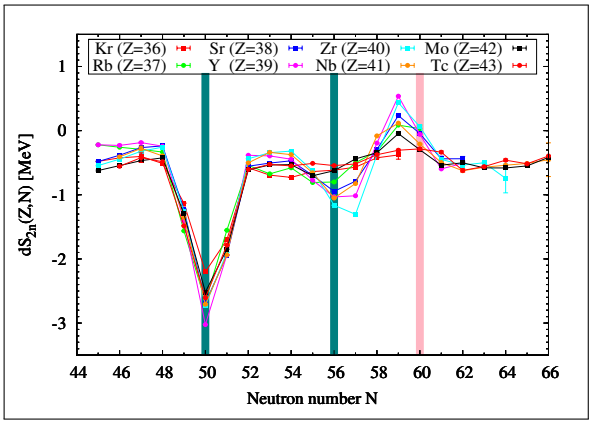

Figure 2.3: Differential variation of the two-neutron separation energy dS_{2n}(Z,N).

The shell closure and sub-shell closure are respectively observed at N=50 and 56. The onset of deformation is clearly identified around N=60.

The mass measurements are just one of the hints for the presence of deformation. The charge radii measurements could additionally confirm the onset of deformation in the region. The charge radii are directly linked with the nuclear shape and their increases at N∼60 constitute an irrefutable proof, see Sec. 2.2.

2.2 Mean square charge radii

Additional informations from mean square charge radii measurements support the conclusions on the onset of deformation. The mean square charge radii variations may be accessed by measuring the optical isotopic shift thanks to laser spectroscopy.
The mean square charge radii variations exclude the contribution from the neutron distribution, therefore they cannot be considered as an absolute measurement of the nuclear deformation. However, the combination of mass and charge measurement are direct observations of the deformation, characterizing qualitatively its amplitude. The mean square charge radii have been systematically measured in the region and a summary is given on Fig. 2.4.

The jump of the mean square charge radii at N=60 is drastic for the Rb's, see Ref. [77]. The same behavior is observed for upper isotones until Mo (Z=42), where a linear trend is restored. The krypton case does not exhibit an increase of the charge radii. The rubidium is thus identified as the first one exhibiting the sudden onset of deformation.

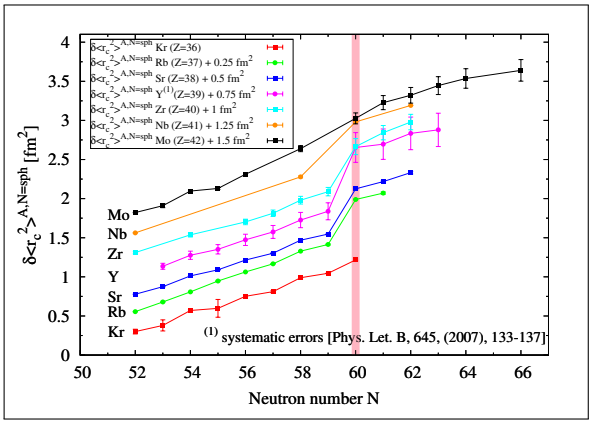

Figure 2.4: Difference in mean square charge radii in the N=60 region shown for krypton [78], rubidium [77], strontium [79, 80, 81], yttrium [82, 83], zirconium [84, 85], niobium [86] and molybdenum [87, 88] given relative to their spherical form. Each isotonic chain is set apart by 0.25 fm^2 for clarity.

3 Low-lying Excited States

3.1 Introduction

Let us consider what happens when filling the valence shells of a "magic" nucleus. Such "magic" nucleus should be spherical. By adding protons and neutrons, it could get deformed.

The spherical-like and ellipsoidal-like (deformed) low-lying nuclear structure can be differentiated in even-even nuclei by the energy of their first and second excited states, $E(2_1^+)$, $E(4_1^+)$ and their ratio $R_{4/2}$. The unified nuclear model predicts a lowering of the $E(2_1^+)$ energies, an increase of the transition strength $B(E2, 2_1^+ \rightarrow 0_1^+)$ and of the $R_{4/2}$ ratio in case of ellipsoidal shape, see Ref. [1, 10, 26, 89].

In the studied region, the nuclei are far from stability and from a shell closure. Thus, the residual nucleon-nucleon interaction becomes more complicated to treat. However, some simplification in model calculations can be applied, for example, the assumption of a specific core associated to a valence space. In general, the valence space and the residual nucleon-nucleon interaction infers the observed nuclear properties.

3.2 Measurements

The systematic comparison of the first $E(2_1^+)$ energies, the $R_{4/2}$ and the $B(E2, 2_1^+ \rightarrow 0_1^+)$ values presents relevant characteristics, see Fig. 2.5 and Fig. 2.6. Their features confirm again the scenario of ellipsoidal shape.

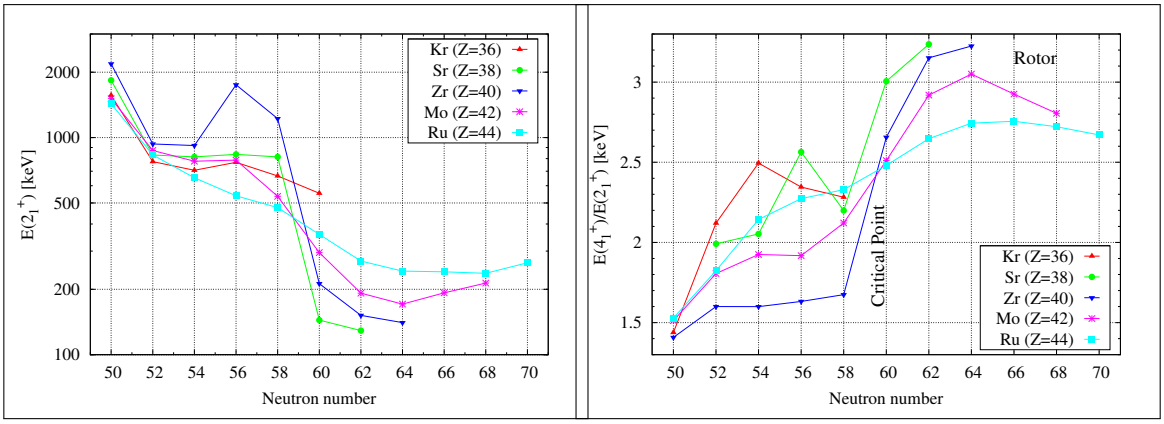

(a) Energies of the first excited 2_1^+ states (logarithmic scale). (b) Ratio of the energies of the first excited 4_1^+ and 2_1^+ states.

Figure 2.5: Energies of the first excited 2_1^+ states (a) and (b) ratio of the energies of the first excited 4_1^+ and 2_1^+ states in the even-even isotopes of Kr, Sr, Zr, Mo and Ru for N⩾50. Values extracted from the Ref. [90].

In the Kr case, the development of deformation was not observed for mass and mean square charge radii measurements, see Sec. 2 on page 40, but it could appear gradually. To investigate this hypothesis, a Coulomb excitation study has been performed at ISOLDE with the MINIBALL array on ^{94}Kr, ^{96}Kr, see Ref. [73, 91], the results are also presented in the Fig. 2.5 and 2.6.

For N$\lesssim$60, the 2_1^+ state energies are around 1 MeV instead of few hundred keV for N$\gtrsim$60. The $R_{4/2}$ ratios also exhibit a large variation passing from ~1.5-2 for N$\lesssim$60 to 3 for N$\gtrsim$60, see Fig. 2.5(b).
The $E(2_1^+)$, $R_{4/2}$ and $B(E2, 2_1^+ \rightarrow 0_1^+)$ systematics for the krypton isotopic chain exhibit a smooth development of deformation.

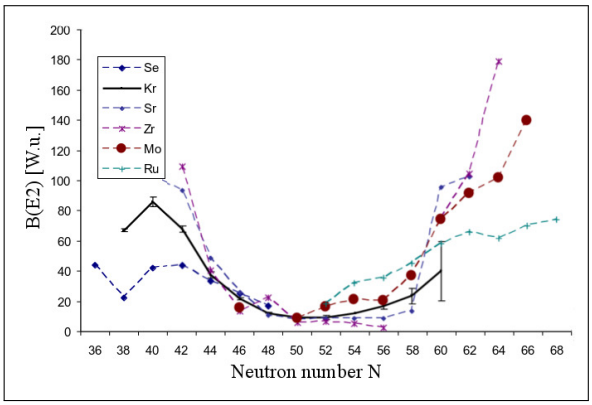

Figure 2.6: Transition strengths B(E2, $2_1^+ \rightarrow 0_1^+$) in the even-even isotopes of Se, Kr, Sr, Zr, Mo and Ru. Picture modified from Ref. [92].

4 The First Theoretical Calculations

In the past, the sudden onset of deformation has been firstly studied via calculations on Zr isotopes, by P. Federman and S. Pittel, with a restricted valence space ($\pi 2_{p1/2}$, $\pi 1g_{9/2}$, $\nu 2d_{5/2}$, $\nu 3s_{1/2}$, $\nu 2d_{3/2}$, $\nu 1g_{7/2}$ and $\nu 1h_{11/2}$) assuming an inert core of strontium ^{88,94}Sr, see Ref. [58, 59, 93], see Fig. 2.7. They interpreted the obtained experimental results as if the deformation in the region is due to the the proton-neutron correlation between the $\pi 1g_{9/2}$ and $\nu 1g_{7/2}$ spin-orbit partners orbitals. Moreover, they mentioned the possible importance of the occupancy of the $\nu 1h_{11/2}$ and its significant correlation with the $\pi 1g_{9/2}$ orbit.

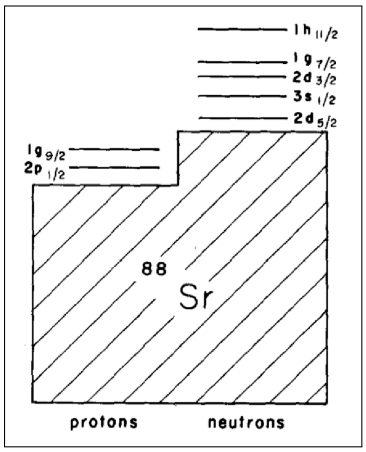

Figure 2.7: Single-particle levels used to describe the Zr-Mo region from Ref. [58].

Further calculations performed for the Mo isotopes needed the inclusion of the $\nu h_{11/2}$ in order to reproduce the features of deformed isotopes [94]. The importance of this rather selective proton-neutron interaction between spin-orbit partner orbitals $\pi 1g_{9/2}$ and $\nu 1g_{7/2}$ was called into question.

A few years later, A. Kumar and M.R. Gunye [63], performed Hatree-Fock-Bogoliubov (HFB) calculations including a larger valence space: $\pi 1f_{7/2}$, $\pi 2p_{3/2}$, $\pi 1f_{5/2}$, $\pi 2p_{1/2}$, $\pi 1g_{9/2}$, $\pi 2d_{5/2}$, $\pi 1g_{7/2}$, $\pi 2d_{3/2}$, $\pi 3s_{1/2}$, $\nu 1g_{9/2}$, $\nu 2d_{5/2}$, $\nu 1g_{7/2}$, $\nu 2d_{3/2}$, $\nu 3s_{1/2}$, $\nu 1h_{11/2}$, $\nu 2f_{7/2}$, $\nu 1h_{9/2}$, $\nu 2f_{5/2}$, $\nu 3p_{3/2}$, $\nu 3p_{1/2}$, with an inert core of $^{60}_{20}$Ca, in oder to reproduce the experimental data in the ^{98}Sr, ^{100,102}Zr, and ^{104,106}Mo, see Fig. 2.8. The larger configuration space helped to reproduce the trend of the experimental data and indicates a non-satisfying use of the ^{94}Sr or ^{88}Sr core. The energy levels are not well reproduced; in addition, even if the tendency is respected the reproduction is not reliable for the E(2_1^+) and the B(E2, $2_1^+ \rightarrow 0_1^+$) values if we compare the difference between the experimental and calculated values for the same spin/parity configuration in the neighboring nuclei (see respectively Fig. 2.8(a) and Fig. 2.8(b)).

However, enlarging the valence space helped to reproduce the sudden onset of deformation, and thus

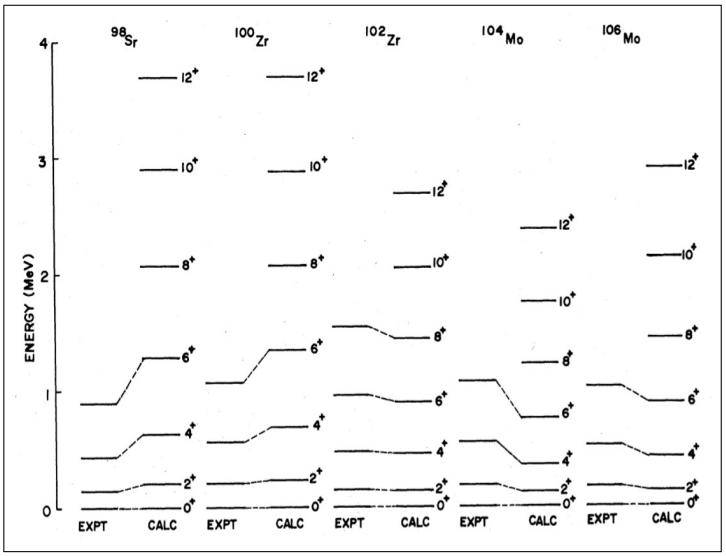

(a) Calculated energy spectra up to $J = 12^+$ in the ^{98}Sr, ^{100,102}Zr, ^{104,106}Mo compared with the corresponding experimental energy spectra.

Nucleus	$Q(2^+)$	$B(E2;2^+\rightarrow 0^+)$ Calc.	Expt.
^{98}Sr	−1.33	0.22	0.22
^{100}Zr	−1.20	0.35	0.23
^{102}Zr	−1.44	0.51	0.66
^{104}Mo	−1.50	0.54	0.43
^{106}Mo	−1.54	0.58	0.43

(b) Static quadrupole moment $Q(2+)$ (eb) and B(E2, $2_1^+ \rightarrow 0_1^+$) (e^2b^2).

Figure 2.8: HFB calculations realized by A. Kumar and M.R. Gunye on the Sr-Zr-Mo region using a large valence space with an inert core of ^{60}Ca, from Ref. [63].

one could propose the hypothesis of the presence of another interaction than the neutron-proton interaction between $\pi 1g_{9/2}$ and $\nu 1g_{7/2}$.

Large-scale finite-range drop model calculations (FRDM) with a folded Yukawa single particle potential by P. Moller, J.R. Nix, W.D. Myers and W.J. Swiatecki, see Ref. [95], exhibit the shape transition from spherical to well deformed shape. However, this change occurs gradually in the range N=54-64. The experimental ground state masses, deformation parameters, halflives, Q_β values are well reproduced which is important for astrophysicists. In terms of deformation, the experimental data are better reproduced after the deformation gap (N$\gtrsim$60).

In many articles, the role of the unique-parity down-sloping orbitals from $\nu h_{11/2}$ around N$\sim$60 has been stated as favoring the appearance of a low-energy deformed minimum at around $\epsilon_2 \sim 0.4$, see Ref. [94]. The unnatural parity of those intruder orbitals confers them a low interaction with the neighboring neutron orbitals. The hypothesis of their filling could explain the onset of deformation. The scenario should imply a gradual establishment of deformation corresponding to the consecutive filling of the orbitals. This picture seems not appropriated with regards to the sudden development of deformation observed experimentally.

A phenomenological explanation has been provided by W. Urban and J.A. Pinston [96, 97] concerning the rapid shape change. They spotlighted the importance of the $\nu 9/2[404]$ extruder orbital which should favor the spherical shape. The shape coexistence observed in the ^{97}Sr and ^{99}Zr corroborates such a hypothesis, see Sec. 5, see Fig. 2.9. Indeed, in the N=59 isotones, different deformations are observed for different rotational bands which should correspond to different internal arrangement of the core (different orbitals).

In the specific case of the ^{99}Zr, W. Urban and J.A. Pinston explained that the rotational bands based on the $\nu 9/2[404]$ orbital have the maximum of deformation in the region of around $\epsilon_2 \sim 0.4$ which could be due to the presence of the down-sloping $\nu 1/2[550]$ and $\nu 3/2[541]$ close to the Fermi surface. The observation of rotational bands based on the $\nu 1/2[550]$ and $\nu 3/2[541]$ orbitals at around $\epsilon_2 \sim 0.3$ forces the $\nu 9/2[404]$ orbital to stay inside the core, acting against the deformation. Their work emphasizes the importance of the mentioned neutron orbitals in the onset of deformation, however a major role of the proton-neutron interaction cannot be excluded and it would be of great interest to study the evolution of the deformation with the removal of protons from the $\pi g_{9/2}$ orbitals. Indeed, the latter could interact strongly with the $\nu h_{11/2}$ orbitals.

In the ^{99}Zr, two regular bands of rotational character based on the 575.5, 657.7 and 821.4 keV levels are

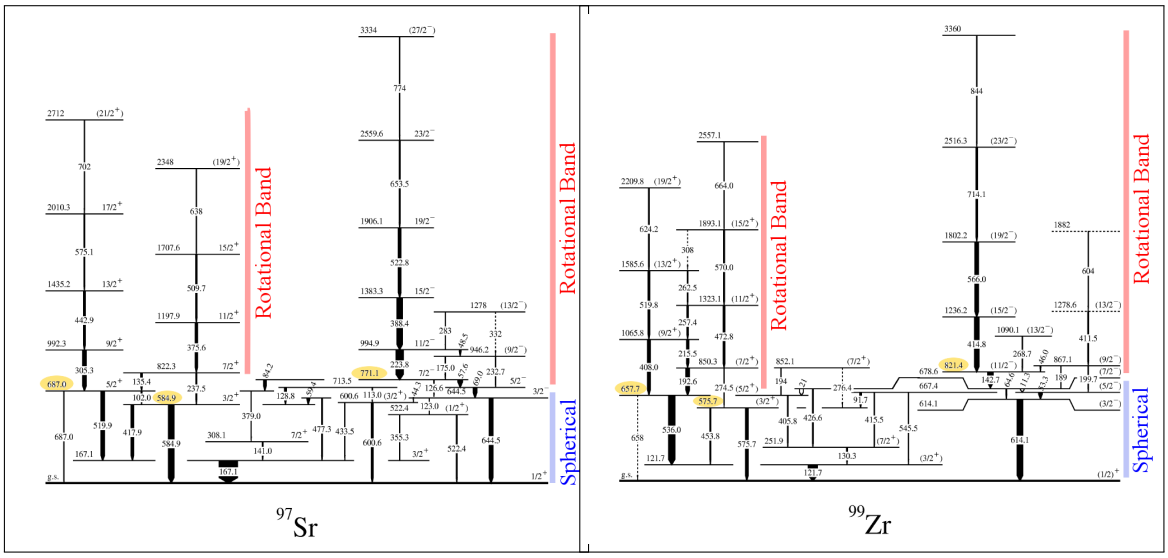

(a) (b)

Figure 2.9: Level scheme in N=59 ^{97}Sr (a) and ^{99}Zr (b) with shape coexistence. The nuclei have been produced by spontaneous fission of ^{248}Cm. Modified pictures from Ref. [55].

observed coexisting with spherical-like excited structure at low energy.
In the ^{97}Sr, two regular bands of rotational character based on the 584.9, 687.0 and 771.1 keV levels are observed coexisting with spherical-like excited structure at low energy. The excited nuclear structure is similar, the rotational bands are shifted according to the filling of protons and neutrons. For example, inside the same isotopic chain, going from N~58 to 60, the rotational bands are lowered taking the place of the spherical-like excited structure. The rotational character replaces the spherical one in their ground state.

5 Shape coexistence

5.1 Definition

Following the definition of J.L. Wood and K. Heyde [98], the shape coexistence is the result of the equilibrium between the tendencies to stabilize the nucleus with spherical or ellipsoidal shapes. The nucleon configurations (orbitals) are almost degenerated and it leads to the observation of several shapes in a short energy range.

Shape coexistence is not a new field of nuclear physics (50 years of investigation), but recently experimental tools have been developed to get an insight into those structures. The nuclear properties used to probe the evidence of shape coexistence are the electric quadrupole moments, inertia parameters, branching ratios, Fermi levels, transition probabilities ($\rho^2(E0)$).

5.2 Regions of shape coexistence

Firstly considered as a singularity of few regions of the nuclear chart, it appears as a universal effect and was observed "practically" everywhere in the chart, Fig. 2.10. The regions of shape transition are usually subject to shape coexistence.

It constitutes one of the main important challenge for theoreticians to explain such behaviors. There are two principal theoretical approaches to describe the phenomenon : the microscopic shell and the mean field models.

The appearance of shape coexistence results from the competition between a residual interaction and an energy gap. It would lower the energy difference between the configurations. This effect is observed around the singly shell and mid-shell closures. In the region (N~ 60, Z~ 40), close to the single shell closure at Z~ 40 and/or N~ 56, the presence of shape coexistence has been proven (an example is given on Fig. 2.11). In those cases, the collectivity of the ground state is suppressed.

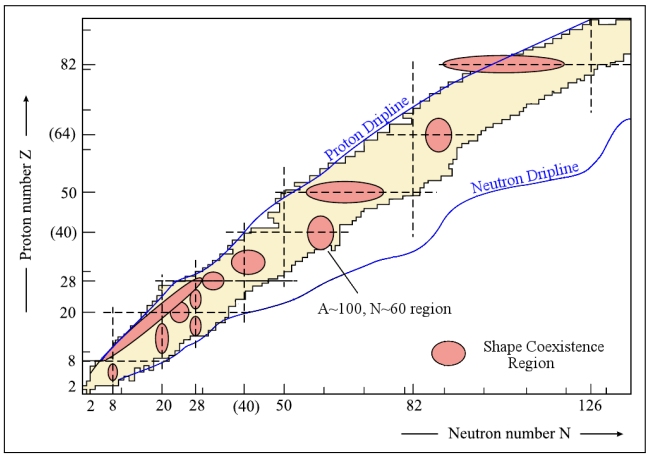

Figure 2.10: Shape coexistence regions already known or under discussions (red). Modified picture from Ref. [98].

5.3 Shape isomers

When there is a rapid shape change, it is reasonable to expect the presence of such isomers. Indeed, in order to change the shape, the nucleons configurations should change and it requires a high level of complexity to rearrange. The transition between different shapes have usually "forbidden" leading to isomerism.

This should result from the crossing of spherical and deformed configurations, see Ref. [99].

The observation of such isomers would constitute a further confirmation of the shape transition.

5.4 Region: A~100, N~60

In this region, many examples can be cited, such as the observation of shape coexistence in the N=58 isotones ^{96}Sr and ^{98}Zr, see Fig. 2.11. Those nuclei have spherical ground states and deformed shapes at higher energies in their excited structure, see Fig. 2.12. In the ^{98}Zr, the E0 transitions of 853 keV and 1859 keV states reveals a basic spherical configuration strongly mixed with the deformed configuration of the deformed band (the band head is the 0^+ at 1436 keV). In general, weakly deformed bands appear at around 1.5 MeV above the spherical ground states. The appearance of E0 transitions exhibits the persistence

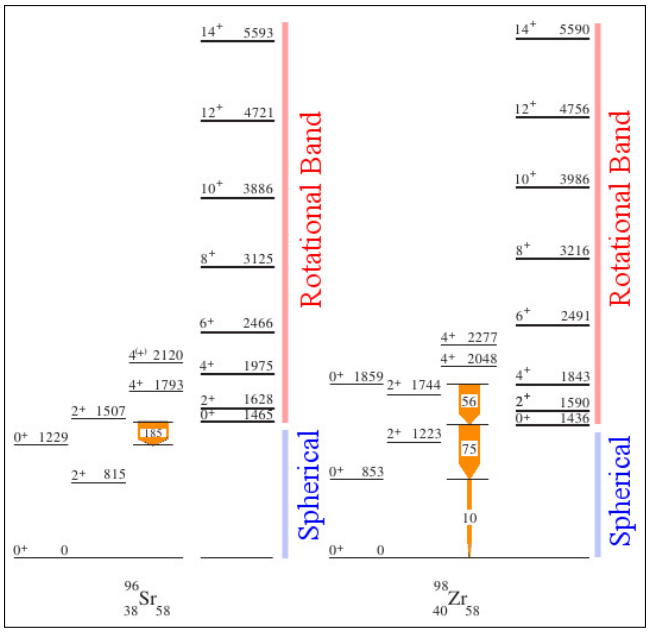

Figure 2.11: Example of shape coexistence in the N=58 isotones ^{96}Sr and ^{98}Zr, see Ref. [100, 101]. The orange vertical arrows indicate E0 transitions with their observed values for $\rho^2(E0) \times 10^3$; the value for ^{96}Sr is the largest known for A>56. The band heads for the ^{96}Sr and ^{98}Zr are respectively the 0^+ at 1465 keV and 1436 keV.

of coexisting structures. The E0 transition strengths are model independent signature of the mixing of configurations with different mean-square charge radii. If two configurations are mixed with the mixing amplitudes a and $\sqrt{1-a^2}$, the E0 transition strength is expressed as:

$$\rho^2(E0) = \frac{Z^2}{R_0^4} a^2(1-a^2)\left[\Delta<r^2>\right]^2 \tag{2.2}$$

with: $R_0 = r_0 A^{1/3}$ and $\Delta<r^2> = <r^2>_1 - <r^2>_2$.

Shape coexistence has also been observed in many N=59 isotones such as ^{96}Rb, ^{97}Sr, ^{98}Y and ^{99}Zr, present at the ground states shape transition, see Fig 2.9,Fig 2.12. They exhibit rotational bands, at around 0.7 MeV, and also single particle like transition scheme on top of the ground states at the same time. In this framework, the transitional nuclei have bands corresponding to the underlying even-even core coupled to the odd-particle; the deformation of the core changes under its interaction with the odd particle.

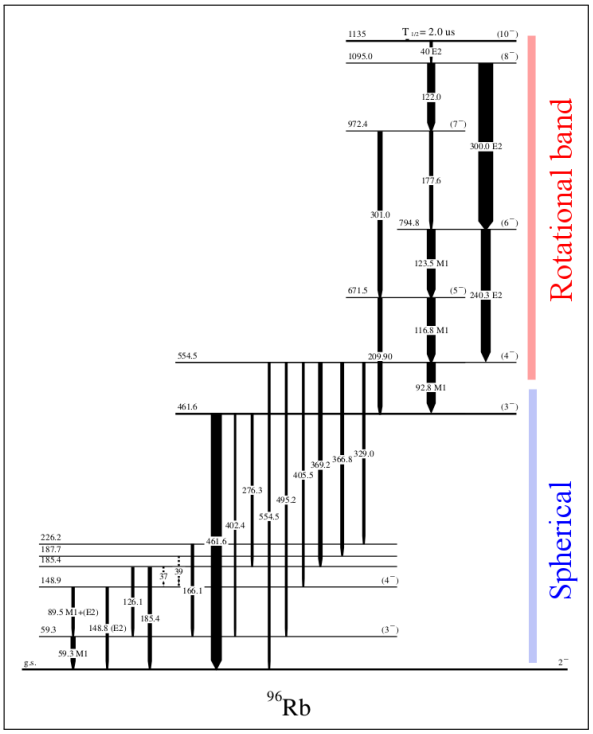

Figure 2.12: Example of shape coexistence in the N=59 isotones ^{96}Rb (presented on the figure), ^{97}Sr, ^{98}Y and ^{99}Zr, see Ref. [53, 55, 102]. Modified picture from Ref. [53].

Most of the calculations in the region predict the possibility for shape coexistence. The presence of shape isomers has been expected for the ^{97,99}Rb isotopes, see Ref [103]. According to the mean field calculations of S. Hilaire and M. Girod, see Ref. [99], using the HFB approach based on the Gogny effective nucleon-nucleon interaction for axially symmetric nuclei, a scenario of shape coexistence for the Rb isotopic chain is possible. On the Fig. 2.13, the potential energy surfaces obtained from those calculations are shown for Rb isotopes.

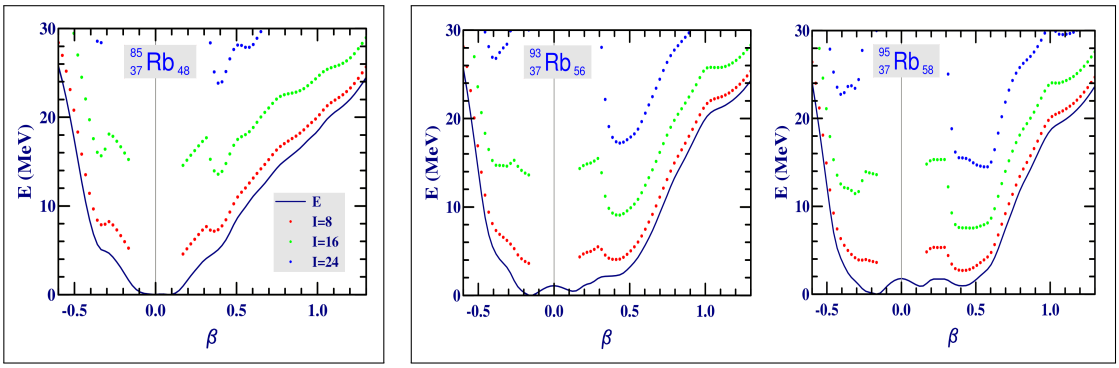

(a) Spherical.

(b) Still spherical-like but gradual appearance of oblate/prolate minima.

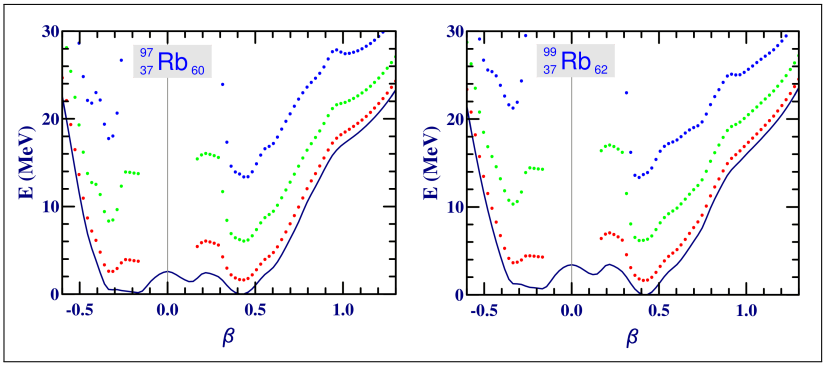

(c) Shape coexistence. Presence of two major minima for oblate and prolate deformation.

Figure 2.13: Potential energy curves for the Rb isotopes obtained by S. Hilaire and M. Girod from mean field calculations using the HFB approach based on the Gogny effective nucleon-nucleon interaction for axially symmetric nuclei, from Ref. [99, 103].

6 Our knowledge on level schemes/excited states of Rb isotopes before the present study

6.1 Spectroscopic informations: tool to probe the shape transition

The amount of known spectroscopic properties, in the heaviest isotopic chains of the deformation region (Sr, Zr, Mo), is enough to be able to give a description of the nuclear interactions in presence. However, the experimental results for lower masses such as the odd-mass Rb isotopes are quite difficult to obtain. The heaviest odd-mass Rb with known nuclear excited states was the ^{95}Rb, see Ref. [104, 105]. The level schemes for ^{93,95,97,99}Rb built on the knowledge of Rb isotopes established before our study are shown on Fig. 2.14.

The excited structures have been essentially studied by isomeric decay and in fission. The ground state magnetic dipole and electric quadrupole moments have been measured as well as the hyperfine structures up to ^{97}Rb, see Fig. 2.15. The spin and parity for the ground states of the latest were also firmly determined from the hyperfine structure studies, excepted for the spin of ^{99}Rb was not measured, the parity of the ^{97}Rb isotope not determined, see the study of C. Thibault et *al.* in Ref. [77]. The development of deformation is observed by a sudden increase of the quadrupole moment at N=60. The magnetic dipole moments of the ground states for N<60 are in good agreement with the spherical states $p_{3/2}$ and $f_{5/2}$. The calculations performed by I. Ragnarsson [106] are based on the experimental study of C. Thibault et *al.* on the magnetic dipole and electric quadrupole moments. The gyro-magnetic factor for N=60 (^{97}Rb) could be explained by the filling of one of the following Nilsson orbitals: $\pi\frac{3}{2}^{+}[431]$, $\pi\frac{3}{2}^{-}[301]$, $\pi\frac{3}{2}^{-}[312]$.

The considerably different deformations require the use of different models for the description of the sperical-like (N< 60) and the deformed (N> 60) Rb isotopes. Particle + Rotor calculations for the deformed Rb isotopes were performed by G. Simpson to clarify the situation on the Rb isotopic chain [103]. The

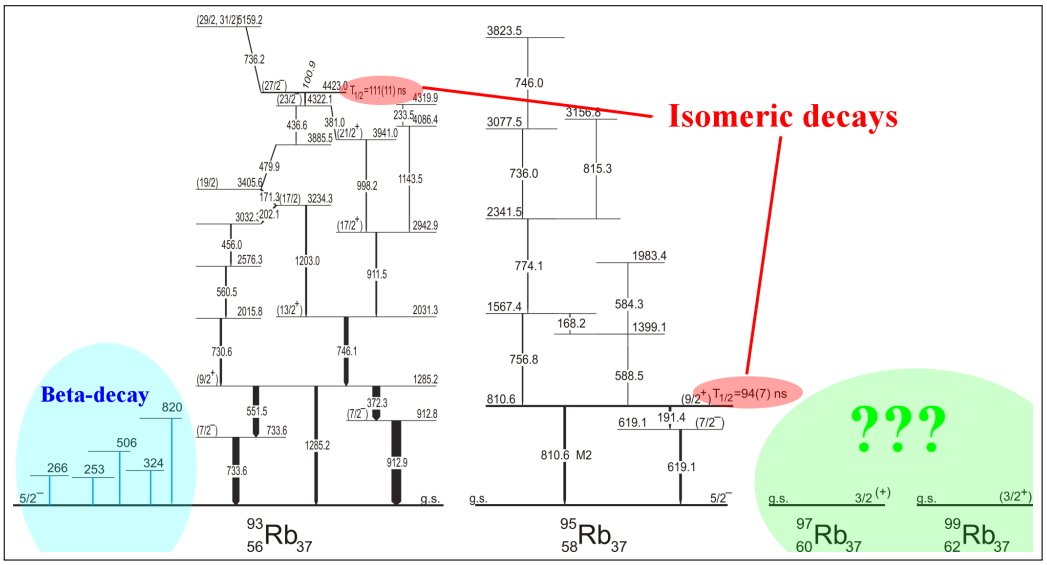

Figure 2.14: Level schemes of ^{93,95,97,99}Rb before the present study. Modified figure, based on the study of G. Simpson et *al.*, see Ref. [104].

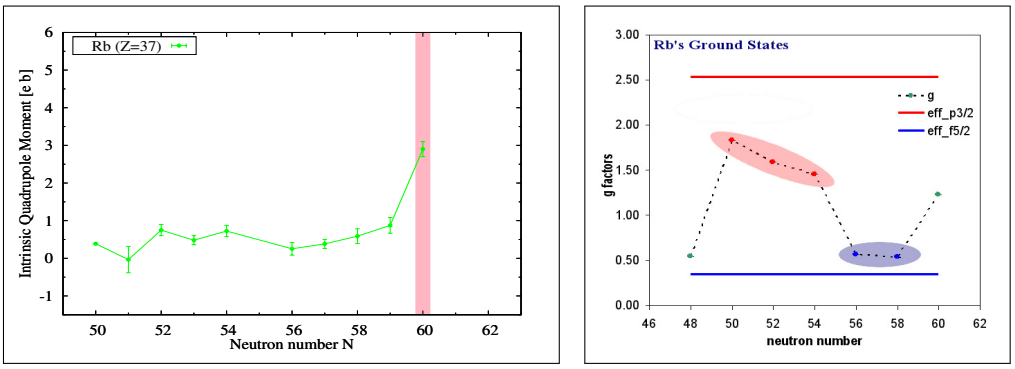

(a) Electric quadrupole moment measurements in the neutron rich Rb region.

(b) Dipole magnetic moment measurements in the Rb isotopes.

Figure 2.15: Ground state properties of Rb isotopes. Figure has been created based on the study of C. Thibault et *al.*, see Ref. [77], for the Rb isotopes, and the nuclear table of N.J. Stones, see Ref. [47].

results will be discussed and compared with experimental data.

For the spherical case, i.e. lighter mass isotopes ^{93,95}Rb, shell model calculations have been performed using an inert core of ^{78}Ni and the gwbxg interaction with the NushellX code, see Ref. [107], in order to reproduce the already known level schemes. The use of shell model is particularly appropriated for spherical-like nuclei.
The results are shown on the Fig. 2.16(a). The energy level scheme tendency of known transitions in the ^{93}Rb are well reproduced. Predictions on the same parametrization have been also performed for the ^{95}Rb.

Concerning the deformed isotopes, combining the nuclear spin, the deformation and the magnetic dipole moment the spin can possibly be assigned. From the study of C. Thibault et *al.*, I. Ragnarsson calculated with a particle + rotor model the magnetic dipole moment for the different possible Nilsson orbitals, see Ref. [106, 108]. Several sets of parameters have been employed to reproduce the measured magnetic dipole moments, they are summarized in the Tab. 2.1.

The inconsistency of the experimental and theoretical magnetic dipole moment values for the $\pi\frac{3}{2}^-[312]$ orbital discounted this possibility. The similar magnetic dipole moments obtained for the $\frac{3}{2}^+[431]$ and $\frac{3}{2}^-[301]$ does not permit to discriminate them. Unfortunately, the study of C. Thibault et *al.* could not

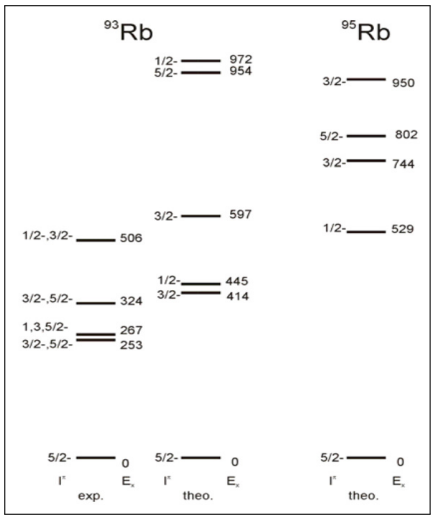

(a) NuShellX calculations (shell model nuclei).

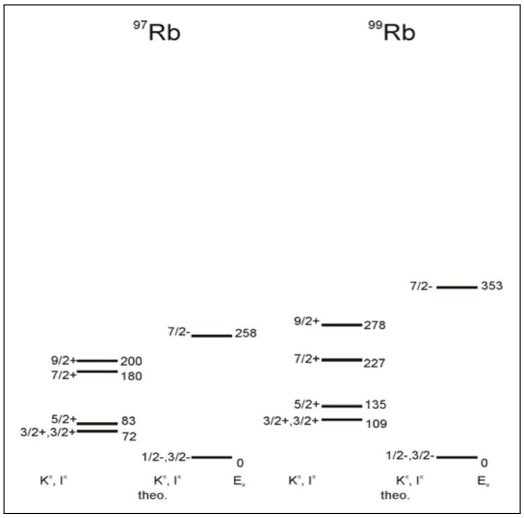

(b) QPRM calculations (deformed nuclei).

Figure 2.16: Theoretical and experimental level schemes of Rb isotopes.
The theoretical schemes for ^{93,95}Rb (a) are from shell model calculations while ^{97,99}Rb are obtained using the quasi-particle-rotor model (QPRM) (b). From Ref. [103].

K	I^π	Q_s [eb]	μ [μ_N]	Orbital
3/2	$3/2^-$	0.6	1.9	$\pi\frac{3}{2}^-$[301]
3/2	$3/2^+$	0.6	1.99	$\pi\frac{3}{2}^+$[431]
3/2	$3/2^-$	0.6	0.7	$\pi\frac{3}{2}^-$[312]
Experimental Values		0.6	1.84	-

Table 2.1: Low lying properties predicted by QPRM calculations. Values from Ref. [77, 106].

determine the electric quadrupole moment sign, which could help to assign a specific configuration to the ground state, see Ref. [77].

The knowledge of the B(E2) transition strengths at low energies should allow to identify the active orbital. The Coulomb excitation study of odd-mass Rb isotopes should provide more informations on the low lying structure, such as the level energies and the transition strengths of the transitions. Those studies should complete the β-decay and/or spontaneous fission investigations which are not governed by the same selection rules and cannot access to the low-lying states observables as in Coulomb Excitation.

6.2 Theoretical calculations on odd-mass neutron-rich Rb isotopes by Rodriguez-Guzman et *al.*

HFB-D1S/D1M calculations [51, 75, 109] allowed some predictions on the charge radii and mass, they were discussed previously. In this Subsubsec., one focus on the description of the theoretical results obtained concerning the levels and involved Nilsson orbitals.
In order to describe the onset of deformation in the Rb isotopes, the proton and neutron single-particles energies are plotted as a function of the quadrupole moment in the closest ^{98}Sr (Z=38, N=60) even-even nucleus, see Fig. 2.17(a). Indeed, the calculations on odd-mass nuclei are quite scarce. The experimental excitation energies and spin parity assignments are compared to the HFB-EFA Gogny-D1S calculation results, see Fig. 2.17(b).

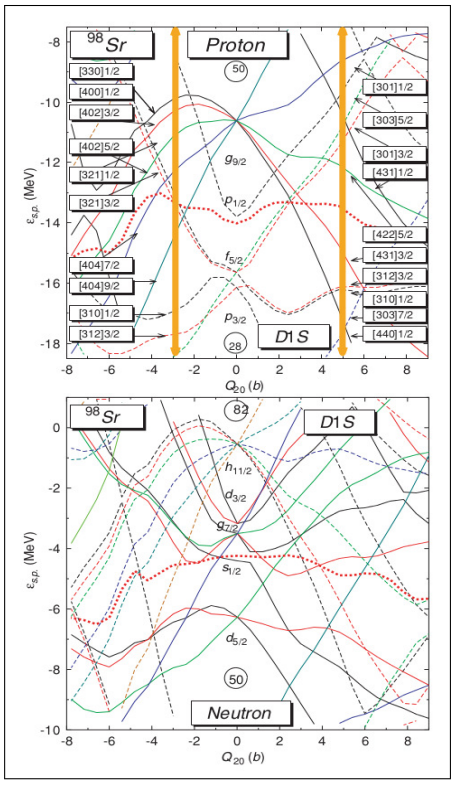

(a) Single-particle energies for protons and neutrons in ^{98}Sr as a function of the axial quadrupole moment Q_{20}. The Fermi level is depicted as a thick dashed red line. The results have been obtained with the Gogny-D1S EDF. Asymptotic Nilsson quantum numbers $(N, n_z, \Lambda)K^\pi$. The orange arrows are placed on the energy minima in the oblate and prolate cases.

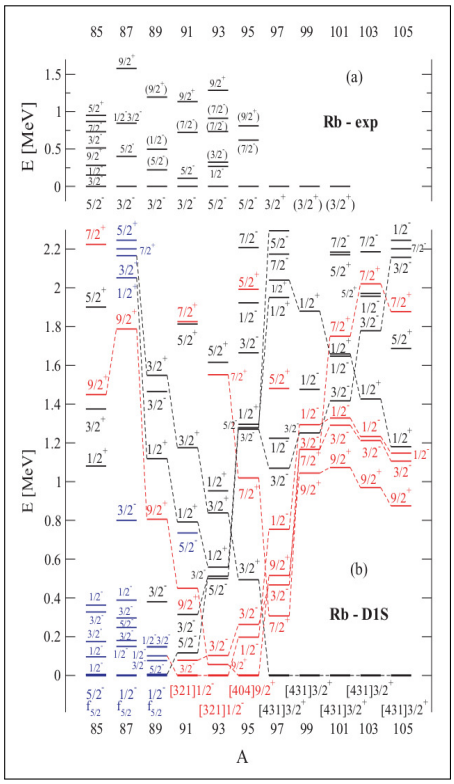

(b) Experimental excitation energies (top) and spin parity assignments compared with Gogny-D1S HFB-EFA results (bottom) for one quasi-proton states in odd-A Rb isotopes. Prolate configurations are shown by black lines, oblate ones by red lines, and spherical ones by blue lines.

Figure 2.17: HFB Gogny-D1S calculations on the single-particle energies and excited states in ^{97}Rb.
(a) Comparison between the experimental and theoretical excitation energies and spin parity assignments. The quasi-particle states are identified by their K^π quantum number.
(b) Single-particle energies for protons and neutrons in ^{98}Sr.
From Ref. [51, 75, 109].

On the Fig. 2.17, the single-particles energies exhibit minima for oblate and prolate deformation regions at around $|Q_{20}| \sim 5$ b.
The nuclei start to be deformed when the valence protons fill the down-sloping $\pi g_{9/2}$ orbitals. On the neutron side, approaching N=60, the valence neutrons start to fill the down-sloping $\nu h_{11/2}$ orbitals for important deformation ($Q_{20} \sim 4-5$ b).
The strong sensitivity to the occupancy of the considered single-particle orbitals, resulting in the sudden onset of deformation, can be explained as originating from the strong n-p interaction polarizing the core. This polarization should favor the population of the $g_{9/2}$ orbitals for the same deformation.
Moreover, this scenario is in agreement with the Jahn-Teller consideration, in which the nuclear states close

to the Fermi level avoid a high density and prefer the higher energy gaps which leads to deformation, see Ref. [110, 111].
In our case, the unpaired proton ($^{A}_{37}$Rb) gives the spin and parity of the nucleus ground state, and thus, the jump from the $\frac{5}{2}^{-}$[303] to the $\frac{3}{2}^{+}$[431] orbital has to occur. However, one has to mention the importance of the proton-neutron interaction between the $g_{7/2}$ and $g_{9/2}$ spin-orbit partner orbitals acting in favor of the deformation.

The results obtained for the excited energies on Fig. 2.17(b) reproduce well the shape change. However, the spin and parity assignments in the slightly deformed $^{91-95}$Rb differ from the experimental observations. This can be explained by a quasi-degenerated oblate and prolate states in the low-lying energies. But note that the deformation jump is well reproduced between the weakly deformed $^{91-95}$Rb and well deformed prolate $^{97-101}$Rb, as well as the most probable $\frac{3}{2}^{+}$[431] orbital assignment for the ^{97}Rb.

7 Conclusion

A clear identification of the band-head spins, their deformations and the Nilsson orbitals on which the rotational bands are built should give insights into the mechanism responsible of the sudden onset of deformation.

Rotational bands have been already identified in the closer to stability isotopic chains at N∼60, exhibiting a deformation in their ground states. Mass and mean square charge radii measurements confirmed the phenomenon and determined the limit of the onset of deformation. Complementary, Coulomb excitation studies were performed to understand the low lying structure in the region and extract more information concerning the importance of the residual nucleon-nucleon interaction.

On a first approach, theoretical model calculations involved the residual proton-neutron interaction between the $\pi g_{9/2}$ and $\nu g_{7/2}$ spin-orbit partners as the issue of the problem. However, further calculations taking into account a larger valence space, obtained a better agreement with the experimental results (for the Mo isotopes). Thus, the importance of the residual n-p interaction may be questioned.
More data are requested to distinguish the deformation drivers which may act on the residual proton-neutron interaction. The nature of many of the nuclides in the region make their experimental study challenging (e.g. short life-time, chemical nature).

Concerning the rubidium, placed at the corner of the sudden onset of deformation, Coulomb excitation studies could cover all the mentioned observables in order to understand the mechanisms involved in the development of deformation.
In the rubidium isotopic chain, the ground states showed also a rapid onset of deformation at ^{97}Rb. Nevertheless, the detailed nuclear structure of the nuclei could not yet be investigated. The existence of rotational bands could be expected in the odd-mass neutron-rich rubidium isotopes at N$\gtrsim$60 and the single-particle configuration on top of which the rotational bands are built has to be identified. The ordering of proton orbitals in the well deformed ^{97}Rb is not yet known. The study of the low-lying nuclear structure via Coulomb excitation in the odd-mass Rb isotopes would constitute one of the best way to gain information on the active proton orbitals.

Furthermore, shape isomers are expected for the Rb isotopes close to N∼60. However, in case of low energy and long lived isomers it would be difficult to identify.

Similar Coulomb excitation studies have already been performed at CERN with REX-ISOLDE and the MINIBALL array for the odd-mass and odd-odd Cu isotopes, see Ref. [112]. It has shown the strong potential to gain informations both on the single particle-like and collective states in the exotic nuclei.

The physics motivations, related to the study of the discussed onset of deformation an more precisely its mechanisms, justify naturally the experimental study of the low lying structure of ^{93,95,97,99}Rb by Coulomb excitation.

Chapter 3

Coulomb excitation - probe of nuclear structure

The Coulomb excitation is a "purely" electromagnetic interaction, consisting in a collision between two nuclei at an energy lower than the Coulomb barrier. In such a reaction, if the nuclear interaction can be neglected or treated as a perturbation, the reaction is qualified as a "safe" Coulomb excitation. In the case of non negligible nuclear interaction compared to the electromagnetic interaction, the reaction is qualified as "unsafe" Coulomb excitation. In the following, the reactions would be considered as "safe"-like Coulomb excitation. The electromagnetic interaction in presence confers the main properties of the observed de-excitation.

1 Coulomb excitation: a probing tool

1.1 Introduction

In the following section, one describes briefly the opportunities that the Coulomb excitation presents [113]. At first, it has been developed as a tool to investigate low-lying states of nuclei. The respect of the "safe" requirement involves a low excitation energy.
The Coulomb excitation has been extensively used to study the nuclear structure of nuclei produced close to the beta stability valley. The use of Radioactive Ions Beam (RIB) opened up new perspectives for this technique. The Coulomb excitation is governed by specific selection rules different from other kinds of reactions. This technique is nowadays extensively used for short lived radioactive nuclei.

1.2 Historical developments

The Coulomb excitation is a well known excitation reaction used as a trustworthy tool. As a matter of fact, this process has been theoretically studied in the 30's, see Ref. [114]. It's only twenty years later, when the possibility to populate rotational states in deformed nuclei described by A. Bohr and B. Mottelson [115], that the process has been unearthed. Being in good agreement with the semi-classical theory calculations of K. A. Ter-Martirosyan [116] it was experimentally confirmed by T. Huss and C. Zupancic [117]. At that time only light beams were delivered in the nuclear facilities and just a few excited levels could be populated. The development of heavy ion beams allowed the possibility of multiple Coulomb excitations by stronger electromagnetic fields.

1.3 Overview and classical picture of the Coulomb excitation phenomenon

In the present introduction, the description will be restricted to the pure (or "safe) Coulomb excitation, i.e. well below the Coulomb barrier, so that no penetration into the strong nuclear field occurs. The strong interaction is considered as negligible compared to the electromagnetic interaction. The excitation will only be caused by the electromagnetic interaction and only the matrix elements of the electromagnetic operator are in play.

In order to respect the condition of exclusive electromagnetic interactions, the collision should have a wave length (projectile) smaller than the closest approach distance occurring in a head-on collision. One can evaluate the relative position to the Coulomb barrier via the following parameter (usually called Sommerfeld parameter), see Ref. [113] :

$$\eta = b/2\lambda\!\!\!^{-}_{projectile} \tag{3.1}$$

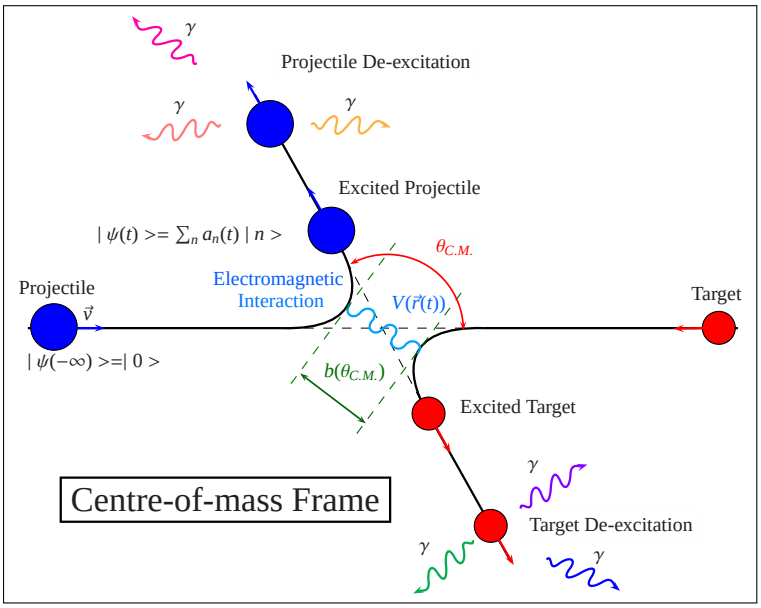

Figure 3.1: Coulomb excitation kinematics in the centre of mass.

where: $\begin{cases} b\text{: distance of closest approach in a head-on collision,} \\ \lambda\!\!\!^{-} = \frac{\hbar}{p} = \frac{\hbar}{mv}\text{: wave length.} \end{cases}$

Expressed in terms of velocity:

$$\eta = \frac{Z_1 Z_2 e^2}{\hbar v} \tag{3.2}$$

where: $\begin{cases} Z_1, Z_2\text{: charge numbers of projectile and target nucleus,} \\ v\text{: projectile velocity far away from the target.} \end{cases}$

The monopole-monopole interaction $\frac{Z_1 Z_2 e^2}{r}$ expressing the Coulomb repulsion does not excite the nuclei but can describe the tendency of the kinematics to follow a "perturbed" Rutherford scattering.
η is the parameter describing this point charge interaction. It constitutes an important parameter to estimate the strong interaction involved in the process (comparison with the Rutherford scattering).

For a safe Coulomb excitation one needs to have:

$$\eta \gg 1 \tag{3.3}$$

In this framework, the relative motions of nuclei can be described classically, in terms of wave packets, with dimensions small compared to the dimensions of classical hyperbolic orbit. Thus, the reaction kinematics can be approximately described by hyperbolas.

$$\left(\frac{d\sigma}{d\Omega}\right)_{Rutherford} = \frac{1}{4} a^2 \sin^{-4}\left(\frac{\theta}{2}\right) \tag{3.4}$$

Where: $\begin{cases} a = \frac{b}{2} = \frac{Z_1 Z_2 e^2}{\mu v^2}, \\ \mu = \frac{m_{projectile} m_{target}}{m_{projectile} + m_{target}}\text{ : reduced mass,} \\ \theta\text{ : polar angle,} \\ v\text{ : velocity.} \end{cases}$

During the collision, there is a certain probability P_n to populate the given nuclear state $|n>$. The differential cross section to populate such state could be written as:

$$\left(\frac{d\sigma}{d\Omega}\right)_n = \left(\frac{d\sigma}{d\Omega}\right)_{Rutherford} P_n \tag{3.5}$$

n specifies the level and the magnetic quantum number.

In the classical framework the excitation is realized by the time-dependent electromagnetic field. The projectile moves along the hyperbolic orbit according to the classical equations of motion, see Fig. 3.1 and 5.8. One needs to solve the time-dependent Schrödinger equation of motion:

$$i\hbar\frac{\partial}{\partial t}|\psi(t)>=(H_0+V(\vec{r}(t)))|\psi(t)> \tag{3.6}$$

Where: $\begin{cases} H_0\text{: Hamiltonian of the free nucleus,} \\ V(\vec{r}(t))\text{: electromagnetic potential of interaction,} \\ \vec{r}(t)\text{: time dependent position,} \\ |\psi(t)>\text{ : time dependent wave function of the nucleus.} \end{cases}$

One can consider the nucleus in its ground state for t= $-\infty$ and $|n>$ for t= $+\infty$, with V($\vec{r}(-\infty)$) =V($\vec{r}(+\infty)$) = 0 leading to $|\psi(-\infty)>=0$, and $|\psi(+\infty)>=|n>$ when the state after the collision is $|n>$.
The final nuclear state $|n>$ is defined as $|n>=|I_n m_n>$

The excitation amplitude is defined as:

$$a_n =< n|\psi(+\infty)> \tag{3.7}$$

With the energy E_n solution of free nucleus for the the eigenstate $|n>$, in other terms, i.e.:

$$H_0|n>=E_n|n> \tag{3.8}$$

and the excitation probability can be written as:

$$\begin{aligned} P_{0\to n} &= |a_n|^2 \qquad\qquad \text{, or} \\ P_{i\to f} &= \frac{1}{2I_i+1}\sum_{m_i,m_f}|a_{I_f m_f, I_i m_i}|^2 \end{aligned} \tag{3.9}$$

To solve the Eq. 3.6, several methods can be used, among them, the perturbation expansion valid for small and adiabatic excitation with negligible nuclear interaction. The excitation amplitudes are used in the determination of the involved cross section, angular distribution of γ-rays including polarization process.
The physics state $|\psi>$ can be expanded in terms of eigenstates and excitation amplitudes for the unperturbed Hamiltonian H_0:

$$|\psi(t)>=\sum_n a_n(t)e^{-\omega_n t}|n> \quad \text{, with: } \omega_n=\frac{E_n}{\hbar} \tag{3.10}$$

The Eq. 3.6 can be rewritten as a set of linear differential coupled equations:

$$i\hbar\dot{a}_n(t)=\sum_m < n|V(t)|m > e^{i(E_n-E_m)t/\hbar}a_m(t) \tag{3.11}$$

In order to fit in the classical picture, the energy lost by the projectile (given to the target nucleus) should be rather small to be neglected (the energy transfer should not change significantly the orbits):

$$\frac{\Delta E_n}{E_{kinetic}} \ll 1 \text{ , with: } \Delta E_n = E_n - E_0 \tag{3.12}$$

where E_n is the excited state energy of the target nucleus ($|n>$), $E_{kinetic}=\frac{1}{2}\mu v^2$ is the centre-of-mass energy and E_0 is the energy at rest.

The reaction will populate mainly the low-lying states, but sometimes the high-lying states are also weakly populated by violating the Eq. 3.12, i.e. $\frac{\Delta E_n}{E_{kinetic}} \sim 1$. The adiabatic nature of the Coulomb excitation enforces the system to be able to excite a high lying state $|n>$ only if: the collision time is short compared to the nuclear period (in other terms: $\hbar/\Delta E_n$), or, a collision time of the same order of magnitude as the nuclear period of the transition $|0>\to|n>$.

The collision time τ is estimated as the duration it takes for the projectile to travel the distance of closest approach when the scattering angle is θ:

$$b(\theta)=a\left(1+\frac{1}{sin\frac{\theta}{2}}\right) \tag{3.13}$$

The adiabadicity of the collision is evaluated via the parameter ξ, which is the product between the collision time τ and the nuclear frequency: $f_{nuclear} = \frac{\Delta E_n}{\hbar}$, $\xi_{0\to n} = \frac{\Delta E_n \tau}{\hbar}$ ([1]), leading to:

$$\xi_{0\to n}(\theta) = \xi_{0\to n}\frac{1}{2}\left(1 + \frac{1}{sin\frac{\theta}{2}}\right) \text{, with: } \xi_{0\to n}(\theta) = \xi_{0\to n}(\pi) = \frac{\Delta E_n}{\hbar}\frac{a}{v} \tag{3.14}$$

We can now re-express the energy loss as:

$$\frac{\Delta E_n}{E_{kinetic}} = \frac{2\xi_{0\to n}}{\eta} \tag{3.15}$$

For a classical picture of one step processes, one needs the conditions: $\eta \gg 1$ and $\xi \lesssim 1$ leading to $\frac{\Delta E_n}{E_{kinetic}} \ll 1$. For heavy ions, $\eta \sim$ 10-500 and ξ becomes large but without violating the condition $\frac{\Delta E_n}{E_{kinetic}} \ll 1$.

Moreover, it is important to note that for large ξ the excitation probabilities decrease exponentially with ξ, see Sec.4 on page 62 and Fig. 3.2.
For a safe Coulomb excitation, the adiabatic requirement should respect the condition $\xi \lesssim 1$.

In order to estimate the magnitude of excitation energies, one can calculate the strength by the matrix elements which can be approximated by the value of the interaction $V(\overrightarrow{r}(t))$ at the closest approach and the collision time:

$$< n|\int_{-\infty}^{+\infty} V(\overrightarrow{r}(t))|0 > \approx < n|V(b(\theta))|0 > \tau\,, \tag{3.16}$$

leading to the parameter:

$$\chi_{0\to n} \approx \frac{< n|V(b(\theta))|0 > b(\theta)}{2\hbar v}. \tag{3.17}$$

Expressed in $\hbar$ units, $\chi_{0\to n}$ permits to evaluate the number of quanta exchanged during the collision time τ for the excitation of the state $|n>$. It translates also the possibility to excite more than one state.

- if χ is small, few quanta of energy are exchanged and the excitation probability is low,
- if χ is large and ξ relatively small, the state is well excited and more quanta are exchanged.

In order to quantify the impact of multipole orders, one can decompose χ as:

$$\chi = \sum_{\lambda}\chi^{(\lambda)}, \tag{3.18}$$

With $\chi^{(\lambda)}$ the partial of multipole order λ. To give an idea of the order of magnitude of the probability to excite $|n>$ by developing onto multipoles, one can express their upper limits:

$$\begin{cases} \chi^{(0)} & = & \frac{Z_1 Z_2 e^2}{\hbar v} = \eta & \text{, the monopole part} \\ \chi^{(1)} & \lesssim & 10 & \\ \chi^{(2)} & \lesssim & 10 & \text{, the quadrupole part} \\ \chi^{(3)} & \lesssim & 0.5 & \\ \chi^{(4)} & \lesssim & 0.1 & \end{cases} \tag{3.19}$$

The higher the multipole order, the smaller is the excitation probability.
For $\theta = 180°$, the quadrupole moment can be approximated as a function of $\chi^{(2)}$ expressing the quadrupole part of the Coulomb interaction between a projectile and a nucleus, as:

$$V(b) \approx \frac{Z_1 eQ}{b^3} \text{, with } Z_1 e\text{: charge of the projectile} \tag{3.20}$$

leading to:

$$\chi^{(2)} \approx \frac{Z_1 eQ}{2\hbar b^2} \tag{3.21}$$

The introduction of the χ parameter highlights again the strong relation between the observables, the deformation and more precisely with the intrinsic quadrupole moment.

1. $|0> \to |n>$ can only occur if $\xi_{0\to n} \lesssim 1$

2 The Electromagnetic interaction in Coulomb excitation

In this brief introduction to the electromagnetic interaction, an overview of the link between the Coulomb excitation experimental observables and the electromagnetic operator is presented.

2.1 The Multipole-Multipole interaction in the electromagnetic framework

In presence of charge and current distribution, the magnetic and electric moments are expressed as a series of multipole moments.
In case of collision, the Hamiltonian describing the nucleus can be expressed as:

$$H_{Collision} = H_1^0 + H_2^0 + W_{12} \tag{3.22}$$

with: H_1^0 and H_2^0 are the Hamiltonians of free particles,
W_{12} is the Hamiltonian of the multipole-multipole electromagnetic interaction between the projectile and target nuclei.

The electromagnetic interaction Hamiltonian between the beam particle and the target can be expressed as, see Ref. [113, 118]:

$$W(1,2) = \int\int d\tau_1 d\tau_2 \frac{\rho_1(\vec{r'}_1)\rho_2(\vec{r'}_2) - \frac{1}{c^2}\vec{j}_1(\vec{r'_1})\vec{j}_2(\vec{r'_2})}{|\vec{r} + \vec{r'_1} - \vec{r'_2}|} \tag{3.23}$$

where: $\begin{cases} \rho_1(\vec{r'}_1) \text{ and } \rho_2(\vec{r'}_2) \text{ are the charge distributions,} \\ \vec{j}_1(\vec{r'}_1) \text{ and } \vec{j}_2(\vec{r'}_2) \text{ are the current distributions,} \\ \vec{r'}_1, \vec{r'}_2 : \text{coordinates of target and projectile,} \\ \vec{r} : \text{relative coordinates.} \end{cases}$

2.1.1 Stationary Treatment

In a first approach, the electric and magnetic interactions can be considered as independent (no electromagnetic interaction). One can separate the Hamiltonian of interaction in an electric and magnetic part as:

$$W_{\text{Stationary}}(1,2) = W_{\text{Electric}}(1,2) + W_{\text{Magnetic}}(1,2) \tag{3.24}$$

with: λ the multipole order and μ their projection, see Ref. [113], and:

$$\begin{cases} W_{\text{Electric}}(1,2) = & \sum_{\lambda_1\lambda_2\mu_1\mu_2} c(\lambda_1,\lambda_2) \begin{pmatrix} \lambda_1 & \lambda_2 & \lambda_1+\lambda_2 \\ \mu_1 & \mu_2 & -(\mu_1+\mu_2) \end{pmatrix} \\ & \times \mathcal{M}_1(E\lambda_1,\mu_1)\mathcal{M}_2(E\lambda_2,\mu_2)\frac{1}{\vec{r}^{\lambda_1+\lambda_2+1}} Y_{\lambda_1+\lambda_2,-(\mu_1+\mu_2)}(\vec{r}) \\ W_{\text{Magnetic}}(1,2) = & \sum_{\lambda_1\lambda_2\mu_1\mu_2} c(\lambda_1,\lambda_2) \begin{pmatrix} \lambda_1 & \lambda_2 & \lambda_1+\lambda_2 \\ \mu_1 & \mu_2 & -(\mu_1+\mu_2) \end{pmatrix} \\ & \times \mathcal{M}_1(M\lambda_1,\mu_1)\mathcal{M}_2(M\lambda_2,\mu_2)\frac{1}{\vec{r}^{\lambda_1+\lambda_2+1}} Y_{\lambda_1+\lambda_2,-(\mu_1+\mu_2)}(\vec{r}) \end{cases}$$

$\mathrm{M}(\mathrm{E}\lambda,\mu)$ and $\mathcal{M}(M\lambda,\mu)$ are respectively called the electric and magnetic multipole moments. They are defined as [25]:

$$\begin{cases} \mathcal{M}(E\lambda,\mu) &= \int \rho(\vec{r})\vec{r}^{\lambda} Y_{\lambda\mu}(\hat{r}) d\tau \\ \mathcal{M}(M\lambda,\mu) &= \dfrac{-i}{c(\lambda+1)} \int \vec{j}(\vec{r})\vec{r}^{\lambda}\vec{L} Y_{\lambda\mu}(\hat{r}) d\tau \end{cases} \tag{3.25}$$

with: $\begin{cases} \vec{L} = -i\vec{r}\times\vec{\nabla} : \text{orbital moment,} \\ \rho(\vec{r}) = \sum_{k=1}^{A} e(k)\delta(\vec{r} - \vec{r_k}) : \text{charge distribution,} \\ e(k) = 0 : \text{for neutron and } e(k) = +e : \text{for proton (charge),} \\ Y_{\lambda\mu}(\hat{r}) : \text{spherical harmonic function.} \end{cases}$

The sensitivity of electric and magnetic multipole moments, related respectively to the charge and current distributions, are explicitly introduced in their definition. Their matrix elements represent most of the nuclear structure properties such as the quadrupole deformation.

2.1.2 Dynamic Treatment

Since the collision process is a dynamic process the electric and magnetic multipole terms will interact together. Indeed the charge current densities will be modified by the relative motion of the two nuclei. An electromagnetic interaction needs to be taken into account. If the retardation effects are negligible and $\vec{r}$ is still a function of time as $\frac{\dot{\vec{r}}}{c} \ll 1$, then, a simple electromagnetic term can be added as:

$$W_{Dynamic}(1,2) = W_{Electric}(1,2) + W_{Magnetic}(1,2) + W_{Electromagnetic}(1,2) \tag{3.26}$$

The charge-current densities can be expressed as, see Ref. [113]:

$$\left\{ \begin{array}{lcl} \vec{j'}_1 & = & \vec{j}_1 + \dot{\vec{r}} \ \rho_1 \\ \rho'_1 & = & \rho_1 + \frac{1}{c^2}\dot{\vec{r}} \cdot \vec{j}_1 \end{array} \right. , \tag{3.27}$$

Those considerations lead to:

$$\begin{array}{rcl} W_{Electromagnetic}(1,2) & = & \sum_{\lambda_1\lambda_2\mu_1\mu_2} ic(\lambda_1,\lambda_2)\{\mathcal{M}_1(E\lambda_1,\mu_1)\mathcal{M}_2(M\lambda_2,\mu_2) - \mathcal{M}_1(M\lambda_1,\mu_1)\mathcal{M}_2(E\lambda_2,\mu_2)\} \\ & & \times \frac{\dot{\vec{r}}}{c}\frac{1}{\vec{r}^{\lambda_1+\lambda_2+1}}\left\{ \left(\begin{array}{ccc} \lambda_1 & \lambda_2 & \lambda_1+\lambda_2 \\ \mu_1 & \mu_2 & \mu \end{array} \right) \frac{1}{\lambda_1+\lambda_2} \vec{L}Y_{\lambda_1+\lambda_2,\mu}(\theta,\phi) \right. \\ & & \left. - \left(\begin{array}{ccc} \lambda_1 & \lambda_2 & \lambda_1+\lambda_2-1 \\ \mu_1 & \mu_2 & \mu \end{array} \right) \sqrt{\frac{\lambda_1}{\lambda_2(\lambda_1+\lambda_2)}} \vec{\Phi}_{\lambda_1+\lambda_2,\lambda_1+\lambda_2-1,\mu}(\theta,\phi) \right. \end{array} \tag{3.28}$$

with: $\vec{\Phi}_{lJ\mu}$ the spherical harmonic vector defined in Ref. [119], θ is the polar angle, ϕ is the azimuth angle. The interaction of the mutual electric and magnetic terms of the electromagnetic operator is expressed as an antisymmetric combination of its matrix elements.

2.2 $\mathbf{B}(L\lambda, I_i^\pi \rightarrow I_f^\pi)$ strength

During the experiment, the intensity of the different gamma transitions are measured as a function of time. The electromagnetic interaction strengths associated to each of them are directly linked to the matrix elements of the electromagnetic operator.

2.2.1 Definition

The general definition of the electromagnetic transition strength of multipolarity λ is:

$$\begin{array}{rcl} B(L\lambda, I_i \rightarrow I_f) & = & \sum_{M_f,\mu} | < \tau_f, I_f M_f | \mathcal{M}(L\lambda\mu) | \tau_i, I_i M_i > |^2 \\ & = & \frac{1}{2I_i+1} | < \tau_i, I_i || \mathcal{M}(L\lambda) || \tau_f, I_f > |^2 \end{array} \tag{3.29}$$

The reduced matrix elements are defined by the Wigner-Eckart theorem, see Ref. [1]:

$$< \tau_i, I_i, M_i | \mathcal{M}(L\lambda\mu) | \tau_f, I_f, M_f >= (-1)^{I_i - M_i} \left(\begin{array}{ccc} I_i & \lambda & I_f \\ -M_i & \mu & M_f \end{array} \right) < \tau_i, I_i || \mathcal{M}(L\lambda) || \tau_f, I_f > \tag{3.30}$$

2.2.2 Electromagnetic excitation/De-excitation

The B(Lλ,I$_i$ $\rightarrow$I$_f$) strength is directly proportional to the partial γ ray transition probability of multipolarity $L\lambda$. Moreover, the excitation and de-excitation transition strengths, respectively B(Lλ,I$_i$ $\rightarrow$I$_f$) and B(Lλ,I$_f$ $\rightarrow$I$_i$), are linked together with a geometrical spin factor as:

$$B(L\lambda, I_f \rightarrow I_i) = \frac{2I_i+1}{2I_f+1} B(L\lambda, I_i \rightarrow I_f) \tag{3.31}$$

Each multipole matrix element describes the electromagnetic excitation/de-excitation of the considered nuclear transition.

2.2.3 Weisskopf Model

This precursor model can be used to determine accurately the width of a measured γ-ray transition, however it can provide a reasonable estimation comparing the strengths associated to this transition and the average strength in the specific mass region of the given nucleus. One should determine if the transition from a hypothetic single particle state is accelerated/decelerated. It provides in a first approach the information of the collective or single particle character of the state.
The strength defined as $S = \frac{\Gamma_\gamma}{\Gamma_W}$, the ratio of the experimental width over the estimated width from the Weisskopf model, is commonly used to calculate the branching ratios. The width of the γ-rays directly linked to the lifetime of the state τ as: $\Gamma_\gamma = \hbar\tau$.
The model is based on the following considerations:
- The nucleus is separated in a inert core (spectator nucleons) and a valence particle,
- The γ-ray transitions occur between the states $J_{final} = I + \frac{1}{2}$ and $J_{initial} = \lambda + I + \frac{1}{2}$,
- The radial part of the initial and final wave functions u(r) should respect the condition:

$$\begin{cases} u(r) = C^{st} & \text{, if } r \leqslant R, \\ u(r) = 0 & \text{, if } r > R. \end{cases}$$

Within the Weisskopf model, the Γ_W width of the transition of energy E_γ [MeV] and multipolarity λ are given as:

$$\begin{cases} \Gamma_W(E\lambda) = & \hbar\frac{4.4(\lambda+1)}{\lambda[(2\lambda+1)!!]^2}\left(\frac{3}{\lambda+3}\right)^2\left(\frac{E_\gamma}{197}\right)^{2\lambda+1} R^{2\lambda}.10^{21} \quad [eV] \\ \Gamma_W(M\lambda) = & \hbar\frac{1.9(\lambda+1)}{\lambda[(2\lambda+1)!!]^2}\left(\frac{3}{\lambda+3}\right)^2\left(\frac{E_\gamma}{197}\right)^{2\lambda+1} R^{2\lambda-2}.10^{21} \quad [eV] \end{cases} \tag{3.32}$$

From the strength (S), the reduced transition probabilities can be found as:

$$\begin{cases} B_{W.u.}(E\lambda) = & \left(\frac{3}{\lambda+3}\right)^2\left(1.2A^{\frac{1}{3}}\right)^{2\lambda} \quad [e^2fm^{2\lambda}] \\ B_{W.u.}(M\lambda) = & \frac{10\hbar}{\pi}\left(\frac{3}{\lambda+3}\right)^2\left(1.2A^{\frac{1}{3}}\right)^{(2\lambda-2)} \quad [\mu_N^2 fm^{2\lambda-2}] \end{cases} \tag{3.33}$$

In such way, the different transition strengths can be estimated on the same basis and expressed in the single-particle units, called also Weisskopf units [W.u.]. As a matter of comparison the reduced transition strengths of single particle character are of around a few W.u. instead of around 100 W.u. for the collective-like transitions.

3 Condition of the application of Semi-classical description

The semi-classical description of the process is essential in the Coulomb excitation. A quantum description can be done, but most of the results exhibited during the Coulomb excitation are described in the semi-classical framework. However, a quantum theory treatment can be applied to check the magnitude of the error generated by the semi-classical approximation.

As mentioned above the bombarding energy should be sufficiently lower than the Coulomb barrier and should satisfy the condition: $\eta \gg 1$, see Eq.3.2 on page 56.

In a pure semi-classical description, the kinematics should follow the Rutherford scattering including the Rutherford cross section. However, in this case, the excitations generated in the orbits have to be neglected. At these energies, during the excitation process, energy and momentum transfers can occur. The energy transfer has to be negligible compared to the total energy in order to respect the semi-classical description:

$$\Delta E_n / E \ll 1 \tag{3.34}$$

In practice, this relation is not fulfilled by all nuclear states $|n>$. Indeed the excitation probabilities associated to each state are different. For weak inelastic processes the excitation may happen only if the frequency corresponding to the excitation is $\lesssim \frac{1}{\tau}$. As seen above, this condition can be expressed as:

$$\xi_0 \lesssim 1 \tag{3.35}$$

Considering now an excitation with many exchanges of quanta (strong excitation χ>1), such that the processes are not weak, the condition $\xi_0 \lesssim \chi$ has to be fulfilled:

$$\eta \gg \chi \tag{3.36}$$

As said the momentum transfer should be relatively small such as:

$$\Delta l/l \ll 1 \tag{3.37}$$

For low excitation probability, the momentum transfer can be described as $\Delta l \leq 1$ because of the possibility to use the perturbation theory, which is not the case for strong excitations.
In the case of strong excitation probability, the angular momentum transfer is estimated as :$\Delta l \sim \lambda\chi^{(\lambda)}\lambda$. Thus,

$$\eta \gg \chi^{(\lambda)}\lambda \tag{3.38}$$

Neglecting the energy and angular momentum transfer at the orbit, the collisions can be determined just from the initial intrinsic wave functions of the projectile and target, $|\Psi^{projectile}_{intrisic}>$ and $|\Psi^{target}_{intrisic}>$ respectively.

$$i\hbar\frac{\partial}{\partial t}|\Psi_{intrisic}(t)>=\left(H_0(\text{projectile})+H_0(\text{target})+W(\text{projectile},\text{target},\vec{r}(t))-\frac{Z_1Z_2e^2}{r(t)}\right)|\Psi_{intrisic}(t)> \tag{3.39}$$

with: $|\Psi_{intrisic}(-\infty)>=|\Psi^{projectile}_{\text{intrinsic, g.s.}}>|\Psi^{target}_{\text{intrinsic, g.s.}}>$ (target and projectile are assumed at there ground states before the collision)
W(projectile, target, $\vec{r}(t)$) describes the multipole-multipole interactions
$\vec{r}(t)$: centre-of-mass coordinates.

Since the problem can be separated, the Schrödinger equation to solve is of the form:

$$i\hbar\frac{\partial}{\partial t}|\Psi(t)>=(H_0+V(t))\,|\Psi(t)> \tag{3.40}$$

Thus, V(t) can be expressed as:

$$V(t)=\sum_{\lambda=1,\mu}^{\infty}\frac{4\pi Z_1 e}{(2\lambda+1)}(-1)^{\mu}\bar{S}_{L\lambda\mu}(t)\mathcal{M}(L\lambda,-\mu) \tag{3.41}$$

with the electric and magnetic excitation S-matrices defined as in Ref. [113]. The S-matrices express the probability amplitude of the excitation.

4 First Order of perturbations approximations

In this frame, the coupling between weakly excited states and strongly excited states can be evaluated via the perturbation theory, and the high-lying states can be neglected (low excitation probabilities).
However, if the high-lying states are strongly coupled to the considered excited state, the considered perturbations start to be not adequate. Moreover even if the high-lying states are not excited they should nevertheless influence the excitation of lower states.
The phenomenon associated is called polarization effect, see Ref.[113]. During the calculation one can add extra levels to optimize properly this effect, such as in GOSIA, see further Chap 5.

4.1 Excitation

At the first order the excitation amplitudes of the state $|I_fM_f>$ from the ground state $|I_0M_0>$ is given by:

$$a_{I_fM_f,I_0M_0}=\frac{1}{i\hbar}\int_{-\infty}^{+\infty}<I_fM_f|V(t)|I_0M_0>e^{\frac{i}{\hbar}(E_f-E_0)t}dt \tag{3.42}$$

4.1.1 Electric excitation

For an electric excitation, the excitation amplitude results in, see Eq.3.41 on the preceding page,3.25 on page 59:

$$\begin{aligned} a_{I_f M_f, I_0 M_0} &= \frac{4\pi Z_1 e}{i\hbar} \sum_{\lambda\mu} \frac{(-1)^\mu}{2\lambda+1} < I_f M_f | \mathcal{M}(E\lambda, -\mu) | I_0 M_0 > S_{E\lambda\mu} \\ &= \frac{4\pi Z_1 e}{i\hbar} \sum_{\lambda\mu} \frac{1}{2\lambda+1} < I_0 M_0 | \mathcal{M}(E\lambda, -\mu) | I_f M_f >^* S_{E\lambda\mu} \\ &= \frac{4\pi Z_1 e}{i\hbar} \sum_{\lambda\mu} \frac{1}{2\lambda+1} (-1)^{I_0 - M_0} \begin{pmatrix} I_0 & \lambda & I_f \\ -M_0 & \mu & M_f \end{pmatrix} \times < I_0 \| \mathcal{M}(E\lambda) \| I_f > S_{E\lambda\mu} \end{aligned} \tag{3.43}$$

Differential cross section Usually the differential cross section resulting from the excitation of nuclear states is written:

$$d\sigma_E = \sum_\lambda d\sigma_{E\lambda} \quad ; \quad d\sigma_{E\lambda} = \left(\frac{Z_1 e}{\hbar v}\right)^2 a^{-2\lambda+2} B(E\lambda, I_0 \to I_f) df_{E\lambda}(\theta, \xi) \tag{3.44}$$

with the differential cross section function as:

$$df_{E\lambda}(\theta, \xi) = 4\pi \left\| \frac{(\lambda-1)!}{(2\lambda+1)!!} \right\|^2 R^2_\lambda(\theta, \xi) d\Omega / \sin^4\left(\frac{\theta}{2}\right) \tag{3.45}$$

where, $\begin{cases} R^2_\lambda(\theta,\xi) &= \sum_\mu |R_{\lambda\mu}(\theta,\xi)|^2 \\ R_{\lambda\mu}(\theta,\xi) &= \int_{-\infty}^{+\infty} Q_{\lambda\mu}(\epsilon, w) e^{i\xi[\epsilon \sinh w + w]} dw \end{cases}$

with the eccentricity $\epsilon = \frac{1}{sin\left(\frac{\theta}{2}\right)}$, $\xi = \frac{a}{v}\frac{E_f - E_0}{\hbar}$, w is related to the position and the time dependence as: $r = a[\epsilon \cosh w + 1]$, $t = \frac{a}{v}[\epsilon w + w]$, and, the collision function: $Q_{E\lambda\mu}(\epsilon, w) = a^\lambda \frac{(2\lambda-1)!!}{(\lambda-1)!} \sqrt{\frac{\pi}{2\lambda+1}} r(w) \bar{S}_{E\lambda\mu}$

Finally, the cross section is proportional to the transition strength and the excitation:

$$\sigma_{E\lambda} = \left(\frac{Z_1 e}{\hbar v}\right)^2 a^{-2\lambda+2} B(E\lambda, I_0 \to I_f) f_{E\lambda}(\xi) \tag{3.46}$$

The total electric cross section function $f_{E\lambda}(\xi)$ is represented on the Fig.3.2.

4.1.2 Magnetic excitation

For a magnetic excitation the amplitude is, see Eq. 3.25 on page 59, 3.41 on the facing page:

$$a_{I_f M_f, I_0 M_0} = \frac{4\pi Z_1 e}{i\hbar} \sum_{\lambda\mu} \frac{1}{2\lambda+1} < I_f M_f | \mathcal{M}(M\lambda, -\mu) | I_0 M_0 > S_{M\lambda\mu} \tag{3.47}$$

Differential cross section Usually the differential cross section resulting from the excitation of nuclear states is written:

$$d\sigma_M = \sum_\lambda d\sigma_{M\lambda} \quad ; \quad d\sigma_{M\lambda} = \left(\frac{Z_1 e}{\hbar c}\right)^2 a^{-2\lambda+2} B(M\lambda, I_0 \to I_f) df_{M\lambda}(\theta, \xi) \tag{3.48}$$

with the differential cross section function as:

$$df_{M\lambda}(\theta, \xi) = 4\pi \left\| \frac{(\lambda-1)!}{(2\lambda+1)!!} \right\|^2 R^2_{M\lambda}(\theta, \xi) d\Omega / \sin^4\left(\frac{\theta}{2}\right) \tag{3.49}$$

where, $\begin{cases} R^2_{M\lambda}(\theta,\xi) &= \sum_\mu |R_{M\lambda\mu}(\theta,\xi)|^2 \\ R_{M\lambda\mu}(\theta,\xi) &= \int_{-\infty}^{+\infty} Q_{M\lambda\mu}(\epsilon, w) e^{i\xi[\epsilon \sinh w + w]} dw \end{cases}$

And, the collision function: $Q_{M\lambda\mu}(\epsilon, w) = \frac{a^\lambda c}{v} \frac{(2\lambda-1)!!}{(\lambda-1)!} \sqrt{\frac{\pi}{2\lambda+1}} r(w) \bar{S}_{M\lambda\mu}$.

Finally, the cross section is directly linked with the transition strength and the excitation:

$$\sigma_{M\lambda} = \left(\frac{Z_1 e}{\hbar c}\right)^2 a^{-2\lambda+2} B(M\lambda, I_0 \to I_f) f_{M\lambda}(\xi) \tag{3.50}$$

The total magnetic cross section function $f_{M\lambda}(\xi)$ is represented on the Fig.3.2.

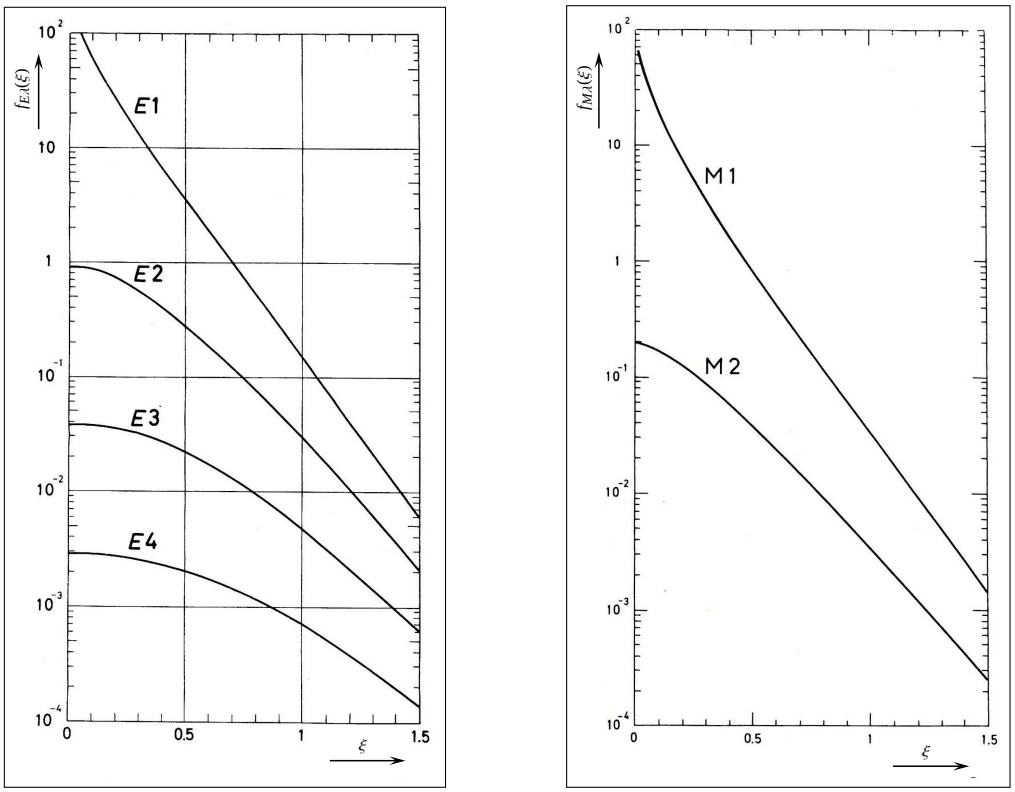

Figure 3.2: The total cross section function $f_{E/M\lambda}(\xi)$ for electric/magnetic dipole and quadrupole excitations in logarithmic scale. Modified from Ref. [113].

4.2 Excitation and De-excitation

In "safe" Coulomb excitation experiment, the nuclear states are excited by a purely electromagnetic interaction favoring deeply the electric mode. The ratio of electric and magnetic excitation cross sections exhibit such rule:

$$\frac{\sigma_{E\lambda}}{\sigma_{M\lambda}} \sim \left(\frac{c}{v}\right)^2 \quad \text{, in our experiment} \frac{v}{c} \sim 0.07, \quad \text{thus,} \quad \frac{\sigma_{E\lambda}}{\sigma_{M\lambda}} \sim 200 \tag{3.51}$$

For example, the electric E2 excitation mode is more favored than the magnetic M1 excitation mode.
In contrary, the de-excitation is not governed by the same selection rules, and therefore, lower multipole transitions, if possible, are favored.
This aspect is illustrated by the total cross section function $f_{E/M\lambda}(\xi)$ on Fig. 3.2.

4.3 Multipole-Multipole excitation

Usually projectile and target particles are assumed spherical-like and the multipole-multipole excitations are neglected. However, for a collision between deformed nuclei, corrections to the excitation amplitudes can be achieved. The semi-classical picture can be modified accordingly but this effect is of the order of $\frac{1}{\eta^2}$. For a safe Coulomb excitation, the condition $\eta \gg 1$ should be respected, thus the multipole-multipole excitations vanish or can be treated as perturbations.

4.4 Quantum effects

In order to refine the semi-classical picture quantum mechanical effects could be taken into account. However, a simple consideration of the initial and final velocities can rather compensate the excitation amplitudes by replacing respectively a and ξ_{if} by:

$$a_{if} = \frac{Z_1 Z_2 e^2}{m_o v_f v_i}; \quad \xi_{if} = \frac{Z_1 Z_2 e^2}{\hbar}\left(\frac{1}{v_f} - \frac{1}{v_i}\right) \tag{3.52}$$

Those considerations have been experimentally confirmed, see Ref. [113].

5 Higher orders of perturbation

For high transition probabilities or forbidden transitions, the excitation by more than one virtual photon starts to influence the excitation cross section. Higher perturbation orders need to be taken into account. The excitation of high spin states is then possible via the absorption of at least 2 virtual photons. This process is usually called multi-step Coulomb excitation, exciting the final states via the excitation of intermediate state(s).
In the higher perturbation orders, the excitation amplitudes can be written as:

$$a_{if} = \sum_{(\lambda)} \sum_{z} a_{izf}^{(\lambda)} \tag{3.53}$$

with : i, z, f denote respectively the initial, intermediate and final nuclear states.

5.1 Second Order of perturbation

For the second order of perturbation the excitation amplitudes are found to be:

$$a_{if} = a_{if}^{(1)} + \sum_{z} a_{izf}^{(2)} \tag{3.54}$$

The second order term can be rewritten as:

$$a_{izf}^{(2)} = \left(\frac{1}{i\hbar}\right) \int_{-\infty}^{+\infty} < f|V(\vec{r}(t))|z > e^{i\omega t} dt \times \int_{-\infty}^{+\infty} < z|V(\vec{r}(t))|f > e^{i\omega' t} dt \tag{3.55}$$

As mentioned above, the excitation of higher states can be reached through the excitation of intermediate states. Note that intermediate states can be higher in energy than the final populated state, thus a decay occurs in the population of such state.
If the direct excitation ($I_0 \rightarrow I_f$) is small, an indirect excitation such as a double excitation ($I_0 \rightarrow I_z \rightarrow I_f$) can occur, see Ref. [120].

$$\sigma_{E2,E2} \sim \frac{1}{4} a^{-2} \sigma_{E2}(I_0 \rightarrow I_z) \sigma_{E2}(I_z \rightarrow I_f) \tag{3.56}$$

One can take as example the following case:

$$\begin{aligned} \frac{\sigma_{E2,E2}}{\sigma_{E4}} &= 2.1 \frac{A_1 Z_1^2}{E_{MeV}} \frac{B(E2, 0 \rightarrow 2) B(E2, 2 \rightarrow 4)}{e^2 B(E4, 0 \rightarrow 4)} \\ &\sim 10^3 \frac{B(E2, 0 \rightarrow 2) B(E2, 2 \rightarrow 4)}{e^2 B(E4, 0 \rightarrow 4)} \end{aligned} \tag{3.57}$$

The double excitation is well favored compared to the direct excitation.
For the second perturbation order the total transition probability can be written, see Eq. 3.9, as:

$$\begin{aligned} P_{i \rightarrow f} &\propto |a_{if}|^2 \\ &\propto |a_{if}^{(1)}|^2 + |a_{if}^{(2)}|^2 + 2|a_{if}^{(1)} a_{if}^{(2)}| \end{aligned} \tag{3.58}$$

The three different terms are respectively the excitation amplitude of the first, second order and an interference term. The diagonal matrix elements and their signs are directly accessible. The second order term $a_{if}^{(2)}$ contains the diagonal matrix element corresponding to the electric quadrupole operator, $< i||\mathcal{M}(E2)||i >$. The average value of the electric quadrupole operator is the static electric quadrupole moment of the state $|i >$. In general terms, the diagonal matrix elements express the static moments of the nucleus. The non-diagonal elements represent the transitional moments.

$$< Q > = < i|\hat{Q}|i > \tag{3.59}$$

The access to the electric quadrupole moment Q is a direct measurement of the charge distribution inside the nucleus. The charge distribution is representative of the nuclear shape (deformation). The second order of the perturbation gives a direct access to the diagonal matrix element, notably the quadrupole moment. The amplitude and the sign of this matrix element will determine the type of the deformation (for example prolate, oblate in axially symmetric deformation).

5.2 Static Electric Quadrupole moment effect or Reorientation effect

The reorientation effect has been predicted by Breit and Lazarus, see Ref. [121, 122, 123]. An electric field gradient of the bombarding particle is created at the excitation of the nucleus. A reorientation of the nuclear axis can be operated by such a strong and inhomogeneous electric field gradient.
Compared to the electric field gradient present in crystalline structure the electric field gradient in Coulomb excitation can be calculated accurately (no lattice) by the model. The interaction of the electric field gradient with the static quadrupole moment is still possible considering the short collision time ($\sim 10^{-20}$s) because the projectile and the target are close (in the present configuration the electric field gradient is 12 orders of magnitude larger than in a lattice).

The reorientation of the nuclear spin modifies the angular distribution of the γ-rays. The excitation cross section and the angular distribution can be influenced by the static quadrupole moment of the considered excited state. The first order amplitudes (direct excitations) interfere with the second order amplitudes.

Taking the example of a 2^+ state, the interaction can be constructive in a prolate rotor ($Q(\mathrm{J}^\pi) > 0$)or destructive for oblate ($Q(\mathrm{J}^\pi) < 0$).

The resulting shift can be written as :

$$\Delta E = -\frac{e^2 Q(J^\pi)}{16 a_0^3} \tag{3.60}$$

Note that the quadrupole measurement via the reorientation effect process is sensitive to the proton number of the target nucleus. Then, changing the target nature could help to clearly identify the reorientation effect.

The principal interest of the reorientation effect lies in the possibility to measure the quadrupole moment of the excited states. The technique has been largely investigated via the quadrupole moment measurement of 2^+ states in the even-even nuclei.

5.3 De-orientation process

During the collision, the projectile can be firstly excited reaching a certain excited state (I_f). Before a γ-decay, the scattered projectile and the target recoil nucleus exit the target into the vacuum highly excited and ionized. At that time, the scattered projectile decays rapidly by gamma emissions. However, the strong fluctuations of the hyperfine fields can lead to a de-orientation of the nuclear state, see Ref. [26].

The main hyperfine interaction responsible of the de-orientation comes from the interactions between the magnetic dipole moment of the considered nuclear state and the atomic hyperfine magnetic field. [2]

The de-orientation effect depends on the recoil velocity, the atomic and nuclear spins, the lifetimes of the excited states considered and some dephasing effects. In the GOSIA code, the de-orientation effect is restricted to a two-states model, see Ref. [124, 125].

The possible de-orientation effect affects the angular distribution of the de-exciting nucleus. This attenuation can be taken into account with the attenuation factor $G(\tau)$, including the dependence on the spin and lifetime. The different processes are summarized on Fig. 3.3.

2. If the atomic hyperfine magnetic field is well known, the de-orientation effect could be used to measure the magnetic dipole moment of the excited states.

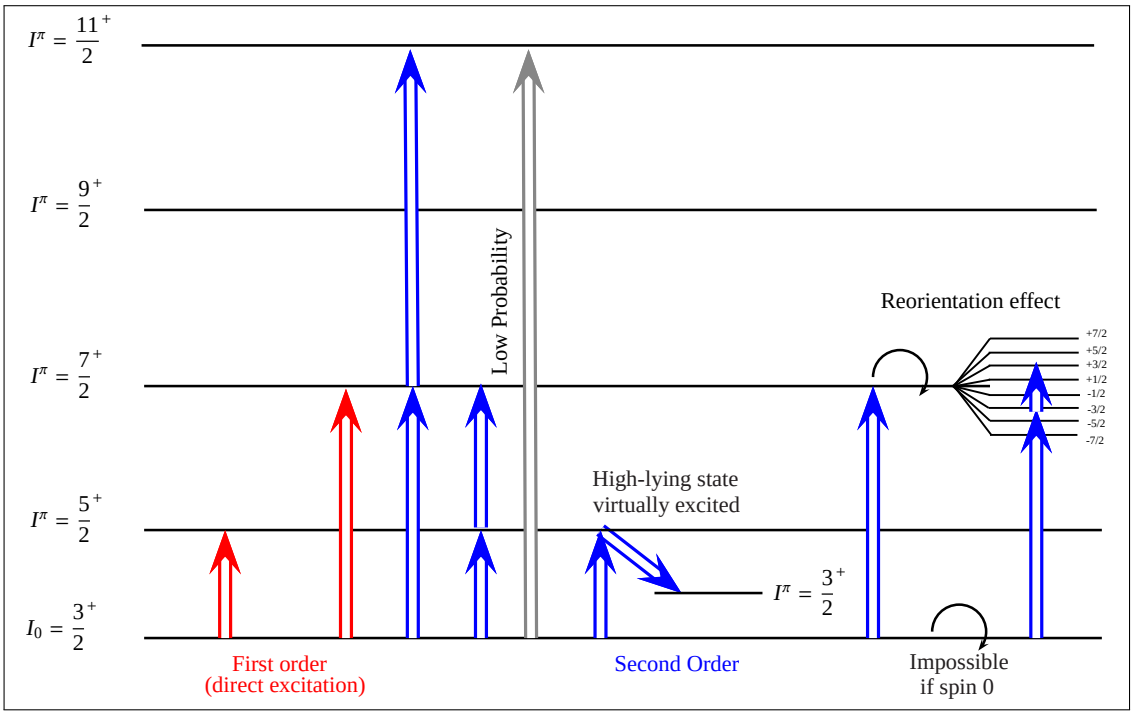

Figure 3.3: Different excitation possibilities.

6 Which informations can be extracted from Coulomb excitation?

In Coulomb excitation the matrix elements of the electromagnetic multipole operator can be determined. In order to understand the meaning of the matrix elements, several parameters are used, such as the electric quadrupole moment related to specific diagonal matrix elements.

6.1 The Experimental Observables

In even-even nuclei, the first 2^+ states and the B(E2,$0_1^+ \rightarrow 2_1^+$) strengths are correlated together. The evolution of B(E2,$0_1^+ \rightarrow 2_1^+$) and 2_1^+ energy over the neutron/proton number reflects some characteristics of the nuclear structure in presence. Generally, a development of deformation exhibits an increase of the reduced transition strengths B(E2,$0_1^+ \rightarrow 2_1^+$) and a decrease of the E(2_1^+) energies. On contrary, close to the (sub)shell closures, the inverse tendency is observed, the E(2_1^+) energies increase and the B(E2,$0_1^+ \rightarrow 2_1^+$) decrease. Their behaviors help to understand the nuclear medium with extreme N/Z ratios, for example the Kr and Sr cases presents at the studied shape transition which are discussed in the Chap. 2 on page 39.
Other bench-marks are used such as the ratio between the magnetic and electric transition strengths B(M1)/B(E2).The odd-even cases are less trivial, notably due to the broken pairs of nucleons (single-particle), like in the studied Rb isotopes case (one proton more than Kr isotopes).

The collectivity of the nucleus generates most of the time, a collective deformation, which can fit for example in rigid rotor nuclei model. Comparing two collective nuclei close to each other in the chart, the differences in their B($L\lambda$, $J_i^\pi \rightarrow J_f^\pi$) strengths (electric and magnetic) coupled with their energies can help to draw more precisely the underlying structures of those nuclei.

The study of shape transitions constitutes a key ingredient to understand the strong interaction, where the nuclear structure change quickly by adding/subtracting a few nucleons. Generally, the nuclear shape changes from spherical to deformed shape. Among the possible observables highlighting a clue of sphericity, the energy level scheme can show a single particle like behavior, without any rotational band.

Collective and single particle like nuclear feature observed at the shape transition are discussed more in details in the Chap. 2 and 6.

6.2 Particle + Rotor Model

For "rotational" nuclei, the nuclear states result mainly from the valence space and rotation wave function. This consideration engenders simple relations between electromagnetic properties inside rotational band and between the bands.
The electromagnetic interaction contrary to the strong interaction is well known. The study of magnetic and electric moments, the associated transitions probabilities can be used to probe the nuclear structure.
Considering the Particle + Rotor model, neglecting the Coriolis interaction, such relations can be established in a simple picture.

The reduced transition probabilities are :

$$B(M\lambda; I_{Initial}K \rightarrow I_{Final}) = \sum_{\mu, M_{Final}} |< I_{Final}M_{Final}K \mid \mathcal{M}_{\lambda\mu} \mid I_{initial}M_{Initial}K >|^2 \tag{3.61}$$

The dipole and quadrupole electromagnetic properties are discussed in the following, since they constitute the most probable de-excitation channels in safe Coulomb excitation.

6.2.1 Magnetic Dipole Properties

The magnetic dipole moment of deformed nucleus can be separated in two terms: the first one is associated to the collective rotation and the second one describes the contribution from the valence nucleons:

$$\vec{\mu} = \underbrace{g_R\vec{R}}_{Collective\ rotation} + \underbrace{\sum_i^A \left(g_i^{(l)}\vec{l_i} + g_i^{(s)}\vec{s_i}\right)}_{Valence\ nucleon} \tag{3.62}$$

with: $\begin{cases} \vec{s_i} \text{ the intrinsic spin and } g_i^{(s)} \text{ the gyromagnetic factor associated to the intrinsic spin of the valence nucleon } i \\ \vec{l_i} \text{ the orbital spin and } g_i^{(l)} \text{ the orbital gyromagnetic factor of the valence nucleon } i \\ \vec{j_i} = \vec{l_i} + \vec{s_i} \text{ total moment of the nucleon } i \end{cases}$

The gyromagnetic factors of free nucleons are found experimentally as: $g_s^{p,free}$=5.58, $g_s^{n,free}$=-3.82, $g_l^{p,free}$=1, and $g_l^{n,free}$=0. The nuclear magnetic moment is defined as $\mu =< \mu_z >$. After some developments, the magnetic moment μ is found as, see Ref. [89]:

$$\mu = g_R I + (g_K - g_R)\frac{K^2}{I+1}\left\{1 + (2I+1)(-1)^{I+\frac{1}{2}}b_0\delta_{K,\frac{1}{2}}\right\} \tag{3.63}$$

b_0 is the magnetic decoupling parameter defined as:
$\sqrt{\frac{3}{4\pi}}\frac{q\hbar}{2M_pc}(g_\Omega - g_R)\,b_0 \equiv -\sqrt{2} < \Omega = \frac{1}{2}|\mathcal{M}(M1, \mu = 1)|\Omega = -\frac{1}{2} >$ and linked to the intrinsic decoupling parameter a as $(g_\Omega - g_R)\,b_0 = (g_l + g_R)a - \frac{1}{2}(-1)^l(g_s + g_K - 2g_l)$.
For a rotor, the moment of inertia can be expected proportional to the protons number, see Ref. [25], thus:

$$g_R = \frac{Z}{A} \tag{3.64}$$

However, it has been proven that the g_R values go away from the $\frac{Z}{A}$ ratio, see Ref. [126, 127], for deformed and superdeformed nuclei. In the region ($A \sim 100, N \sim 60$), the rotation g-factor can be approximated by: $g_R \approx 0.7\frac{Z}{A}$.
The magnetic dipole reduced transition probability within a rotational band is defined as:

$$B(M1; I_{Initial} \rightarrow I_{Final}) = \frac{3}{16\pi}\frac{e^2}{m^2}K^2\,(g_K - g_R)^2 < I_{Initial}K10 \mid I_{Final}K >^2 \left(1 + b_0\delta_{K,\frac{1}{2}}(-1)^{I>+\frac{1}{2}}\right)^2 \tag{3.65}$$

6.2.2 Electric Quadrupole Properties

Lets consider a deformed nucleus as a charged liquid drop, its surface can be described by an ellipsoid. For the followings, only the axially symmetric nuclei along the z axis are discussed. The quadrupole moment associated is, see Ref. [25]:

$$Q_0 = \frac{2}{5}ZR^2\left(\left(\frac{c}{a}\right)^2 - 1\right)\left(\frac{c}{a}\right)^{-\frac{2}{3}} \tag{3.66}$$

Q_0 is the intrinsic electric quadrupole moment expressed in the frame of reference of the nucleus. a and c are the semi-axis of the ellipsoid. The electric quadrupole moment expressed in the laboratory frame is called spectroscopic quadrupole moment, corresponding to the average value of the quadrupole operator. The intrinsic quadrupole moment can be expressed as a function of the deformation parameter β:

$$Q_0 = \frac{3}{\sqrt{5\pi}} ZR^2\beta\left(1 + \frac{1}{8}\sqrt{\frac{5}{\pi}}\beta\right) \tag{3.67}$$

Quadrupole moment and matrix elements The Coulomb excitation allows to determine the matrix elements, see Ref. [26]. To access to the shape of the nucleus, the quadrupole moment Q_0 and the deformation parameter β can be defined from those matrix elements. Moreover, if the quadrupole moment is well known (as for the Rb isotopes), the matrix elements will be defined more precisely.

The quadrupole moment accessible from the experiment is the spectroscopic quadrupole moment. Q is defined as the average of the quadrupole moment operator $Q =< IKM|\hat{Q}|IKM >$.
For point charges:

$$qQ = \sum_i \left(3z_i^2 - r_i^2\right) \tag{3.68}$$

For a continuous charge distribution:

$$\begin{array}{rcll} q\hat{Q} & = & \int \rho_e(\vec{r})\left(3\hat{z}^2 - \hat{r}^2\right)d\tau & , (z = r\cos\theta \text{ in spherical coordinates}) \\ & = & \int \rho_e(\vec{r})\hat{r}^2\left(3\cos^2\theta - 1\right)d\tau & \end{array} \tag{3.69}$$

According to the definition of the electric multipole moment, see 2.1.1:

$$\mathcal{M}(E2,\mu) = \int \rho_e(\vec{r})\vec{r}^2 Y_{2\mu}(\theta,\phi)d\tau \quad \text{,with } Y_{20}(\theta,\phi) = \sqrt{\frac{5}{16\pi}}\left(3\cos^2\theta - 1\right) \tag{3.70}$$

then,

$$\mathcal{M}(E2,0) = \int \rho_e(\vec{r})\vec{r}^2\sqrt{\frac{5}{16\pi}}\left(3\cos^2\theta - 1\right)d\tau \tag{3.71}$$

Finally, a direct relation between the spectroscopic quadrupole moment and the matrix element is found to be:

$$q\hat{Q} = \sqrt{\frac{16\pi}{5}}\mathcal{M}(E2,0) \tag{3.72}$$

and z is parallel to the nuclear spin I,

$$qQ = \sqrt{\frac{16\pi}{5}} < IKM = I|\mathcal{M}(E2,0)|IKM = I > \tag{3.73}$$

Applying the Wigner-Eckart theorem, one obtains:

$$qQ = \sqrt{\frac{16\pi}{5}}(2I+1)^{-\frac{1}{2}} < II20|II >< I||\mathcal{M}(E2)||I > \tag{3.74}$$

In order to obtain the intrinsic quadrupole moment which is used to describe the nuclear shape, a frame of reference change is applied from the laboratory frame to the nucleus. The intrinsic quadrupole moment is linked to the matrix element as:

$$qQ_0 = \sqrt{\frac{16\pi}{5}}\frac{1}{\sqrt{2I_i+1}}\frac{< I_{final}||\mathcal{M}(E2)||I_{initial} >}{< I_{initial}K20|I_{final}0 >} \tag{3.75}$$

Quadrupole moment and transition strength The transitional quadrupole moments ($I_{initial} \neq I_{final}$) are function of the transitional matrix elements, denoted $Q_0^{Transition}$. It describes the transition probability and the collectivity of the nucleus. $Q_0^{Transition}$ is directly a function of the transition strength:

$$B(E2, I_{initial} \rightarrow I_{final}) = \frac{5}{16\pi}\left(qQ_0^{Transition}\right)^2 < I_{initial}K20|I_{final}0 >^2 \tag{3.76}$$

A direct relation between $Q^{Measured}$ and Q_0 can be obtained according to the Eq. 3.75 and 3.73, see Ref. [128]. For axially symmetric nuclei in rotation, the simple relation between the measured and intrinsic quadrupole moment is found as :

$$Q^{Measured} = \frac{3K^2 - I(I+1)}{(I+1)(2I+3)} Q_0 \tag{3.77}$$

Thus, we need to keep in mind that the intrinsic quadrupole moment is derived from the measured quadrupole moment.

6.3 Experimental extraction of electromagnetic properties and nuclear structure

The extraction of electromagnetic properties can be made from the B(M1), B(E2) and their ratio B(M1)/B(E2). Accessing to the relative transition intensities, the electromagnetic branching ratio R_γ can be determined. Let us consider a nuclear state de-exciting by the emission of γ-ray of multipolarity E2 or M1, the branching ratio is found as:

$$R_\gamma = \frac{T_\gamma(M1, I \to I-1)}{T_\gamma(E2, I \to I-2)} \tag{3.78}$$

The transition probabilities T(Lλ;I$_{initial}$ $\to$I$_{final}$) can be evaluated with the transition strengths as, see Ref. [25]:

$$T(L\lambda; I_{initial} \to I_{final}) = \frac{8\pi(\lambda+1)}{\lambda[(2\lambda+1)!!]^2} \frac{1}{\hbar} \left(\frac{E_\gamma}{\hbar c}\right)^{2\lambda+1} B(L\lambda; I_{initial} \to I_{final}) \tag{3.79}$$

For M1 and E2 transitions, one obtains the electric quadrupole and the magnetic dipole transition probabilities as:

$$\begin{cases} T(M1) &= 1.779 \times 10^{13} E_\gamma^3 B(M1)\,, \\ T(E2) &= 1.223 \times 10^{9} E_\gamma^5 B(E2) \end{cases} \tag{3.80}$$

with: E_γ in $[MeV]$, B(E2) in $[e^2 fm^4]$, B(M1) in $[\mu_N^2]$ and T in $[s^{-1}]$.

In the strong coupling of the Particle + Rotor model, the electric quadrupole and magnetic dipole transition strengths ratio can be expressed as:

$$\frac{B(E2; I \to I-2)}{B(M1; I \to I-1)} = 6.87 \times 10^{-1} \frac{E_\gamma^5(E2)}{E_\gamma^3(M1)} R_\gamma(I) \qquad \left[\frac{\mu_N^2}{e^2 b^2}\right] \tag{3.81}$$

and the branching ratio is found as:

$$R_\gamma(I) = 3.49 \times 10^4 \frac{(g_K - g_R)^2 K^2}{Q_0^2} \frac{E_\gamma^3(M1)}{E_\gamma^5(E2)} \frac{|< IK10|(I-1)K >|^2}{|< IK20|(I-2)K >|^2} \tag{3.82}$$

The magnetic moment associated to the orbital of the single nucleon can be determined experimentally from the branching ratio via the g_K gyromagnetic factor.

The experimental branching ratio is determined taking into account the relative intensities corrected in efficiency and by the conversion electron factor:

$$R_\gamma(I) = \frac{N_\gamma(M1)}{N_\gamma(E2)} \frac{\epsilon(E2)}{\epsilon(M1)} \alpha_{Conv.} \tag{3.83}$$

For the extraction, one assumes that the branching ratio are equivalent to the transitions yields ratio.

7 Conclusion

The Coulomb excitation is a purely electromagnetic interaction, the only nuclear properties involved are described by the matrix elements of the electromagnetic multipolar operator. The nucleus undergoes a transition from an initial state ($|initial>$) to a final state ($|final>$) via a pure electromagnetic interaction if the "safe energy" criterion is respected. The final state can decay by emitting a γ-ray or a conversion electron.

The γ-rays intensities observed are directly in relation with the matrix elements $< final||\mathcal{M}(E2)||initial >$ which describe the excitation and decay processes characteristics of the nuclear structure. As mentioned above the matrix elements can directly describe the deformation of the nucleus via a change from the laboratory frame to the nucleus frame.

In this type of experiment, the nuclear structure information is extracted in a model-independent way. The B(E2) values measured via the Coulomb excitation are a benchmark to evaluate the collectivity notably close to magic numbers or shape transitions.

Chapter 4

Experimental Setup

1 Introduction

For Coulomb excitation experiment, the nuclei of interest must be produced in a way allowing to form a Radioactive Ion Beam corresponding to the requested specifications of intensity, purity and energy. This RIB then will be sent on a secondary target where they are submitted to Coulomb excitation.

Using Radioactive Ions Beams implies to face several technical obstacles coming from their unstable nature and from their low cross-sections of production. Since they are produced with low intensities in a very radioactive environment, they have to be extracted and transported away from their production place in order to improve the signal/noise ratio. The highest efficiency from the production passing through beam preparation and transport phases has to be reached.
The short half-lives of the nuclei of interest also imposes to reduce at maximum the process time from the production to the experimental setup built to study their properties.
Furthermore, the produced beam generally contains unwanted contaminants which may be considerably more abundant than the nuclei of interest. These contaminants must be eliminated in order to make the identification of the studied nuclei and to not introduce dead times or biases in the data acquisition system or even damages in the detectors themselves.
Thus, the finest selection is required to be able to perform an efficient and safe experimental study with the purest beam. For example, isobaric separation or ionization processes can be operated to reduce the proportion of contaminants. Due to their radioactive nature, RIB cannot be stopped at any place. The accumulation of radioactive nuclei would lead to dangerous of unreasonable high activities, emphasizing on the importance of a selection.

Two main techniques have been developed to achieve the study of radioactive nuclei far from the beta stability valley: the ISOL and In-Flight techniques, which are described in the following section. Then the production modes will also be presented.

1.1 The production of radioactive beams: ISOL versus In-Flight Fragmentation technique

In order to realized a Coulomb excitation experiment at low energy according to the criteria defined in the Chap. 3 on page 55, the produced radioactive beam needs to respect several conditions:

- its energy has to be lower than the Coulomb barrier in order to neglect the strong interaction compared to the electromagnetic excitation, see Chap. 3 on page 55 and Chap. 5 Sec. 8.
- its purity should be maximized to ascertain the identification of projectile and target nuclei.
- its optics needs to be sufficiently good to avoid complex kinematics.
- its resulting intensity has to be high enough to perform the experiment in a reasonable time.

Nowadays, several techniques are available to produce radioactive beams and among them the In-flight Fragmentation and the ISOL techniques presenting different characteristics.

1.1.1 In-Flight Fragmentation (from few tens MeV/u to GeV/u)

The In-Flight Fragmentation is a part of In-Flight techniques family, and can be used to produce neutron rich isotopes.
The radioactive nuclei are produced by a fragmentation reaction of projectile nuclei(primary beam) impinging on a thin target. Through this reaction radioactive nuclei are created and could be selected and treated by several devices (such as spectrometers, achromatic degraders, slits ...) The wide choice of the primary beam

colliding the thin target allows to produce a large panel of nuclei whose mass is principally lower than the one of the projectile. The beam passing through the target is decelerated in the target. The energy lost in the target is sufficiently weak to produce a secondary beam at high energy (usually at least few tens of MeV/u) and keep reasonable optical beam properties. After the target, the nuclei produced are mass-separated In-Flight. On one hand, one of the main advantage of this technique is the possibility to study nuclei with very short lifetimes, thanks to a relatively short beam transport around the microsecond. On the other hand , the use of a primary target and degraders affects the optical quality of the beam in terms of angular dispersion and of an important energy loss in the target. The intensity of the beam increases with thicker targets but the optical beam properties are degraded. It is a compromise to ensure a relatively good optical beam quality and a high intensity.
The beam intensity is thus limited by the nature of the technique itself. However, since this technique does not include any chemical process, it allows the production of all chemical elements. The counterpart is that isobaric contaminants may be present.

1.1.2 ISOL Technique

The ISOL technique (Isotopic Separation On-Line) [129] as regards to the In-Flight Fragmentation technique presents other advantages and inconveniences. The method consists in bombarding by a primary beam (for example protons, deuterons, or heavy ions) a target sufficiently thick to stop the incoming projectiles. The atoms produced in the target are stopped in a catcher (sometimes the target itself acts as a catcher, as at ISOLDE). The atoms then diffuse/effuse outside the catcher and pass through a transfer line. In order to minimize the transfer time, the target is strongly heated at >2000°C, as well as the transfer line. The atoms then enter the ion source which ionizes and accelerates them.
It is this type of technique that we have used at ISOLDE for the present study.

The final intensity depends mainly on the chemical nature of the studied nuclei. Indeed the chemical processes govern the diffusion and effusion efficiency. The main advantage of this technique comes from the decoupling in a primary and secondary beam. The decoupling infers an optimal optical beam quality and leads to an important chemical selection. On the other hand the diffusion/effusion/ionization process restricts the usage of such a method for nuclei whose lifetimes are higher than several milliseconds.

1.2 Nuclear Reaction Energy Ranges for Production

1.2.1 Low Energy Production

At low energies, the production of radioactive ions occurs above the Coulomb barrier, see Fig. 4.1.
→ For an important impact parameter transfer reactions (see Fig. 4.1(a)) occur, consisting in the transfer of one or several nucleons between the projectile and the target nuclei. In this kind of reaction the final products are not so far from their parent nuclei. Such production has been performed e.g. at Louvain-la-Neuve [130]. Note that those reactions can also be performed on the secondary target (like at ISOLDE with the transfer reaction MINIBALL chamber).

→ For a small impact parameter, the projectile collides the target close to a head-on configuration (central collision), so that excited compound nuclei can be created. The de-excitation of the compound nucleus can occur via fission and fusion-evaporation, and does not depend on the production path.

Fusion-Evaporation (see Fig. 4.1(b)) During the reaction, the projectile and target nuclei fuse to make one excited nucleus, qualified as "compound". The de-excitation pass through the emission of light particles and γ rays. The way that the compound nucleus is created does not influence the way it decays, neither the branching ratio of each decay branch. Neutron deficient nuclei can be produced with light ion beam at low energy. Heavier beams used at higher energies can produce neutron deficient nuclei with lower cross section but further from beta stability.

Fusion-Fission (see Fig. 4.1(c)) For heavy nuclei, the compound nucleus can fission in fragments. The mass sharing in the fission products may be either symmetric or asymmetric.

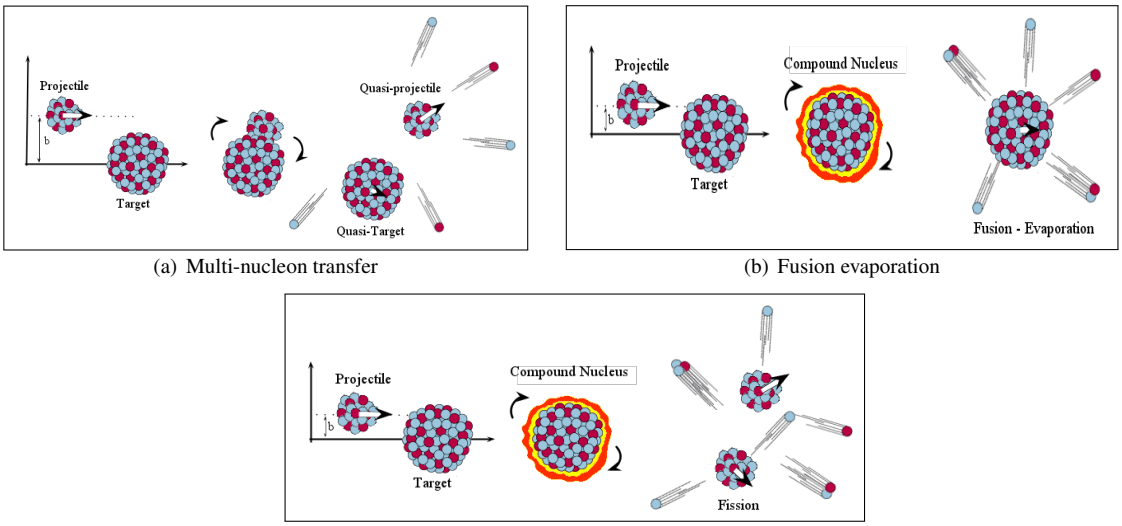

(a) Multi-nucleon transfer

(b) Fusion evaporation

(c) Fusion fission

Figure 4.1: Reactions present at low energy production. (a) Transfer Reaction, characterized with an important impact parameter and products close to the parent nuclei; (b) Fusion-Evaporation, characterized by a small impact parameter, the formation of a compound nucleus and the emission of light nuclei or nucleons; and, (c) Fission, characterized by a small impact parameter, the formation of a compound nucleus and the fission of the compound nucleus in other nuclei (plus sometimes evaporation products);

1.2.2 High Energy Production

Three main processes involved in the reaction of high energetic proton beam are: the fission, the spallation and the fragmentation. The three different reaction are describe in details by J. Benlliure in his lectures [131] and P. Armbruster et al. [132].
The impact of light projectiles on heavy target nuclei at high kinetic energies (~ MeV/u$\leqslant E_{proj} \leqslant$~ GeV/u) favors the emission of light fragments with high neutron/proton ratios similar to those of the target, see Fig. 4.2.

Spallation (see Fig. 4.2(a)) During spallation, the target nucleus emits protons and neutrons [1]. The emission of neutron is the first process involved. Due to the absence of Coulomb barrier, eutrons are easier to emit so that the process favors the production of n-deficient nuclei. However, the nuclei far from stability have not high cross section via this reaction. The main limitation of this technique is the mass of the stable target nucleus used to produce radioactive species.

1.2.3 Medium Energy Production

Between high and low energies, ~ 10 MeV/u $< E_{proj} <$ ~ 100 MeV/u, some "intermediate" phenomenons are taking place, see Fig. 4.2. For high impact parameter, quick fragmentation produces two fragments close to the original projectile-target nuclei. For small impact parameter, the multi-fragmentation becomes the principal channel of production, the couple projectile-target fragments in several light particles.

1.2.4 Fission

The production of neutron rich nuclei is favored in fission reaction of UCx, UCx-Th and other fissile targets. The fission process can be induced by thermal/hot neutrons, low/high energetic proton beam, heavy ions beam, and via photo-fission.

The reaction process chosen to produce a given ion depends on several parameters: first of all, the position of the isotope onto the nuclear chart (proton/neutron rich) close/far from stability; secondly, its chemical nature allowing or not the ISOL technique; thirdly, the half life of the nucleus.

1. A nucleus, created in an excited state above the "p" or "n" emission threshold can emit p/n before reaching an excitation level, where only γ-rays can be emitted.

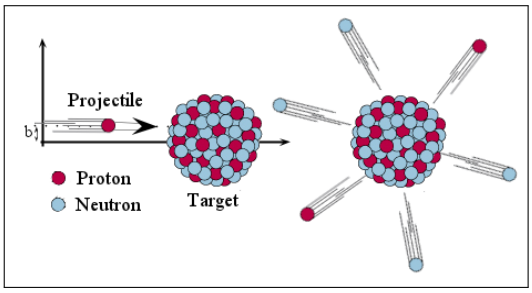

(a) Spallation

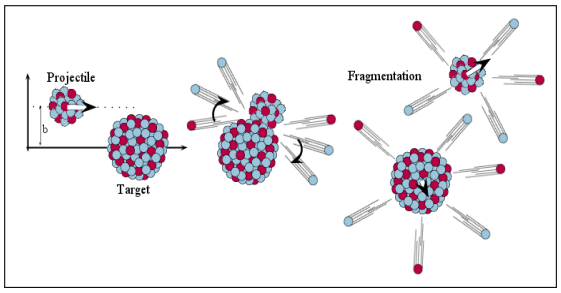

(b) "Quick"-fragmentation

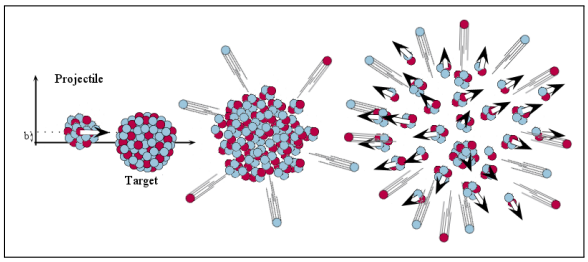

(c) Multi-fragmentation

Figure 4.2: Reactions present at high and medium energy production. (a) Spallation, characterized with a small impact parameter and a product close to the parent nuclei; (b) Fragmentation or "quick fragmentation", characterized by an important impact parameter and the emission of light nuclei or nucleons and products close to the parent nuclei; (c) Multi-fragmentation, characterized by a small impact parameter and the separation of the compound nucleus in many nuclei (sometimes evaporation products i.e. "light");

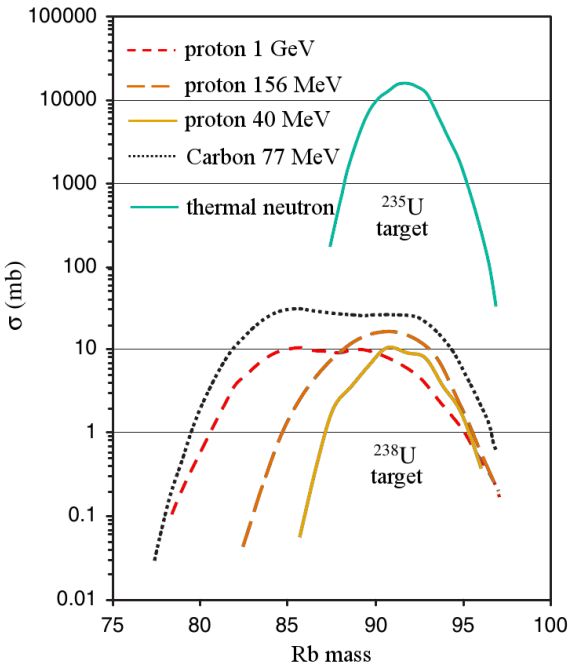

Figure 4.3: Rubidium cross section for several reactions. Modified from Ref. [129], see Ref. [133].

In the present work, the rubidium isotopes are the subject of our interest. A summary of the rubidium production cross section obtained with different reactions using ^{238,235}U target is given in the Fig. 4.3. The production cross section is a part of a long process to choose the right place to study a given nucleus. Indeed, even if the production cross section is important, the half life for example can restrict the amount of the nuclei of interest in the ISOL case.
We have chosen to produce the Rb isotopes in the fission reaction ^{238}U+p(1GeV) and to create a RIB by the ISOL technique at ISOLDE (CERN). We now focus on this technique and the different involved processes.

1.3 Diffusion and Effusion

Diffusion and effusion are the two main processes involved in the extraction of the radioactive Rb atoms from the target. Those processes can be influenced by different ways. A brief introduction of the diffusion and effusion is given to demonstrate the importance of the different parameters involved in an ISOL production.

1.3.1 Diffusion

The diffusion is defined by the random motion of atoms through defects in a solid crystal, they originate from the thermal agitation.

Principles and laws Considering the system at equilibrium (steady state, steady regime) the first Fick's law, see Ref. [134], can be employed:

$$\vec{J} = -D.\overrightarrow{grad}(\vec{C}) \tag{4.1}$$

where: $D = D_0 e^{(-\frac{E_a}{k.T})}$, $\vec{J}$ is the atomic stream, C is the concentration, D is the diffusion coefficient. D_0 is the diffusion constant depending on the crystalline mesh parameter and the vibration frequency of the diffusing atom. E_a corresponds to the energy necessary to jump from a position (site) to another one. D_0 and E_a are called Arrhenius' coefficients.

Between two equilibriums the system is dynamic (transitional regime). The second Fick's law governs the concentration variations:

$$\frac{\partial C}{\partial t} = -div(\vec{J}) = div(D.\overrightarrow{grad}(\vec{C})) \tag{4.2}$$

Taking into account the loss of radioactive ions by radioactive decay occurring during the diffusion process, i.e. $-\lambda C(\vec{r}, t)$, the equation can be re-expressed as:

$$\frac{\partial C}{\partial t} = -div(\vec{J}) = div(D.\overrightarrow{grad}(\vec{C})) + \lambda C(\vec{r}, t) = F \tag{4.3}$$

To determine the diffusion efficiency for an atom to get out of the target, L. Maunoury, see Ref. [135, 136], solved this equation and with the second Fick's law, the diffusion time is found with the form :

$$\tau_{diffusion} = -D\frac{\partial C(\rho, t)}{\partial \vec{r}} 4\pi\rho^2 = \frac{6Q}{\pi^2}\sum_{k=1}^{\infty}\frac{\mu_0}{\mu_k + \lambda}\left(1 - e^{-(\mu_k+\lambda)t}\right) \tag{4.4}$$

where: $Q = F\frac{4}{3}\pi\rho^3$ is the total number of radioactive ions produced by a grain.

More explanations and further investigations are given in Ref. [136, 137].

Temperature If the solid is constituted by more than one polycrystalline structure, thus several phenomenons will happen at the same temperature.

At low temperature($T \lll T_m$), the diffusion is superficial, the atom goes to the neighbor hole if it has sufficient energy, the motion should continue step-by-step.

At medium temperature ($0.3T_m \lesssim T \lesssim 0.5T_m$), close to the most perturbed region of the solid, i.e. seals, the atoms exchange preferentially their position with the neighbors defects in the seals. The diffusion is thus qualified as inter-grains type.

At high temperature ($T \gtrsim 0.7T_m$), the diffusion increases proportionally to the number of defects, following an exponential law. This diffusion takes place inside all the volume and superimposes to the others. The diffusion is thus volumic.

Effusion The effusion is defined as the process permitting to move an atomic nucleus inside the crystalline structure in straight line until the surface of the solid where it gets stuck a certain time, and finally reaches the ionization source.

The term of effusion is generally assigned to the phenomenon describing the path of a gas through a small hole. The "delay" function of effusion can be expressed as, see Ref. [138]:

$$p_v(t) = ve^{-vt} \tag{4.5}$$

v is related to the mean time of effusion $\tau_{effusion}$ by:

$$\tau_{effusion} = \frac{1}{v} = \chi\,(\tau_a + \tau_v) \tag{4.6}$$

where: $\begin{cases} \chi\text{: mean number of collisions with the surfaces met until the ionization source.} \\ \tau_a\text{: average sticking time on the surface correlated to the adsorption enthalpy } H_a\text{, see Ref. [139].} \\ \tau_v\text{: average time between two "sticks", see Ref. [140, 141].} \end{cases}$

More explanations and further investigations are given in Ref. [139, 140, 141].

1.4 Ion Sources

The ions effusing from the catcher pass through a transfer line. Inside the transfer line or a specific ion source, the atoms can be ionized by several techniques depending on the chemical properties of the studied species.

1.4.1 Electron Impact Ionization

This technique is used for chemical elements whose an ionization potential $I_{pot.}$ higher than ~7 eV. The ions are bombarded by mono-energetic electrons knocking out its outer electrons. The cross section of the process is mainly governed by the electron current, the ions density, the charge states and the ionization potential of the given ion. The electron impact ionization is used in ECRIS (Electron Cyclotron Resonance Ion Source), as for example at SPIRAL, Louvain-la-Neuve, TRIUMF, high temperature gaseous discharge cavities and EBIS ion sources. An EBIS ion source has been used to post accelerate our Rb isotopes, see Subsubsec. 2.6.3 on page 84. This method may be applied for a very large number of elements. In counterpart, it is not chemically selective.

1.4.2 Laser Ionization

The atoms present in the transfer line undergo stepwise ionization. The atoms are ionized only if the laser frequency corresponds to atomic transitions. The process is usually performed through two or three ionization steps. The different resonances lead to the continuum, to auto-ionization states or highly excited states. By this way the efficiency and the selectivity of the target-ion source couple can be improved. This technique allows to deliver isobaric pure beam and even isomeric pure beam if the laser bandwidth is sufficiently narrow. As example for more investigation one can cite the laser ionization device present at ISOLDE, RILIS [142, 143], and the following Ref. [144, 145].

1.4.3 Surface Ionization (or Thermal Ionization)

The surface ionization technique consists in a thermal ionization of atoms due to the high temperature of the transfer line (tube). This technique is used for chemical elements with low ionization potential ($I_{pot.}$ <7 eV). The reaction products effuse inside the heated transfer line and interact with its surface. Inside the transfer line, the thermal agitation increases the interaction between the ions and the heated surface, leading to a loose or gain of electron(s).
The thermal ionization process which takes place is described by the Saha-Langmuir equations, see Ref. [133]:

$$\begin{cases} \dfrac{n_i^+}{n_0} = \dfrac{g_i^+}{g_0}\exp\left(\dfrac{e(\phi - I_{pot.})}{kT}\right) & : \quad \text{positive surface ionization, } I_{pot.} < 7 \text{ eV}\,, \\ \dfrac{n_i^-}{n_0} = \dfrac{g_i^-}{g_0}\exp\left(\dfrac{e(E_A - \phi)}{kT}\right) & : \quad \text{negative surface ionization, } I_{pot.} < 7 \text{ eV, } E_A > 1.5 \text{ eV}\,. \end{cases} \tag{4.7}$$

where: $\frac{n_i^+}{n_0}$, $\frac{n_i^-}{n_0}$ are the ratios of ion density to neutral density; $\frac{g_i^+}{g_0}$, $\frac{g_i^-}{g_0}$ are the ratios of statistical weights of ionic and atomic ground state; e is the electron charge; ϕ is the surface work function of the transfer line.

In our case, the Rb ions were produced by surface ionization and accelerated to 60 kV before being charge bred by the EBIS source and post-accelerated by the REX-LINAC. See Fig. 4.6, for more informations on thermo-ionization, see Ref. [146].

1.4.4 Gas Cell Ionization

In this technique, the transfer line can consist in a gas cell filled by noble gas (generally He, Ar) acting as a catcher. The reaction products exiting the target (high charge state) are thermalized in the gas cell. The charge-exchange process lowers their charge state. The high ionization potential of the noble gas lead to an ion charge state usually 1+, 2+. The residues are extracted from the gas cell and guided to a mass separator to be mass analyzed.

1.4.5 Plasma Ion Sources

Usually the plasma ion sources are used to ionize elements that cannot be ionized with the other processes. There are two major types: the hot plasma ion sources and cooled plasma ion sources. In the first case, the plasma is produced from an ionized gas mixture with electrons accelerated between the transfer line and the extraction electrode. In the latter case, the transfer line is cooled down. In such way, the production of noble case elements is favored. The volatile element are transported in an easier way and the isobaric contaminants are reduced.

2 The Radioactive Ion Beam (RIB) facility: ISOLDE

2.1 ISOL

Elaborated for the first time in 1951 by O. Kofoed-Hansen and K.O. Nielsen [147], the ISOL technique has been under intensive developments and is still a powerful tool used nowadays. The investigation of the ISOL technique as a relevant and efficient way to produce radioactive nuclei far from stability has been presented in 1966 at the Swedish conference in Lysekill. In 1989, the first post accelerated beam has been delivered at Louvain-la-Neuve, see Ref. [148, 149, 150]. Since this period, several new radioactive ion beam post acceleration facilities have been constructed. Moreover many similar projects are under commissioning, in progress or being upgraded such as SPIRAL2 (GANIL), see Ref. [151, 152], EURISOL (EURopean Isotope Separation On-Line radioactive ion beam facility), see Ref. [153, 154], ISAC2 (TRIUMF), see Ref. [155].
Among the ISOL facilities, ISOLDE produces stable and radioactive 60 kV beams at CERN since around 50 years, see Ref. [156]. In 1994, the REX-ISOLDE (Radioactive ion beam EXperiments at ISOLDE) post-acceleration project of low energy beams impulsed the exploration of the nuclear chart far from stability opening new opportunities.
A new upgrade of the CERN facilities, has been approved by the INTC Committee, in order to increase the beam intensity and velocity, called HIE-ISOLDE (High Intensity and Energy ISOLDE), see Ref. [157, 158]. The addition of superconducting cavities will help to reach the 10 MeV/u instead of the current 3 MeV/u.

In the following, the ISOLDE facility will be described in more details, including a description of the different phases of transport and preparation of the beam, like the post acceleration. Finally, the experimental setup will be detailed in order to understand the different analysis steps.

2.2 ISOLDE at CERN

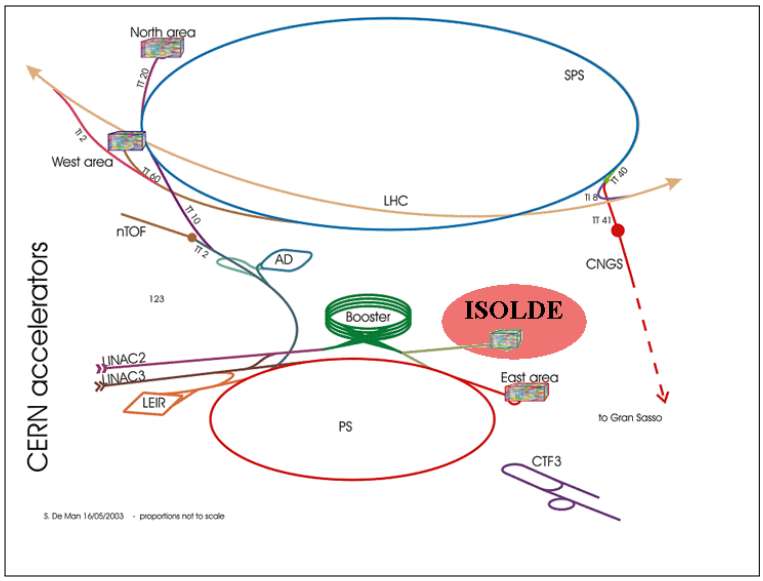

Figure 4.4: CERN Accelerator Complex.

The ISOLDE facility has been in operation since the first experiments in 1967 using the initial synchro-cyclotron, see Ref. [159]. Now, ISOLDE benefits of the CERN accelerators complex situated on the border between France and Switzerland. A sketch of the CERN accelerators complex is given on Fig. 4.4. The proton beam used to produce radioactive nuclei is provided by the PS-Booster. It is a pulsed beam with a 1.2 s time repetition. The impact of protons on a primary target produces the radioactive isotopes of interest. They diffuse and effuse from the primary target and an ionization source allows to accelerate and transport the beam until a mass separator.
ISOLDE has two separators at disposal the HRS (High Resolution Separator) and the GPS (General Purpose Separator). Sketches of the ISOLDE hall, target areas and separators are shown on Fig. 4.5, 4.6.

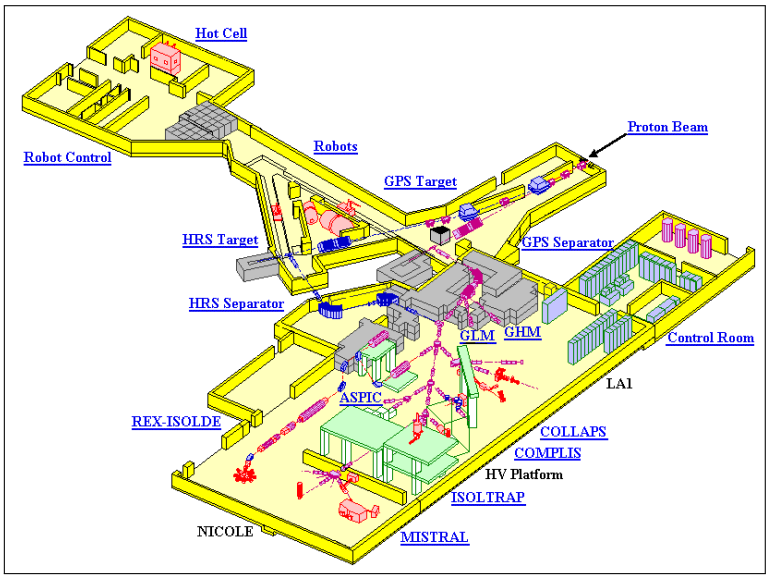

Figure 4.5: ISOLDE hall

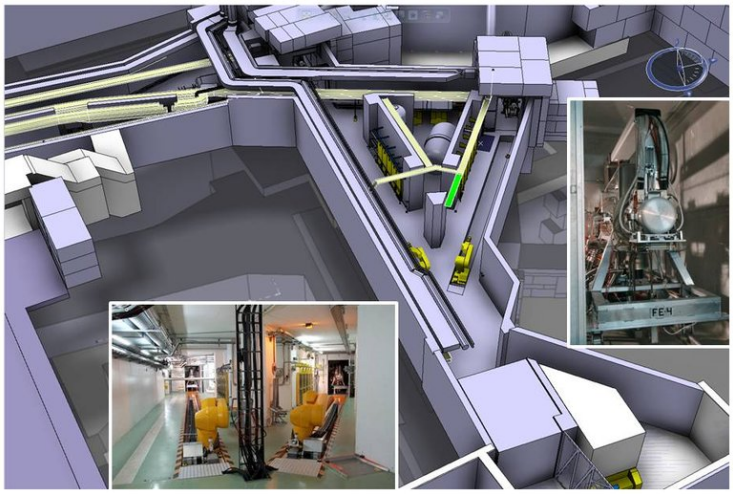

Figure 4.6: Target area and mass separators.

2.3 Production of radioactive beams

The PS-Booster (Proton Synchrotron Booster) is composed of four coupled synchrotrons which deliver to ISOLDE a proton beam of 1.4 GeV up to 4 μA. The proton beam impinging a $^{238}UC_x$ uranium carbide target produces around 10^{13} fission products per seconds. The target is relatively thick $\sim$ 50 mg/cm^2, and important mechanical stress is applied to the target assembly. The studied isotopes (^{93,95,97,99}Rb) are on the neutron rich side of the nuclear chart. The Rb isotopic production yields are shown on Fig. 4.7. For Rb which has a rather small ionization potential $\sim$ 4.2 eV, see Fig. 4.8, surface ionization in target and transfer lines have been used. They were heated at 2000 – 2500 K in order to accelerate the diffusion-effusion processes and to provide a high ionization efficiency. However, as shown in Fig. 4.8, the probability to extract contaminants such as Sr and Y might be of concern, the others (Ga, Ge, ...) have too high ionization potential. The chemical properties of the Rb element are summarized in Appendix B p. 211.

Following the proton pulse, the radioactive ions are spread in time according to their release characteristics. If the release time of the contaminants reaching the experimental setup are different enough, it can be useful to identify their nature.

The identification by release time requires more statistics than the one we obtained.

The main fission products reaching the experimental setup were in majority the rubidium and the

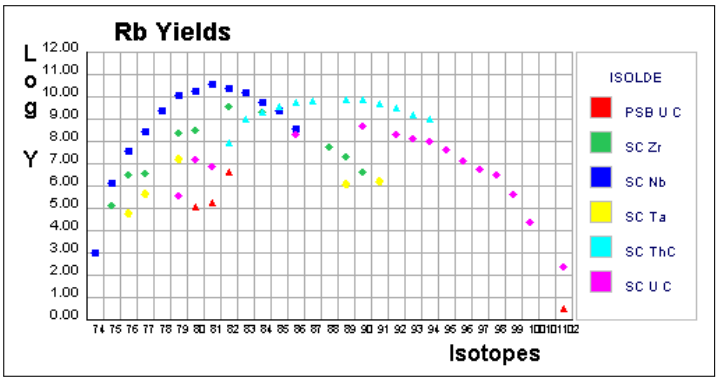

Figure 4.7: Rb release yields obtained at ISOLDE with different target material according to their mass. The previous yields obtained for our cases of interest are represented by purple squares for masses: A=93, 95, 97, 99. PSB: 1.0-1.4 GeV protons, SC: 0.6 GeV protons. Picture from Ref. [160].

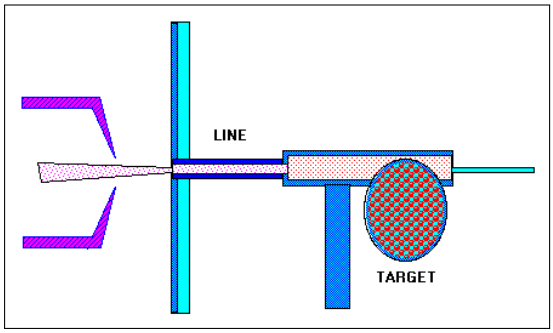

Chemical Elem.	Ionization potential ($I_{pot.}$)
Gallium (Ga)	5.9993 eV
Germanium (Ge)	7.900 eV
Arsenic (As)	9.5 eV
Selenium (Se)	9.7524 eV
Bromine (Br)	11.8138 eV
Krypton (Kr)	13.9996 eV
Rubidium (Rb)	4.1771 eV
Strontium (Sr)	5.6948 eV
Yttrium (Y)	6.217 eV

Figure 4.8: (left) Surface ionization target. (right) Ionization potential of some isotopes produced during the fission process. Picture and values from Ref. [160].

strontium, for example, in the ^{93}Rb one obtained 95% of Rb and 5% of Sr, see Subsec 11.2 on page 125.

2.4 Mass Separation

After the extraction from the ion source, isotopes of several elements are present in the beam. To select the radioactive ions of interest the RIB passes through a mass separator. Inside this magnetic analyzer the mixed beam is separated into isobaric or mono-isotopic beams.The resolving powers $\frac{M}{\Delta M}$ of the GPS and HRS are respectively 2400 and 5000. The GPS provides isobaric beams, while the HRS may eventually provide mono-isotopic beams. "On-line" yield measurements can be performed after the separator (tape station) in order to examine the possibility to make an experiment.

2.5 RFQ Cooler: ISCOOL

Cooling a beam should be understood as the reduction of its axial and radial emittance as well as its energy dispersion. The RFQ Cooler increases the optical properties of the beam, which will be submitted later to another major cooling process inside the Penning trap of REX-ISOLDE, see Subsubsec.2.6.2.

2.6 REX-ISOLDE

2.6.1 Introduction

The project has been proposed in 1994, see Ref. [161], as an experimental setup to bunch, charge breed and post accelerate the radioactive ion beams. The successful results of REX-ISOLDE led to the continuation of the project as a permanent setup at ISOLDE. In order to apply the charge breeding a bunching and cooling of the beam is necessary; it is performed by a Penning trap. The bunched structure helps also to increase

the signal-to-noise ratio considering the low intensities of radioactive beams, and is also necessary for the acceleration process originating from RF cavities. The Fig. 4.9 shows the REX-ISOLDE facility.

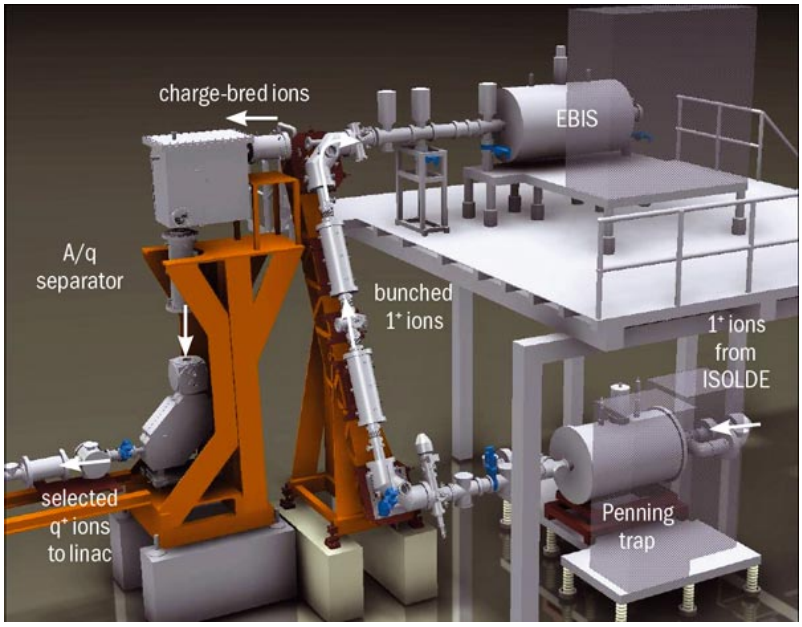

Figure 4.9: REX-ISOLDE. Picture from Ref. [162].

2.6.2 REX-TRAP (Penning Trap)

The beam coming from the ion source at 60 keV is injected inside a Penning trap, see Fig. 4.10. It is captured inside the trap by electromagnetic fields. The Penning Trap is filled with a buffer gas usually a noble gas like Ar [2]; the pressure is around a few 10^{-3} mbar. The collisions of ions with the gas cool down the beam and decelerate it from 60 keV to a few eV conferring a better transversal emittance. The Brillouin limit fixes the maximum intensity inside a magnetic field like for the Penning Trap to the $\sim 10^8/\text{cm}^3$, see Ref. [163] (Trap capacity $\gtrsim 10^6$). The ions are thus bunched. They are extracted from the trap by lowering the potential threshold with a typical extraction time of 10-50 μs, and re-accelerated up to 60 kV. Finally the beam is transported to the EBIS ion source. transversal emittance is significantly improved.

2.6.3 REX-EBIS (Charge Breeder)

The next phase consists in increasing the charge state of the ions in order to be able to post-accelerate them through the LINAC (LINear ACcelerator). This is performed using the Electron Beam Ion Source (EBIS) by electron impact ionization process (A/q<4.5), see Subsubsec. 1.4.1.
The singly-charged ions are injected inside the trap. They are confined radially in the potential by a strong solenoid magnetic field (B=2 T), and, longitudinally by electrical potential barriers. During the confinement ($t_{confinement}$ < 20 ms) the ions are impacted with fast moving mono-energetic electrons from an electron gun ($E_{electron}$ =3-6 keV) with a beam current of 100-500 mA. The electrons are knocked out of the ions. The charge breeding process requires a high vacuum quality, for that purpose, several pumping stations are placed along the beam transport to reach $\lesssim 10^{-11}$ mbar. At a certain time, a given equilibrium charge state (A/q~ 4) is obtained and the bunch is extracted to the REX-LINAC by applying a voltage, see Fig. 4.11.
The phase space overlap between the ions and electrons determines mainly the breeding potential ("cross section"). The limitation of the technique should come from the limit of the overlap.
REX-TRAP and EBIS are synchronized in order to extract and inject properly the beam, respecting the bunching. Thus the charge breeding time in the EBIS is identical to the trapping time in REX-TRAP. The charge breeding time was modified according to the different isotopes of interest. From the extraction of the Penning Trap, a small part of the buffer gas can be transmitted and acts as contaminant after EBIS.
The REX-EBIS platform is submitted to high voltage. At the injection, the platform is subject to 60 kV and

2. A lighter buffer is used for lighter nuclei that we want to study.

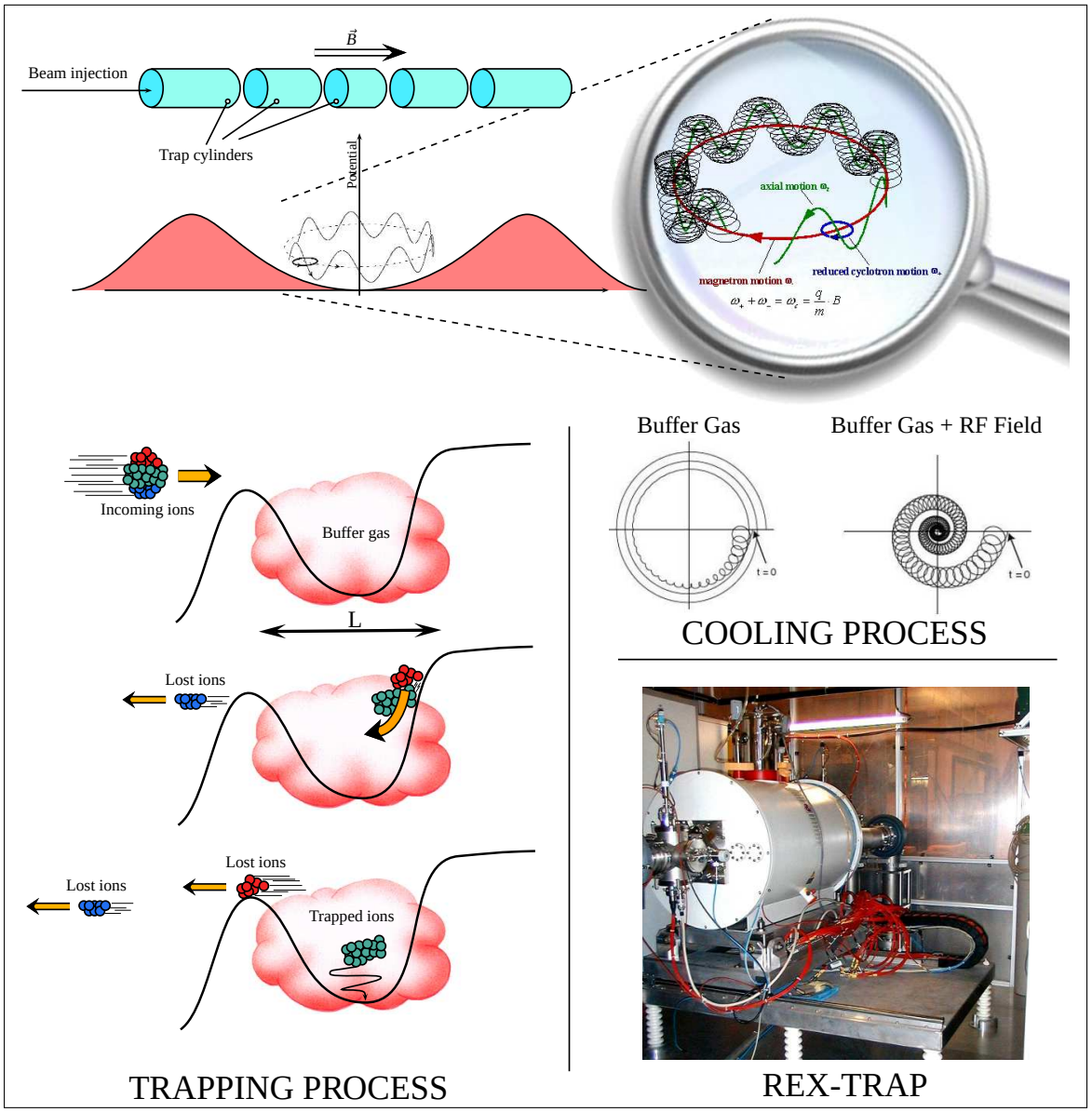

Figure 4.10: The Penning Trap: REX-TRAP. Sketch of the trapping and bunching process realized by the Penning Trap. During the trapping process a part the nuclei bunch from ISOL is rejected (red, blue). The Cooling process is presented according to the buffer gas and RF-Field impact. Its selective capacity is illustrated by looking at the contaminants which are ejected during the cooling process.

switched at ~ 20 kV to convert the ISOLDE energy 60 keV to ~ 20 keV·q in accordance with accelerator specifications.
During the Coulomb excitation study of Rb the repetition rates for the different isotopes were ~ 14.08 Hz (^{93}Rb), ~ 12.20 Hz (^{95,97}Rb) and ~ 14.29 Hz (^{99}Rb), see Tab. 4.1 on page 88.

2.6.4 A/q separator

The residual gas is also ionized and extracted from EBIS. Considering the low intensity of the radioactive beam it is necessary to get ride of the extracted buffer gas to increase the signal-to-background ratio. The amount of contaminants have to be smaller than the intensity of the radioactive beam.
Since the potential lowering of the REX-EBIS electron beam impacts the emittance in terms of energy spreading, limiting the q/A resolution of a standard magnetic separator, a specific one -Nier spectrometer- is used. An electrostatic 90° cylinder deflector and a 90° magnetic bender position in a "S" configuration,

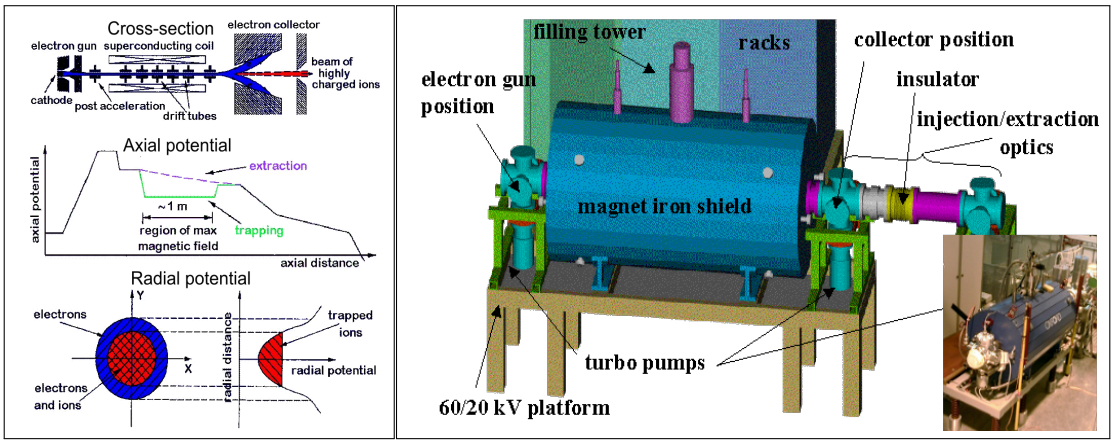

Figure 4.11: REX-ISOLDE Electron Beam Ion Source setup: REX-EBIS. For the injection, the optical devices guide the ion beam to the EBIS and in the opposite sens for the extraction until the Nier-spectrometer. Lenses and reflectors are switched for the injection and extraction. Modified picture from Ref. [162], see Ref. [164].

with a resolution of $\Delta(q/A)/(q/A) = 1/150$. The first deflector separates the ions according to their energies irrespective of their masses to the focal plane. The bending magnet is used to select specific A/q mass-to-charge ratio. To minimize the presence of residual gas [3], a scan over the different A/q is done before the experiment.

2.7 REX-LINAC

ISOLDE is one of the eldest installations for nuclear physics studies at CERN and several other experiments and buildings have been built around the ISOLDE hall. The space limitation motivated the development of REX-ISOLDE associated to a compact Linear Accelerator. The LINAC is designed to keep the possibility to use heavy nuclei with an A/q acceptance of 4.5 and a charge breeder increasing the charge states higher than 1+. The REX-LINAC is constituted by 4 resonator types, presenting different advantages, see Fig. 4.12.
The LINAC beam preparation and post-acceleration are synchronized with the REX-ISOLDE bunching process.

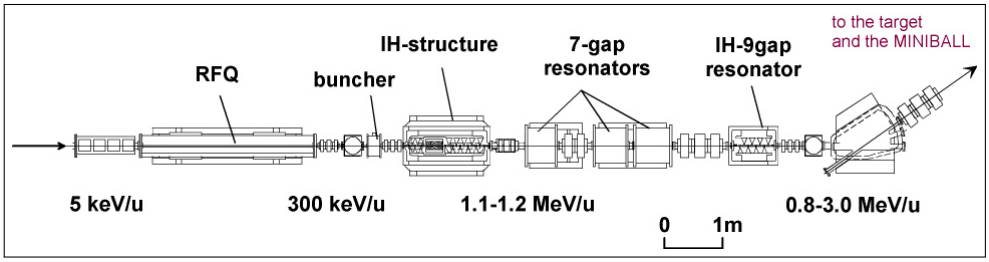

Figure 4.12: REX-LINAC.

2.7.1 RFQ

The first experimental demonstration of a RF acceleration has been performed by R. Wideröe in 1928, see Ref. [165]. Placing a drift tube between two tubes grounded and applying an alternating voltage of 25 kV to the drift tube, he succeeded to accelerate ions up to 50 keV. Several developments followed the highlighting of the possibility of an RF acceleration, among them the Radio-Frequency Quadrupole whom the invention of the concept is attributed to Kapchinskii and Teplyakov in 1970.
The first device, a RFQ, is favored for low energetic beam acceleration and bunching. The extracted particles arriving from REX-EBIS at 5 keV/u are accelerated through the RFQ up to 300 keV/u.

3. Generally, at this stage the contaminants from the primary target with close A/q are not removed.

The 4-vane REX-RFQ are similar to electrodes on which an alternating voltage is applied to accelerate the ions. The field of the RF quadrupole focuses transversally the beam. The spacial modulation performed by the design of the four rods creates smooth bunching of the injected DC-beam and acceleration.

Before the IHS (Interdigital H Structure) two magnetic quadrupole triplet lenses and a rebuncher are placed to reach the acceptances of the IHS.

2.7.2 IHS

The structure type H (or TE "Transverse Electric") is inspired from the RFQ and presents the advantage of an important focusing electric field. Inside the resonator of type IHS, several cylindrical cavity drift tubes of different lengths are mounted on opposite sides alternatively. The resulting magnetic field is directed along the beam line axis. The induced currents on the wall [4] produce electric fields of alternating direction between the drift tubes. The resulting strength pushes the ions along the beam line axis.

The final energy of the ions, at the exit of the IHS, can be adjusted between 1.1-1.2 MeV/u via the gap voltage distribution [5].

2.7.3 7-gap resonator

Three 7-gap resonators accelerate the beam in the range of 0.8-2.2 MeV. The special design consisting of split ring resonators is used for the synchronous particle velocities of: β = 5.4%, 6.0%, 6.6%. The resonance frequency is 101.28 MHz.
The final energy is adjustable by tuning the RF power and phase of the three active resonator.

2.7.4 IH-9-gap resonator

In the earliest project, two identical 7-gap IH structures were envisaged. They had the advantage to provide a wide range of energy (3.7-5.9 MeV/u) with two short cavities. But the 9-gap geometry allowed to match the lowest injection energy of 2.2 MeV/u. The resonance frequency is 202.56 MHz.
The final energy range accessible is 0.8-3.0 MeV/u, see Ref. [166]. The cross sections obtained by Coulomb excitation depends highly on the initial energy and the 9-gap resonator is essential in the LINAC leading to the range of "safe" Coulomb excitation, see Chap. 3 on page 55.

2.7.5 Bender

Finally, after the post acceleration, the beam can be distributed among different beam lines. A bender with a charge an mass selection (A/q) sends the beam to the experimental setup beam line of MINIBALL, where the nuclear structure of the nuclei can be studied. The final energy obtained at the secondary target (MINIBALL Spectrometer) is around 2.84 MeV/u.

2.8 The time structure

The time structure of the beam and the preparation phase of this one is essential for the data acquisition (DAQ). A summary of the relevant signals related to REX-ISOLDE operations sent to the MINIBALL DAQ system, called Marabou, see Ref. [167], are given in the Fig. 4.14.
The PS-Booster (PSB) is able to deliver proton pulses every 1.2 s. A series of such pulses constitutes the so-called Supercycle time. The PSB pulses feed all CERN machines so that only a part of them are sent to the ISOLDE target. The number of pulses in a Supercycle is variable, it was 38 pulses in the case of ^{95}Rb. A specific structure of pulses allocated to ISOLDE takes place, a summary of the different cases which happened during the experiment is given in the Tab. 4.2. An example of the PSB time structure is given in the Fig. 4.14. The corresponding signals to the PSB and proton pulses are sent to the MINIBALL DAQ. The proton pulse signal is called T1.
Due to the ionization of the air in the target area when the protons impinge the primary target, the HV (High Voltage) is switched off to avoid the formation of sparks.

4. azimuthal
5. possible via capacitive plunger.

Arriving from REX-EBIS, the bunched and purified beam is injected into the LINAC. An EBIS injection signal is sent to MINIBALL. This timing signal serves to synchronize the LINAC with the REX-EBIS extraction. For the DAQ, this signal used as a trigger, defines the "In Beam" measurement window.

$^{A}X^{charge}$	$T_{\frac{1}{2}}$ [168]	T_{period}	Beam Gate	$T_{Breeding}$	Eff.	Extrac.	Intensities(*)	Collec.
$^{87}Rb^{21+}$	4.81 10^{10} y *9*	60 ms	10 ms	55 ms	~ 8%			
$^{87}Rb^{23+}$	4.81 10^{10} y *9*	80 ms	2 ms	69 ms	8.7%			
$^{93}Rb^{22+}$	5.84 s *2*	71 ms	——	68 ms	~ 8%	slow	6 10^{6} pps (2 10^{7} μCu)	12 h
$^{95}Rb^{23+}$	377.7 ms *8*	82 ms	——	79 ms	~ 8%	slow	1 10^{6} pps (3 10^{6} μCu)	11 h
$^{97}Rb^{23+}$	169.1 ms *6*	82 ms	——	69 ms	~ 8%	slow	5 10^{5} pps (4 10^{5} μCu)	40 h
$^{99}Rb^{23+}$	54 ms *4*	70 ms	2 ms	69 ms	~ 6%	normal	~few 10^{3} pps	19 h

Table 4.1: Preparation phase settings for REX-TRAP and REX-EBIS. The efficiency is related to REX-TRAP and REX-EBIS. T_{period}: time difference between two injections (switching of the optical devices). A beam gate can be used as a selector. Extrac.= extraction mode, Collec.= approximate collection time of data.* Intensities measured by Faraday Cups.

Isotope	Proton pulses/cycle	Main proton supercycle used
^{93}Rb	14/38	4, 6, 8, 10, 12, 18, 23, 25, 27, 29, 32, 34, 36, 38
^{95}Rb	12/38	4, 6, 8, 10, 13, 18, 21, 23, 26, 28, 33, 38
	14/38	4, 6, 8, 10, 12, 18, 23, 25, 27, 29, 32, 34, 36, 38
^{97}Rb	14/38	4, 6, 8, 10, 12, 16, 18, 20, 23, 28, 30, 33, 37, 38
^{99}Rb	14/38	4, 6, 8, 10, 12, 18, 23, 25, 27, 29, 32, 34, 36, 38

Table 4.2: Proton Supercycles during the experiment. Note that there is not any consecutive proton injection.

The ^{87}Rb isotope has been easily produced thanks to a mass marker added in the standard primary target. The ^{87}Rb stable beam has been used to make tests of the MINIBALL setup.In order to reduce the loss of ^{99}Rb by decay, a shorter extraction has been opted compared to the less exotic cases. The different decay patterns are illustrated on the Fig. 4.13. The different settings of REX-EBIS and REX-TRAP as well as the final intensities obtained at the second target are summarized in the Tab. 4.1.

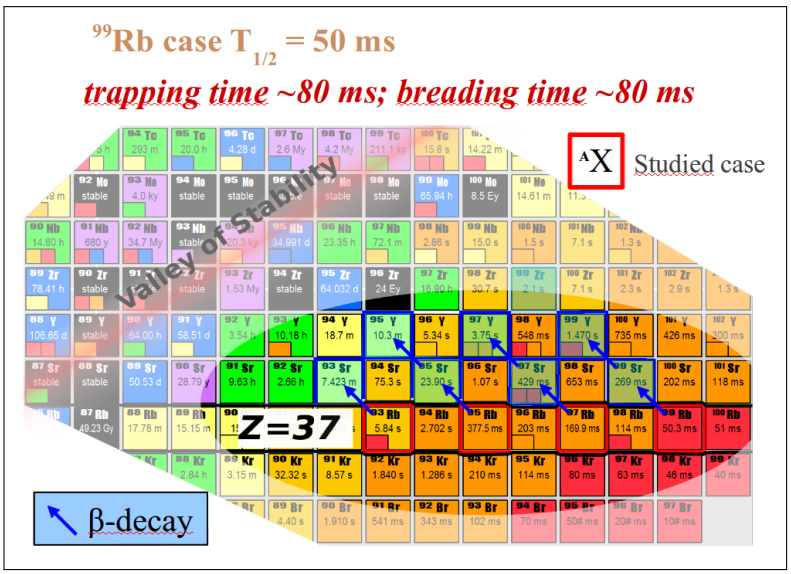

Figure 4.13: Decay patterns of the studied Rb isotopes. The studied cases are framed by a red square, the β-decays are represented with blue arrows.

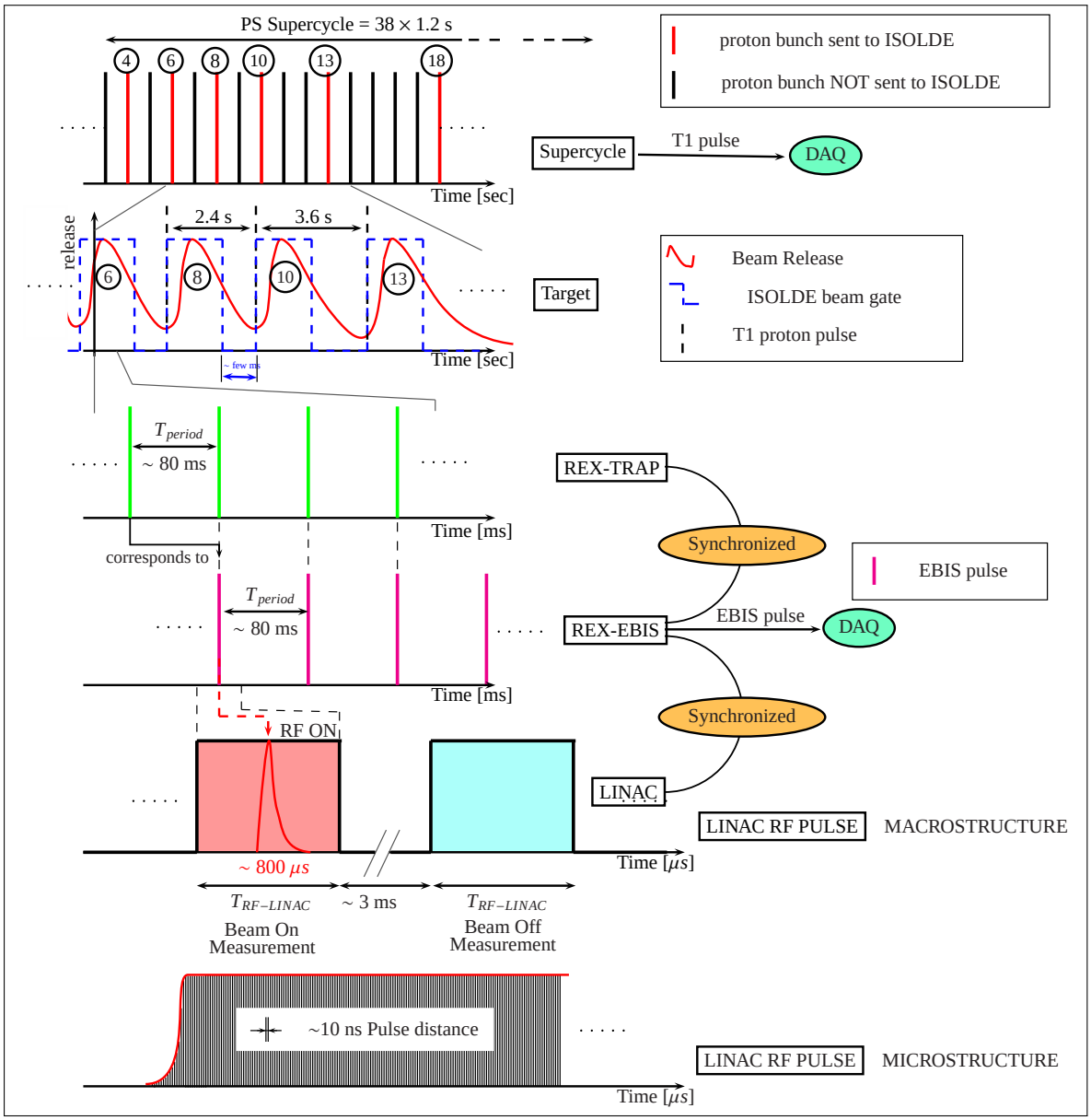

Figure 4.14: Time structure of the beam. The period of the PS Supercycle is not fixed and can be changed. For example the PS Supercycle had a period of 46.8 s = 39 injections every 1.2 s. The injection sequence has been changed during the experiment. For the ^{99}Rb the sequence was principally 1, 2, 3, 4, 5, 6, 7, 8, 9, 10, 11, 12, 13, 14, 15, 16, 17, 18, 19, 20, 21, 22, 23, 24, 25, 26, 27, 28, 29, 30, 31, 32, 33, 34, 35, 36, 37, 38, 39 (injection NORMHRS => ISOHRS in red).

2.9 MINIBALL Setup (γ-ray detection)

At the origins of the REX-ISOLDE project, a high resolution gamma spectrometer was included into the guidelines to perform nuclear structure studies with low intensity radioactive beam from REX-ISOLDE. After some discussions and preliminary works on the spectrometer project, the MINIBALL detector array emerged as a consensus. Most of the tests were realized in Germany while the REX-ISOLDE project was in progress. Finally in 2001, the MINIBALL detector array was operational to perform experiments with radioactive beams.

The MINIBALL array consists of a high resolution HPGe (High Pure Germanium) detector array in a close geometry to optimize the efficiency. In order to perform Doppler correction of in-flight emitted gamma rays, the Germanium detectors are segmented and pulse shape analysis is available in order to increase the

granularity. As mentioned in the previous section the MINIBALL setup is installed after the bending magnet on line at 65°, see Fig. 4.15. The Germanium detector array is placed around the secondary target chamber sketching a ball.

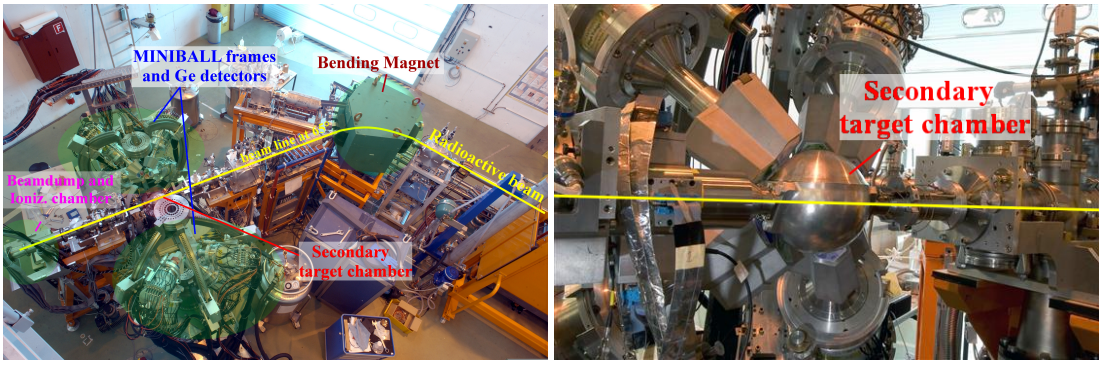

Figure 4.15: MINIBALL setup with the frames holding the Germanium detectors. The beamdump and ionization chamber are placed at the end of the 65° beamline. The secondary target is on the beamline surrounded by the Germanium MINIBALL array. Created from Ref. [169]

2.9.1 The Germanium detectors of the MINIBALL array

The MINIBALL detector array is constituted of 8 cluster detectors. A cluster consists of 3 individual Germanium crystals encapsulated in an aluminum cap. The crystal is electrically separated in 6 segments along the radial direction and around a central electrode called "core". The electrical segmentation improves the intrinsic granularity to 144 individual detecting parts (8 clusters x 3 crystals x 6 segments). The clusters are placed at around 11 cm from the target around the target chamber, see Fig. 4.16.

Seven different energy signals can be extracted separately from the crystal: the energies collected in the segments and the total energy collected by the core. The standard high voltage to deplete the HP Ge MINIBALL crystal is 2.5-4.5 kV. The Germanium detectors are permanently cooled down by liquid nitrogen during the experimental time.

The intrinsic energy resolution of segments and cores are different, respectively $\sim$ 2.8 keV and $\sim$ 2.3 keV.

2.9.2 Electronic modules and DAQ

Specific electronics is used to shape and integrate the most efficiently and accurately the energy signal of γ-ray transitions. Pre-amplifiers associated to "Digital Gamma Finder"(DGF) [6] modules perform respectively the amplification of the raw energy signal coming from the Germanium detector, and the shaping and integration of the energy signals.

Two DGF modules with 8 inputs are dedicated to one crystal. The pre-amplified core signal is sent to a "master trigger channel" in order to readout the associated segment channels only if the gamma energy is collected by the core electrode, constituting the hardware selection. The interaction point of the γ-ray is defined as the hit point where the highest energy is detected. The core energy is assimilated as the total energy. However, the angular information coming from the segment of the interaction point is used to perform the Doppler correction of the in-flight gamma rays.

In order to collect properly the gamma ray energy an add-back algorithm has been implemented to sum the neighboring core energies; indeed the cross talk effect can bias the gamma ray energy determination while collecting the energy in different cores. This effect should be negligible in our case of low gamma ray transition energy range (40 keV-600 keV) but start to be considered for higher gamma ray energies (600 keV-1500 keV). An analysis has been performed with the add-back algorithm but it did not contribute to a considerable increase of the photo-peak intensities. Moreover, another add-back implementation (on Germanium detector) has been performed. However, the results obtained were quasi unchanged. Finally, considering the low energy range covered by our gamma spectra, it has been decided to not apply any add-back algorithm. Of course, the algorithms are not efficient for the low energy range considered, and they could rather distort or deteriorate the energy resolution and energy determination, see Fig. 5.4 in the next chapter.

6. X-ray Instruments Associates, California - www.xia.com

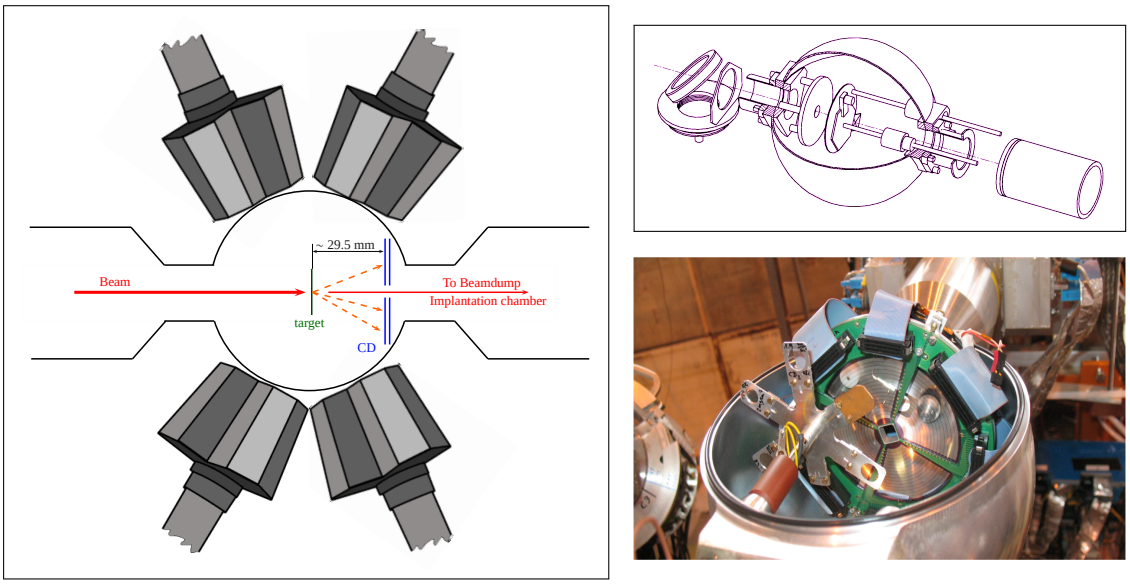

Figure 4.16: Miniball setup - schematic view. When the beam impacts the secondary target, the incident nuclei react with the target. A part of the recoils and ejectiles are detected into the CD detectors. Another part of the reaction products are sent to the ionization chamber or the beamdump. The target-cluster distance is ~ 11 cm.

The particle energy readout is decorrelated from the γ-ray DGF readout (except the particle-γ coincidence time window). The correlation between particle and γ is reconstructed during the event building in software considering the timestamp data.

DGF and time synchronization The Digital Gamma Finder are CAMAC modules with four complete spectroscopic channels. The spectroscopic channels are independent from each other, they process each event separately (Analog part, ADC, FIFO, FPGA). The logical part generates a fast multiplicity used to decide if the event is interesting. An external NIM signal can validate the events, but the limitation of the module imposes the delivery of those ones after a fast trigger of ~ 10μs.

The timestamps synchronization In order to make the experiment several XIA DGF4-C modules have been used. Each of them have a counter (timestamps) which is incremented every 25 ns for each ADC sample. This counter is recorded in the data stream acting as a timestamps signal. The time differences between γ signals is taken as their DGFs timestamps differences. Moreover the DGFs' timestamps need to be synchronized, since their internal 40 MHz clock can drift in time. A simple solution has been applied, one clock has been used as reference distributed to all modules.
The synchronization is done at the "same" time than the busy signal. When DGF modules are not acquiring they send a busy signal to a logical OR module which generates the logical OR operation and distributes the result back to the SYNCH DGF inputs. When the last module starts, their clock are reset to zero.

2.10 Particle detector

During the Coulomb excitation recoil and beam particles are collected into a segmented double-sided silicon strip detector (DSSSD), called CD detector. The particle detector consists in 4 different quadrants, see Fig. 4.17, Tab. 4.3. The front side of the quadrant is constituted by 16 annular p^+n junction strips of 1.9 mm width (2 mm pitch). The back side possesses 24 sectorial n^+n ohmic strips of 3.4° (3.5° pitch). This leads to an important granularity of the CD assembly: 160 discrete detector elements. The total surface is 5000 mm^2 with 93% active. The polar coverage in the laboratory frame is 16.2°-53.3° and the azimuthal coverage represents 83% of the total azimuthal space. The particle detector was placed at ~ 29.5 mm. The outer radius is around 40.9 mm, and inner radius 9 mm. A summary of the characteristics is given in Tab. 4.3.

To avoid an early deterioration of the particle detector, an inner plug can be installed in the center of the CD, reducing the particle flux for the inner strips. In the last configuration, the most relevant information is related to the angular distributions and high laboratory angles (especially in quadrupole

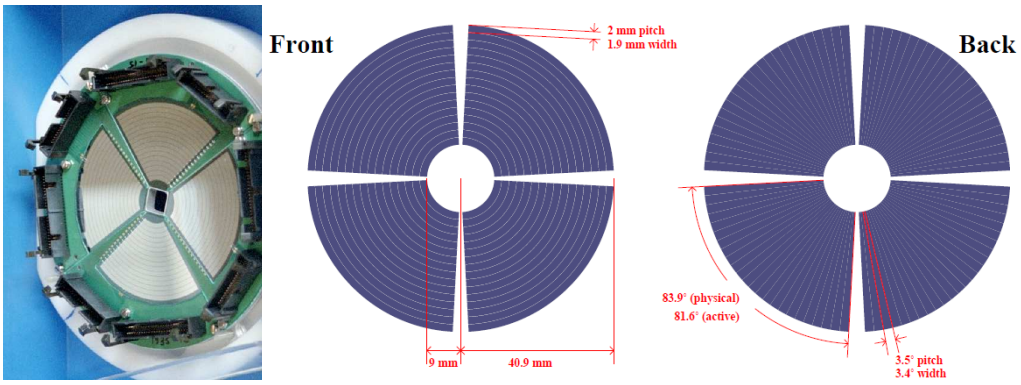

Figure 4.17: CD detector - This DSSSD divided into 4 quadrants, 16 annular strips and 24 sectorial strips is used to detect the position and the energy of the particles incoming on the forward side.

Total area	50 cm^2 (93% active)
Quadrants	4
Annular p^+n junction strips per quadrant	16 (i.e. 64 total)
Sector n^+n ohmic strips per quadrant	24 (i.e. 96 total)
Dead layer thickness	$\sim 0.4 - 0.5$ μm p^+n implantation,
	$\sim 0.2 - 0.3$ μm Al metalization,
	equivalent to 7 μm of Si

Table 4.3: Summary of the main characteristics of the DSSSD used during the Coulomb excitation study.

moment measurements, see Subsec. 5.2 on page 66.).
During an experiment, the leakage current is constantly followed up in order to have an estimation concerning the deterioration of the quadrants. (For example, if the beam intensity is too high the leakage current will increase.)

2.10.1 Electronic modules and DAQ

Silena 7710 quad suppliers, see Ref. [170], provide the bias voltages. The detector bias is applied to the p^+n junction strips.
The pre-amplifiers are composed of RAL-108 charge-sensitive preamplifier boards, see Ref. [171]. The particle signals are sent to the RAL-109 shaping amplifier/discriminators, see Ref. [171], providing a complete analogue electronic instrumentation for each individual CD detector strip. The gain range has been changed several times during the experiment (justifying the process of calibration [7]) by changing the gain resistors between experiments. The assumed full-scale range and lower discriminator was 444 MeV, for the 10 Volts maximum input voltage taken in maximum MADC-32 input. The final particle signals are converted inside a peak-sensing MADC-32 (Mesytec Analogue-to-Digital Converter 32 input channels), see Ref. [172]. The MADC-32 has a similar internal clock as the DGF modules (40 MHz) used for the particle timestamping. The main advantage presented by this type of ADC is the low conversion time reached (1.6 μs in our case [8]).

3 Data Acquisition System

The DAQ (Data Acquisition System) and the electronic modules chosen are used to optimize the γ-particle coincidences detection.

7. Indeed the resistors are slightly different and if the arrangement is changed the gains should be mixed.
8. The dead time is around the conversion time.

3.1 Synchronization with REX-ISOLDE

EBIS pulse and readout Every signal from the REX-ISOLDE beam preparation systems are digitalized by a DGF module. The data acquisition system is synchronized via the EBIS pulse timestamp [9] with the EBIS extraction and the LINAC. At the EBIS extraction, an "ON beam" window of ~ 800 μs is opened to record data, see Fig. 4.18. After the "ON beam" window is closed, the readout of the module is operated and an "OFF beam" window is opened. Around 8 ms after the EBIS pulse the "OFF beam" window is closed (if there is enough time between the "ON beam" and the next EBIS pulse). If an event occurs in the "OFF beam" window a second readout will be forced. All the events arriving 10 ms before the next EBIS pulse are rejected to be ready for the next "ON beam" window. A simple electronic layout of the DAQ trigger generation is summarized in the global picture of the triggering process, see Fig. 4.19.

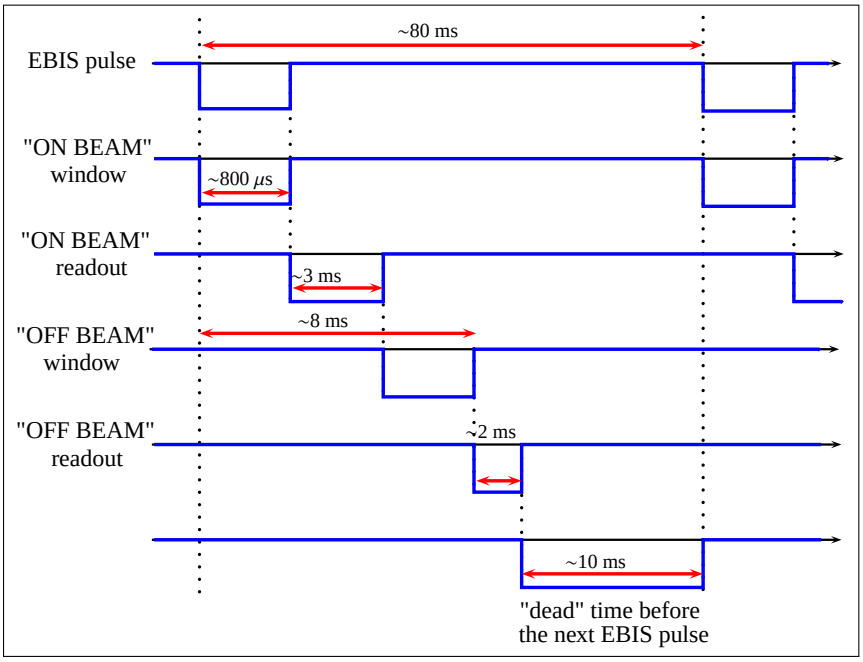

Figure 4.18: For each EBIS cycle, the readout of one event ("ON beam") or more ("ON beam" and "OFF beam") is performed. Typical gate widths are presented.

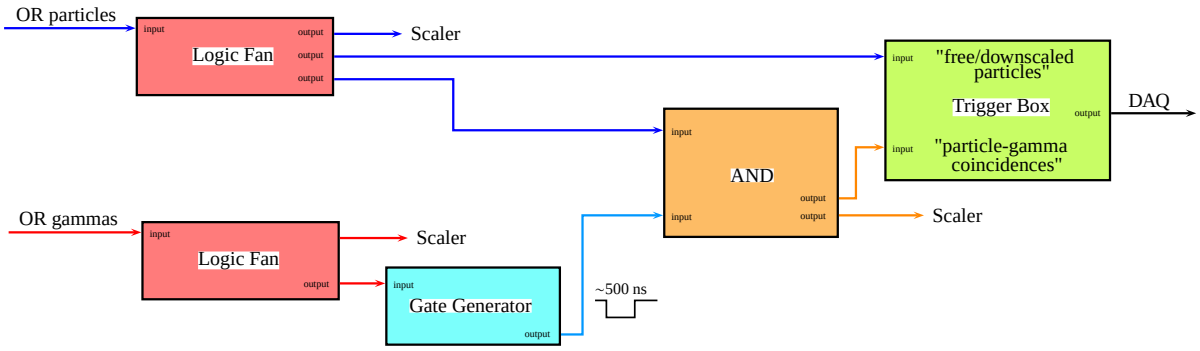

Figure 4.19: DAQ triggering. If a "OR particle" signal arrives in the 4 μs event-building time window outside the "ON beam" window, the "free" particles can be downscaled. The process is applied on each quadrants with the same γ gate constituting 8 DAQ triggers.

The total module readout and data transfer time of XIA DGF4-C modules and MADC-32 need ~ 3-5 μs and have an impact on the acquisition deadtime. The scalers are readout at a 10 Hz rate. They are used to check the beam status and operations giving the particle and gamma rates of the detection systems.

9. including the readout of MINIBALL electronic modules

T1 proton pulse After a proton impact on the primary target, the signal called "T1" is sent to the DAQ. At each proton pulse a main ISOLDE beamgate can be applied to compare the moments with and without RIB. This comparison would be useful if the release time convoluted with the lifetime is sufficiently short. In our experiment, some tests have been performed with the beamgate to identify the radioactive beam components. However, this beamgate has not been used during the accumulation of statistics. A typical proton release

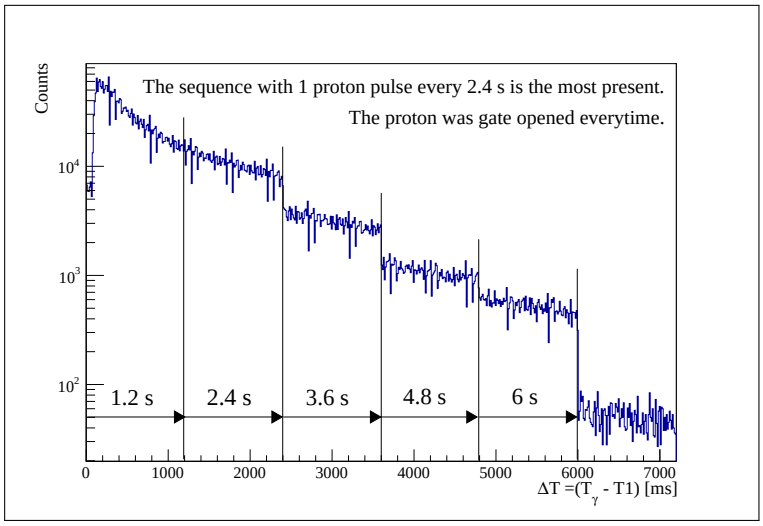

Figure 4.20: Proton Release.

feature observed for the present study is shown on the Fig. 4.20. An exponential decay feature is observed between the "start" and 2.4 s without any truncation. It exhibits that the typical proton pulse sequence for our experiments was constituted mainly with a frequency of one pulse every 2.4 s.

3.2 Particle-γ Coincidence

In our experiment only the events of Coulomb excitation are interesting. In order to reduce the dead time and the amount of data recorded, only the particle-γ coincidences have been stored. In that way, most of the pure elastic scattering can be removed. This selection process is done in hardware with the electronic modules.
The EBIS release is set for a relatively slow/normal extraction, see Fig. 4.21. The slow extraction mode used for ^{93,95,97}Rb has a total extraction time of 620 μs. The normal extraction has been used only for ^{99}Rb in order to minimize the β-decay products and the total extraction time is reduced until 330 μs.

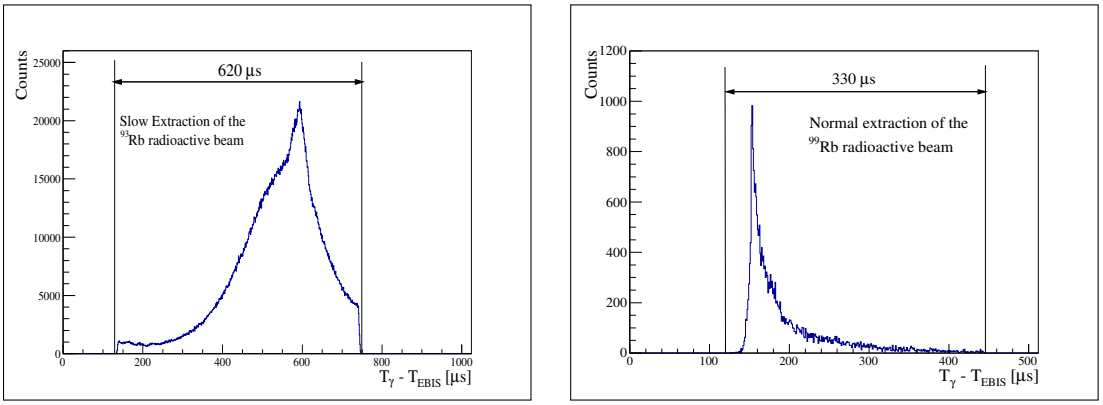

(a) (b)

Figure 4.21: EBIS Release. (a)The slow extraction mode used for ^{93,95,97}Rb has a total extraction time of 620 μs; an example is given on the first plot. (b)The normal extraction has been used only for ^{99}Rb in order to minimize the β-decay products; the total extraction time is reduced until 330 μs.

Each signal from the CD detector passes through RAL108 pre-amplifiers and the RAL109 sampling amplifiers. Afterwards, the signal is sent to constant fraction timing and Gaussian shaping in order to produce both a fast time signal and an energy signal corresponding to the detected particle energy. The front strips signals pass by a Logic Fan-IN Fan-Out (FIFO) where they are merged according to an "OR condition". The resulting signal is shifted in time via a delay module in order to compensate the slower DGF timing signal. The back strip signals are sent to TDC modules (Time-Digital-Converter).
The timing signals of cores are sent to a Logical OR module, the resulting signal opens up a coincidence gate for the particle. The gammas are detected before the particle, thus they are triggering the acquisition waiting for a coinciding particle. On the particle side, a delayed particle trigger has been generated and if it arrives during the gamma gate, the particle energy is recorded by the opening of an ADC gate (without any gate the ADC is passive and does not consider the event). Note that just the particle are conditioned; there is not specific condition applied on the gammas, the particle conditioning is qualified as "downscaling" [10] instead of "single" for the gamma. The downscaling is used when a particle is recorded even if there was not a detected γ-ray. An additional trigger in the DAQ has been added, allowing to verify on-line the correct proportion of Rutherford scattering. The low intensities obtained in our studies allowed to downscale all the events, avoiding the loss of right coincidences. The coincidence treatment is summarized on the Fig. **??**.

10. The events are qualified as downscaled if not any condition are applied on them. Those events are added in addition to the particle-γ coincidence.

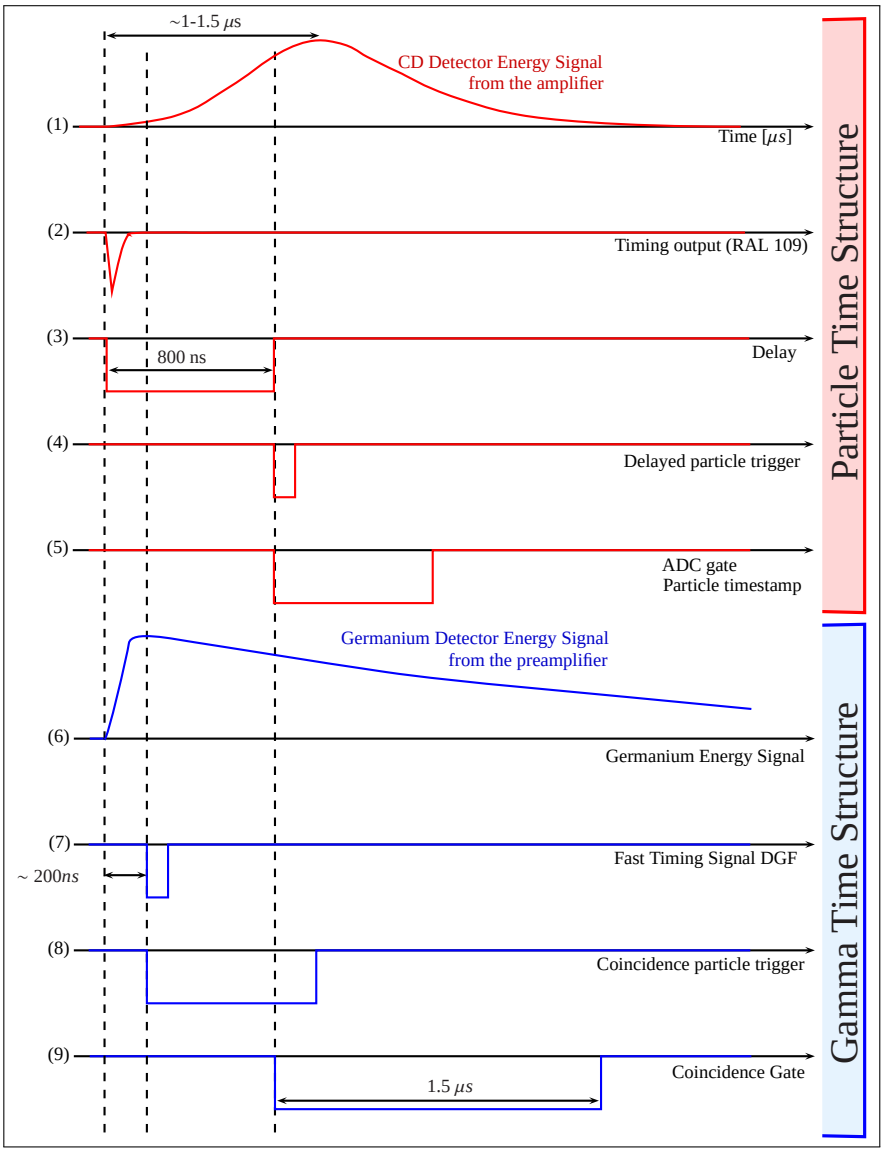

Figure 4.22: Particle-γ condition. (1) Energy signal of the scattered particles (RAL109) with longer rising time than the Germanium detector (6). (2) Time signal of the particles. (3),(4) The particle trigger needs to be delayed ~ 800 ns in order to make coincidence. (5) The delayed particle trigger opens a coincidence gate ~ 800 ns. (6) The rising time of the Germanium detector is shorter than for the particles, however the DGF are not able to send a timing signal in a short time, and a processing time of ~ 200 ns is needed to output a Fast Timing Signal (7). (8) After the coincidence trigger an ADC gate ~1.5 μs is opened.

4 Ionization Chamber

The beam arriving at the secondary target has often more than one component. The undesired components constitute a source of dead time and could damage the detectors by an increase of the hits rate.
The main sources of contaminants result from ISOLDE target (isobaric contaminants with the same A) and from the combination of REX-TRAP and REX-EBIS releasing buffer gases in the LINAC. The ISOLDE separators (HRS and GPS) are used only to separate nuclei according to their mass A, and there is no Z selection, resulting in possible isobaric contaminants in the beam. The Nier separator present after REX-EBIS has a limit of resolution around 0.02 A/q; even if slits are used to stop a part of the contaminants some of them could pass if their A/q values [173] are close to the one of the isotope of interest.

In order to determine precisely the beam components an ionization chamber is used at the end of the MINIBALL beamline, see Fig. 4.23.

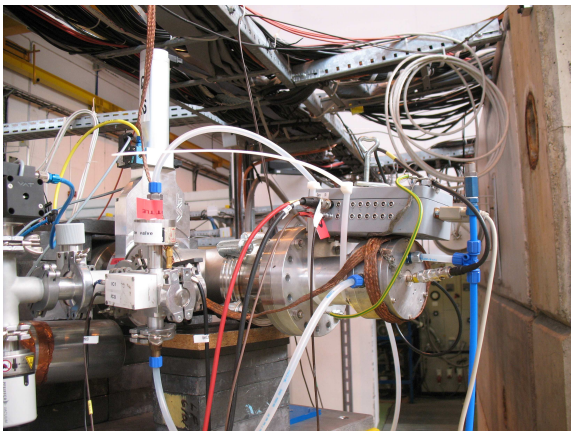

Figure 4.23: Ionization chamber.

The ionization chamber consists of a ΔE - E telescope. The ΔE detector is a chamber filled with a CF4 gas. The incoming particles, passing through the chamber, loose a part of their energy by ionizing the surrounding gas particle(s). A potential difference between electrodes carry off the charges for collection. The remaining energy is detected inside a silicon detector.

The energy lost by charged particle in a material can be determined by the equation of Bethe, see Ref. [174].

The amplitude of the corresponding signal is proportional to $\frac{q^2}{A}$. It is important to note that q is the charge of the ions and not its proton number Z. Nevertheless, every nuclide may enter the chamber with different charges (or acquired a different charge state in the ionization chamber), so that they will not all loose the same energy amount in the gas. Studies realized by Vinzenz Bildstein [175], on the MINIBALL ionization chamber parameters dependencies, led to the formulation of an empirical solution to setup the gas pressure:

$$P[mbar] = 1000 \times \frac{30}{Z_{proj}} \cdot \frac{1.57}{3.69} \tag{4.8}$$

5 Conclusion

Depending on the nucleus of interest, neutron/proton rich, several reaction mechanisms exist. The neutron rich nuclei are generally produced in fission or fragmentation. On contrary, the neutron deficient nuclei are usually favored in spallation.
At the production target a large background from multiple nuclear reactions is present. The transport of radioactive beam far from their production place allows to increase the signal/noise ratio.
Even if the isotope of interest is well produced, the efficiency of all the different stages should be the best (low intensities) and the fastest as possible (short lived). At some point high count rates of contaminants coming from the production or preparation stages need to be removed by accurate selections.

The two principal techniques, In-Flight and ISOL, used to produce nuclei far from stability have been presented and compared. Both of them were developed to optimize the efficiency, the intensity and selectivity of the production.
The technique used to produce the Rb isotopes was the ISOL technique at ISOLDE (CERN). The chemical nature of the Rb element confers to it an easier production. Produced after the impact of proton beam with an energy of 1 GeV on the UC-x primary target, the different isotopes were thermalized in a catcher. Extracted from the latest, they were ionized (surface ionization). After their exit from the ion source, they are mass/charge analyzed and accelerated up to 60 keV. The beam is then purified (Penning Trap) and charge bred (EBIS) to be post-accelerated up to 3.0 MeV/u. Finally, the RIB is delivered to the experimental setup for study.

To study the low-lying nuclear states of Rb isotopes via Coulomb excitation, the MINIBALL array was used. Specially designed for that purpose, the high absolute efficiency ($\sim$ 20% at 250 keV), the high resolution and high granularity, have been optimized to operate optimum Doppler correction of in-flight γ-rays with low intensity beams.

The data acquisition system has been elaborated for the establishment of particle-gamma coincidence, synchronized on the post acceleration, aiming to reduce the dead time.

In Coulomb excitation, the matrix elements of the electromagnetic operator related to the nuclear excited states are generally normalized on known matrix element(s), in order to obtain absolute values. In our case, none of the excited states of ^{97,99}Rb were known. The matrix elements were normalized onto the target excitation. The knowledge of the beam purity and beam components is thus crucial to obtain reliable matrix elements. To overcome the impact of contaminants on target excitation, an ionization chamber has been installed at the end of the beamline.

Chapter 5

The Analysis of Coulomb excitation Experiment

1 Introduction

The different stages of the whole analysis process are presented in this chapter. The first part of the analysis has been focused on the extraction of raw data. The event building and particle-γ rays correlations were done at the same time as the conversion into root format, see Ref. [176].
After a pre-calibration of the detectors, a pre-analysis can be performed to check the validity of the extraction code. A more precise calibration with sources and reactions have been performed afterwards due to their dependencies (such as the CD calibration depending on the Doppler correction). The increase of the signal/noise ratio requires specific treatments such as the rejection of a part of the events. Carefully applied, the identification of the nucleus nature and of some of its nuclear characteristics are eased. For example, the creation and treatment of γ-γ matrices are used to assign the transition nature (e.g. from ^{99}Rb). However, a Compton rejection can be performed to favor the photoelectric events.
At the end of the analysis of raw data, the γ-ray transitions can be identified and their intensities extracted. Afterwards, those informations have been introduced into the GOSIA code to perform a proper extraction of the matrix elements of the electromagnetic operator for the studied nuclei.

2 Extraction of Raw Data

The data acquisition system stores the data stream following a similar pattern to MBS systems "med", see Ref. [167]. An extraction code, written in C/C++ language, has been written to transfer the data from the "med" format to a "root" format. This extraction based on a standard code (used on-line) has been developed by Hans Törnqvist and myself for Coulomb excitation experiment offline analysis [1].
During the extraction, the low particle energies are excluded from the analysis by applying a threshold, because they are difficult to correlate with gamma due to the background noise. The data stream in the medfile is arranged in bunches of time, constituting a MINIBALL event. Inside each MINIBALL event, the particles and gammas are stored also according to time and module but there is not any correlation between particles and gammas. Conditions in time have to be applied in order to build correctly the events.

3 First Data Treatment at the Extraction Development Phase: Particle-Gamma Correlations and Event Building

As mentioned, each hit is ordered in time and module. No correlation between hits and types of hits (particle, γ-ray) is established.
After a pre-calibration of the detectors (alignment of signals on a same channel number), a first treatment is applied to shorten the processing time, consisting in the rejection of low particle and γ-ray energies. The amount of resulting statistics is submitted to a scan in order to record temporarily the characteristics of the hits inside MINIBALL event bunches.
The ADC (particles) and DGF (γ-rays) channels of the MINIBALL array (including all cores and segments) are then calibrated.
After the calibration, the prompt and random particle-γ ray coincidences have to be identified. A gate on the difference between particle and γ-ray detection times is applied. The time windows selecting the

1. The code is adapted for the specific module used for the current experiment, it includes the MADC-32

prompt/random events are defined as shown in the Fig. 5.1. In order to increase the signal/noise ratio a subtraction of the random events is done on the prompt events. The window associated to random events is positioned before the prompt events in order to avoid the short-lived isomers present after the random subtraction. Applying this first selection, the processing time of the analysis is quicker thanks to smaller number of events to handle.

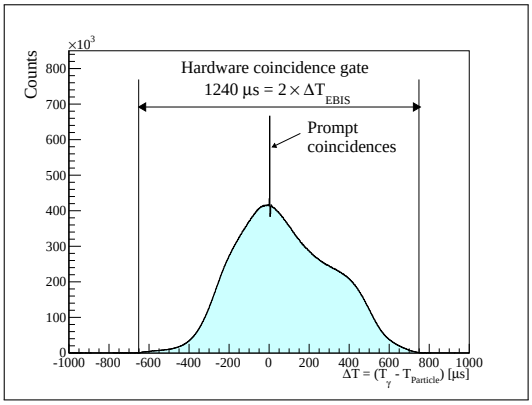

(a) Nb. of coincidences vs particle-γ time difference.

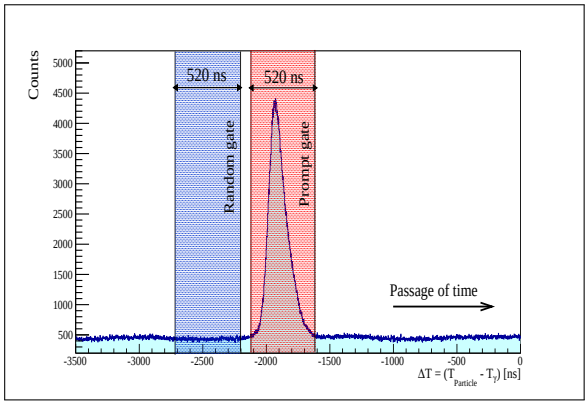

(b) Zoom on the prompt peak.

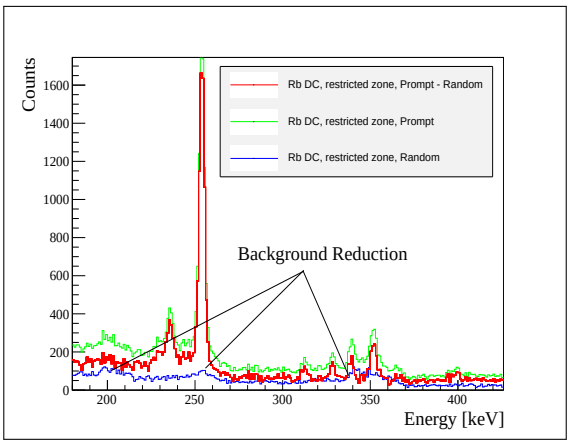

(c) (Prompt - Random) Subtraction

Figure 5.1: Prompt/Random Coincidences - Time difference particle-γ for ^{97}Rb (a) without any condition, (b) for the restricted kinematic zone; (c) Energy spectra of ^{95}Rb for the restricted kinematic zone defined later on the Fig.5.7(b) on page 110.

3.1 CD Detector Algorithm

To avoid an eventual "cross talk" in the particle events, an add-back algorithm has been implemented, consisting to apply the following considerations:

- the detecting element with the highest collected energy hit is considered as the interaction "point" (detectors where the particle enters inside the CD detector). Its coordinates (θ,ϕ) are taken into account for the correction of the Doppler effect
- the energy of the neighboring elements are added to the hit of highest energy

However, the quality of the Doppler correction was not improved significantly. The weak impact of this cross talk effect algorithm led to reject it from the analysis.

3.2 Cluster "add-back" Algorithm

For gamma energy, the gamma hit is considered occurring in the segment with the highest signal, and the energy collected inside the core is taken as the integration of energies inside the crystal, corresponding to the γ-rays. The segment position informations were used in the Doppler correction. The use of the standard

add-back algorithm for the Germanium detector has been investigated. The reduction of efficiency at low energies when using the application of the algorithm avoided the perspective to use it in the analysis, see Fig. 5.4 on page 106. The MINIBALL efficiency is treated in the Subsec. 4.4 on page 105.

3.3 γ-γ Coincidences

Finally, in order to identify γ-rays cascades and build the level scheme, γ-γ coincidences analysis were used. The Sec. 9 on page 117 is specially dedicated to the γ-γ matrices creation and treatment since it plays an important role to build the level scheme.

4 Germanium Detectors

4.1 The γ-ray Spectroscopy and Interactions

In order to detect the γ-ray transitions, they should interact with matter and deposit some energy inside. Usually the energy collection is done via the ionization of the neighboring atoms. The electromagnetic nature of the γ-rays confers them an important interaction with the electrons present in the matter. A part of the γ-ray energy can be transmitted partially or totally to the electron(s). A cascade of electrons can be created in such way. The collection of those electrons creates a certain current representative of the γ-ray energy.

Three major interactions, acting in the range of our experiments are described in the followings: the photoelectric effect, the Compton effect and the pair creation, see Ref. [177].
During a photoelectric event, the total energy of the photon is absorbed by the crystal.
In order to create an electron-positron pair, the physical system needs to have more energy than the electronic pair mass (> 1022 keV). The pair creation does not play an important role in the energy range of the present study.
The case of Compton effect is treated more in details in the followings.

4.1.1 Compton and Rayleigh Effects

The Compton effect is an inelastic scattering on an electron. A part of the γ-ray energy is transmitted to the electron via kinetic energy. The energy and momentum are conserved leading to:

$$h\nu = \frac{m_0 c^2 \alpha}{1 + \alpha(1 - \cos\theta)} \tag{5.1}$$

where: $\alpha = \frac{h\nu_{incident}}{m_{e^-}c^2}$, m_{e^-} is the electron mass, θ is the scattering angle between the incident direction and the scattering gamma, $h\nu$ is the energy of the scattering γ-ray.

For energies $\gtrsim$200 keV, the Compton effect starts to play an important role. According to the Klein-Nishina formula [178], the differential cross section can be expressed as:

$$\frac{d\sigma_e}{d\Omega} = \frac{r_{e^-}^2}{2} \frac{1}{[1 + \alpha(1 - \cos\theta)]^2} \left(1 + \cos^2\theta + \frac{\alpha^2(1 - \cos\theta)^2}{1 + \alpha(1 - \cos\theta)}\right) \tag{5.2}$$

The differential cross sections normalized at $\theta = 0$ is given in the Fig. 5.2 for different energies.

The Rayleigh effect may be considered as a specific case of the Compton effect. During the Rayleigh process the γ-ray is scattered as for the Compton. However the incident γ-ray does not transmit kinetic energy to the electron, thus $E_{\gamma,incident} = E_{\gamma,scattered}$.

The importance of the different main effects is summarized in the Fig. 5.3.

4.2 The Germanium: a Semiconductor

The Germanium detectors are p-n junctions, doped n or p, with a large depleted volume. When they are polarized by a high voltage an active zone appears. Thermal or photon excitations can force the electron to pass in the band gap [2]. The following ionizations create many electron-hole pairs. The charges thereby

2. ~ 0.77 eV for Germanium to get free electron)

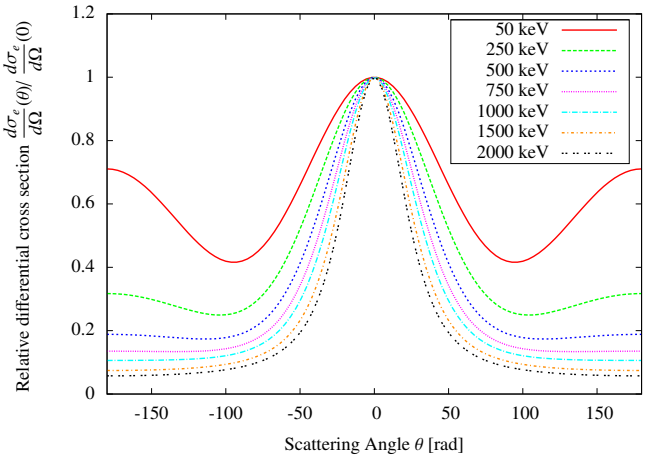

Figure 5.2: Relative differential cross section of Compton effect for different incident gamma energies.

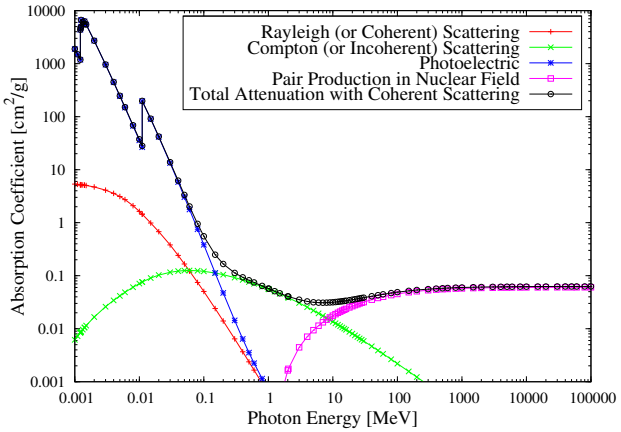

Figure 5.3: Absorption coefficient of Germanium (Z=32) related to physics phenomenons. Calculated from Ref. [179]. In the range of the low γ-ray energies in our experiment, the photoelectric effect, coherent scattering and Compton scattering are competing. At high energies ($\gtrsim$ 1 MeV), most of the γ-rays are scattered in a small solid angle. In contrary, at low energy ($\lesssim$ few keV), the γ-rays are also scattered in large angle. The materialization of electron and positron from a γ-ray starts to compete with the Compton effect at around 8 MeV.

created can be collected. The number of collected charges is proportional to the original energy of the excitation: Eγ $\simeq$kN (According to the Ref. [177], k$\sim$2.96 eV). The collected charges are then transformed in an electrical impulse sent to the DAQ.

In order to limit the thermal excitation, considered as noise in nuclear structure studies, the Germanium detectors are maintained at low temperature with a liquid nitrogen cryostat.

4.3 Energy Calibration of Germanium Detectors

The energy calibration of Ge detector has been performed using an (^{152}Eu,^{133}Ba) source. The characteristic γ-ray transition energies of the sources used during the calibration can be found in the Ref. [180].
Firstly, the segments are roughly calibrated on the same channel for the on-line analysis.Secondly, each segment is calibrated on the energy corresponding to the sources, see Fig. 5.4. Finally, the calibration of each detecting element is checked manually one-by-one in order to correct the set of calibration values. A linear calibration has been envisaged in a first approach. However the non-linearity of the Germanium response directed our final choice on a quadratic calibration.

4.4 MINIBALL Array Efficiency

The efficiency has been determined using ^{152}Eu ($T_{\frac{1}{2}}$ =13.537(*6*) y), ^{133}Ba ($T_{\frac{1}{2}}$ =10.51(*5*) y) and ^{60}Co ($T_{\frac{1}{2}}$ =1925.28(*14*) d) sources, placed at the target position.
Knowing the activities of the sources at a certain time, the number of awaited gammas can be estimated. The ratio of ^{152}Eu transitions allows us to determine the relative efficiency for different energies over an important range from 80 keV to 1500 keV. The absolute efficiency has been determined using the ^{60}Co source with a peak at 1332.492(4) keV ($I_{\gamma}^{abs.}$ = 99.9826(*6*) %). According to the efficiency found for the Cobalt peak a normalization factor can be applied to the ^{152}Eu relative efficiency found in order to obtain the absolute efficiency for the whole energy range. Note that most of the γ-transitions in our experiments are $\sim$ 40-600 keV.
As mentioned, an addback algorithm could be employed. The addback has a beneficial impact on the efficiency at high energies (> 600 keV). The most important informations extracted from different Coulomb excitations performed are at low γ-ray energies, where the addback could reduce the efficiency. Thus, it had not been employed in the analysis.

The efficiencies are expected with the following forms:

$$ln(\epsilon_{\gamma}) = \sum_{i=0}^{4} a_i(\ln(E_{\gamma}[keV])) \tag{5.3}$$

The following coefficients have been obtained:

	a_0	a_1	a_2	a_3	a_4
Without Addback	-2262	1530	-377	41	-1.6
With Addback	-1884	1268	-310	33	-1.3

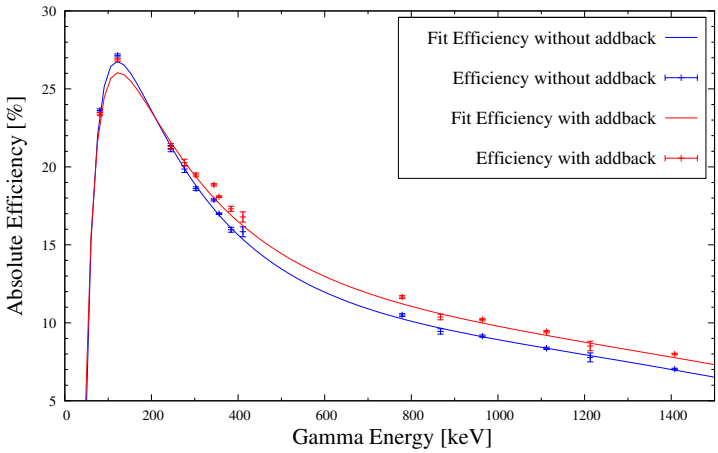

Figure 5.4: MINIBALL cluster efficiency performed for ^{152}Eu and ^{133}Ba sources.

The calibration points and efficiency curve of the Eq. 5.3 are shown in the Appendix B on the Fig. 5.4 on the next page. Absolute efficiencies of 20% and 10% are obtained respectively at 250 keV and 900 keV.

5 Doppler Correction

During a "standard" Coulomb excitation experiment, the excited beam and recoil nuclei emit their γ-rays mainly in flight. A Doppler shift is attached to such emission according to the respective particle motion and γ-ray energy and angle.
The energy detected in the laboratory frame is shifted and does not correspond to the characteristic gamma

energies observed in the intrinsic frame. In order to derive the original energy, Doppler corrections must be applied :

$$E_{lab} = \gamma \frac{E_{intr.}}{1 - \beta \cos(\theta)} \tag{5.4}$$

where: $\beta = \frac{v}{c} = \sqrt{1 - \frac{1}{\gamma^2}}$ is the velocity, E_{lab} is the γ-ray energy detected in the laboratory frame, $E_{intr.}$ the γ-ray energy in the intrinsic frame and $\gamma = \frac{1}{\sqrt{1-\beta^2}}$ is the relativistic factor. Thanks to the CD detector, the determination of the kinetic energy and position of the particle is possible. Correlating γ-rays and particle hits via the time difference $T_{particle-\gamma}$, Doppler corrections can be performed. All the couples γ-particle entering inside the prompt and random gate are Doppler corrected constituting the Doppler corrected spectra, see Sec. 3 on page 101.

The calculation used to extract the angle between the emitted γ-ray and particle is:

$$\theta = \arccos\left[\sin(\theta_{Part.})\sin(\theta_\gamma)\cos(\phi_{Part.} - \phi_\gamma) + \cos(\theta_{Part.})\cos(\theta_\gamma)\right] \tag{5.5}$$

To summarize the correction of the Doppler effect is possible knowing the energy and position of both particle and γ-ray hits.

6 Germanium Detector Positioning

The Germanium detectors are mounted on rotative arms allowing to change the distance cluster-chamber and the angles (θ_{lab}, ϕ_{lab}, α), see Fig. 5.5 on the next page. The couple (θ, ϕ) denotes the position of the central axis of the cluster and α corresponds to the rotation of the cluster around its "symmetry" axis. Thanks to indicating rulers on the arms the mechanical positions of Germanium detectors are roughly known.
To refine the Germanium detectors positioning, a transfer reaction $^2H\left(^{22}Ne,\ ^{23}Ne\right)p$ has been used due to firstly the disponibility at anytime of ^{22}Ne from REX-EBIS (rest gas) and secondly the kinematic and decay properties of this reaction. The reaction is performed sending a ^{22}Ne beam at 2.25 MeV/u on a Deuterium polyethylene target.
During the transfer reaction the first $\frac{1}{2}^+$ excited state at 1017 keV of ^{23}Ne can be populated. The short lifetime 178*(10)* ps of the first excited level insures a de-excitation "in-flight"($\frac{1}{2}^+ \rightarrow \frac{5}{2}^+$ $(g.s.)$) leading to proper Doppler corrections. The optimization of the position is done by the convolution of :

- the minimization of the FWHM (Full Width Half Maximum), i.e. Doppler correction optimization.
- the relative position of "segments-core" peaks (relative shifts to each other).

The ^{23}Ne products cannot be detected by the CD detectors. The reaction allows a maximum scattering angle of 4.3°. The ^{23}Ne were assumed to be ejected along the beamline ($\theta = 0$, $\phi = 0$), thus the angle between the excited particle and the γ-ray corresponds to the γ-ray detected angle in the laboratory frame. Moreover, the proton reaching the CD detector can be used for the Doppler corrections via its angle and energy.
During the optimization of the Doppler corrections, an additional tunable parameter corresponding to the distance between the detecting element and the target could be added in the optimization loop.

The MINIBALL angles obtained after the positioning treatment are summarized in Appendix B p. 212.

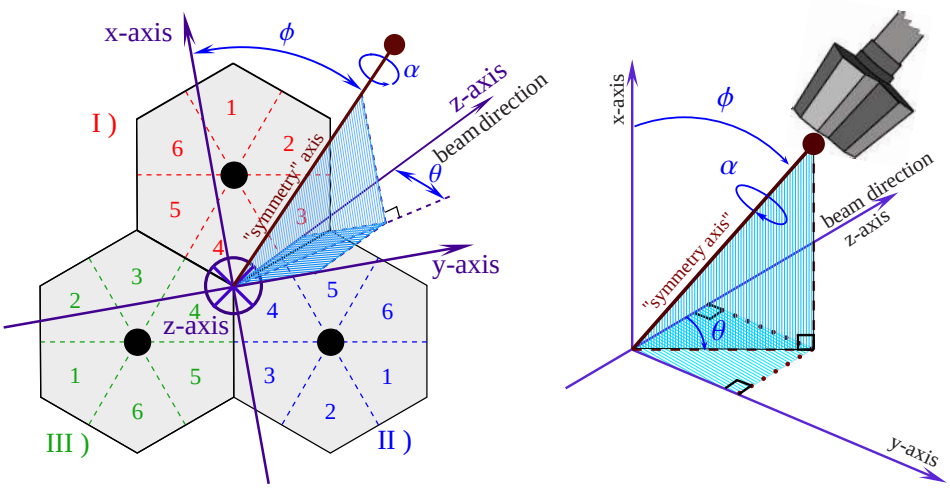

Figure 5.5: MINIBALL reference position system of clusters. The couple (θ, ϕ) are the angular position of the central axis of the cluster and α corresponds to the rotation of the cluster around its "symmetry" axis.

7 Particle Detectors

7.1 Centering of the beam

The CD detector has to be well centered with respect to the beam. Otherwise, the cylindrical symmetry is broken and the angles deduced for the detectors will be erroneous. Moreover, the Doppler correction and the matrix elements will be affected. Indeed, the angles will change but also the angular coverage used to extract and integrate the matrix elements. The dependency of the azimuth angle with the scattering angle would need to be introduced in all the analysis process.

The target and CD detector are fixed on the reaction chamber. Due to the compact geometry of the setup, the influence of the positioning of each device could be potentially important. However, the mechanical conception of the chamber ensures a sufficient precision to neglect the mechanical errors (at most 0.5 mm) introduced with the positions of each device in the vacuum chamber.

The vacuum chamber and target have been geometrically positioned with laser tripod positioning system. Therefore, the main contribution of a possible offset should come from the beam deviation.

The Fig. 5.6 represents the number of particles detected in the CD detector in polar coordinates for the Coulomb excitation reaction of ^{93,95,97,99}Rb with the ^{60}Ni target. The beam and the CD detector are well centered along the beam axis for ^{93,95,97,99}Rb. The low beam intensity obtained for the ^{99}Rb led to a low statistics collection. Thus, a high binning has been applied on the Fig.5.6(d) in order to distinguish a feature. We can only confirm that the beam is not deviated significantly to be observed.Some annular and sectorial strips were damaged or broken and removed from the analysis treatment. They are visible on the Fig. 5.6(c) for which one recorded a consequent amount of data compared for the other studied nuclei.
The resulting angles of the CD detector are summarized in the Tab. 5.1 on the facing page.

7.2 Energy Calibrations

The difference phases to obtain a proper calibration are presented by order of application in the followings.

7.2.1 α Source Pre-Calibration

A preliminary calibration of the annular strips can be performed to obtain a rough on-line calibration used during the experiment. It consists in a triple alpha source of ^{239}Pu, ^{241}Am and ^{244}Cm, with alpha energies of 5.156 MeV, 5.486 MeV, and 5.805 MeV. This is the easiest way to calibrate the annular strips thanks to its "offline" implementation. However, in our experiment, the energy range of the alphas is far from the kinetic energy of the beam particles ($\sim$ 270 MeV). Thus, the alpha sources are not the best candidates to

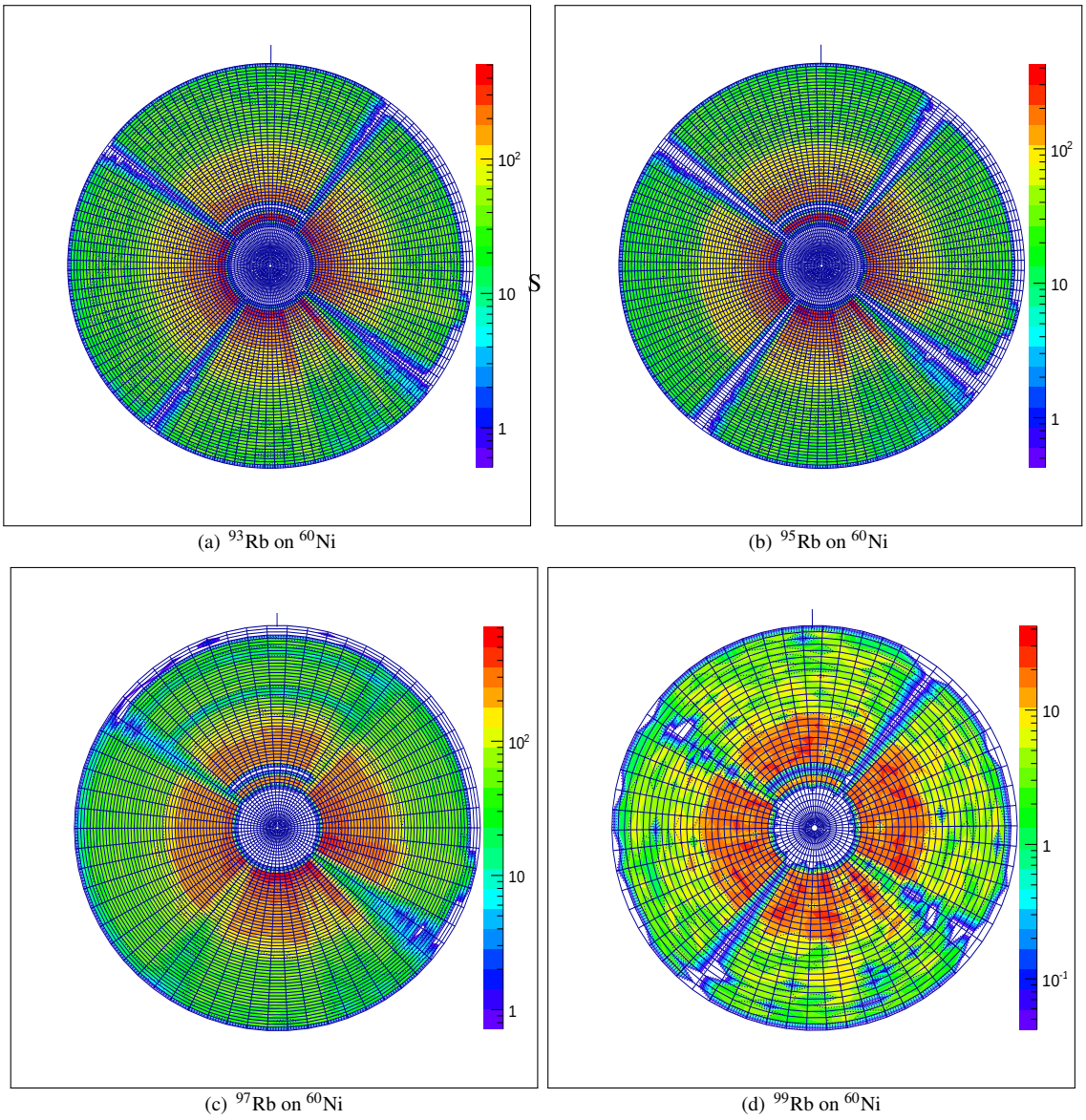

(a) ^{93}Rb on ^{60}Ni (b) ^{95}Rb on ^{60}Ni

(c) ^{97}Rb on ^{60}Ni (d) ^{99}Rb on ^{60}Ni

Figure 5.6: Centering of the particle detector and beam. Some annular and sectorial strips were damaged or broken. In case of damage they produced a low signal which could affect the statistics. To be rid of this problem those detecting elements were removed during the analysis.
(a) The ^{93}Rb radioactive beam on ^{60}Ni. The beam and CD detector are well centered;
(b) The ^{95}Rb radioactive beam on ^{60}Ni. The beam and CD detector are well centered;
(c) The ^{97}Rb radioactive beam on ^{60}Ni. The beam and CD detector are relatively well centered; and
(d) The ^{99}Rb radioactive beam on ^{60}Ni. The beam and CD detector are well centered. The low binning applied due to the low statistics has the tendency to shade off the contours.

finely calibrate the CD detector, and then, other methods presented in the followings has been employed to properly calibrate the CD detector.

7.2.2 A/q=4 Cocktail Beam Calibration

In order to refine the pre-calibration, we used a cocktail beam available at anytime from REX-EBIS (presence of residual nuclei $^{12}C^{3+}$, $^{16}O^{4+}$, $^{20}Ne^{5+}$, $^{40}Ar^{10+}$, $^{84}Kr^{21+}$ with a parametrization of A/q=4) scattered on a ^{196}Pt target (2.0 mg/cm^2). The known kinematic properties of the cocktail beam were used to calibrate the CD detector.

Stopping power and kinematic calculations have been done, with the SRIM and LISE packages, for each nucleus of the cocktail beam taking into account the beam velocity of each before and after the target according to their scattering angle. The same calculations have been realized for the Rb isotopes. The particles are not able to reach the E detector which is a PAD detector positioned behind the CD detector, see Subsec. 8.2 on page 115. It confirms that they are stopped in the ΔE-detector. Thus, just the calibration of the ΔE detector (CD) is necessary.

Annular Strip	$<\theta>$[degree]	θ_{min}[degree]	θ_{max}[degree]
Strip 0	53.7	53.0	54.3
Strip 1	52.3	51.6	53.0
Strip 2	50.8	50.0	51.5
Strip 3	49.1	48.	49.9
Strip 4	47.4	46.6	48.3
Strip 5	45.6	44.7	46.5
Strip 6	43.6	42.6	44.6
Strip 7	41.5	40.4	42.5
Strip 8	39.2	38.1	40.3
Strip 9	36.8	35.6	38.0
Strip 10	34.2	32.9	35.5
Strip 11	31.5	30.1	32.8
Strip 12	28.5	27.1	30.0
Strip 13	25.4	23.9	27.0
Strip 14	22.2	20.6	23.8
Strip 15	18.8	17.1	20.4

Table 5.1: Angles of each different strip constituting the ΔE particle detector.

We performed kinematic calculations with the LISE++ package, see Ref. [181], in order to evaluate the deposited energy inside each detecting element of the CD, for each nucleus constituting the cocktail beam. The energy and θ-angle after the scattering reaction are relatively well known. The couple ($E_{kinetic}$ vs θ) are summarized in the Tab. B.6 on page 214 in Appendix.

Each annular strip and sectorial strip were firstly aligned by quadrants on the same channel. Then, they were calibrated in order to obtain the same values as given by the kinematic calculation realized via LISE++, see Tab. B.6 on page 214.

The calibration obtained by fitting with the LISE ++ calculations (A/q=4 beam particles) does not constitute the best set of calibration parameters considering the width of the Doppler corrections.The obtained calibration coefficients are applied on Rb data, a gain shift has been observed and the coefficients have to be corrected.

7.2.3 Rb Data Calibration

Finally, the calibration coefficients obtained from the "A/q=4 calibration" are refined directly with the ^{A}Rb(^{60}Ni,^{60}Ni)^{A}Rb data by optimizing the Doppler correction of each annular strip (^{60}Ni target thinckness 2.1 mg/cm^2). The final calibration performed for the ^{93}Rb is shown on the Fig. 5.7(a).

The obtained kinematics has been fitted by LISE++ kinematics calculations with the incident beam energy as free parameter, see Fig. 5.7(a). The set of calibration are well reproduced around $E_{beam} \sim 180-200$ MeV. Firstly this result was considered as inconsistent due to a largely lower beam energy compared to the REX-ISOLDE settings for which a beam energy of around ~274 MeV is found.

From the last calculations, the Doppler corrections are optimized for an incident beam energy of around ~180-200 MeV, which is lower than the experimental value of the beam energy ~ 2.85 MeV/u. Firstly, this result was considered as inconsistent. Further investigations have been performed as the minimization of

the FWHM [3] with the couple (ϕ_{CD}, $E_{beam}^{incidente}$), see Subsec. 7.3 on the facing page. This difference can be partially explained by the energy loss in the target.

The excitation and de-excitation processes have different time range. Indeed the excitation is a quick process of around 10^{-20} s and the de-excitation around 10^{-12} s. Thus, the excitation is supposed to occur in the target. However, with such considerations the γ-rays are mainly emitted after the target (or at the end) with an important beam energy loss. This scenario explains the lowering of the beam energy used to obtained the best Doppler corrections. The latter energy does not correspond to the kinetic energy at the excitation point (in the target) but the kinetic energy of the nucleus when the γ de-excitation occurs.

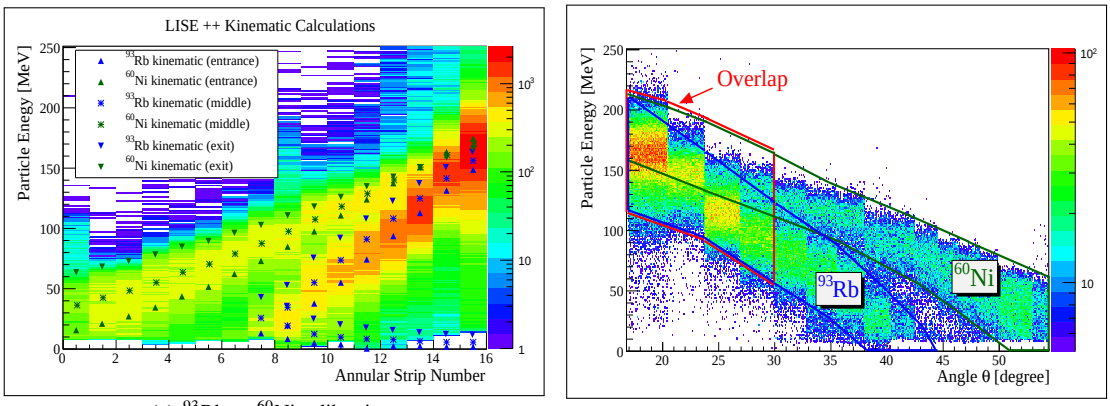

(a) ^{93}Rb on ^{60}Ni calibration.

(b) Identification of the restricted kinematic zone.

Figure 5.7: Calibration obtained for the reaction ^{93}Rb on ^{60}Ni target.
(a) The final calibration of the CD detector is shown. The results obtained with LISE ++ for an incident beam energy of 180 MeV are shown for different depths of interaction (entrance, middle and exit of the target);
(b) The Coulomb excitation of ^{93,95,97,99}Rb isotopes on ^{60}Ni leads to a kinematic overlap, not allowing the identification of the particle nature. A restricted kinematic zone can be defined for the detection of target nuclei for which there is no overlap. The restricted kinematic zone corresponds to the total target kinematic (observed in the CD detector) minus the overlap part.

7.2.4 Doppler Correction, Calibration and Beam Velocity

The particle energy and angle informations will be used to determine the velocity of the in-flight decaying nucleus and thus the expected Doppler correction.

During the collision, the profile of the beam phase space is not perfect, and spacial and velocity dispersions are present (the phase space is not punctual). In addition, the beam passing through the target is submitted to the stopping power of the target matter. An angular ($\Delta\theta$) and velocity ($\Delta\beta$) dispersion needs to be associated to such path.

The resulting Doppler-corrected spectra quality depends highly on the CD calibration (energy and position). Indeed even if the Germanium detector energy and position calibrations were done properly, the CD detector resolution is the predominant factor for high quality Doppler corrections.

The resulting kinematics of Rb isotopes on ^{60}Ni have an overlap at low $\theta_{Lab.}$. The identification of the particle nature in the CD detector is not possible in this region. Under this condition, the type of Doppler correction is uncertain. The Doppler correction applied on the projectile or target nuclei without knowing the particle nature would enlarge the width of the peak. Thus, a specific kinematic zone without any overlap has been used to integrate the γ-ray intensities, see Fig. 5.7(b).

3. Full Width Half Maximum of the energy peaks

7.3 CD Azimuth Angle Optimization

In order to perform the possible best Doppler shift correction, a position calibration of the CD-detector in the MINIBALL target chamber has been done. If the polar angle θ_{CD} of the annular strip is well known, nevertheless the azimuth angle is determined within a constant, and the sectorial segments can be rotated around the beam axis.
A nominal value of the azimuth angle ϕ_{CD} is obtained by measuring the angle manually inside the secondary target chamber. To determine the offset angle $\Delta\phi_{CD}$ of the CD detector, an optimization of the energy resolution has been performed with the reactions ^{A}Rb(^{60}Ni,^{60}Ni)^{A}Rb. It consists in the minimization of the FWHM of the energy peak with the $\Delta\phi_{CD}$.
The Coulomb excitation kinematics, with the following reaction ^{A}X($^{A'}$Y,$^{A'}$Y$^{(*)}$)^{A}X$^{(*)}$, is close to the Rutherford scattering. In a first approach, the Rutherford scattering can be considered as the kinematics of a Coulomb excitation reaction. If the nature of the particle is clearly distinguishable, the reconstruction of the kinematic products can be performed.

The reconstruction of the kinematics has been performed for the restricted kinematic area, see Fig. 5.8. The Rutherford scattering has been used to optimize the offset angle $\Delta\phi_{CD}$ of the CD detector and the average beam energy. As mentioned the beam energy should correspond to the incident beam energy averaged by the stopping power of the target. The restricted kinematic zone corresponds to high θ angle, then high deposited energy in the target. Logically, a lower "incident beam energy" compared to the LISE++ calculations should be found for this optimization.
According to the target thickness (2.5 μm) and the incident beam energy (23 μm/s) the beam time to pass through the target is around $\simeq$ 0.1 ps, thus more than 90 % of the γ-rays are emitted after the target (the typical lifetimes of the nuclear states should be around a few ps).
The minimization for ^{93,97}Rb(^{60}Ni,^{60}Ni)^{93,97}Rb reactions are shown on the Fig. 5.9, 7.3.

The minimization process for ^{93}Rb on ^{60}Ni converges to the solution: $\Delta\phi_{CD}$ = 5°, $E_{beam}^{incidente}$=170-130 MeV. For this reaction the FWHM is sensitive to both parameters.
Concerning the ^{97}Rb on ^{60}Ni reaction, the minimization process converges to the solution: $\Delta\phi_{CD}$ = 5°, $E_{beam}^{incidente}$=170-130 MeV. However, the optimization is less sensitive to the energy. The 103 keV transition (of a low lying state) should have a longer lifetime compare to the transitions shown for the ^{93}Rb on ^{60}Ni reaction, and, it can explain the lower sensitivity to the energy.

Considering the restricted kinematic events, the amount of γ-ray transitions observed corresponds to the same set of excitation process for the beam/target particles. Thus, a proper extraction of matrix elements from the intensities of the reconstructed spectra can be obtained.

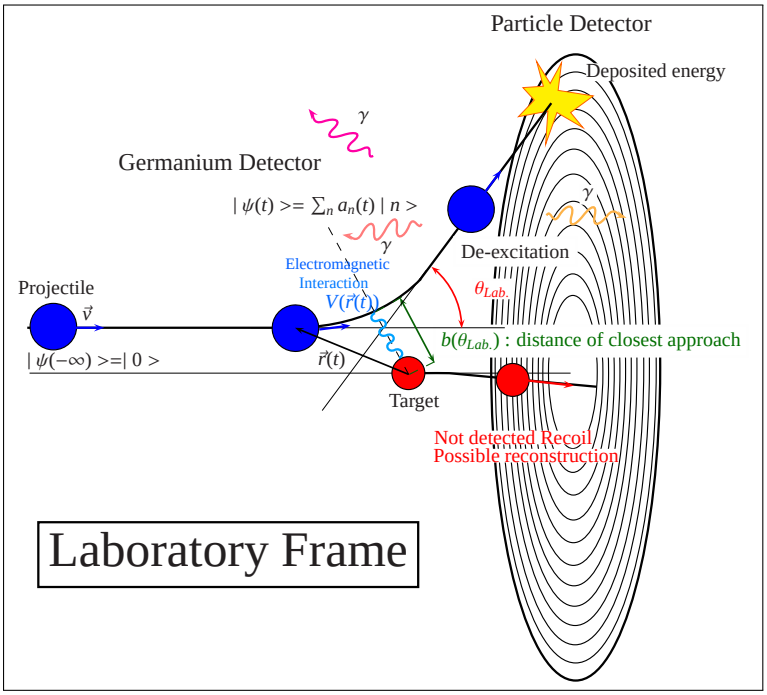

Figure 5.8: Coulomb excitation kinematics in the laboratory frame. When one of the particle (target/ejectile) is detected, the other one can be reconstructed following the Rutherford scattering, close to the Coulomb excitation kinematics. On the picture, the ejectile is detected.
In our case, inside the restricted kinematic zone the target scattering angle is detected. The target energy, ejectile energy and scattering angle are deduced from the Rutherford scattering.

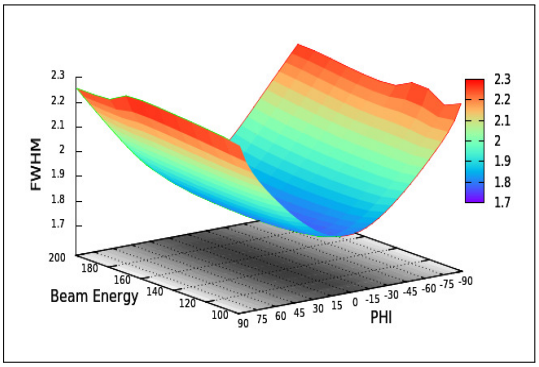

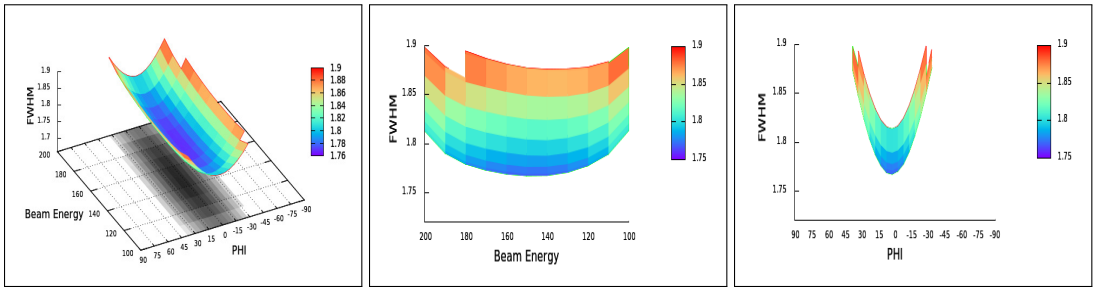

Figure 5.9: CD azimuth angle and beam energy optimization of ^{97}Rb on ^{60}Ni for the transition 103 keV.

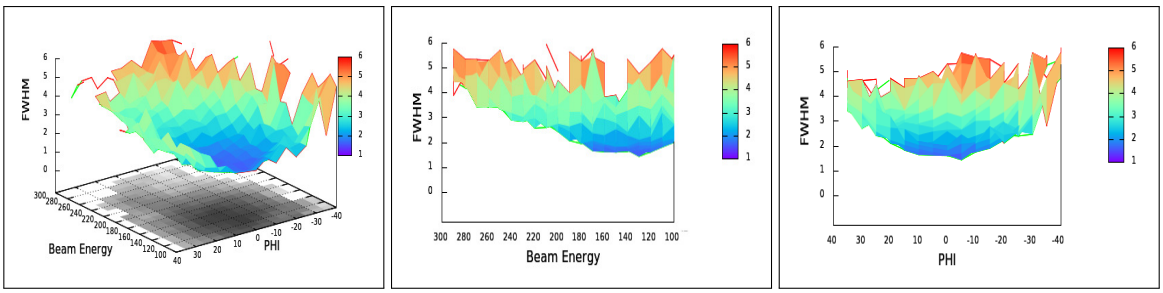

(a) ^{93}Rb on ^{60}Ni for the transition 324 keV.

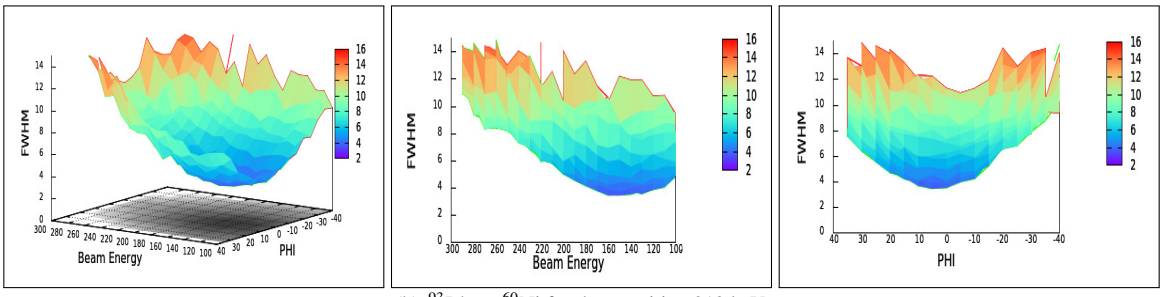

(b) ^{93}Rb on ^{60}Ni for the transition 913 keV.

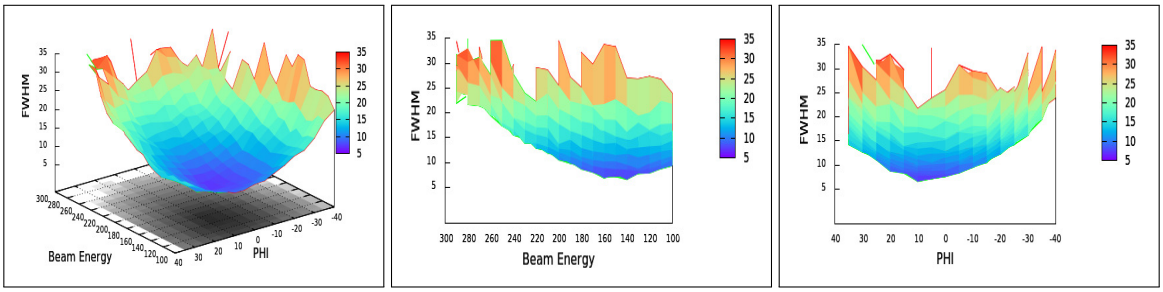

(c) ^{93}Rb on ^{60}Ni for the transition 1332 keV.

Figure 5.10: CD azimuth angle and beam energy optimization for ^{93}Rb on ^{60}Ni (low statistics).

8 Kinematic and "Safe" Coulomb Excitation Considerations

From the optimization of the Doppler corrections, the obtained beam energy corresponds to the average projectiles energy at the target exit (for the chosen angular coverage). The possible Coulomb excitation should occur inside the target, thus for a higher projectile energy than the one found for the optimization. The following section treats the different kinematics using the average energy of the incident beam assuming that the excitation occured at the middle of the target.

8.1 "Safe" Coulomb Excitation and Coulomb Barrier

The Coulomb excitation process remains valid as long as the nuclear interaction is negligible compared to the electromagnetic interaction, i.e. under the Coulomb barrier energy:

$$E_{Coul.} = \frac{Z_{Target} Z_{Proj.} e^2}{R_{min.}} \quad \text{[MeV]} \tag{5.6}$$

with $e^2 = 1.44$ fm.MeV and $R_{min.}$ [fm] is the minimum distance between the target and the projectile which allows to neglect the strong interaction, see Ref. [182], see Tab. 5.2 and Chap.3 on page 55.
During the collision, the two nuclear surfaces should be distant by at least a "safe" distance Δ_{safe}. The distance of closest approach in the centre-of-mass (CM) based on a pure Rutherford scattering is given by:

$$b_{Coul.}(\theta) = a_0 \left(1 + \frac{1}{\sin\left(\frac{\theta_{CM}}{2}\right)} \right) \quad \text{[fm]} \tag{5.7}$$

where: $a_0 = 0.71999 \left(1 + \frac{A_{Proj.}}{A_{Target}} \right) \frac{Z_{Proj.} Z_{Target}}{E_{Proj.}}$ [fm], $E_{Proj.}$ in [MeV], see Ref. [113].

This condition can be expressed in terms of nuclear surfaces. The estimation of Δ_{safe} takes into account the nuclear force (a few fm) and the surface diffuseness of the nuclear density distribution, see Ref. [182, 183]. It can be determined by comparing theoretical and experimental cross sections for different beam energies, see Ref. [184]. Typical values for Δ_{safe} are found to be close to 5 fm, see Ref. [182, 183]. The minimum Δ according to the Ref. [182], is $\Delta = 3.2$ fm.

$$R_{min.} = R_{Proj.} + R_{Target} + \Delta \tag{5.8}$$

where, $R_{Proj./Target}$ can be calculated as: $R_i = 1.28 A_i^{\frac{1}{3}} - 0.76 + 0.8 A_i^{-\frac{1}{3}}$ (it exists different way to calculate the nuclear radius depending on the investigated region of the chart), see Ref. [182]; $R_{min.} = R_{min.}^{safe}$ if $\Delta = \Delta_{safe}$. The "safe" Coulomb excitation condition, see Ref. [185], is fulfilled if:

$$b(\theta) \geq R_{min.}^{safe} \tag{5.9}$$

According to the Ref. [113] p. 277, the maximum available energy is:

$$E_{Lab.}^{max} = \frac{Z_1 Z_2 \left(1 + \frac{A_{Proj.}}{A_{Target}} \right) e^2}{A_1^{\frac{1}{3}} + A_2^{\frac{1}{3}} + 2} \quad \text{[MeV]} \tag{5.10}$$

According to the calculations realized with the approximations of the Ref. [113], our experimental conditions would be too close to the Coulomb Barrier, see Fig. 5.11. However, other more realistic calculations, like LISE++ calculations in Tab. 5.2, place them in a "safe" Coulomb excitation case.
For example, the maximum available energy is around 265 MeV for the ^{93}Rb, the maximum energy to consider the excitation as "safe" is of around 264 MeV according to the LISE++ calculations. However, such calculations does not take into account the energy lost in the target, placing the different configurations in the "safe" Coulomb excitation case.

The angles of the CD detector in the centre-of-mass framework are presented in the Tab. 5.3.

Isotope	$R_{min.}^{LISE}$ [fm] Ref. [185]	$R_{min}^{safe,LISE}$ [fm] Ref. [185]	$R_{min.}^{safe,pheno.}$ [fm] Ref. [113]	$E_{CM}^{max.,pheno.}$ [MeV] Ref. [185]	$E_{CM}^{max.,LISE}$ [MeV] Ref. [181]	$E_{Lab.}^{max.,pheno.}$ [MeV] Ref. [113]	$E_{Lab.}^{max.,LISE}$ [MeV] Ref. [181]
^{93}Rb	12.21	14.01	12.46	119.76	103.8	244	264.8
^{95}Rb	12.25	14.05	12.50	119.38	104.7	242.3	270.5
^{97}Rb	12.29	14.09	12.54	119	105.5	240.5	276.3
^{99}Rb	12.32	14.12	12.57	118.64	106.3	238.8	282.0

Table 5.2: Energies and distances for a "safe" Coulomb excitation. $R_{min.}^{LISE}$: minimum radius to feel the strong interaction at first order. $R_{min}^{safe,LISE}$: minimum radius for which the "safe" conditions are fulfilled. pheno: phenomenological calculations. LISE: calculations realized with the LISE++ package, see Ref. [181].

Projectile	Target	Energy [MeV/u]	θ_{CM1}	θ_{CM2}	θ_{CM3}	θ_{CM4}
^{93}Rb	^{60}Ni	2.85(3)	46.6	169.9	70.5	144.9
^{95}Rb	^{60}Ni	2.85(3)	47.2	169.2	70.9	144.6
^{97}Rb	^{60}Ni	2.85(3)	47.6	168.3	70.2	144.6
^{99}Rb	^{60}Ni	2.85(3)	48.1	168.0	70	144.3

Table 5.3: Kinematics of the different experiments, obtained from Ref. [181]. The energies and target used during the experimental analysis are shown. The centre-of-mass angles of the CD detector used to extract the informations of the scattered particles. θ_{CM1} and θ_{CM2} are the extreme angles of the CD related to Rb in the centre-of-mass frame. θ_{CM3} and θ_{CM4} are the extreme angles of the CD related to Ni in the centre-of-mass frame. With such beam energy the Sommerfeld parameter η fulfilled the "safe" conditions, $\eta \simeq 97 \gg 1$ (dependance in Z_p and Z_t).

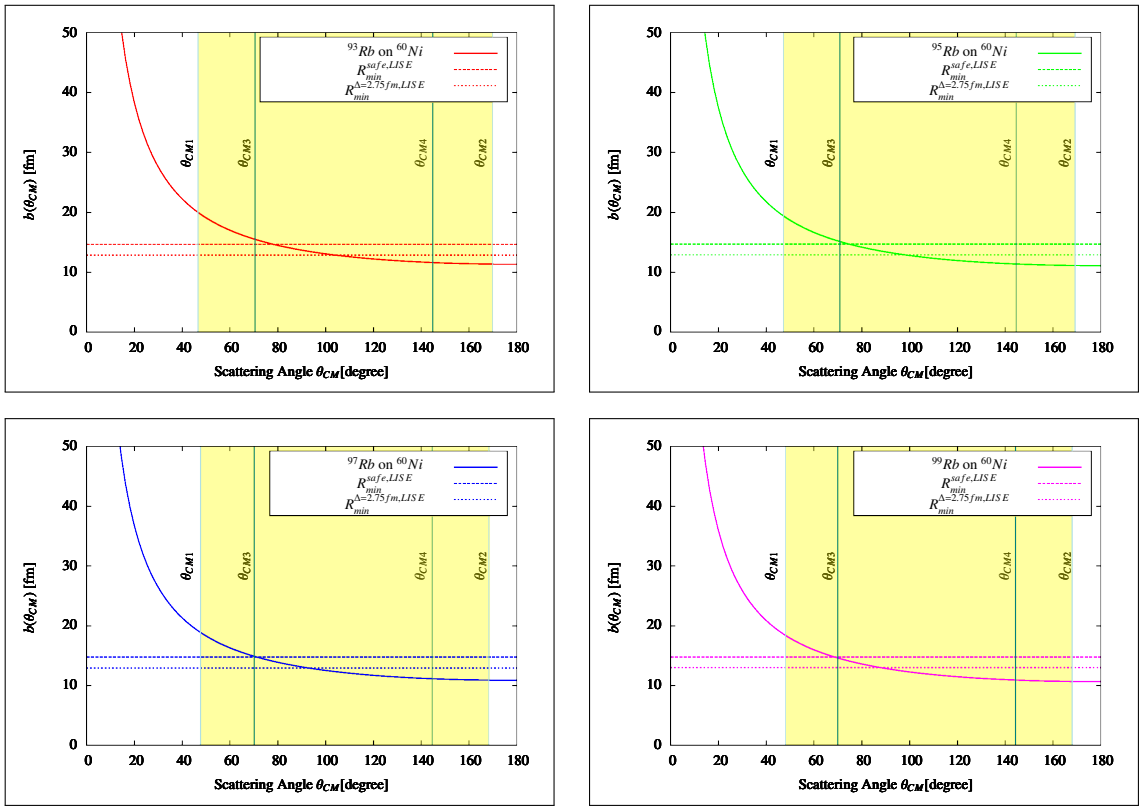

Figure 5.11: Distance of closest approach in the center-of-mass frame. The minimal distance for a "safe" Coulomb excitation R_{min}^{safe} is shown with the dashed line. The range of the CD detector is shown in yellow.

8.2 Kinematics and Scattered Nuclei Detection

In the Chap. 3 on page 55, we mentioned that the trajectories of the scattered particles could be treated classically. Thus, the point mechanics relations can be used. The conservation of the transverse momentum implies that, the projectile and target are scattered in opposite direction in the reaction plane.

The collision takes place with a Rb isotope on a ^{60}Ni target of 2.1 mg.cm^{-2} at around 2.85 MeV/u of incident energy. The velocity of the Rb isotopes is around 7.8 % of the light velocity so that the relativistic effects cannot be neglected when correcting the Doppler effect.

The Fig. 5.12 summarizes the parameters of the ^{93}Rb(^{60}Ni,^{60}Ni)^{93}Rb reaction. Those curves show that the projectile and target are not easy to distinguish for low scattering angle in the CD detector (overlap).

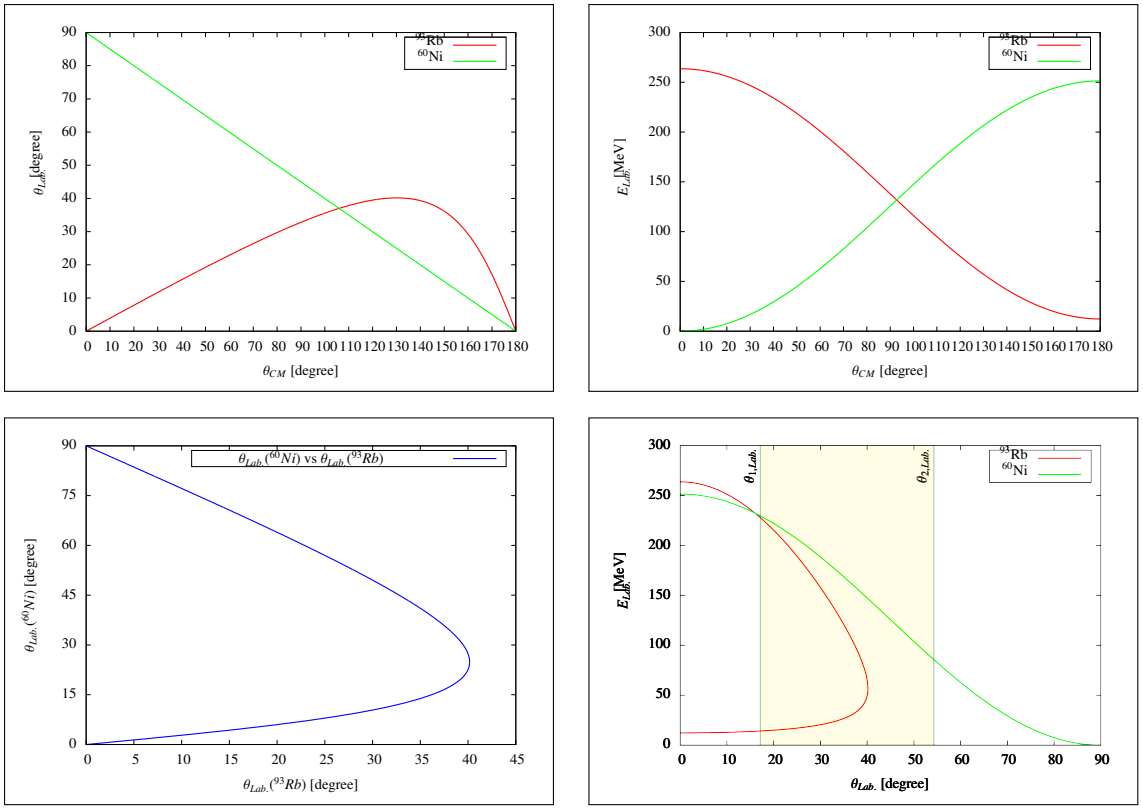

Figure 5.12: Kinematics of the reaction ^{93}Rb(^{60}Ni,^{60}Ni)^{93}Rb. The energy deposited in the target and the kinematic have been calculated by the LISE package. The angles $\theta_{1,Lab.}$ and $\theta_{2,Lab.}$ correspond to the extreme angles of the CD detector. The yellow surface represents the angular coverage of the CD detector. The kinematics associated to the Rb and Ni are respectively drawn in red and green. At low θ angles there is an overlap of the projectile and target nuclei detection leading to an uncertain determination of the detected particle nature.

The detection of scattered particles is possible in good conditions if:

- The energy resolution is high enough to distinguish projectile and target nuclei. It should be sufficient to apply proper Doppler correction on the γ-ray energies.
- The particle detectors are able to work until a typical frequency of a few kHz, and support the amount of incoming particle.
- The granularity needs to be sufficient to determine the angle and the nature of the scattered particle (usually determined via the kinematics). The highest granularity of the particle detector will help to make Doppler corrections, however the γ-rays detector should also have an important granularity, since it is working by pairs. Indeed a precise determination of the angle between the γ-emitting particle and the γ-ray is the keystone for proper Doppler corrections.

The silicon detector used during the experiment is described in the Chap. 4 on page 73. The central hole on the CD detector let pass the particles scattered at low angles (higher cross section). They correspond to

low impact parameter with a low probability of electromagnetic excitation, see Chap. 3 on page 55.

The Tab. 5.4 presents the different results concerning the energy deposited in the target, see Ref. [186, 187]. In each case the deposited energy in the target is less than the energy transfered in the collision: after the target 33.0-35.3 μm of silicon are still necessary to stop the nucleus, which is less than the thickness of the CD detector silicone layer. Thus, the scattered nuclei are stopped in the CD detector, and they will be accumulated in the CD detector. Their radioactive nature will contribute to the background by their decays (β and γ decays).

Projectile	Target	Deposited Energy [MeV]	Angular Straggling [mrad]	Si Thickness to stop [μm]
^{93}Rb	^{60}Ni	34	6.8	33.1
^{95}Rb	^{60}Ni	34	6.6	33.8
^{97}Rb	^{60}Ni	34	6.5	34.5
^{99}Rb	^{60}Ni	34	6.3	35.2

Table 5.4: SRIM calculations, see Ref. [186, 187]. The simulation of the energy deposited in the ^{60}Ni target is less than the energy transfered during the collision. The angular straggling is around 6.3-6.8 mrad, which is smaller than the smallest detecting element of the CD detector (1.3 °). The mean trajectory has been assumed straight without any scattering. In our experimental cases, the scattering imposes a higher deposited energy in the target and a slightly larger angular straggling.

9 The γ-γ Coincidences

9.1 Why γ-γ Matrices?

The investigation of low excited states from a totally new level scheme requests a tool to be able to identify and build the different γ-rays cascades. If during the de-excitation process, the γ-rays from the same cascade can be detected in different detectors at the same time, they are qualified as "coincident" γ-rays. A coincidence time gate between 2 γ-rays can be defined and applied to identify coincident γ-rays thus nuclear transitions. However, the detection chains have a timestamp of 25 ns and several other delays are engendered before the treatment of the signal.

The projections of the γ-γ matrices insure the identification of coincident γ-ray transitions. An example of γ-γ matrix and projections are shown on Fig. 5.13. The process is repeated for different transition energies until obtaining a consistent result (level scheme).

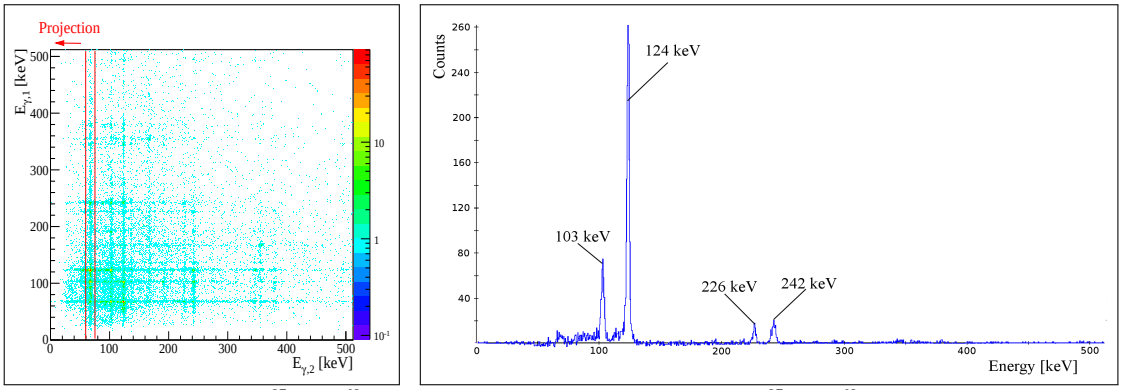

(a) γ-γ matrix of the reaction ^{97}Rb on ^{60}Ni.

(b) Gate of γ-γ matrix of the reaction ^{97}Rb on ^{60}Ni for the transition 68 keV.

Figure 5.13: Treatment of the γ-γ matrix of the reaction ^{97}Rb on ^{60}Ni. The γ-γ matrix is symmetrized thus the x-axis and y-axis are equivalent.

9.2 How to Choose the Coincidence Gate?

The coincidence gate should be as short as possible to optimize the ratio $\frac{N^{\gamma}_{\text{true coincidence}}}{N^{\gamma}_{\text{random coincidence}}}$.
The best correlation time gate has been found studying the amount of prompt coinciding γ-rays as a function of the width of the time window. The Fig. 5.14 shows the characteristic behavior for ^{99}Rb. As expected the amount of coincidences increase when opening the time window. After a certain time, the increase saturates characterizing the time for which afterwards the coincidence are just random.
From those results, a 250 ns coincidence has been adopted for all the γ-γ matrices.

9.3 Compton suppression

The Compton scattering impacts directly the identification of γ-ray transition energies creating events with lower energies than the γ-ray (photo-electric). The Compton events can overlap the photo-electric events in terms of energy.
The rejection of such event is usually done using detection materials surrounding the HPGE detector (called Compton suppressor), unfortunately the MINIBALL array does not possess such suppressors yet.
However, according to the Klein-Nishina formula, see Eq 5.2 on page 103 and Fig. 5.2 on page 104, an optimal angular coverage minimizing the Compton events can be found. The "labeled" Compton events can be subtracted from the whole set of coinciding events.

A simple rejection according to the angle between the two detected gammas was performed. An optimized rejection angle ($\sim 40°$) has been taken for a complementary analysis of the level schemes identification, see

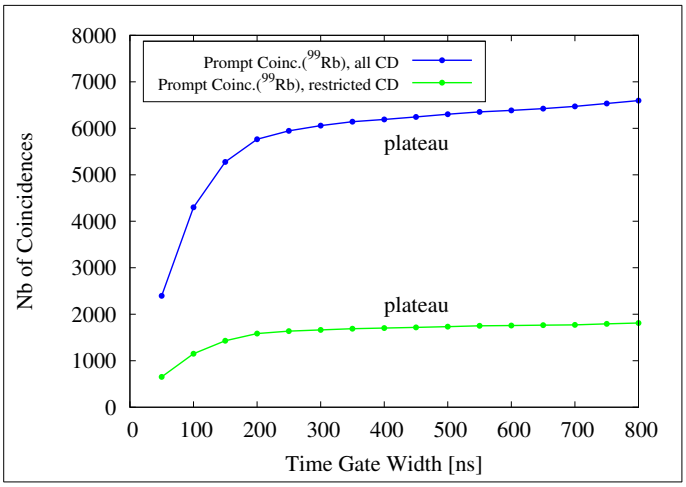

Figure 5.14: γ-γ coincidence gate for ^{99}Rb. The "all CD" label corresponds to the total angular coverage of the CD detector. The "restricted CD" label corresponds to the angular coverage of the CD detector for whom there is no overlap of the beam and target nuclei in the kinematics.

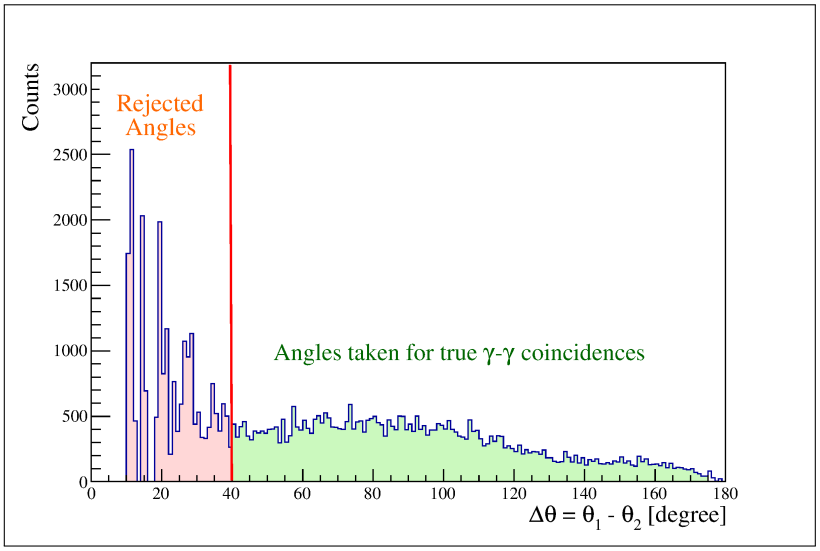

Figure 5.15: Compton rejection angle - The number of γ-γ coincidences is plotted versus the angle between the two detected γ-rays. According to the statistics, an angle of 40° has been adopted for the Compton rejection. It is lower than the minimum observed in the differential cross section of the Compton events, see Fig.5.2 on page 104.

Fig. 5.15.

An illustration of the obtained Compton suppression is presented on Fig. 5.16.

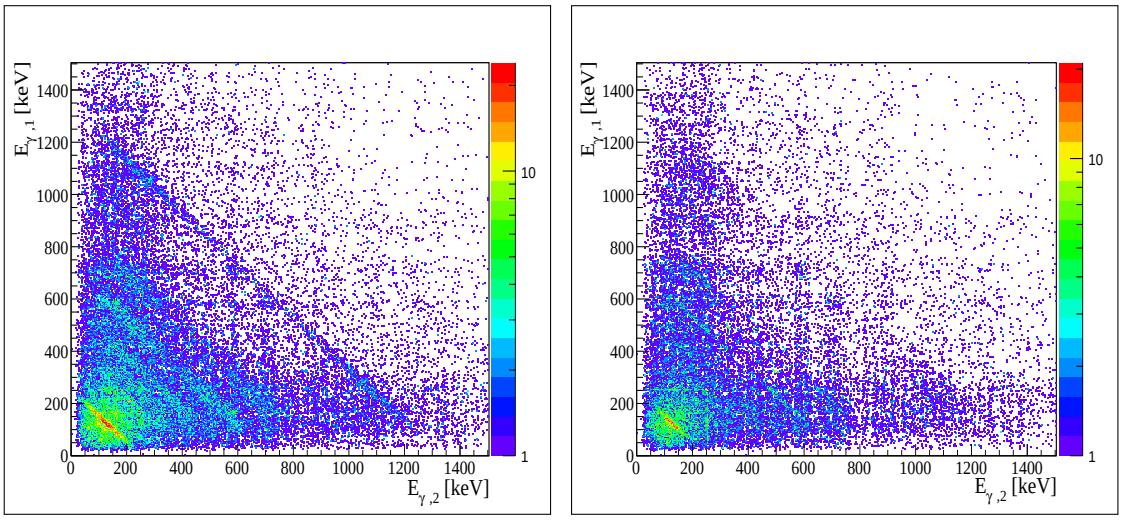

(a) Without Compton Suppression.

(b) With Compton Suppression, $\Delta\theta = \theta_1 - \theta_2$=40°.

Figure 5.16: Treatment of the Compton suppression. The γ-γ matrix of the reaction ^{93}Rb on ^{60}Ni for the restricted kinematic zone is presented without Compton suppression on Fig. (a) and with Compton suppression on Fig. (b).

10 Beam contaminations

In Coulomb excitation experiments the relative γ-ray intensities of the projectile and target nuclei constitutes the essence of the results. Thus, the determination of beam impurities/components appears like one of the main concerns of Coulomb excitation experiments with post-accelerated beam from an ISOL production.

10.1 Source of contaminants

As mentioned in the Chap. 4 on page 73, the beam delivered at ISOLDE via REX-ISOLDE is never pure. The reason comes from the nature of the production, transport and acceleration techniques. There are three main sources of contaminants coming between the ISOL production and the delivery at the experimental setup.

The first source comes from the ISOL production technique itself. During the proton impact on the primary target a multitude of nuclides are produced and the Rb isotopes of interest represent a very small fraction of the total yields. A first selection happens after the production thanks to the mass spectrometer HRS which leads ideally to have a single mass number beam. However, if the isobars are not well separated and isobaric contaminants can also be present.

The second source is related to the β-decaying nature of the beam, bringing the daughter nuclei along the transport, the beam manipulations and the beam decays "In-Flight".

The third source appears with the post acceleration technique. During the trapping and breeding processes, the best compromise between the Trapping/Breeding/Intensity has to be performed. Moreover, another important contaminant is the gas contained inside REX-TRAP and REX-EBIS which can be transmitted until the secondary target.

In certain cases the β-decay could be an advantage. Recently the production of ^{98}Sr has been performed via the decay in-trap of the ^{98}Rb parent. Setting the trapping time to optimize the proportion and the intensity of Sr, a Coulomb excitation has been successfully performed, see Ref. [188].

10.2 Beam components or beam Impurities

During the data analysis, several methods have been investigated to determine qualitatively and quantitatively the beam impurities. In the followings of this Subsec., the different techniques are presented but they don't represent the exhaustive list of possible techniques (for example, the laser system RILIS was not used and the impurities determination techniques related to it will not be discussed).

10.2.1 Ionization Chamber and T1 pulse

The ionization chamber consists in a ΔE gas volume and a silicon detector leading to an identification in mass number (A) and charge (q), see Sec. 4 on page 97. The energy deposited in the gas is proportional to $\frac{q^2}{A}$. q is the charge of the ion. A selection according to $q/A \cong 1/4$ is done through the transport. An analysis of the ionization chamber data is given in the Subsec. 11.1 on page 124.

The deposited energy (ΔE) can be correlated with the time difference between the proton impact and the detection in the ionization chamber, t=$T_{Ion.Chamb.}$-T1. This technique is used mainly to identify the stable and radioactive components with different mass number (A). The halflife must be of the order of the time between two proton pulses (~ 1.2 s).

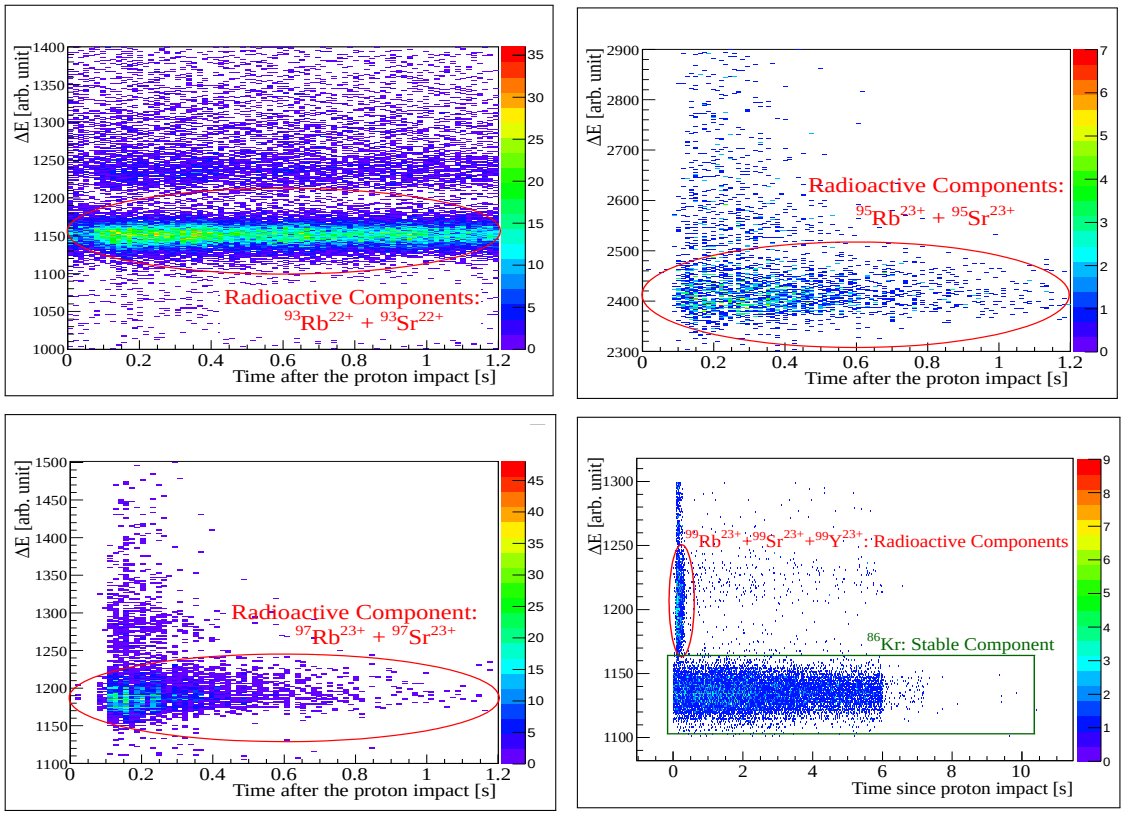

Figure 5.17: Correlation between the ΔE detector of the ionization chamber and the time since proton impact for the ^{93,95,97,99}Rb beams. The stable ^{86}Kr is well identified. However the radioactive components have the same mass number and it is difficult to identify them by the ΔE informations only. The release time of the different isotopes are not well known and are difficult to determine. To separate properly the different isotopes and quantify their amounts, the deconvolution of the release is necessary.

The release times of the different chemical elements are not well known and are difficult to determine. To separate properly the different isobars and quantify their amounts, the deconvolution of the release would be necessary. For this reason this technique did not give clear enough results to identify and quantify the radioactive components with the same mass (A).

The detection of nuclei correlated with the time after the proton impact has been used during the online setting of the radioactive beams to identify the radioactive/stable components for a specific mass (A).

The stable isotopes are easy to identify in our case. On the Fig. 5.17, the stable ^{86}Kr is well seen, however the radioactive components, coming from the β-decay of ^{99}Rb and its daughter nuclei: ^{99}Sr and ^{99}Y, cannot be separated. They have the same mass number and their ΔE signals are overlapping.The stable ^{86}Kr could come from the production from REX-EBIS.
The trapping and breeding time has been set in such a way to optimize of course the amount of Rb isotopes and minimize the amount of contaminants, see the technical report of F. Wenander [189].

10.2.2 CD detector

Since the transport (mass spectrometers, Nier-spectrometer, EBIS) is selective according to A/q, the number of possible contaminants is very restricted. Using the CD detector, the mass number (A) of the impinging nuclei may be deduced from the measured total energy correlated with the detection angle; thus, the contaminants amounts and their nature may be determined:

$$E_{CD} = \frac{1}{2} A u \beta^2 \tag{5.11}$$

where: E_{CD} is the collected energy by the CD detector in [MeV], A is the mass number, $\beta = \frac{v}{c}$, u is the atomic mass unit.
The energy lost in the target and the relative cross section can be taken into account in the kinematics.

During the Rb experiments, three different targets have been employed also for this purpose : ^{60}Ni, ^{120}Sn and ^{196}Pt. In our experiments, no contaminants have been identified after applying the time gates related to prompt gamma and the associated random windows. By using different targets, the angular cross sections change and the deposited energies in the target also. According to the deposited energy with different targets some contaminants could be identified (not in our case).

10.2.3 Beam dump

A coaxial Germanium detector is positioned next to the beam dump. The γ-rays and X-rays detected by it are used to identify the beam components and natural radioactivity present.

The coaxial Germanium detector of the beam dump has been calibrated with a ^{152}Eu source. The γ-rays coming from the source and the beam components were recorded at the same time.

As an example, the analysis of the beam dump detector is given for the ^{93}Rb beam, see Fig. 5.18 and Tab. 5.5. The expected result would be the presence of γ-rays from the radioactive decays of the Rb, Sr, and Y isotopes, and the X-rays from the species present in the shielding elements (concrete, lead pave, ...). If the beam is not pure, the amount of radioactive components could be estimated from the relative intensities of the observed γ-rays.
In all the cases of Rb radioactive beams, the main "contaminants" are the daughter nuclei. The other detected γ-rays comes from the Pb shield surrounding the devices.

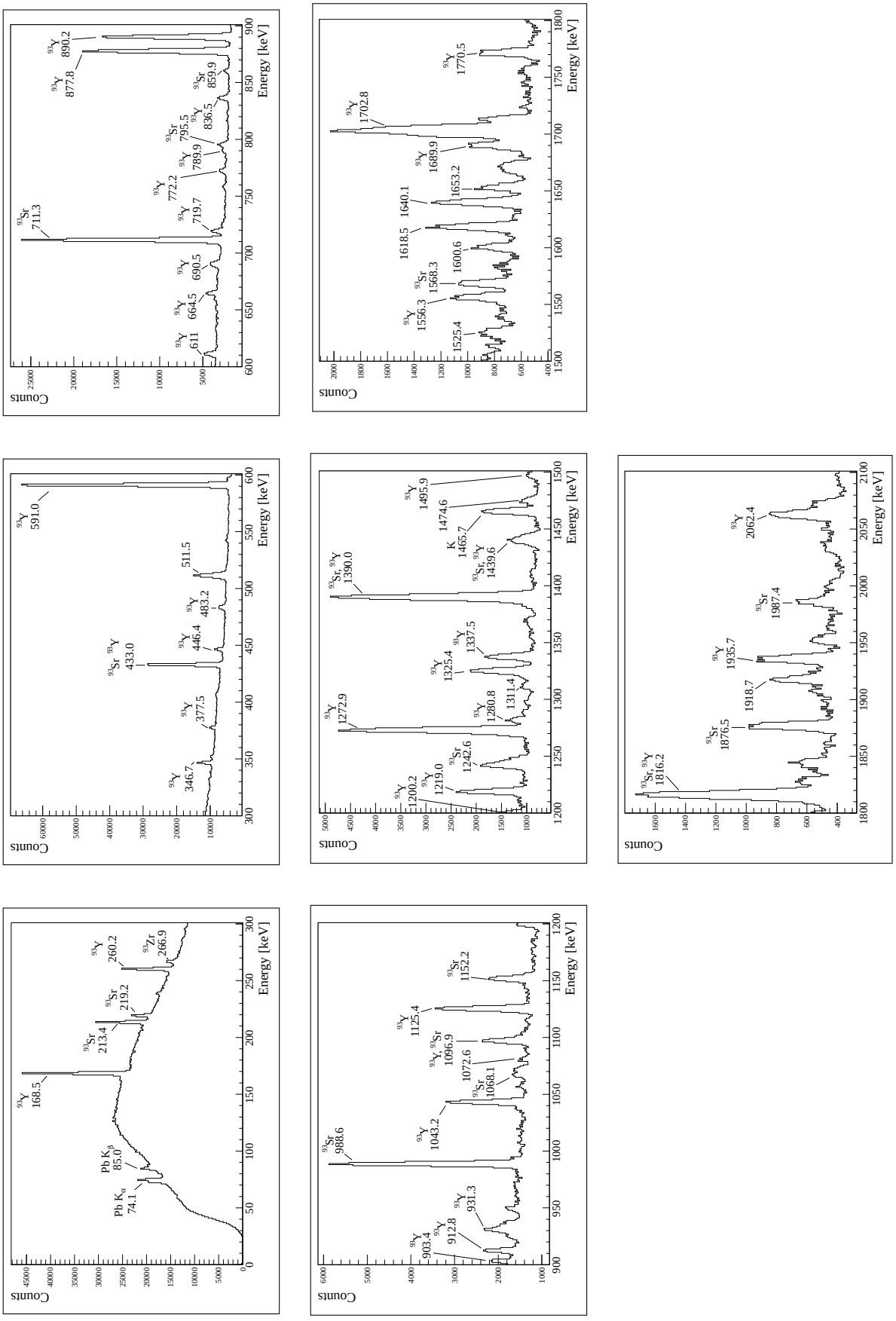

Figure 5.18: Beamdump Spectrum for ^{93}Rb radioactive beam. The presence of the β-decay daughter nuclei is well seen: ^{93}Sr, ^{93}Y and ^{93}Zr

E_γ [keV]	Associated Nuclide(s)
74.1	Pb K_α
85.0	Pb K_β
168.5	^{93}Y
213.4	^{93}Sr
219.2	^{93}Sr
260.2	^{93}Y(260.1 keV)
266.9	^{93}Zr(266.9 keV)
346.7	^{93}Y(346.4 keV)
377.5	^{93}Y(377.4 keV)
433.0	^{93}Sr(433.1 keV), ^{93}Y(432.7 keV)
446.4	^{93}Y(446.2 keV)
483.2	^{93}Y(482.0 keV)
511.5	From e^+/e^- pair annihilation
591.0	^{93}Y(591.2 keV)
611.0	^{93}Y(610.9 keV)
664.5	^{93}Y(663.6 keV)
690.5	^{93}Y(690.5 keV)
711.3	^{93}Sr(709.95 keV), ^{93}Y(710.3 keV)
719.7	^{93}Y(718.3 keV)
772.2	^{93}Y(771.2 keV)
789.9	^{93}Y(788.7 keV)
795.5	^{93}Sr(793.7 keV)
836.5	^{93}Y(834.5 keV)
877.8	^{93}Y(875.7 keV)
890.2	^{93}Y(888.1 keV)
903.4	^{93}Y(901.0 keV)
912.8	^{93}Y(910.2 keV)
931.3	^{93}Y(927.8 keV)
988.6	^{93}Sr(986.0 keV)
1043.2	^{93}Y(1040.6 keV)
1068.1	^{93}Sr(1068 keV)
1072.6	^{93}??(?? keV)
1096.9	^{93}Sr(1196.7 keV), ^{93}Y(1094.0 keV)
1125.4	^{93}Y(1122.5 keV)
1152.2	^{93}Sr(1148 keV)
1200.2	^{93}Y(1196.2 keV)
1219.0	^{93}Y(1215.48 keV)
1242.9	^{93}Sr(1238 keV)
1272.9	^{93}Y(1269.5 keV)
1280.0	^{93}Y(1277.9 keV)
1311.4	^{93}??(?? keV)
1325.0	^{93}Y(1321.2 keV)
1337.5	^{93}Y(1332.5 keV), ^{93}Sr(1334.5 keV)
1390.0	^{93}Sr(1385.2 keV), ^{93}Y(1387.1 keV)
1439.6	^{93}Y(1434 keV), ^{93}Sr(1437 keV)
1465.7	K
1474.6	^{93}??(?? keV)
1495.9	^{93}Y(1492.1 keV)
1525.4	^{93}??(?? keV)
1556.3	^{93}Y(1551.6 keV)
1568.3	^{93}Sr(1562 keV)
1600.6	^{93}??(?? keV)
1618.5	^{93}??(?? keV)
1640.1	^{93}??(?? keV)
1653.2	^{93}??(?? keV)
1689.9	^{93}Y(1684.8 keV)
1702.8	^{93}Y(1694.1 keV), ^{93}Y(1699.1 keV)
1770.5	^{93}Y(1765.4 keV)
1816.2	^{93}Sr(1808 keV), ^{93}Y(1811 keV)
1876.5	^{93}Sr(1869.7 keV)
1918.7	^{93}??(?? keV)
1935.7	^{93}Y(1928.8 keV)
1987.4	^{93}Sr(1978.3 keV)
2062.4	^{93}Y(2063.6 keV)

Table 5.5: Contaminants and natural radioactivity found in the beamdump detector for ^{93}Rb radioactive beam.

10.2.4 ISOLDE Beam gate

The ISOLDE beam gate consists in electrostatic deflectors which stop the beam just after the primary target. The amount of contamination coming from EBIS has been evaluated by comparing the measurements with and without the ISOLDE beam gate. The trapping and breeding time have been notably optimized in such way.

Usually, the beamgate is used to reduce the amount of particles impinging on the CD detector (selection in release time). If the intensity is too high, the silicon detectors are deteriorated and if the experiment doesn't request the total products from the ISOL target, the beam gate can be closed. In our case, the total intensity was sufficiently low and without any contaminants to let the beam gate opened for the whole Coulomb excitation experiments [4].

10.2.5 β-decay

The radioactive beam brings along its daughter nuclei. The proportion of daughter nuclei produced during the transport until the secondary target can be calculated from their known half-lives. However, the recoil energy of the decay can de-confine them in REX-TRAP and REX-EBIS. This process reduces the

4. during the accumulation of statistics

amount of daughter nuclei on the secondary target, see Tab. 5.6.

The radial electrical potential of the trap is around 10-15 V, which is low compared to the recoil energy calculated. The radial confinement in the trap is provided by a magnetic field of 3 T. The axial potential is around 170 V.

The radial electrical potential of REX-EBIS is around 400 V and can let escape some recoil nuclei. Regarding the axial potential of around 600-700 V, an almost complete confinement is achieved.

However, the amount of daughter nuclei lost by beta decay is difficult to evaluate, because it depends on several parameters: the recoil energy, the confining potential and the geometry.

Isotope (parent)	Mass [a.m.u.]	Q_β [MeV]	Max. Recoil Energy [eV]
^{93}Rb	92.9220419 (81)	7.465 (9)	365.976
^{93}Sr	92.9140256 (81)	4.140 (12)	123.459
^{93}Y	92.909583 (11)	2.895 (10)	65.513
^{95}Rb	94.929303 (23)	9.284 (21)	541.019
^{95}Sr	94.9193588 (80)	6.090 (7)	244.930
^{95}Y	94.9128206 (78)	4.451 (7)	137.767
^{97}Rb	96.937352 (33)	10.432 (28)	661.641
^{97}Sr	96.926153 (21)	7.470 (16)	351.299
^{97}Y	96.918134 (13)	6.689 (11)	285.663
^{99}Rb	98.94538 (13)	11.38 (11)	765.642
^{99}Sr	98.933241 (86)	7.530 (19)	349.388
^{99}Y	98.924636 (26)	7.568 (14)	352.742

Table 5.6: Q_β values for the different nuclides, see Ref. [65].

In our case, the daughter nucleus of ^{97}Rb, ^{99}Rb and ^{99}Sr, respectively ^{97}Sr, ^{99}Sr and ^{99}Y, were already well known, but the β-decay gave us an occasion to study them.

10.2.6 Release

The intensity of the beam after the proton impact on the primary target is called a release curve. If the release time of a specific species is far from the release time of contaminants and short enough as compared to the PSB Supercycle (multiple of 1.2 s), thus a selection of the nuclei of interest can be performed.
For example, tagging on a specific γ-ray energy, one could evaluate the half life of the species at the origin of the transition. The amount of γ-rays, detected along the difference in time between the proton impact and their detection in the MINIBALL array, is the convolution of the release coming from the primary target and the half life of the nucleus (β-decay).
The difference between the Rb and Sr isobars release times was too small to be able to separate the different species.

11 Ionization Chamber

11.1 Calibration

Initially used to set the different devices along the beam transport, the ^{87}Rb has also been employed to calibrate the ionization chamber. The stable ^{87}Rb is produced from a mass marker in the primary target, see Fig. 5.19.
The stable ^{87}Rb is charge bred in REX-EBIS up to 21+ (A/q=4.1429) (or 23+) and sent through the LINAC with a A/q$\approx$ 4.14, close to the settings of the radioactive beam A/q=4.13-4.30.

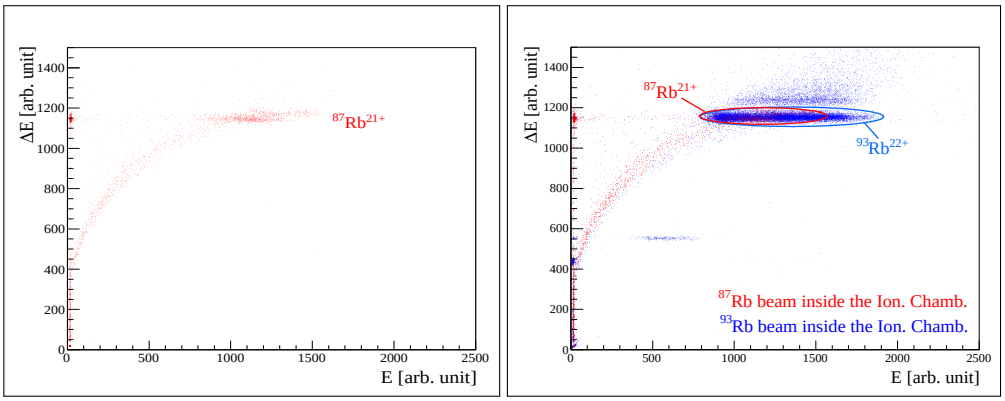

Figure 5.19: Ionization Chamber. The ^{87}Rb mass marker.

11.2 Analysis of the Ionization Chamber Telescope

The results of the ionization chamber are shown for the different radioactive beams on the Fig. 5.20.

Some components coming from REX-EBIS were identified in the ionization chamber by closing the ISOLDE beamgate, e.g. $^{38}Ar^{9+}$. The ^{86}Kr is present in the ^{99}Rb radioactive beam. It has an A/q close to the Rb isotopes and can be brought along from REX-TRAP/REX-EBIS.
An applet is provided by the REX-ISOLDE team on the website of the setup, see Ref. [173], allowing to identify easily the contaminants candidates in terms of their selection in A/q.

Concerning the ^{93}Rb, there are some rebounds in the ΔE detector corresponding to a bad collection of the energy, see Fig. 5.19. At some point the gain of the E detector flipped, explaining the two different spots along the abscissas. If one observes carefully and with attention the plot, the two drops are also seen for the $^{38}Ar^{9+}$ contaminant.

The results has been summarized inside the Tab. 5.7.

Beam	Nuclide	Composition [%]	Relative ratio [%]		A/q
^{93}Rb	$^{93}Rb^{22+}$	64 (0.5)	94.5 (0.6)	for Rb+Sr	4.2273
	$^{93}Sr^{22+}$	4 (0.5)	5.5 (0.3)	for Rb+Sr	4.2273
	$^{93}Nb^{22+}$	7.5 (0.3)			4.2273
	$^{38}Ar^{9+}$	0.7 (0.1)			4.222
^{95}Rb	$^{95}Rb^{23+}$	64 (4)	75 (3)	for Rb+Sr	4.1304
	$^{95}Sr^{23+}$	21 (2)	25 (3)	for Rb+Sr	4.1304
^{97}Rb	$^{97}Rb^{23+}$	74 (4)	80 (2)	for Rb+Sr	4.2174
	$^{97}Sr^{23+}$	17 (1)	20 (2)	for Rb+Sr	4.2174
	$^{97}Nb^{22+}$	0.23 (0.05)			4.227
	$^{38}Ar^{9+}$	0.1 (0.05)			4.222
	$^{21}Ne^{5+}$	0.4 (0.1)			4.2
^{99}Rb	$^{99}Rb^{23+}$	6.5 (5)	6.5 (4)	for Kr+Rb+Sr+Y	4.304
	$^{99}Sr^{23+}$ + $^{99}Y^{23+}$	8.5 (5)	8.4 (0.4)	for Kr+Rb+Sr+Y	4.304
	$^{86}Kr^{20+}$	85 (1)	85 (1)	for Kr+Rb+Sr+Y	4.3
	$^{99}Rb^{23+}$		43 (3)	for Rb+Sr+Y	4.304
	$^{99}Sr^{23+}$ + $^{99}Y^{23+}$		57 (3)	for Rb+Sr+Y	4.304

Table 5.7: Beam composition found with the ionization chamber. The "Composition" are normalized on the total number of particles detected inside the ionization chamber. Some components at low ΔE energy cannot be identified and contribute to the background.
The "Relative ratio" are normalized to the identified components (indicated in the fifth column).

This technique was the most precise to identify the amount of the different isotopes. The amount of the

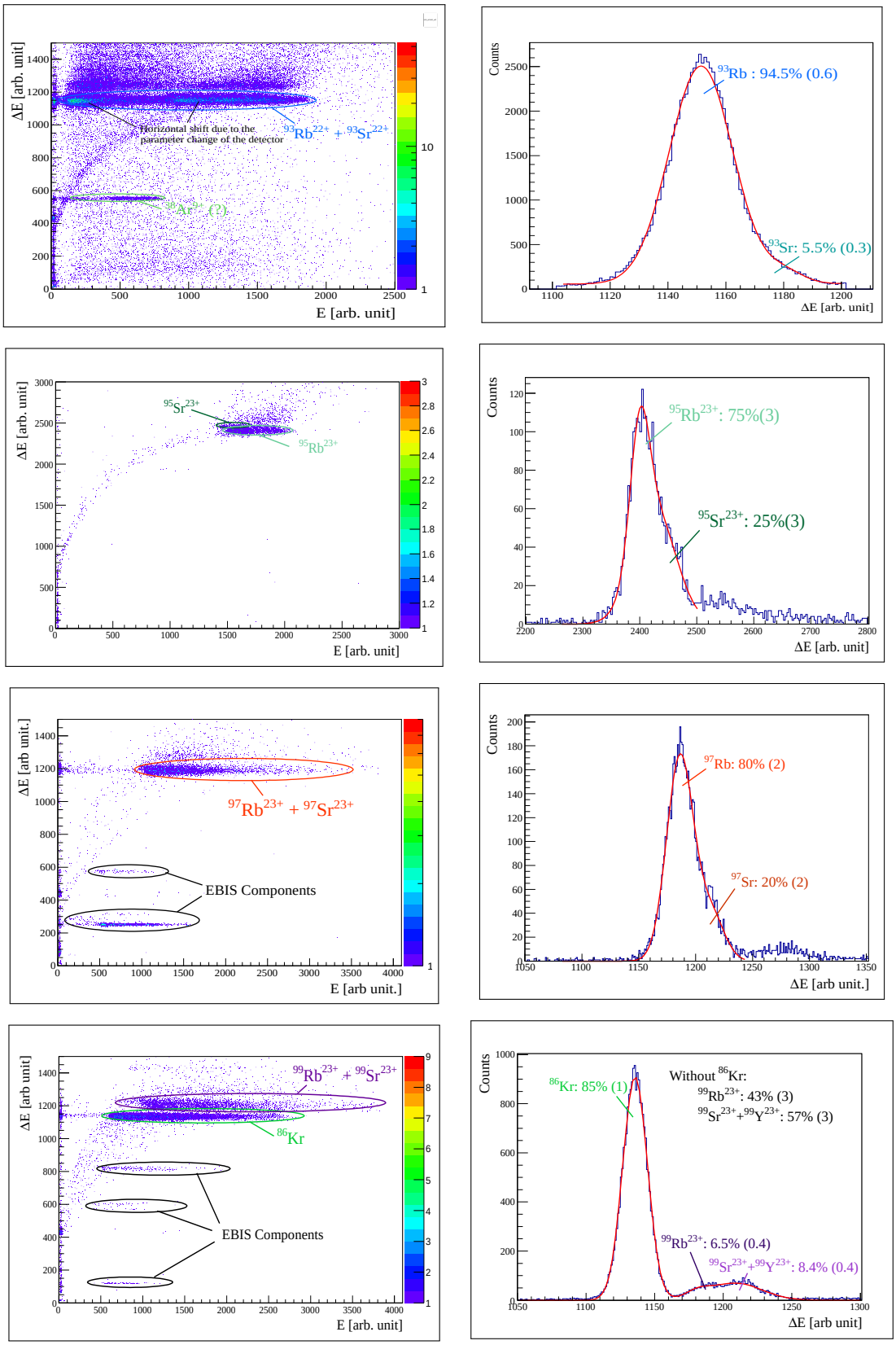

Figure 5.20: Ionization Chamber. The results of the ΔE-E detector inside the ionization chamber are shown for the different radioactive beams. Thanks to the ionization inside the gas a part of the energy is deposited and the rest is collected inside a silicon detector placed at the end of the beamline.

β-decay products increases with shortening the lifetime. However the increase is not a simple proportional law because a part of the recoiling nuclei are lost in the Penning Trap.

12 Extraction of Matrix Elements

As mentioned in the Sec. 7 on page 70, the analysis of such Coulomb excitation experiment aims to the extraction of the matrix elements. The code GOSIA has been used for this purpose. This code has been developed at the Rochester University in 1980, mainly by Tomasz Czosnyka, see Ref. [190, 191, 192, 193]. The code is regularly updated by the collaboration.

The code performs a "least squares" minimization of calculated and experimental transition yields using the coupled channel in the semiclassical picture.
To be more explicit, GOSIA adjusts each matrix element according to the minimization of the χ^2 in order to reproduce the observed γ-ray intensities versus the scattering angle. The χ^2 values are calculated taking into account the spectroscopic data already known.

This section describes the different parameters used for the matrix elements extraction. Several files are used to describe the experiment and the nuclei properties. The steps to extract the matrix elements are described in details in the following chapter.

12.1 The code GOSIA

12.1.1 Calculated Intensities

The minimization algorithm is an iterative process converging on local solutions. GOSIA operates a minimization of the χ^2, comparing the observed intensities and the calculated intensities from the matrix elements. The matrix elements are modified for the next iteration. The process stops when the χ^2 value is low enough, or when a certain number of iterations is applied without important modification of the χ^2 or when a certain number of iterations is applied.

Due to the time difference between the excitation (collision) and decay (γ-ray emission) of excited states, respectively $\simeq 10^{-20}$ s and $\simeq 10^{-12}$ s, the two different processes are treated sequentially and independently. As mentioned previously the energy found for the Doppler corrections does not correspond to the energy at the excitation time, but at the "average" energy at the exit of the target. However, only the projectile energy at the excitation point is the relevant, and the energy entered into GOSIA corresponds to the average beam energy at the middle of the target.

The electromagnetic de-excitation of a nuclear state populated by Coulomb excitation is described in GOSIA via the double differential cross section over the particle and γ-ray solid angle, see Ref. [113]:

$$\frac{d^2\sigma}{d\Omega_{Particle} d\Omega_\gamma} = \sigma_{Rutherford}(\theta_{Particle}) \sum_{\lambda\mu} R_{\lambda\mu}(I_{Initial}, I_{Final}) Y_{\lambda\mu}(\theta_\gamma, \phi_\gamma) \tag{5.12}$$

where:
- $\theta_{Particle}$: scattering angle of the particle,
- θ_γ: angle of the γ-ray,
- $\Omega_{Particle}$: solid angle for the particle detection,
- Ω_γ: solid angle for the γ-ray detection,
- $R_{\lambda\mu}(I_{Initial}, I_{Final})$: statistical tensor of electromagnetic decay for the transition $I_{Initial} \rightarrow I_{Final}$,
- $\sigma_{Rutherford}(\theta_{Particle})$: Rutherford cross section.

Single-step excitation The statistical tensor of decay describing the electric and magnetic transitions is expressed for a single-step excitation as:

$$R_{\lambda\mu}(I_{Initial}, I_{Final}) = \frac{1}{2\gamma(I)\sqrt{\pi}} G_\lambda \rho_{\lambda\mu} \sum_{\lambda_d \lambda'_d} \delta_{\lambda_d} \delta_{\lambda'_d} F_\lambda(\lambda_d \lambda'_d I_{Final} I_{Initial}) \tag{5.13}$$

where:
- $F_\lambda(\lambda_d \lambda'_d I_{Final} I_{Initial})$: correlation coefficient between the magnetic sub-states of the $I_{Initial}$ and I_{Final} nuclear states, usually called Ferentz-Rosenzweig coefficient, see Ref. [194],
- δ_{λ_d}: amplitude of the transition $I_{Initial} \rightarrow I_{Final}$ with the multipolarity λ_d. This amplitude is proportional to the matrix element $<I_{Initial}||\mathcal{M}(E\lambda_d)||I_{Final}>$, see Ref. [194],
- $\rho_{\lambda\mu}$: polarization tensor of the nuclear state I_z from a single-step Coulomb excitation $I_0 \rightarrow I_z$,
- G_λ: attenuation factor,
- $\gamma(I)$: emission probability.

The polarization tensor describing the population of magnetic sub-states m_f after the excitation of the corresponding nuclear states I from the initial state I_0 can be expressed as:

$$\rho_{\lambda\mu} = \frac{\sqrt{2I+1}}{2I_0+1} \sum_{m_0 m_f m'_f} (-1)^{I-m'_f} \begin{pmatrix} I & \lambda & I \\ -m'_f & \mu & m_f \end{pmatrix} a^*_{Im'_f, I_0 m_0} a_{Im_f, I_0 m_0} \tag{5.14}$$

Multi-step excitation As mentioned multi-step excitations to a final nuclear state I_{Final} can also occur. During this process, the probability to populate the nuclear states via the decay of higher nuclear states cannot be excluded. The statistical tensor of electromagnetic decay is re-expressed as:

$$R^{multi-step}_{\lambda\mu}(I_{Initial}, I_{Final}) = R_{\lambda\mu}(I_{Initial}, I_{Final}) + \sum_z R_{\lambda\mu}(I_z, I_{Final}) H_\lambda(I_{Final}, I_z) \tag{5.15}$$

The nuclear states I_z are intermediate states through which the excitation occurs to feed the state I_{Final} and H_λ depends on the emission probability ($\delta_{\lambda_d}(I_z \rightarrow I_{Final})$).

12.1.2 De-orientation

The attenuation related to the de-orientation effect (G^d_λ) for the recoil in vacuum should be taken into account. Indeed the hyperfine interaction, taking place between the electron and the nucleus, perturbs the population of magnetic substates. As a consequence an attenuation of the angular distribution is observed. The γ-rays angular distribution is expressed as a sum of the Legendre Polynomia $P_k(x)$ as:

$$W(\theta_\gamma) = \sum_{odd\ k} a_k P_k(\cos(\theta_\gamma)) \tag{5.16}$$

with: a_k proportional to ρ_k and $F_\lambda(\lambda_d \lambda'_d I_{Final} I_{Initial})$ For an electromagnetic decay by γ-ray of type E2, the angular distribution is found as:

$$W_{E2}(\theta_\gamma) = 1 + a_2 P_2(\cos(\theta_\gamma)) + a_4 P_4(\cos(\theta_\gamma)) \tag{5.17}$$

Including the de-orientation effect, the E2 angular distribution can be written :

$$W_{E2}(\theta_\gamma) = 1 + a_2 G^d_2 P_2(\cos(\theta_\gamma)) + a_4 G^d_4 P_4(\cos(\theta_\gamma)) \tag{5.18}$$

where: G^d_λ takes into account the de-orientation effect according to the de-excitation time, the spin and the gyro-magnetic factor [5] of the nuclear state. If the gyro-magnetic factor is not known, it is evaluated using the approximation $g \approx \frac{Z}{A}$.

Attenuation factor The attenuation factor has been already mentioned in the Chap. 5.3 on page 66. G_λ takes into account the angular distribution corrections due to the geometry of the detecting elements and corrections due to the de-orientation effect. The coefficient corrects the effect of the relativistic Lorentz boost, the finite size of the detecting elements and its time perturbation caused by the de-orientation effect (depolarization).
GOSIA uses a modified version of the original two-state de-orientation model of Abragam and Pound, see Ref. [195].

5. The gyro-magnetic factor (g) is usually gfactor.

12.1.3 Geometry

The attenuation related to the experimental setup depends on its geometry, the materials and the γ-ray energy. The introduced geometry of the detectors in GOSIA is based on a coaxial type. The attenuation due to surrounding materials, such as the capsule material (Al) which can stop X-rays, is also taken into account. The experimental γ-rays yields are obtained summing over the cluster array, they constitute inputs of the code. An efficiency curve can be associated to the yield in order to correct them.
The particle detector is represented by a cylindrical volume placed perpendicularly to the beamline axis [6].

12.1.4 Conversion Electrons

The raw experimental yields serves as input parameters. However as mentioned previously, the electromagnetic decays are partially converted and corrections have to be included. The internal conversion coefficients for the different nuclei can be calculated inside GOSIA, but they have been extracted from the online application "BrIcc v2.3S Conversion Coefficient Calculator", see Ref. [124, 125, 196, 197].

12.1.5 Nuclear Structure

Some nuclear structure data are available for the ^{60}Ni target. The Coulomb excitation can populate the first 2_1^+ nuclear state of the target at 1332.518(5) keV. Its static quadrupole moment is known $Q = +0.03(5)$. The half life is 0.77(4) ps. The transition strength is B(E2)=12.5 W.u.
The associated matrix elements $< 0_1^+ \| E2 \| 2_1^+ >$ and $< 2_1^+ \| E2 \| 2_1^+ >$ have been included in the minimization calculation.

After the shape transition, none of the excited structures of Rb isotopes are known. The only available informations are the gyromagnetic factors of the ground states and their quadrupole moments.

12.2 Particle Kinematic Integration

Finally, the result of GOSIA is expressed as the integrated yield of each γ-ray transition from each excited state I. In order to reproduce the experimental transition yields, the double differential cross section integrations needs to take into account the azimuth angular coverage of each $\theta_{Particle}$ describing the particle detector. In our case the angular coverage is simulated via annular cylindrically symmetric volumes along the beamline axis. The empty spaces separating the different quadrants of the CD detector have been not taken into account.
The incident particle loss energy passing through the target. GOSIA is not able to evaluate the stopping powers in the target. The energy loss can be expressed as a sequential list of stopping power inside the target (different values of stopping power are associated to different thicknesses). The γ-ray and Rutherford cross section can be respectively integrated over the total Germanium and CD detector solid angles. However, in our case the overlap of kinematics impose to integrate on the restricted set of events. The calculated intensities(or yields) are found as:

$$Y_\gamma^{Calculated} = \int_{E_{Min.}}^{E_{Max.}} dE \frac{1}{\frac{dE}{dx}} \int_{\theta_{Particle,Min.}}^{\theta_{Particle,Max.}} \sin(\theta_{Particle}) d\theta_{Particle} \int_{\phi_{Particle}} \frac{d^2\sigma(I_{Initial} \rightarrow I_{Final})}{d\Omega_{Particle} d\Omega_\gamma} d\phi_{Particle} \quad (5.19)$$

The ratio of the yields is assumed equivalent to the experimental intensities ratios, and one can have a direct access to the transition strengths.

12.3 Minimization

In the code, the studied nucleus can be defined as target or projectile. Again due to the kinematics overlap, the studied nucleus is chosen as the target nuclei (identifiable). Several targets can be used in the same minimization process, for which the angular coverage is properly defined.
This technique should work pretty well at condition that least one transitional matrix element is known. If not, the normalization of the different matrix elements is impossible.
An alternative version of the code GOSIA2 has been used and permits to treat at the same time the target and projectile excitation leading to an easier normalization of the matrix elements. Generally like in our case, the

6. The empty spaces between the detecting elements are neglected.

projectile matrix elements are normalized to the target excitation.

During the minimization process, all the unknown nuclear properties of the nuclear states are treated as free parameters or can be forced to evolve inside a specific range. In addition, the integration over a large angular distribution contributes to reduce the sensitivity. In order to optimize the minimization process and reduce the systematic errors, the totality of the spectroscopic data needs to be included.

The lowest requirement is the input of the relative experimental yields and the angular coverages.

12.4 Error determination

The statistical errors on the non-diagonal matrix elements are determined using the intensities of the related transitions of the projectile and target nuclei. They are the most important errors, due to the important errors found for the γ-ray intensities.

The systematic errors found for the matrix elements come principally from the uncertainties on the beam energy, the error on the target matrix elements used to normalize.

After Doppler correction, some of the peaks cannot be identified due to their too close energies, and they form e.g. doublet, triplet. In our cases, one observe some γ-ray transitions coming from the same nucleus. Their respective intensities can be summed or dispatched in two different transitions. This error has to be taken into account if the intensities have the same order of magnitude. In our case, one doublet are present in each ^{93,95}Rb. Fortunately, those transitions were already known and the respective intensities of the double peaks have been evaluated from the present data set and the previous studies. The resulting error would be taken as the enlargement of the errors on the two respective γ-ray intensities. The presence of the higher transition would impact on the minimization "more" than its intensities.

In the ^{93,95}Rb, the level scheme are already well known and the coupling to unknown excited states is very small and thus neglected. I contrary, the ^{97,99}Rb states are not known and the potential coupling to unknown transition can influence significantly the matrix elements calculated with the minimization process. One can cite the appearance of virtual excitations influencing the Coulomb excitation cross section and thus the diagonal matrix elements (second order treatment).
Extra states have been added on top of the rotational bands. The systematics observed in the energies of the rotational bands has been used to placed them in energy. The influence of such introduction is discussed in the following Ref. [198] notably in terms of parity nature.

The description of the different numerical processes to obtain the error is presented in the GOSIA User's manual [192]

13 Conclusion

A specific code has been developed to perform such Coulomb excitation analysis with all the requested tools to extract from the raw data the relevant informations. Trees of events has been created creating correlation between particles and γ-rays hits. Several algorithms have been investigated to "reconstruct" the event, to improve their quality and increase the statistics. Their small impact on the data imposes to reject their use.
The ratio signal/noise has been mainly improved by the substraction of a random set of events taken before the prompt events.
After the calibration of the different detectors, the efficiency of the γ-ray detectors has been performed, insuring an appropriated normalization of the transition intensities.
In order to integrate the different γ-ray transition intensities, Doppler correction has been applied on the data. To be able the application of such correction the position of the detectors of the whole setup had to be well known.
The importance of the beam components sometimes including a important proportion of contaminants has been evaluated with an ionization chamber. The presence of contaminants changes the excitation of the target/projectile nuclei. It can deteriorates the normalization of the projectile excitation matrix elements with the target excitation matrix elements. Finally, to extract the matrix elements of the electromagnetic

multipolar operator the Coulomb excitation sofware GOSIA has been used.

Chapter 6

Results

1 Introduction

The results of the Coulomb excitation experiments on ^{93,95,97,99}Rb are presented in this chapter by case by case. The ^{95,97,99}Sr and ^{99}Y nuclei are also discussed, giving new insight on neighboring nuclei.
Level schemes and excitation transition strengths are deduced from the present work. Some coincidence spectra are given for ^{97}Rb as example of typical analysis used to deduce the level schemes.
Candidates for unknown transitions are sought by scanning spectra gated on previously known transitions or transitions already assigned to a specific nucleus.

2 ^{93}Rb case

In this Coulomb excitation experiments, the reduced transition strengths of the ^{93}Rb isotope are obtained from the corrected γ-ray transition yields (efficiency and conversion electron corrections). They are normalized to the target excitation using its known transition strength of the first excited state B(E2, $0_1^+ \rightarrow 2_1^+$).
The ^{60}Ni target has been chosen because it permits to fulfill the "safe" Coulomb excitation conditions and the high energy of the first excited state avoids an overlap with the expected low transition energies. The entire set of data corresponding to the ^{93}Rb is discussed in this section.

The Coulomb excitation of the ^{93}Rb isotope has been taken as an experimental reference in order to test and validate our analysis treatment, justifying at the same time the use of the MINIBALL experimental setup for such study.

2.1 Analysis

2.1.1 Prompt/Random Subtraction

In order to operate a data selection and improve the Signal/Noise ratio, the subtraction of random events to prompt events has been applied using prompt particle-γ condition. Similar subtractions have been applied for each cases. A representation of the time difference between the particle and gamma detection ($T_{Particle}-T_\gamma$) is given for the ^{93}Rb case on Fig. 6.1 on the next page. The prompt and random coincidence time-window are equal in time. Sometimes, the random coincidence gate is taken larger than the prompt one and a rescaling is applied on it; however, in such case the decay lifetimes will be averaged. No conditions are applied on the particle-γ ray coincidences except the application of thresholds to reject low particle/γ-ray energy events (their nature cannot be determined).

2.1.2 Doppler correction

As mentioned previously, the Doppler correction has been produced in two main different ways. The first is applied using the restricted kinematics and the other on the total kinematics. The advantage of the first case is the absence of overlap between the target and projectile events, leading to a correct identification of the particle nature. In the second case the resolution and the peak ratios are deteriorated, however the statistics is higher in the overlap zone.
Using the restricted kinematics zone, the Rutherford scattering kinematics can be adopted. Detecting the position of a particle hit in the CD detector, the projectile and scattering angles can be calculated by giving the incident beam energy. The Doppler corrected spectra for the projectile/target particle are shown on the Fig. 6.3(landscape).

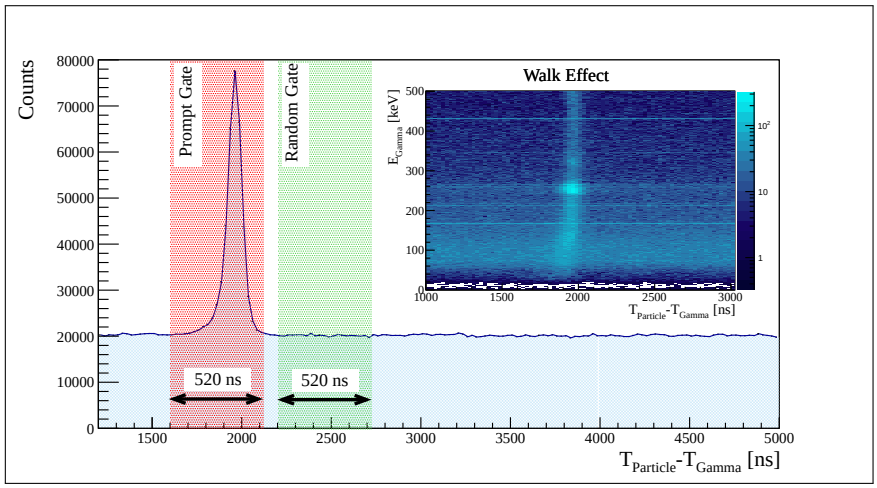

Figure 6.1: Prompt/Random Coincidences - Time difference particle-γ for mass A=93.

2.2 Gamma ray Intensities

The γ-ray intensities obtained in the Coulomb excitation are given on the Tab. 6.2(landscape) for the restricted kinematics. The raw intensities extracted from the data set have been corrected considering the absolute efficiency of the detectors and the conversion electron coefficients. The latest were assumed of pure M1 or E2 type.

2.3 The nuclear structure at low energy

The level schemes have been constructed using single γ-ray intensities and γ-γ coincidences. The level scheme of ^{93}Rb is presented on the Fig. 6.2.

A self-coincidence has been identified at 253 keV analyzing the intensities of the related peaks in multiple projections of γ-γ matrices. The relative intensities have been estimated taking in to account the intensities found in projections.

The single spectra led also to highlight the long lived nature of the nuclear state at 266 keV. Comparing the Doppler corrected and non-Doppler corrected spectra, we could identify that the 266 keV transition has relatively long lifetime. Taking into account that the time of flight between the target and the CD detector is around ~2 ns, we could estimate that the lifetime of the transition is around the same value.

The more intense 253 keV transition has been observed as prompt, thus the half life of 57 μs previously deduced is discounted. The wrong assignment has already been reported by J.J. Ressler et *al.*, see Ref. [199, 200, 201]. New transitions have been identified compared to the beta-decay studies.

A summary of the estimated half-live from the previous and the present studies is given on Tab. 6.1.

Nucleus	E_{level} [keV]	I^{π}	$T_{\frac{1}{2}}$
^{93}Rb	0 (g.s.)	5/2-	5.84 (2) s
	253.39 (3)	3/2-, 5/2-	~~57 (15) μs~~
	266.86 (3)	1/2-, 3/2-, 5/2-	2.0 (2) ns
	323.95 (3)	3/2-, 5/2-	< 0.7 ns
	506.01 (4)	1/2-, 3/2-	< 0.7 ns
	733.40 (24)	(7/2-)	
	820.52 (3)		
	912.71 (24)	(7/2-)	

Table 6.1: Estimated half-live and spins for ^{93}Rb from previous experiments.

Sometimes, the nucleus emitting γ-ray is difficult to identify for some transitions with low intensities, see Tab. 6.3(landscape). Some of them are not in coincidence with strong transitions and cannot be confirmed.

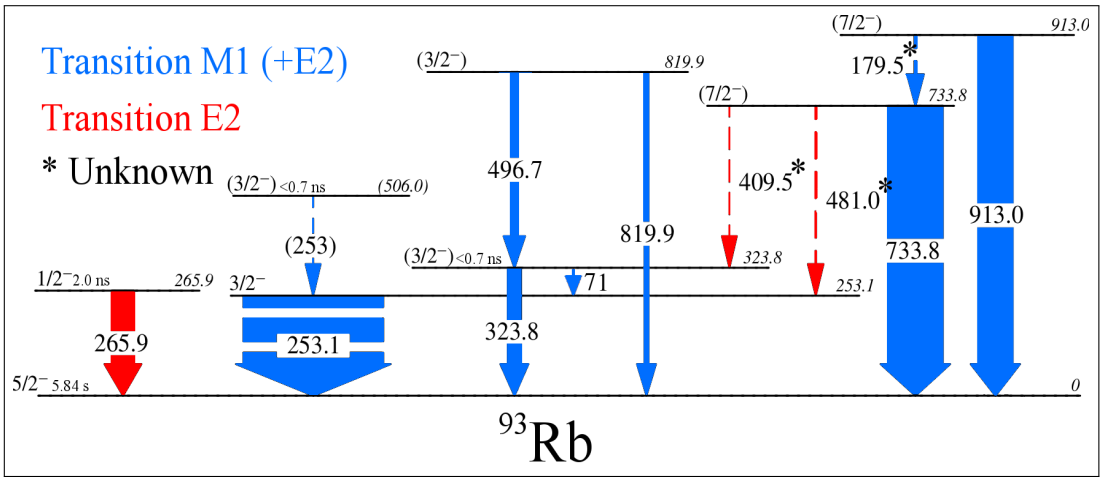

Figure 6.2: ^{93}Rb level scheme. The nuclear spin I^{π} and the energy of the states are given respectively at the left/right. The energy of the transition are positioned in the middle or beside the transition arrow. The width of the transition is proportional to the observed transition intensity.

However, the high purity of the beam (~ 5% of Sr and ~ 95% of Rb) emphasizes that those transitions should come from the ^{93}Rb nucleus or one of its beta-decay daughter nuclei, see Sec. 11.2 on page 125.

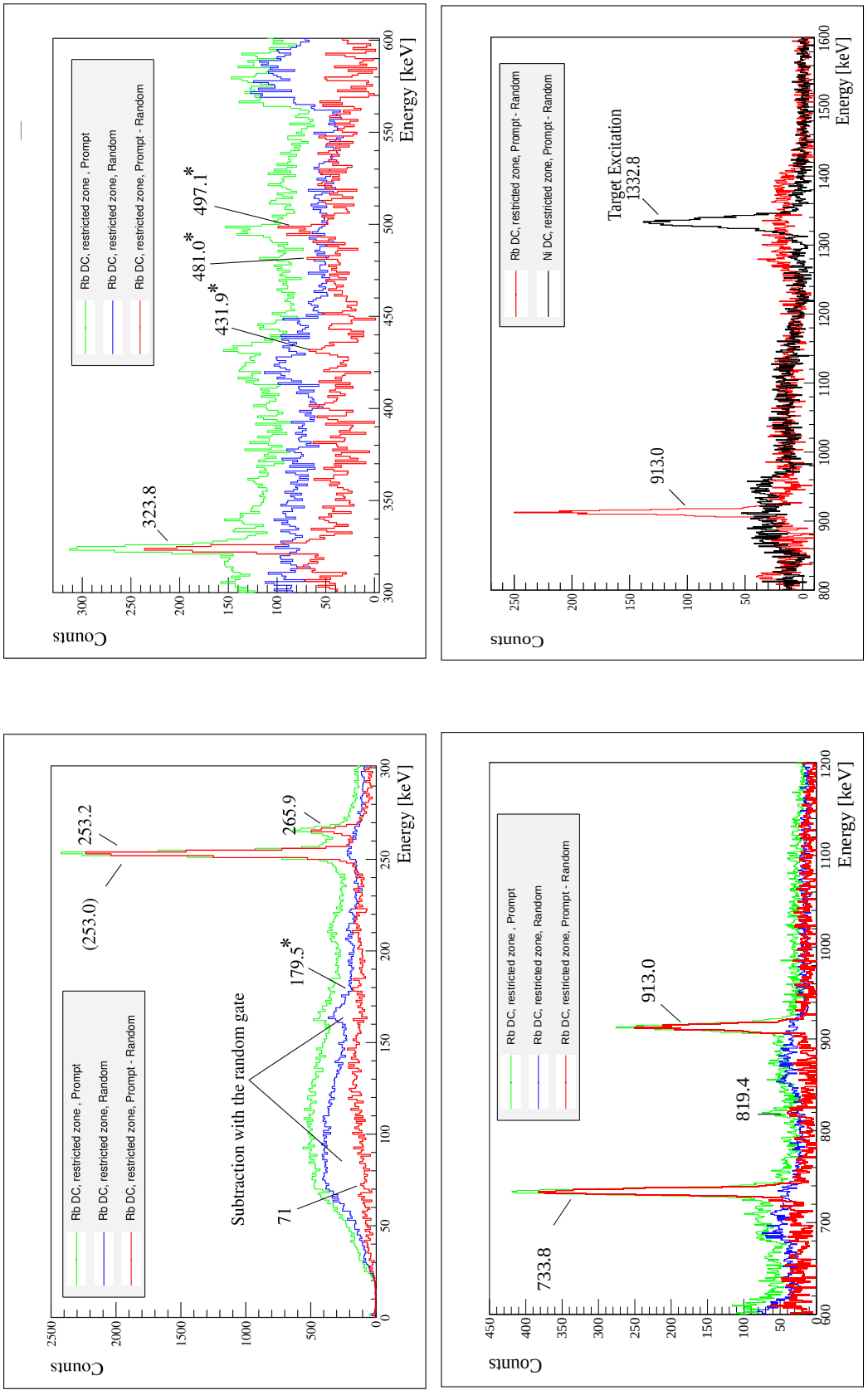

Figure 6.3: γ-ray Energy Spectra for ^{93}Rb (restricted zone). (*) Unknown.

$I^{\pi}_{Initial}$	I^{π}_{Final}	E_γ [keV]	$I_\gamma^{Meas.}$	Coef. (M1)	Coef. (E2)	$I_{Eff+Conv}$(M1)	$I_{Eff+Conv}$(E2)	Observation
(3/2-)	3/2-	71 (2)	38 (20)	0.377	3.40	259 (136)	826 (435)	(γ-γ (253,497))?, rest. kin. (extremely weak),①
(7/2-)	(7/2-)	179.5 (5)	107 (20)	0.03	-	446 (83)	-	
3/2-	5/2-	253.2 (6)	7425 (105)	0.01239	-	35910 (508)	-	γ-γ (70)
(3/2-)	3/2-	253.0 (5)	~153 (33)	0.0124	-	740 (162)	-	②
1/2-	5/2-	265.9 (1)	1178 (152)	-	0.0276	-	5948 (767)	
(3/2-)	5/2-	323.8 (2)	707 (45)	0.00671	-	3956 (252)	-	
(7/2-)	(3/2-)	409.4 (15)	-	-	0.00641	-	-	pmr93DC, ③
(7/2-)	(3/2-)	481.0 (15)	40 (19)	-	0.00386	-	290 (138)	
(3/2-)	(3/2-)	497.1 (4)	357 (37)	0.00241	-	2645 (274)	-	
(7/2-)	5/2-	733.8 (5)	2935 (62)	0.000994	-	27706 (585)	-	
(3/2-)	5/2-	819.9 (6)	218 (19)	0.000781	-	2191 (191)	-	
(7/2-)	5/2-	913.0 (6)	1854 (48)	0.000618	-	19765 (512)	-	
Target Excitation		1332.8 (5)	2196 (50)	-	-	-	29940 (682)	

Table 6.2: ^{93}Rb γ-ray intensities. $I_\gamma^{Meas.}$ are the raw intensities measured. Coef. (M1) and Coef. (E2) are respectively the M1 and E2 conversion electron coefficients calculated from Ref. [196]. $I_{Eff+Conv}$(M1) and $I_{Eff+Conv}$(E2) are intensities with efficiency correction and conversion electrons correction. Some comments or observations are added in case of difficulties to determine the properties of the transition. In order to respect a proper ratio between intensities, the identification of the particle is necessary. For that purpose, the detected particles in the restricted kinematic zone have been treated.
Observation legend :
– rest. kin. : restricted kinematics spectra with Doppler corrections (A=93), with random subtraction
– pmr93DC : spectra with Doppler corrections (A=93), with random subtraction, all kinematics
– γ-γ (E_γ [keV]) : observation of the transition in the projection of the γ-γ matrix for an energy gate at E_γ, with Doppler correction (A=93), random subtraction, all kinematics
Observation comments :
① possible transition of ^{93}Rb between the level 323.8 and 253.1
② The intensity of the 253.23 and 253.0 keV transitions are estimated using the single and γ-γ spectra and their related efficiencies.
③ The intensity is too weak in the restricted zone, however the transition is observed in random subtracted spectra for all the kinematics.

$I^{\pi}_{Initial}$	I^{π}_{Final}	E_{γ} [keV]	$I^{Meas.}_{\gamma}$	Coef. (M1)	Coef. (E2)	$I_{Eff+Conv}$(M1)	$I_{Eff+Conv}$(E2)	Observation
?	?	314.1 (6)	93 (30)	0.00723	0.01548	510 (165)	514 (166)	rest. kin.
?	?	401.3 (3)	96 (18)	0.00684	0.00399	620 (116)	618 (116)	rest. kin.
?	?	431.9 (5)	176 (24)	0.00335	0.0054	1189 (162)	1192 (163)	rest. kin.
Target Excitation		1332.8 (5)	2196 (50)	-	-	-	29940 (682)	

Table 6.3: Unknown or Weak γ-ray intensities for the ^{93}Rb case. $I^{Meas.}_{\gamma}$ are the raw intensities measured. Coef. (M1) and Coef. (E2) are respectively the M1 and E2 conversion electron coefficients calculated from Ref. [196]. $I_{Eff+Conv}$(M1) and $I_{Eff+Conv}$(E2) are intensities with efficiency correction and conversion electrons correction. Some comments or observations are added in case of difficulties to determine the properties of the transition. In order to respect a proper ratio between intensities, the identification of the particle is necessary. For that purpose, the detected particles in the restricted kinematic zone have been treated.
Observation legend :
– rest. kin. : restricted kinematics spectra with Doppler corrections (A=93), with random subtraction

2.4 Extraction of matrix elements and transition strengths with GOSIA2 calculations for ^{93}Rb

The transitions strengths deduced from the γ-ray yields are normalized to the target excitation. In order to treat simultaneously the target and projectile excitation a new version of GOSIA has been used : GOSIA2. The relative intensities were extracted from the restricted kinematics zone. They are given in the Tab. 6.2(landscape).
The corrected transition yields of the target excitation ($0^+_1 \rightarrow 2^+_1$) are input to GOSIA2. The different characteristics of the first excited level of the ^{60}Ni are well known and used as inputs, see Tab. 6.4. The

Levels			
Index	$I^\pi_{nb.}$	Energy [keV]	$T_{\frac{1}{2}}$ [ps]
1	0^+_1		stable
2	2^+_1	1333.518(5)	0.77

I^π_{Final}	$I^\pi_{Initial}$	Transition Energy [keV]	Q [eb]	Matrix Elt.(*)
2^+_1	0^+_1	1332.501(5)	-	$0.306^{0.308}_{0.303}$
2^+_1	2^+_1	-	0.03(5)	$-0.137^{-0.113}_{-0.161}$

$I^\pi_{nb.}$	Lifetime [ps]	Calculated Lifetime [ps]	Error [ps]	Exp. Yield	Calc. Yield	Error [%]
2^+_1	1.11 (0.06)	1.039	0.06	25110	25180	0.3

Table 6.4: Properties of the first excited states ($0^+_1 \rightarrow 2^+_1$) of the ^{60}Ni (target nucleus). (The minimization calculations stopped at 0.3%, it corresponds to the experimental error.) (* error bars put in the minimization code)

minimization routine fits the matrix elements of the ^{93}Rb. The matrix elements of the target (^{60}Ni) has been fixed to their adopted values, see Tab. 6.4, see Ref. [168].

The known characteristics from previous experiments [104] are used as input in GOSIA2 and are used to constrain the minimization: level schemes, lifetimes, quadrupole moments, known matrix elements and branching ratios.

In the present case, additional information like the lifetime of the 266 keV states were already known. Consequently, one tried to evaluate the influence of the different parameters in the minimization. The transition strengths obtained with the GOSIA2 minimization are given in the Tab. 6.6.
The weight applied on the matrix elements does not change significantly the minimization, as well as the low quadrupole moment of the ^{93}Rb. Nevertheless, in our case, the introduction of branching ratios constrains noteworthy the matrix elements.

I^π_{Final}	$I^\pi_{Initial}$	Energy [keV]	Transition strength$^{\text{Upper Error}}_{\text{Lower Error}}$ no BR/LT; w=1	BR/LT; w=0.5	BR/LT; w=1	BR/LT ; w=1; Q	
(3/2−)	(5/2−)	253	$0.046^{+0.011}_{-0.002}$	$0.044^{+0.011}_{-0.002}$	$0.044^{+0.011}_{-0.002}$	$0.043^{+0.010}_{-0.001}$	B(E2) [e^2b^2]
(1/2−)	(5/2−)	266	$0.016^{+0.005}_{-0.004}$	$0.018^{+0.004}_{-0.003}$	$0.017^{+0.004}_{-0.003}$	$0.017^{+0.003}_{-0.001}$	
(3/2−)	(5/2−)	324	$0.002^{+0.002}_{-0.002}$	$0.002^{+0.002}_{-0.002}$	$0.002^{+0.002}_{-0.002}$	$0.002^{+0.001}_{-0.001}$	
(7/2−)	(5/2−)	734	$0.033^{+0.003}_{-0.005}$	$0.032^{+0.003}_{-0.004}$	$0.032^{+0.003}_{-0.005}$	$0.034^{+0.002}_{-0.003}$	
(3/2−)	(5/2−)	820	$0.015^{+0.007}_{-0.003}$	$0.014^{+0.005}_{-0.002}$	$0.014^{+0.005}_{-0.002}$	$0.013^{+0.003}_{-0.001}$	
(7/2−)	(5/2−)	913	$0.036^{+0.008}_{-0.009}$	$0.034^{+0.002}_{-0.008}$	$0.034^{+0.002}_{-0.008}$	$0.037^{+0.001}_{-0.006}$	
(3/2−)	(3/2−)	252	$0.012^{+0.079}_{-0.013}$	$0.013^{+0.080}_{-0.014}$	$0.013^{+0.08}_{-0.014}$	$0.013^{+0.079}_{-0.013}$	
(7/2−)	(3/2−)	481	$0.003^{+0.004}_{-0.003}$	$0.003^{+0.004}_{-0.003}$	$0.003^{+0.004}_{-0.003}$	$0.003^{+0.003}_{-0.002}$	
(7/2−)	(3/2−)	409	$0.025^{+0.020}_{-0.007}$	$0.023^{+0.018}_{-0.007}$	$0.023^{+0.02}_{-0.007}$	$0.025^{+0.015}_{-0.007}$	
(3/2−)	(3/2−)	497	$0.004^{+0.079}_{-0.005}$	$0.007^{+0.068}_{-0.008}$	$0.011^{+0.091}_{-0.012}$	$0.016^{+0.012}_{-0.005}$	
(7/2−)	(7/2−)	179	$0.002^{+2.4}_{-0.003}$	$0.001^{+2.3}_{-0.002}$	$0.002^{+2.3}_{-0.003}$	$0.002^{+1.8}_{-0.002}$	
(3/2−)	(5/2−)	253	$0.003^{+5.8}_{-0.004}$	$0.001^{+6.0}_{-0.002}$	$0.002^{+6.2}_{-0.003}$	$0.001^{+6.0}_{-0.001}$	B(M1) [μ^2_N]
(3/2−)	(5/2−)	324	$0.003^{+5.8}_{-0.004}$	$0.001^{+6.0}_{-0.002}$	$0.001^{+6.0}_{-0.002}$	$0.001^{+6.0}_{-0.001}$	
(3/2−)	(3/2−)	252	$0.002^{+6.3}_{-0.003}$	$0.000^{+6.0}_{-0.000}$	$0.000^{+6.0}_{-0.000}$	$0.000^{+6.0}_{-0.000}$	
(3/2−)	(3/2−)	497	$0.018^{+0.011}_{-0.005}$	$0.014^{+0.004}_{-0.003}$	$0.013^{+0.003}_{-0.003}$	$0.011^{+0.002}_{-0.002}$	
(7/2−)	(7/2−)	179	$0.066^{+0.053}_{-0.035}$	$0.063^{+0.05}_{-0.033}$	$0.063^{+0.050}_{-0.033}$	$0.068^{+0.052}_{-0.035}$	

Table 6.6: Transition strengths extracted with the GOSIA2 code for the ^{93}Rb case. Constraint added during the minimization: BR = branching ratio, LT = lifetime , Q = quadrupole moment , w = weight of the matrix elements.

The Coulomb excitation is not sensitive towards the M1 matrix elements. For example, in our case, the B(M1) transition strengths are consistent with zero within the error bars, except for the 497 keV and 179 keV transition which are relatively mixed according to the minimization calculation, see Tab. 6.6.

3 ^{95}Rb case

3.1 Analysis

Similar analysis than for the ^{93}Rb isotope have been performed for the ^{95}Rb case, see Subsec. 2. The Doppler corrected spectra for the projectile/target particle are shown on the Fig. 3.3(landscape).

3.2 Gamma ray Intensities

The γ-ray intensities obtained in the Coulomb excitation are given on the Tab. 6.7, 6.8(landscape) for the restricted kinematics. The raw intensities extracted from the data set have been corrected considering the absolute efficiency of the detectors and the conversion electron coefficient. The latest were assumed of pure M1 or E2 type.

3.3 The nuclear structure at low energy

The level scheme has been constructed using single γ-ray intensities and γ-γ coincidences. The level scheme of ^{95}Rb is presented on the Fig. 6.4.

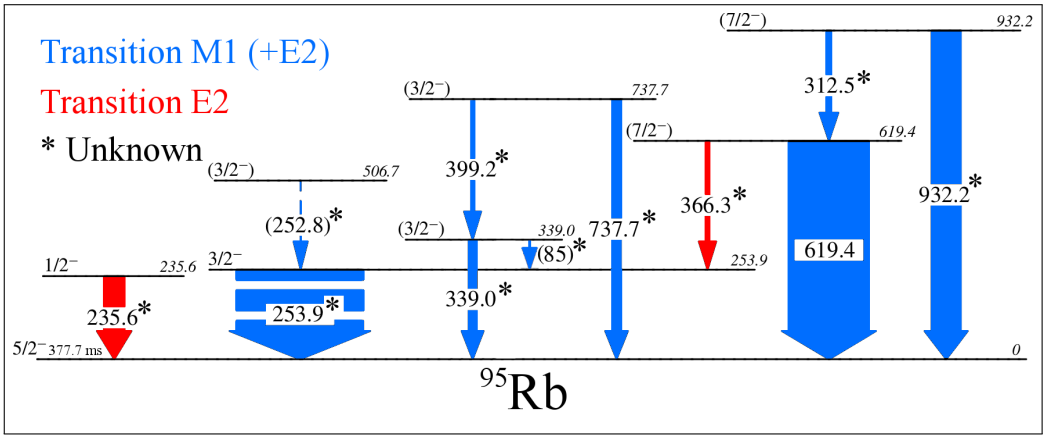

Figure 6.4: ^{95}Rb level scheme. The nuclear spins I^{π} and the energy of the nuclear states are given respectively at the left/right. The energy of the transition are positioned beside the transition arrow. The width of the transition is proportional to the observed transition intensity.

A self-coincidence has been identified at 254 keV analyzing the intensities of the related peaks in multiple projections of γ-γ matrices. The relative intensities have been estimated taking into account the intensities found in the projections.
The single spectra led also to highlight the long lived nature of the nuclear state at 236 keV. Comparing the Doppler corrected and non-Doppler corrected spectra we could identify that the 236 keV transition has relatively long lifetime. Taking into account that the time of flight between the target and the CD detector is around ~2 ns, we could estimate that the lifetime of the transition is around the same value. New transitions have been identified compared to the beta-decay studies. The 85 keV transition has been observed in coincidence with the 254 keV energy and in the single spectra, it can correspond to the 71 keV transition in the ^{93}Rb isotope.

Sometimes, the nucleus emitting γ-ray is difficult to identify for some transitions with low intensities, see Tab. 6.9(landscape). Some of them does not coincide with strong transitions and cannot be confirmed. However, the high purity of the beam excludes the contaminant possibility and emphasizes that those transitions should come from the ^{95}Rb or one of its beta-decay daughter nuclei, see Sec. 11.2 on page 125.

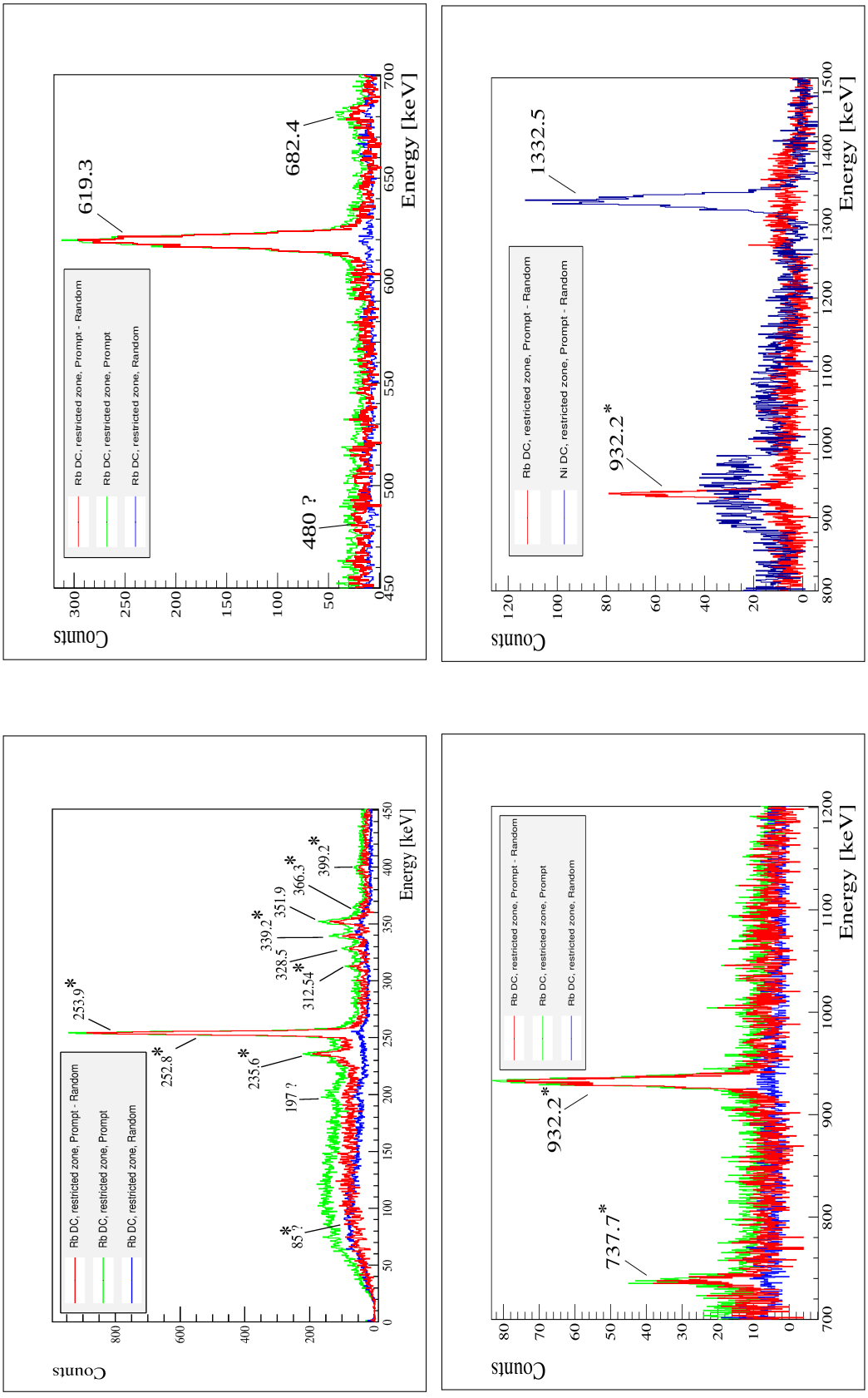

Figure 6.5: Gamma ray Energy Spectra for ^{95}Rb radioactive beam (restricted zone). (*) Unknown.

$I^{\pi}_{Initial}$	I^{π}_{Final}	E_{γ} [keV]	$I_{\gamma}^{Meas.}$	Coef. (M1)	Coef. (E2)	$I_{Eff+Conv}$(M1)	$I_{Eff+Conv}$(E2)	Observation
1/2-	5/2-	235.6 (2)	961 (228)	-	0.0423	-	4598 (1091)	
3/2-	5/2-	253.9 (10)	5934 (93)	0.0123	-	28741 (450)	-	γ-γ (85,384)
(3/2-)	3/2-	252.8 (10)	~135 (45)	0.0123	-	652 (217)	-	①
(7/2-)	(7/2-)	312.5 (3)	232 (30)	0.00732	-	1269 (164)	-	
(3/2-)	5/2-	339.2 (4)	376 (41)	0.006	-	2165 (236)	-	
(7/2-)	3/2-	366.3 (5)	161 (33)	-	0.00923	-	979 (201)	
(3/2-)	(3/2-)	399.2 (4)	147 (27)	0.00404	-	943 (173)	-	
(7/2-)	5/2-	619.3 (1)	3798 (67)	0.001452	-	32422 (572)	-	
(3/2-)	(3/2-)	737.7 (3)	411 (30)	0.000982	-	3891 (284)	-	
(7/2-)	(3/2-)	932.2 (2)	1386 (40)	0.000592	-	14944 (431)	-	
Target Excitation		1332.5 (3)	1772 (43)	-	-	-	24159 (586)	

Table 6.7: ^{95}Rb γ-ray intensities. $I_{\gamma}^{Meas.}$ are the raw intensities measured. Coef. (M1) and Coef. (E2) are respectively the M1 and E2 conversion electron coefficients calculated from Ref. [196]. $I_{Eff+Conv}$(M1) and $I_{Eff+Conv}$(E2) are intensities with efficiency correction and conversion electrons correction. Some comments or observations are added in case of difficulties to determine the properties of the transition. In order to respect a proper ratio between intensities, the identification of the particle is necessary. For that purpose, the detected particles in the restricted kinematic zone have been treated.
Observation legend :
– γ-γ (E_{γ} [keV]) : observation of the transition in the projection of the γ-γ matrix for an energy gate at E_{γ}, with Doppler correction (A=95), random subtraction, all kinematics
Observation comments :
① The intensity evaluation of 253.9 and 252.8 keV transition are done comparing the single and γ-γ spectra.

$I^{\pi}_{Initial}$	I^{π}_{Final}	E_{γ} [keV]	$I_{\gamma}^{Meas.}$	Coef. (M1)	Coef. (E2)	$I_{Eff+Conv}$(M1)	$I_{Eff+Conv}$(E2)	Observation
(7/2+)	(3/2+)	204.0 (20)	-	-	-	-	-	prompt, random
(3/2+)	(3/2+)	328.5 (2)	239 (32)	0.00648	0.01329	1349 (181)	1358 (182)	rest. kin., γ-γ (352)
(3/2+)	1/2+	351.9 (2)	750 (52)	0.00548	0.01054	4425 (307)	4447 (308)	rest. kin., γ-γ (328)
(9/2+)	(7/2+)	682.4 (20)	-	-	-	-	-	prompt, random
Target Excitation		1332.5 (3)	1772 (43)	-	-	-	24159 (586)	

Table 6.8: ^{95}Sr γ-ray intensities. $I_{\gamma}^{Meas.}$ are the raw intensities measured. Coef. (M1) and Coef. (E2) are respectively the M1 and E2 conversion electron coefficients calculated from Ref. [196]. $I_{Eff+Conv}$(M1) and $I_{Eff+Conv}$(E2) are intensities with efficiency correction and conversion electrons correction. Some comments or observations are added in case of difficulties to determine the properties of the transition. In order to respect a proper ratio between intensities, the identification of the particle is necessary. For that purpose, the detected particles in the restricted kinematic zone have been treated.
Observation legend :
– prompt : prompt spectra without Doppler correction, all kinematics
– random : random spectra without Doppler correction, all kinematics
– rest. kin. : restricted kinematics spectra with Doppler corrections (A=95), with random subtraction
– γ-γ (E_{γ} [keV]) : observation of the transition in the projection of the γ-γ matrix for an energy gate at E_{γ}, with Doppler correction (A=95), random subtraction, all kinematics

$I^{\pi}_{Initial}$	I^{π}_{Final}	E_{γ} [keV]	Observation
(3/2-)	3/2-	85 (2)	γ-γ (254), It could correspond to the transition between the 339.2 keV and 253.9 keV levels, similar to the 71 keV transition in the ^{93}Rb.
(3/2-)	(3/2-)	197 (2)	γ-γ (339), It could correspond to a level above the 253.9 kev, between the 339.2 keV level and a hypothetic level at around 536 keV.
(7/2-)	(3/2-)	280.4 (30)	γ-γ (254,339), It could correspond to the transition between the level 619.4 keV and 339.2 keV
?	?	283 (2)	γ-γ (254), It could correspond to a level above the 253.9 kev, between the 253.9 keV level and a hypothetic level at around 536 keV.
(7/2-)	3/2-	383.8 (30)	γ-γ (254), It could correspond to the transition between the 619.4 keV and 235.62 keV levels.
(7/2-)	3/2-	480 (3)	γ-γ (254), It could correspond to the transition between the 737.7 keV and 253.9 keV levels, or decay from the daughter nucleus ^{95}Sr

Table 6.9: Unknown or Weak γ-ray intensities for the ^{95}Rb case. Some comments or observations are added in case of difficulties to determine the properties of the transition. The present transition are too weak to be identified in the restricted kinematics plots.
Observation legend :
– γ-γ (E_{γ} [keV]) : observation of the transition in the projection of the γ-γ matrix for an energy gate at E_{γ}, with Doppler correction (A=95), random subtraction, all kinematics

3.4 Extraction of matrix elements and transition strengths with GOSIA2 calculations

The transitions strengths values deduced from the γ-ray yields are normalized to the target excitation, see Tab. 6.4. In order to treat simultaneously the target and projectile excitation the GOSIA2 has been used. The relative intensities were extracted from the restricted kinematic zone. They are given in the Tab. 6.7(landscape).

I^{π}_{Final}	$I^{\pi}_{Initial}$	Energy [keV]	Tr. strength$^{\text{Upper Error}}_{\text{Lower Error}}$ no BR/LT; w=1 ; Q	
1/2−	5/2−	236	$0.018^{+0.004}_{-0.004}$	B(E2) $[e^2b^2]$
3/2−	5/2−	254	$0.055^{+0.010}_{-0.007}$	
(3/2−)	5/2−	339	$0.003^{+0.001}_{-0.003}$	
(7/2−)	5/2−	619	$0.055^{+0.005}_{-0.004}$	
(3/2−)	5/2−	738	$0.023^{+0.003}_{-0.003}$	
(7/2−)	5/2−	932	$0.048^{+0.004}_{-0.003}$	
(3/2−)	3/2−	252	$0.012^{+0.005}_{-0.012}$	
(7/2−)	3/2−	366	$0.093^{+0.034}_{-0.038}$	
(3/2−)	(3/2−)	399	$0.071^{+0.258}_{-0.071}$	
(7/2−)	(7/2−)	312	$0.002^{+0.213}_{-0.002}$	
(3/2−)	(3/2−)	254	$0.002^{+5.0}_{-0.002}$	B(M1) $[\mu_N^2]$
(3/2−)	5/2−	339	$0.002^{+5.0}_{-0.002}$	
(7/2−)	(5/2−)	619	$0.025^{+0.030}_{-0.010}$	
(3/2−)	5/2−	738	$0.058^{+0.039}_{-0.015}$	
(7/2−)	5/2−	932	$0.018^{+0.013}_{-0.009}$	
(3/2−)	3/2−	252	$0.000^{+6.0}_{-0.000}$	
(3/2−)	(3/2−)	399	$0.109^{+0.042}_{-0.041}$	
(7/2−)	(7/2−)	312	$0.174^{+0.034}_{-0.035}$	

Table 6.10: Transition strengths extracted with the GOSIA2 code for the ^{95}Rb case. Constraint added during the minimization: BR = branching ratio, LT = lifetime , Q = quadrupole moment , w = weight of the matrix elements in the minimization process.

Contrary to the ^{93}Rb case, the low amount of known branching ratio cannot constrain the minimization process and it leads to relatively high B(M1). However, the minimization process merges probably on a local solution for which the B(M1) deviate from zero (low M1 sensitivity of Coulomb excitation). The M1 matrix elements have been changed and does not impact the minimization on the E2 transition strengths.

4 ^{97}Rb case

4.1 Analysis

Before the present study, the excited structure of the ^{97}Rb nucleus was completely unknown, which added an extra difficulty to assign the transition to a specific nucleus. Fortunately, a clear identification of the decay parents was possible mainly thanks to a high beam purity (~ 75% Rb, ~ 25% Sr), see Subsec. 11.2 on page 125.
The amount of ^{97}Sr in the beam allowed to realize its Coulomb excitation at the same time. Thus, the excitation engendered by the ^{97}Sr needs to be taken into account during the normalization. It is meaningful to estimate that the Sr and Rb nuclei excite in the same way the target nucleus thanks to their close (A,Z) combinations. The excitation yields observed from the target would be assumed coming for the Sr and Rb nuclei proportionally to their respective presence in the beam.

Similar analysis than for the previous cases has been performed for the ^{97}Rb case, see Sec. 2, 3.
The Doppler corrected spectra for the projectile/target particle are shown on the Fig. 6.6(landscape).

4.2 Gamma ray Intensities

The γ-ray intensities obtained in the Coulomb excitation are given on the Tab. 6.11(landscape) for the restricted kinematics. The raw intensities extracted from the data set have been corrected considering the absolute efficiency of the detectors and the conversion electron coefficient. The latest were assumed of pure M1 or E2 type.

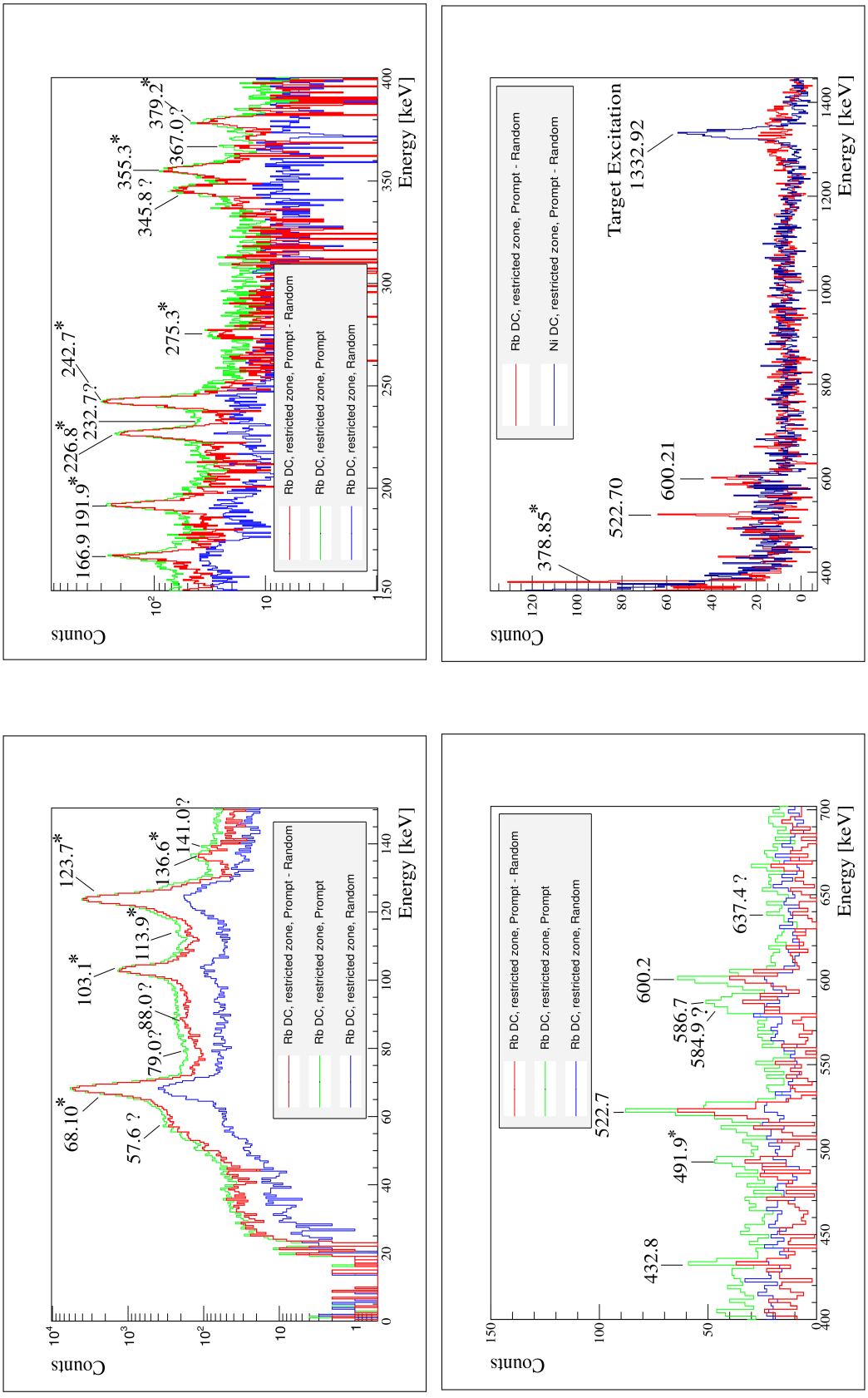

Figure 6.6: Gamma ray Energy Spectra for ^{97}Rb radioactive beam (restricted zone). (*) Unknown.

K^π	I_i^π	I_f^π	E_γ [keV]	$I_\gamma^{Meas.}$	Coef. (M1)	Coef. (E2)	$I_{Eff+Conv}$(M1)	$I_{Eff+Conv}$(E2)	Observation
3/2+	(5/2+)	3/2+	68.10 (1)	24668 (202)	0.424	-	182607 (1495)	-	
3/2+	(9/2+)	(7/2+)	103.1 (2)	5915 (101)	0.1333	-	25497 (435)	-	
3/2+	(7/2+)	(5/2+)	123.7 (1)	20670 (144)	0.0807	-	83499 (582)	-	
3/2+	(13/2+)	(11/2+)	136.6 (6)	259 (45)	0.0623	-	1037 (180)	-	
3/2+	(7/2+)	3/2+	191.9 (2)	1297 (44)	-	0.0887	-	5872 (199)	
3/2+	(9/2+)	(5/2+)	226.8 (3)	1274 (46)	-	0.0485	-	6010 (217)	
3/2+	(11/2+)	(9/2+)	242.7 (3)	1826 (51)	0.0138	-	8632 (241)	-	
1/2+	(9/2+)	9/2+	275.3 (3)	127 (16)	0.01003	0.0244	644 (81)	653 (82)	rest. kin.
3/2+	(11/2+)	(7/2+)	345.8 (4)	516 (28)	-	0.0112	-	4352 (203)	
1/2+	(1/2+)	3/2+	355.3 (3)	729 (34)	0.0807	-	83499 (582)	-	①
3/2+	(13/2+)	(9/2+)	379.2 (6)	261 (22)	-	0.0083	-	1623 (137)	
?	?	?	492.0 (10)	-	-	-	-	-	pmr97DC
Target Excitation			1332.9 (5)	542 (25)	-	-	-	7387 (341)	

Table 6.11: ^{97}Rb γ-ray intensities. $I_\gamma^{Meas.}$ are the raw intensities measured. Coef. (M1) and Coef. (E2) are respectively the M1 and E2 conversion electron coefficients calculated from Ref. [196]. $I_{Eff+Conv}$(M1) and $I_{Eff+Conv}$(E2) are intensities with efficiency correction and conversion electrons correction. Some comments or observations are added in case of difficulties to determine the properties of the transition. In order to respect a proper ratio between intensities, the identification of the particle is necessary. For that purpose, the detected particles in the restricted kinematic zone have been treated.
Observation legend :
– rest. kin. : restricted kinematics spectra with Doppler corrections (A=97), with random subtraction
– pmr97DC : spectra with Doppler corrections (A=97), with random subtraction, all kinematics
Observation comments :
① possible overlap with the 355 keV of ^{97}Sr

K^π	I_i^π	I_f^π	E_γ [keV]	$I_\gamma^{Meas.}$	Coef. (M1)	Coef. (E2)	$I_{Eff+Conv}$(M1)	$I_{Eff+Conv}$(E2)
1/2+	3/2+	1/2+	166.9 (2)	986 (42)	0.0405	-	4053 (173)	-
1/2+	(3/2+)	3/2+	432.8 (3)	-	-	-	-	-
1/2+	(1/2+)	1/2+	522.7 (3)	203 (19)	-	0.0032	-	1558 (146)
1/2+	3/2+	1/2+	586.7 (6)	100 (16)	0.0018	0.0023	826 (132)	826 (132)
1/2+	(3/2+)	1/2+	600.2 (6)	113 (29)	0.0017	0.0022	946 (243)	946 (243)
Target Excitation			1332.9 (5)	542 (25)	-	-	-	7387 (341)

Table 6.12: ^{97}Sr γ-ray intensities. $I_\gamma^{Meas.}$ are the raw intensities measured. Coef. (M1) and Coef. (E2) are respectively the M1 and E2 conversion electron coefficients calculated from Ref. [196]. $I_{Eff+Conv}$(M1) and $I_{Eff+Conv}$(E2) are intensities with efficiency correction and conversion electrons correction. Some comments or observations are added in case of difficulties to determine the properties of the transition. In order to respect a proper ratio between intensities, the identification of the particle is necessary. For that purpose, the detected particles in the restricted kinematic zone have been treated.

K^π	I_i^π	I_f^π	E_γ [keV]	$I_\gamma^{Meas.}$	Coef. (M1)	Coef. (E2)	$I_{Eff+Conv}$(M1)	$I_{Eff+Conv}$(E2)	Observation
1/2+	3/2+	1/2+	88.0 (4)	273 (97)	0.232	1.627	1360 (483)	2900 (1030)	rest. kin., random, ①
1/2+	(1/2+)	3/2+	113.9 (4)	85 (40)	0.1135	0.632	355 (167)	520 (245)	rest. kin., γ-γ (355), ②
1/2+	7/2+	3/2+	141.0 (15)	-	-	-	-	-	random, prompt, ②
1/2+	3/2+	1/2+	417.9 (6)	-	-	-	-	-	random, prompt, ②
?	?	?	57.6 (10)	-	-	-	-	-	prompt, random, ③
?	?	?	79.0 (15)	-	-	-	-	-	pmr97DC, prompt, random, ④
?	?	?	232.7 (10)	-	-	-	-	-	pmr97DC, prompt, random, ⑤
?	?	?	367 (2)	-	-	-	-	-	random, prompt
?	?	?	584.9 (25)	-	-	-	-	-	random, prompt, ②
?	?	?	637.4 (30)	-	-	-	-	-	pmr97DC, rest. kin.
Target Excitation			1332.9 (5)	542 (25)	-	-	-	7387 (341)	

Table 6.13: Unknown or Weak γ-ray intensities for the ^{97}Rb case. $I_\gamma^{Meas.}$ are the raw intensities measured. Coef. (M1) and Coef. (E2) are respectively the M1 and E2 conversion electron coefficients calculated from Ref. [196]. $I_{Eff+Conv}$(M1) and $I_{Eff+Conv}$(E2) are intensities with efficiency correction and conversion electrons correction. Some comments or observations are added in case of difficulties to determine the properties of the transition. In order to respect a proper ratio between intensities, the identification of the particle is necessary. For that purpose, the detected particles in the restricted kinematic zone have been treated.
Observation legend :
– prompt : prompt spectra without Doppler correction, all kinematics
– random : random spectra without Doppler correction, all kinematics
– rest. kin. : restricted kinematics spectra with Doppler corrections (A=97), with random subtraction
– pmr97DC : spectra with Doppler corrections (A=97), with random subtraction, all kinematics
– γ-γ (E_γ [keV]) : observation of the transition in the projection of the γ-γ matrix for an energy gate at E_γ, with Doppler correction (A=97), random subtraction, all kinematics
Observation comments :
① isomer populated in Coulomb excitation, probably ^{97}Sr
② probably ^{97}Sr
③ isomer probably ^{97}Sr
④ isomer populated in Coulomb excitation
⑤ isomer ?
A none exhaustive list of transitions from daughter nuclei of ^{97}Rb observed as random and prompt transitions has been established. Those transitions like 141.4 keV and 417.9 keV of ^{97}Sr nuclei were already known from previous studies. The 113.9 (4) keV transition can correspond to the transition between the ^{97}Rb levels at energies 191.8 keV and 68.1 keV.

4.3 The nuclear structure at low energy

The level schemes have been constructed using single γ-ray intensities and γ-γ coincidences. A level scheme can be drawn uncovering the underlying nuclear structure. The level schemes of ^{97}Rb and ^{97}Sr are presented on the Fig. 6.7. A rotational band is observed in the ^{97}Rb denoting the presence of deformation as expected. No different single-particle levels have been clearly identified in the present Coulomb excitation experiment. One would need to look for a different approach in order to shed light on the expected shape-coexisting structures in ^{97}Rb.

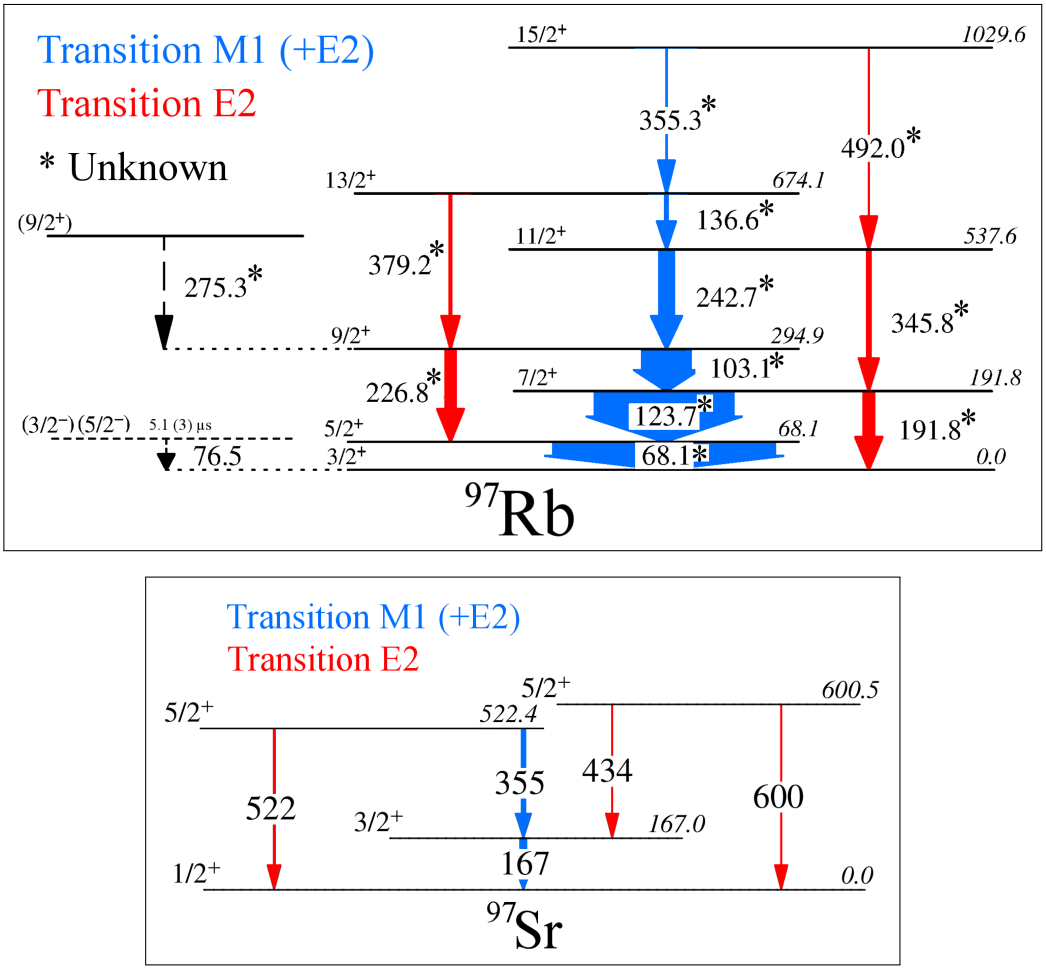

Figure 6.7: ^{97}Rb and ^{97}Sr level schemes. The nuclear spins I^{π} and the energy of the nuclear states are given respectively at the left/right. The energy of the transition are positioned beside the transition arrow. The width of the transition is proportional to the observed transition intensity. The isomeric transition of 76.5 keV has been identified by G. Simpson et *al.* and has been added in order to give a complete picture. However the latest isomer has not been observed in the present work. It should correspond to another single particle configuration, possibly from the $\frac{3}{2}^{-}$[312] orbital or the $f_{\frac{5}{2}}$ orbit [202].
The 275.3 keV transition has been observed in coincidence with the 103.1 keV and 123.7 keV transitions and placed on top of the 294.9 keV level.

Sometimes, the nucleus emitting γ-ray is difficult to identify for some transitions with low intensities. Too low in intensity to coincide with strong transition, they cannot be confirmed. However, the high purity of the beam ($\sim$ 75% Rb, $\sim$ 25% Sr) emphasizes that those transitions should come from the ^{97}Rb or one of its beta-decay daughter nuclei, see Subsec. 11.2.

Projections used to build the level schemes are presented as example for the ^{97}Rb case on the Fig. 6.8(landscape) and for the ^{97}Sr case on the Fig. 6.8. Sometimes, the most intense transitions such as the 68.1 keV or the daughter nuclei transitions (e.g. 167 keV) of the Rb isotopes are found in coincidence with incompatible transitions. They can be consider as "random" coincidences. The same effect is observed for the gated transition for which self coincidences can appear considering the time structure of the beam and setup.

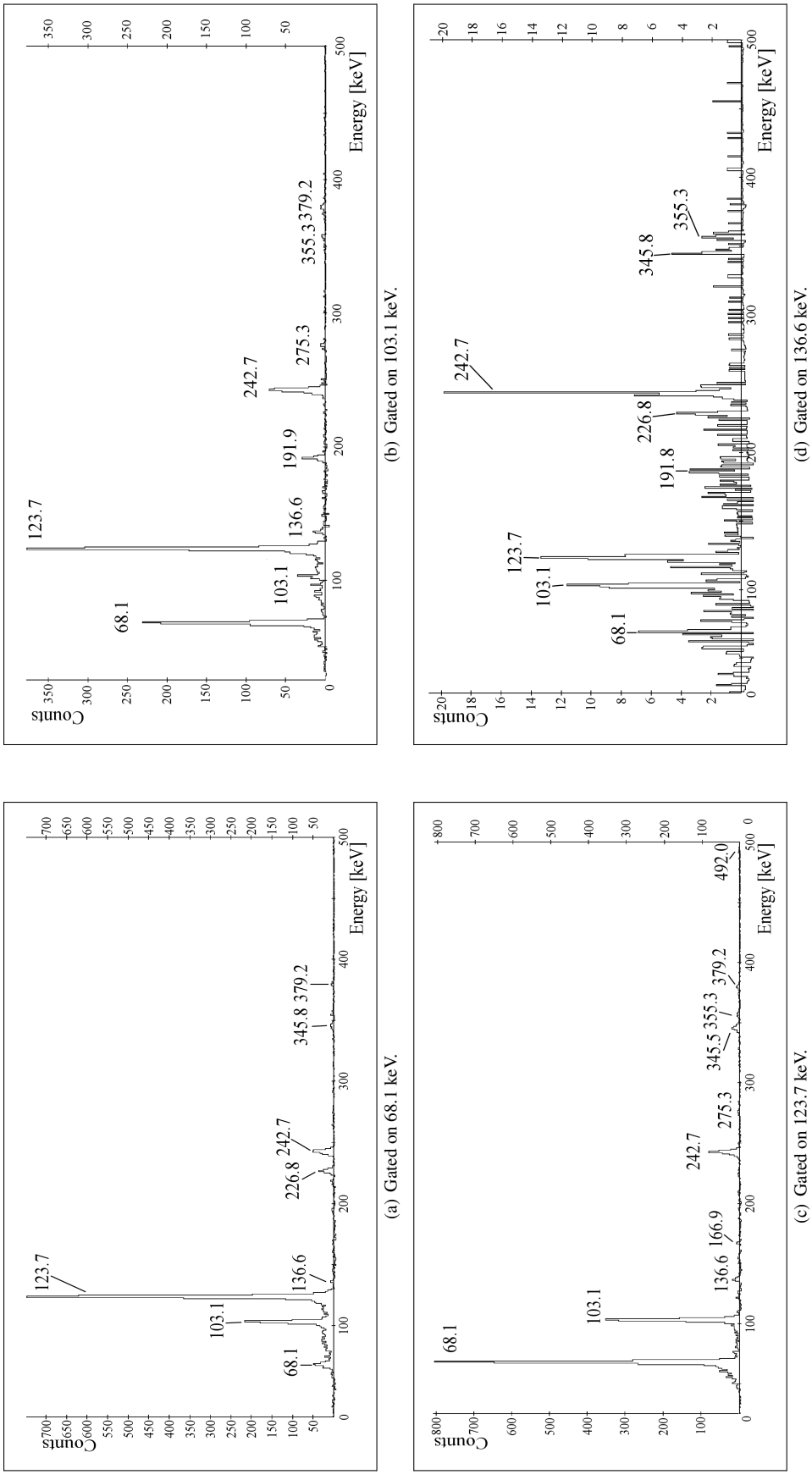

Figure 6.8: Projections of γ-γ matrix for the ^{97}Rb case. The transition of 76.5 keV corresponding to the isomeric state identified by G. Simpson et *al.* has not been observed due to its long lived nature. The 275.3 keV transition has been observed in coincidence with the 103 keV and 123.7 keV and placed on top of the 123.7 keV.

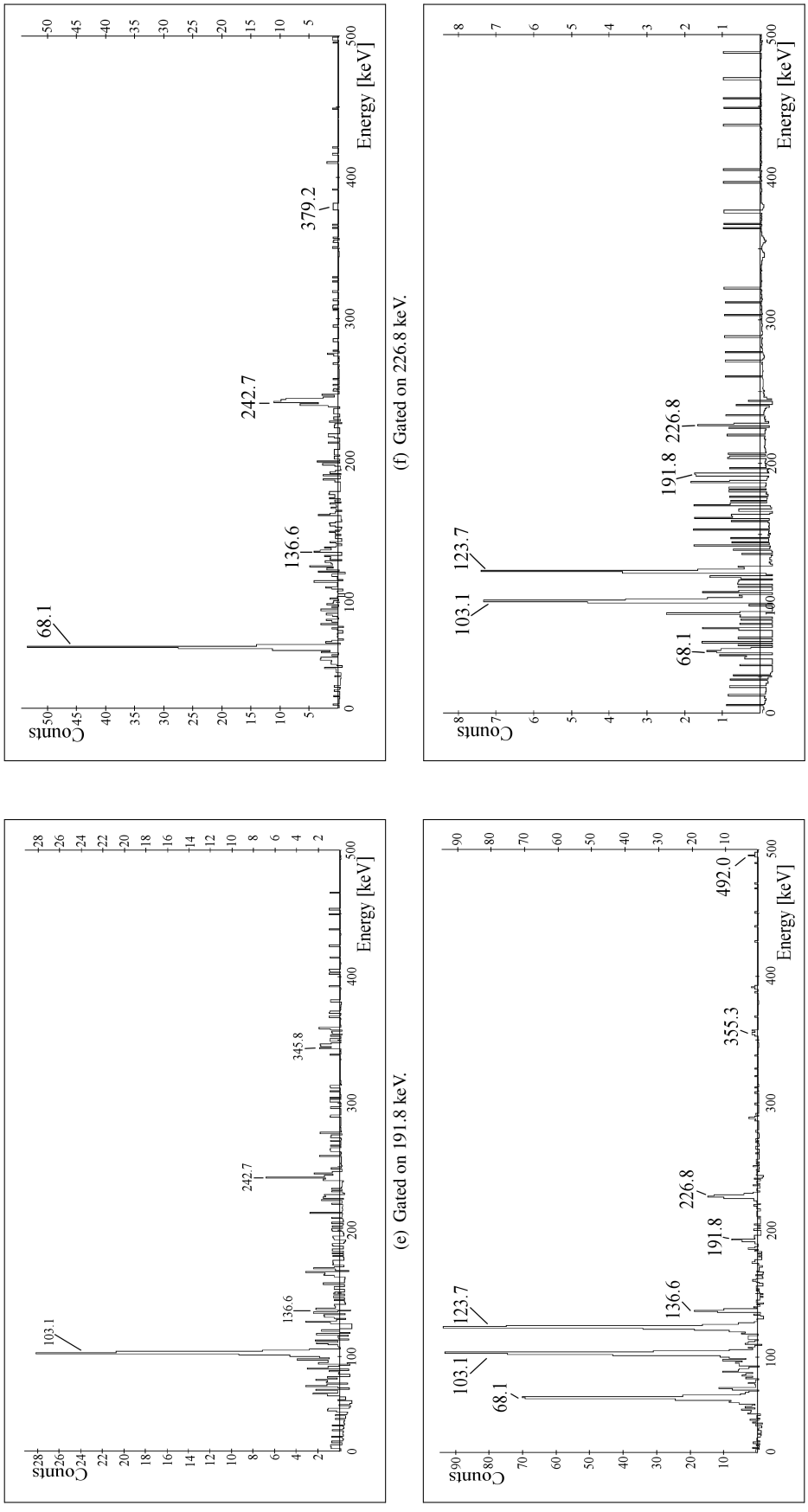

Figure 6.8: Projections of γ-γ matrix for the ^{97}Rb case. The transition of 76.5 keV corresponding to the isomeric state identified by G. Simpson et *al.* has not been observed due to its long lived nature. The 275.3 keV transition has been observed in coincidence with the 103 keV and 123.7 keV and placed on top of the 123.7 keV.

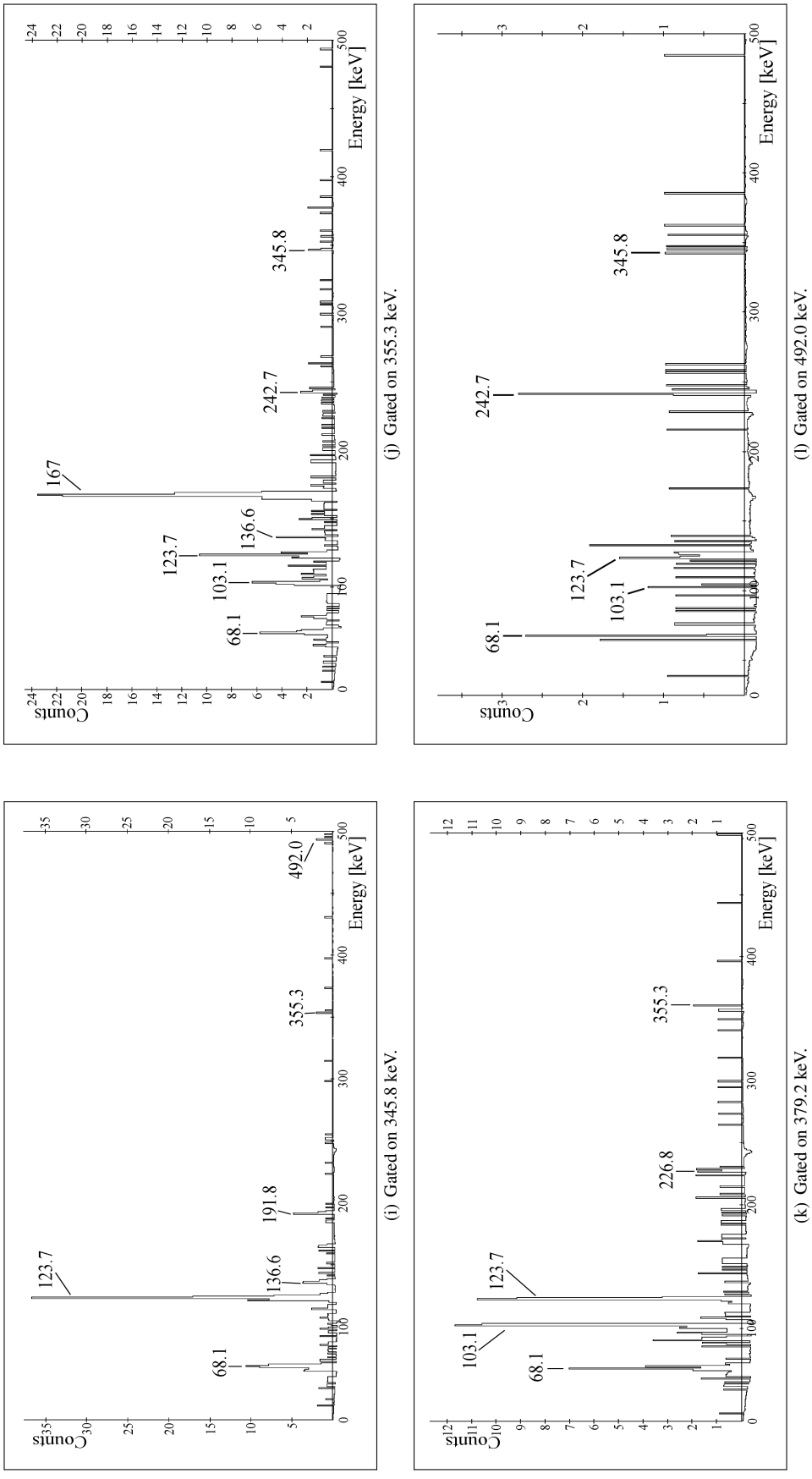

Figure 6.8: Projections of γ-γ matrix for the ^{97}Rb case. The transition of 76.5 keV corresponding to the isomeric state identified by G. Simpson et *al.* has not been observed due to its long lived nature. The 275.3 keV transition has been observed in coincidence with the 103 keV and 123.7 keV and placed on top of the 123.7 keV.

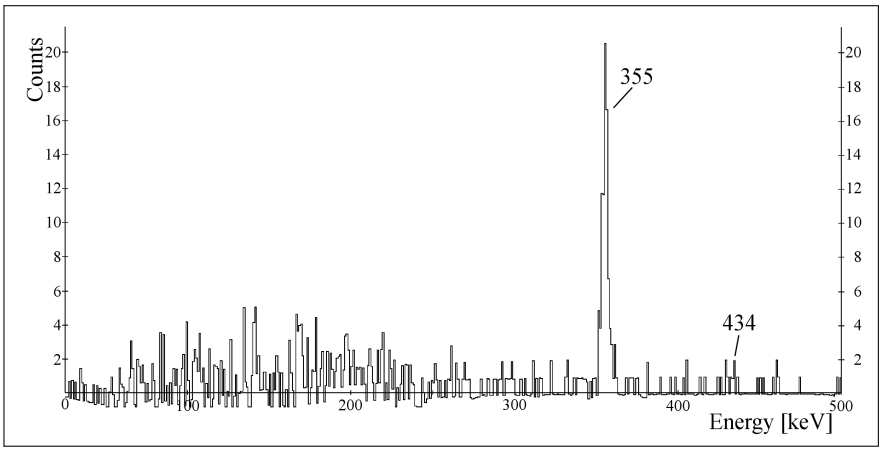

Figure 6.8: Projections of γ-γ matrix for the ^{97}Sr case gated on the 167 keV transition energy.

4.4 Extraction of matrix elements and transition strengths with GOSIA2 calculations

The input of GOSIA2 requires the corrected transition yields of the target excitation ($0_1^+ \rightarrow 2_1^+$), see Tab. 6.4.

I^{π}_{Final}	$I^{\pi}_{Initial}$	Tr. Energy /Level[keV]	Transition strengths$^{\text{Upper Error}}_{\text{Lower Error}}$ no Q	Q(rigid rotor)	
5/2+	3/2+	68 / 68	$0.285^{+0.127}_{-0.025}$	$0.313^{+0.042}_{-0.032}$	B(E2) [e^2b^2]
7/2+	3/2+	192 / 192	$0.235^{+0.016}_{-0.031}$	$0.262^{+0.037}_{-0.043}$	
7/2+	5/2+	124 / 192	$0.386^{+0.360}_{-0.207}$	$0.407^{+0.183}_{-0.242}$	
9/2+	5/2+	227 / 295	$0.265^{+0.041}_{-0.015}$	$0.268^{+0.025}_{-0.019}$	
9/2+	7/2+	103 / 295	$0.199^{+0.095}_{-0.033}$	$0.207^{+0.046}_{-0.036}$	
11/2+	7/2+	346 / 538	$0.160^{+0.032}_{-0.007}$	$0.150^{+0.009}_{-0.008}$	
11/2+	9/2+	243 / 538	$0.149^{+1.40}_{-0.150}$	$0.178^{+0.170}_{-0.178}$	
13/2+	9/2+	379 / 674	$0.257^{+0.051}_{-0.096}$	$0.313^{+0.044}_{-0.049}$	
13/2+	11/2+	137 / 674	$0.052^{+0.285}_{-0.052}$	$0.000^{+0.149}_{-0.000}$	
5/2+	3/2+	68 / 68	$0.225^{+3.26}_{-0.201}$	$1.22^{+2.57}_{-1.22}$	B(M1) [μ_N^2]
7/2+	5/2+	124 / 192	$0.344^{+0.046}_{-0.036}$	$0.384^{+0.049}_{-0.041}$	
9/2+	7/2+	103 / 295	$0.391^{+0.051}_{-0.031}$	$0.398^{+0.031}_{-0.028}$	
11/2+	9/2+	243 / 538	$0.135^{+0.077}_{-0.019}$	$0.127^{+0.025}_{-0.015}$	
13/2+	11/2+	137 / 674	$0.387^{+0.441}_{-0.132}$	$0.502^{+0.193}_{-0.136}$	

Table 6.14: Transition strengths extracted with the GOSIA2 code for the ^{97}Rb case. Constraint added during the minimization: BR = branching ratio, LT = lifetime , Q = quadrupole moment , w = weight of the matrix elements.

The B(E2) transitions strengths, found for this Rb isotope, are one or two orders of magnitude higher than in the previous ^{93,95}Rb cases.

Regarding to the systematics present in the rotational band additional states can be added in order to guide the minimization. Their introduction confers a more realistic treatment, constraining the highest states found experimentally (excitation of high-lying states, multi-step excitation).

5 ^{99}Rb case

5.1 Analysis

Similar analysis than for the previous cases has been performed for the ^{99}Rb case, see Sec. 2, 3, 4. The Doppler corrected spectra for the projectile/target particle are shown on the Fig. 6.9(landscape).

5.2 γ-ray Intensities obtained

The γ-ray intensities obtained in the Coulomb excitation are given on the Tab. 6.15, 6.16, 6.17(landscape) for the restricted kinematics. The raw intensities extracted from the data set have been corrected considering the absolute efficiency of the detectors and the conversion electron coefficients. The latest were assumed of pure M1 or E2 type.

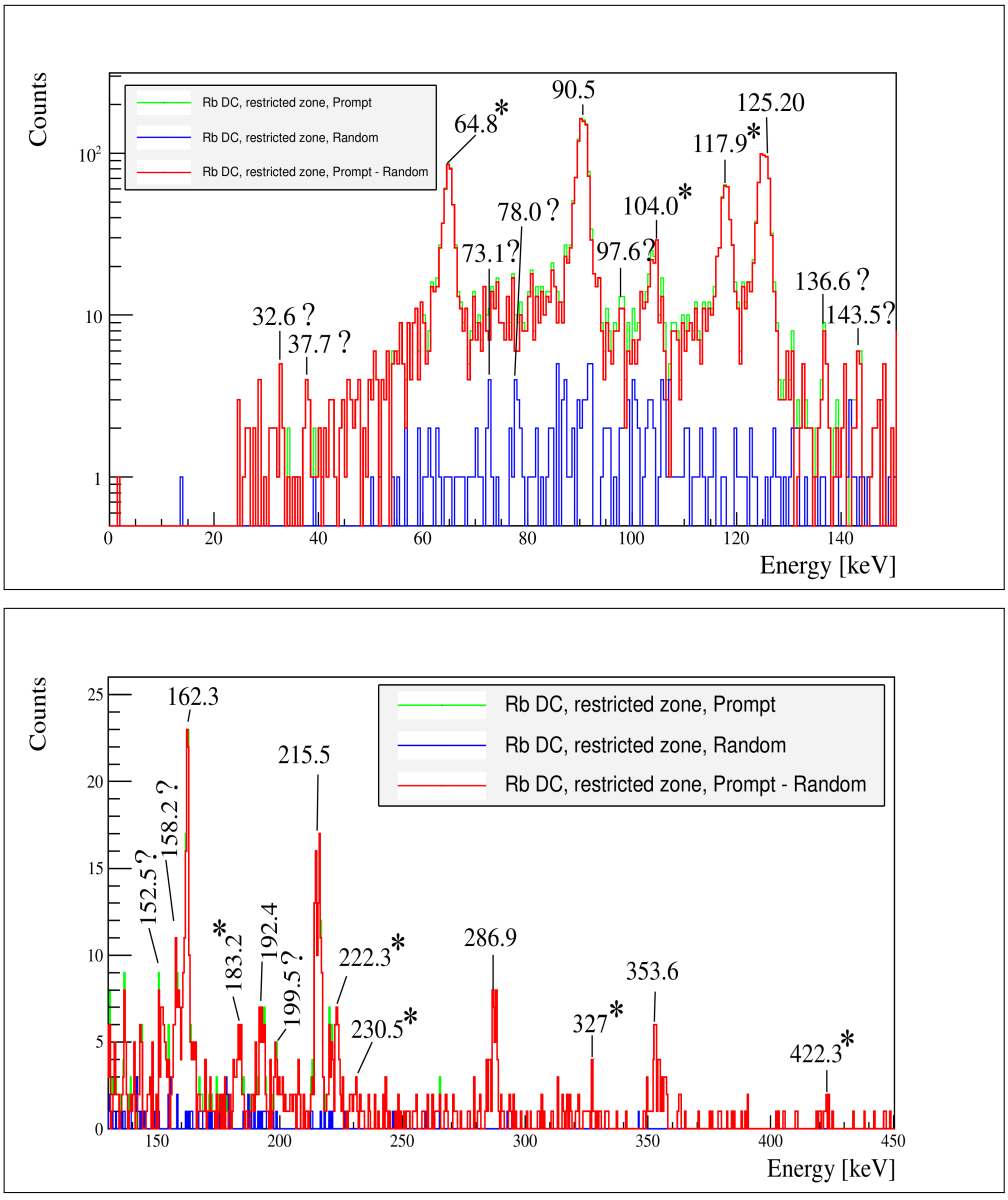

Figure 6.9: Gamma ray Energy Spectra for ^{99}Rb radioactive beam (restricted zone). (*) Unknown.

K^{π}	I^{π}_{Final}	$I^{\pi}_{Initial}$	E_{γ} [keV]	$I_{\gamma}^{Meas.}$	Coef. (M1)	Coef. (E2)	$I_{Eff+Conv}$(M1)	$I_{Eff+Conv}$(E2)	Observation
(3/2+)	(5/2+)	(3/2+)	64.8 (7)	320 (22)	0.487	-	2692 (185)	-	rest. kin.
(3/2+)	(9/2+)	(7/2+)	104.0 (2)	88 (13)	0.1299	-	377 (56)	-	rest. kin.
(3/2+)	(7/2+)	(5/2+)	117.9 (1)	249 (21)	0.0922	-	1017 (86)	-	rest. kin.
(3/2+)	(7/2+)	(3/2+)	183.2 (15)	26 (11)	-	0.1050	-	117 (50)	rest. kin.
(3/2+)	(9/2+)	(5/2+)	222.3 (6)	42 (14)	-	0.0521	-	197 (66)	rest. kin.
(3/2+)	(11/2+)	(9/2+)	223.0 (30)	~22 (22)	0.01725	-	100 (100)	-	pmr99DC
(3/2+)	(11/2+)	(7/2+)	327 (3)	~9 (9)	-	0.01364	-	51 (51)	pmr99DC
Target Excitation			1332	-	-	-	-	-	①

Table 6.15: ^{99}Rb γ-ray intensities. $I_{\gamma}^{Meas.}$ are the raw intensities measured. Coef. (M1) and Coef. (E2) are respectively the M1 and E2 conversion electron coefficients calculated from Ref. [196]. $I_{Eff+Conv}$(M1) and $I_{Eff+Conv}$(E2) are intensities with efficiency correction and conversion electrons correction. Some comments or observations are added in case of difficulties to determine the properties of the transition. In order to respect a proper ratio between intensities, the identification of the particle is necessary. For that purpose, the detected particles in the restricted kinematic zone have been treated.
Observation legend :
– rest. kin. : restricted kinematics spectra with Doppler corrections (A=99), with random subtraction
– pmr99DC : spectra with Doppler corrections (A=99), with random subtraction, all kinematics
Observation comments :
① Low excitation not even measurable for the restricted kinematics

K^{π}	I_i^{π}	I_f^{π}	E_{γ} [keV]	$I_{\gamma}^{Meas.}$	Coef. (M1)	Coef. (E2)	$I_{Eff+Conv}$(M1)	$I_{Eff+Conv}$(E2)	Observation
(3/2+)	(5/2+)	(3/2+)	90.5 (1)	753 (32)	0.191	-	3573 (152)	-	rest. kin.
(3/2+)	(7/2+)	(5/2+)	125.2 (1)	494 (23)	0.078	-	1991 (93)	-	rest. kin., ①
(3/2+)	(7/2+)	(5/2+)	162.3 (2)	60 (13)	0.0391	-	244 (53)	-	rest. kin.
(3/2+)	(11/2+)	(9/2+)	192.4 (15)	32 (12)	0.0250	-	137 (51)	-	rest. kin.
(3/2+)	(7/2+)	(3/2+)	215.5 (15)	93 (10)	-	0.0583	-	432 (46)	rest. kin.
(3/2+)	(11/2+)	(9/2+)	230.5 (15)	~5 (5)	0.0157	-	23 (23)	-	rest. kin.
(3/2+)	(9/2+)	(5/2+)	286.9 (15)	41 (14)	-	0.0521	-	222 (76)	rest. kin., pmr99DC
(3/2+)	(11/2+)	(7/2+)	353.6 (25)	37 (13)	-	0.01011	-	220 (77)	rest. kin., pmr99DC
(3/2+)	(13/2+)	(9/2+)	422.3 (15)	-	-	0.00580	-	-	rest. kin., pmr99DC, ①

Table 6.16: ^{99}Sr γ-ray intensities. $I_{\gamma}^{Meas.}$ are the raw intensities measured. Coef. (M1) and Coef. (E2) are respectively the M1 and E2 conversion electron coefficients calculated from Ref. [196]. $I_{Eff+Conv}$(M1) and $I_{Eff+Conv}$(E2) are intensities with efficiency correction and conversion electrons correction. Some comments or observations are added in case of difficulties to determine the properties of the transition. In order to respect a proper ratio between intensities, the identification of the particle is necessary. For that purpose, the detected particles in the restricted kinematic zone have been treated.
Observation legend :
– rest. kin. : restricted kinematics spectra with Doppler corrections (A=99), with random subtraction
– pmr99DC : spectra with Doppler corrections (A=99), with random subtraction, all kinematics
Observation comments :
① The error bar of the intensity has been enlarged due to the presence of the 125.3 keV transition from ^{99}Y

K^{π}	I_i^{π}	I_f^{π}	E_{γ} [keV]	$I_{\gamma}^{Meas.}$	Coef. (M1)	Coef. (E2)	$I_{Eff+Conv}$(M1)	$I_{Eff+Conv}$(E2)	Observation
?	?	?	32.6 (20)	4 (4)	-	-	-	-	rest. kin., prompt
?	?	?	37.7 (20)	8 (4)	-	-	-	-	rest. kin., prompt
?	?	(9/2+)	73 (2)	8 (2.5)	0.347	3.06	51 (16)	153 (48)	random, γ-γ(90,125,116,103), ①, ②
?	?	?	78.0 (15)	-	-	-	-	-	random, ②
?	?	?	97.6 (15)	23 (15)	0.1548	1.062	103 (67)	183 (119)	rest. kin.,
?	?	?	136.6 (15)	14 (12)	0.0619	0.308	56 (48)	69 (59)	rest. kin.
?	?	?	143.5 (15)	8 (8)	0.0543	0.257	32 (32)	38 (38)	rest. kin.
?	?	?	152.5 (15)	26 (11)	0.0461	0.2050	105 (44)	121 (51)	rest. kin., random, γ-γ(125,91) ③
?	?	(7/2+)	158.2 (3)	36 (12)	0.0419	0.18	146 (49)	165 (55)	rest. kin., random, γ-γ(125,91) ④
?	?	?	199.5 (20)	10 (10)	0.0231	0.0784	43 (43)	46 (46)	rest. kin.
?	?	(9/2+)	777 (2)	6 (4)	0.000876	0.000994	58 (39)	58 (39)	rest. kin., ⑤

Table 6.17: Unknown or Weak γ-ray intensities for the ^{99}Rb case. $I_{\gamma}^{Meas.}$ are the raw intensities measured. Coef. (M1) and Coef. (E2) are respectively the M1 and E2 conversion electron coefficients calculated from Ref. [196]. $I_{Eff+Conv}$(M1) and $I_{Eff+Conv}$(E2) are intensities with efficiency correction and conversion electrons correction. Some comments or observations are added in case of difficulties to determine the properties of the transition. In order to respect a proper ratio between intensities, the identification of the particle is necessary. For that purpose, the detected particles in the restricted kinematic zone have been treated.
Observation legend :
– prompt : prompt spectra without Doppler correction, all kinematics
– random : random spectra without Doppler correction, all kinematics
– rest. kin. : restricted kinematics spectra with Doppler corrections (A=99), with random subtraction
– γ-γ (E_{γ} [keV]) : observation of the transition in the projection of the γ-γ matrix for an energy gate at E_{γ}, with Doppler correction (A=99), random subtraction, all kinematics
Observation comments :
① Unknow decay or from daughter nuclei ^{99}Sr ^{99}Y ② It could be an isomer similar than for 97Rb
③ Probably populated in Coulex and decay of ^{99}Y
④ Probably populated in Coulex and decay of ^{99}Y
⑤ Probably decay of ^{99}Sr

5.3 The nuclear structure at low energy

The level schemes have been constructed using single γ-ray intensities and γ-γ coincidences. A level scheme can be drawn uncovering the underlying nuclear structure. The level schemes of ^{99}Rb and ^{99}Sr are presented on the Fig. 6.10.

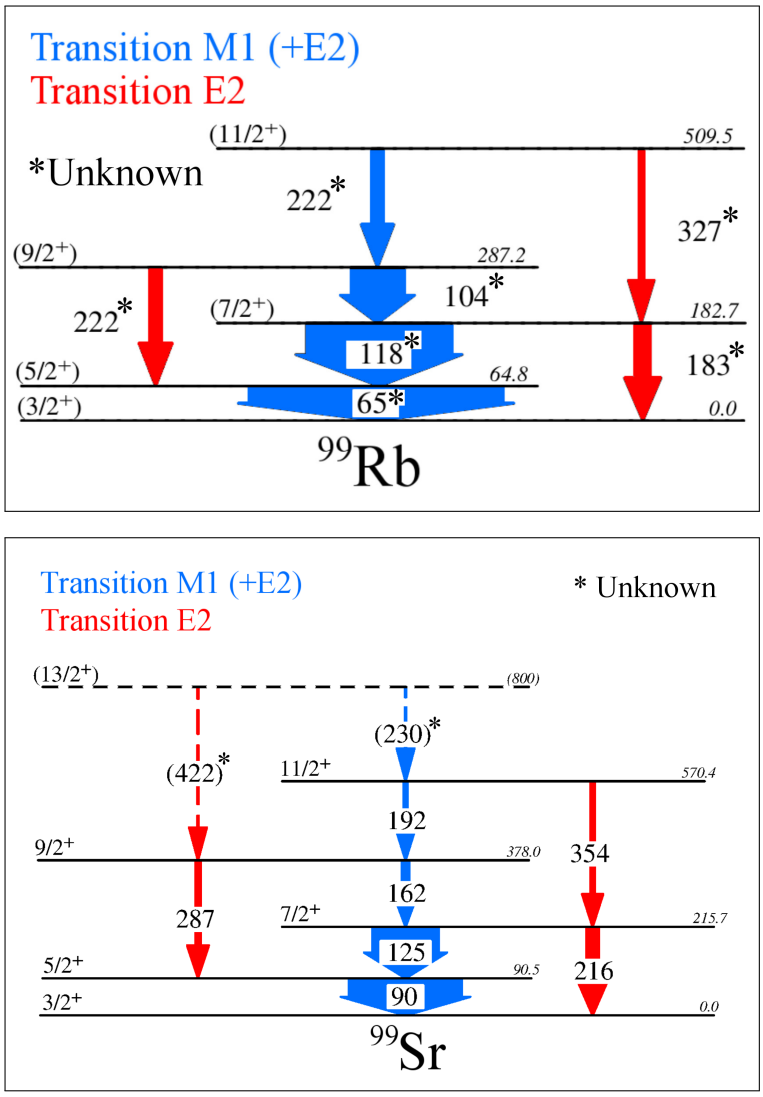

Figure 6.10: ^{99}Rb and ^{99}Sr level schemes. The nuclear spins I^{π} and the energy of the nuclear states are given respectively at the left/right. The energy of the transition are positioned beside the transition arrow. The width of the transition is proportional to the observed transition intensity.

Sometimes, the nucleus emitting γ-ray is difficult to identify for some transitions with low intensities. Too low in intensity to coincide with strong transition, they cannot be confirmed.

As shown on Fig. 6.7 and Fig. 6.10, there is a striking similarity between the ground-state rotational bands of ^{97}Rb and ^{99}Rb. This situation is equivalent than for the ^{98,100}Sr isotopes, which has already been discussed by Lhersonneau et *al.* in the Ref. [56]. The two Sr isotopes have identical deformations within errors ($\beta_2 \simeq 0.4$). Considered as perfect rigid rotors, the same behavior is expected for the ^{97,99}Rb isotopes.

5.4 Matrix elements and transition strengths with GOSIA2 calculations

Normalization As in the ^{97}Rb case, the large amount of ^{99}Sr in the beam contributes to excite the target nuclei. The presence of the ^{86}Kr in the beam will affect in the same way the target excitation. Indeed, even if none of the transitions of the Kr isotope have been identified, the Kr can still excite the target. The

normalization of the intensities is not facilitated in such case, because the target excitation does not come only from the Rb nuclei. Moreover, the target excitation of the ^{60}Ni was not observed.
The matrix element of the electromagnetic operator could not be extracted since there is not any experimental reference to normalize them, such as the matrix element corresponding to the target excitation used in the ^{97}Rb case.

6 Discussion

6.1 Introduction

The analysis of the Coulomb Excitation via the GOSIA code provided a lot of transitional and diagonal matrix elements for the Rb isotopes; however, the number of observables and their accuracies are not sufficient to constrain them firmly. The transitional matrix elements can be translated in reduced transition strengths and the diagonal matrix elements in static quadrupole moments. More generally the matrix elements of the electromagnetic operator tell us how important is the electromagnetic coupling between the different nuclear states.
The main information discovered from this experiment will be synthesized and discussed in this section. The results obtained for the ^{97}Rb isotope, the first exhibiting deformed ground state, will be compared to theoretical calculations. The values obtained from the analysis will be put in perspectives.

6.2 Nuclear Structure before N=60 : the ^{91,93,95}Rb isotopes

The ^{93,95}Rb isotopes have similar excited structures and should have as well similar configurations. They both present single-particle like low lying structures. At the N=56 sub-shell closure, the inversion of the ground state spins configurations between ^{91}Rb(N=54, $3/2^-$) and ^{93}Rb(N=56, $5/2^-$) can be explained by a repulsive tensor force between the $\nu g_{7/2}$ and $\pi f_{5/2}$ orbit, see Fig. 6.11, see Ref. [203, 204, 205]. By filling the $\nu g_{7/2}$ orbit the tensor force will repulse the $\pi f_{5/2}$ orbit up in energy. At the same time, the $\pi 2p_{3/2}$ orbit is attracted and reach lower excitation energy.
The $\pi 2p_{3/2}$ and $\pi f_{5/2}$ orbits are quasi-degenerated in energy. A small variation in their single particle energies caused by e.g. tensor force when filling the $\nu g_{7/2}$ orbit, could move one or the other closer to the Fermi level.

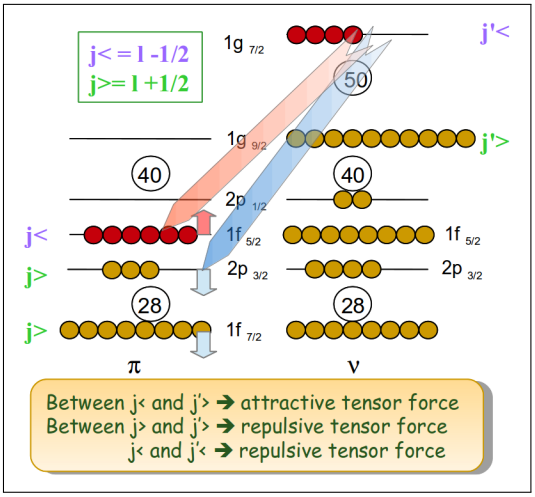

Figure 6.11: Tensor force at the N=56 sub-shell closure in the Rb isotopes. The energy of the orbital changes according to their spins: if they are anti-parallel the tensor force is attractive, if they are parallel the force is repulsive.

In the present experiment, new low-lying transitions have been identified in the ^{93,95}Rb isotopes. This experiment reports for the first time the strong similarities of the low-lying states of the ^{95}Rb with the ^{93}Rb isotope. Both should have similar configurations, as proven for the higher-lying and isomeric states (populated by β-decay), see Ref. [104, 206]. By adding two neutrons the low-lying structure is almost unchanged.

A shell model description for higher-spin states of the ^{91,93,95}Rb has been provided by shell model calculations using the m-scheme code ANTOINE in the Ref. [104]. They aimed to confirm the different proposed dominant configurations in the region for which the following orbitals $\pi f_{5/2}$, $\pi g_{9/2}$, $\nu d_{5/2}$, $\nu g_{7/2}$ and $\nu h_{11/2}$ are near the Fermi level.
The calculations used a valence space based on a ^{78}Ni core, including the $\pi 1f_{5/2}$, $\pi 2p_{1/2}$, $\pi 2p_{3/2}$, $\pi 1g_{9/2}$, $\nu 2d_{5/2}$, $\nu 3s_{1/2}$, $\nu 2d_{3/2}$, $\nu 1g_{7/2}$ and $\nu h_{11/2}$ orbits. The calculations performed for ^{91,93}Rb and ^{95}Y are presented

in the Fig. 6.12. For convenience, the 5/2- state is placed at 0 keV for both experimental and calculated values.

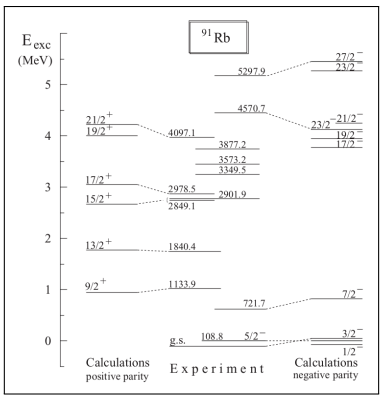

(a) Comparison of the excited state energies between the experimental and the shell model calculation values in the ^{91}Rb.

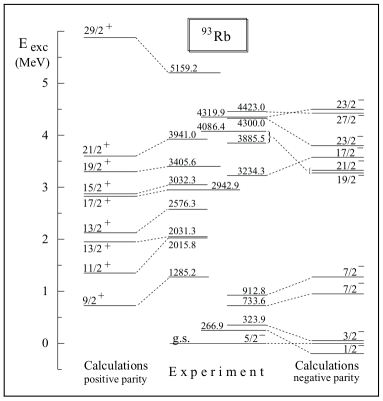

(b) Comparison of the excited state energies between the experimental and the shell model calculation values in the ^{93}Rb.

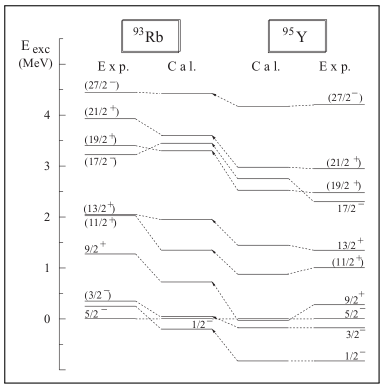

(c) Comparison of the excited state energies between the experimental and the shell model calculation values in the ^{93}Rb and ^{95}Y.

Figure 6.12: Shell model calculation realized in order to compare the experimental and calculated values of the yrast and near-yrast states in the ^{91,93}Rb and ^{95}Y. From Ref. [104].

The calculations for the negative parity states reproduce properly the excited pattern observed in the ^{93}Rb nuclei. The results for the ^{93}Rb are compared to the ^{95}Y for which the same interaction has been used. The ordering of the low lying states, specially for the $3/2^-$ and $5/2^-$ is respected. One can reasonably assume that the results would be the same for the ^{95}Rb nucleus, according to its very similar excited structure.
However, in the calculations, the $1/2^-$ state is not in accordance with the experiment. The $1/2^-$ state is observed experimentally with an "isomeric" nature at around 250 keV in the ^{93,95}Rb isotopes.

The Coulomb excitation technique allowed the extraction of transition strengths. It is more sensitive to E2 excitation constrains efficiently the B(E2), providing confident results. However, the B(M1) are weakly constrained.
Indeed, comparing states of ^{93}Rb and ^{95}Rb with similar configurations, they should have close transition strengths, which is the case for the B(E2) transition strengths. However, the low sensitivity of the technique regarding the M1 cannot allow us to deduce any physics properties from them. Actually, even if some of the matrix elements present small error bars, it does not mean that the result is correct but only that locally a minimum is found.
The shell-model calculations reproduce well the higher-spin low excitation energy structures in the ^{93,95}Rb isotopes. However, in Coulomb excitation we can observe a larger variety of low-spin and low excitation energy states. Those ones cannot be easily identified within the shell-model calculations. In the following Subsec., new calculations performed on the Rb isotopes for $N \geqslant 60$ are presented in order to give a physical interpretation of the structure change observed experimentally.

6.3 Nuclear Structure at N⩾60 : the ^{97,99}Rb cases.

As shown on Fig. 6.7 and 6.10, there is a striking similarity between the excited structure of the ^{97}Rb and ^{99}Rb isotopes, presenting both rotational bands. The observation of rotational bands is a direct proof of the non-sphericity of the ground states. The different Nilsson orbitals involved in the appearance of deforamtion are sown on Fig. 6.13.

In ^{97}Rb, the 275.3 keV transition has been placed on top of the 294.9 keV level, according to the single spectra and coincidences analysis. The nature of the corresponding state is not known and cannot be confirmed with the present set of data. However, some propositions could be done regarding the systematics present in the neighboring nuclei. Similar configurations are found in neighboring nuclei of the region, such as the $\nu g_{9/2}$ orbit configuration observed for example at 1133.9 keV in the ^{91}Rb, at 1285.2 keV in the ^{93}Rb and at 1133.9 keV in the ^{95}Rb isotopes; one proposes to explain the presence of the 275 keV transition as coming from a similar configuration. With such configuration, the spin and parity assignment of the $9/2^+$ to the related state can be favored with the possibility of M1(+E2) transitions.

6.3.1 Isomeric decay study

In the meantime [1], the ^{97}Rb isotopes has been studied by G. Simpson et *al.* via fission with thermal neutron at the Institut Laue-Langevin with LOHENGRIN, see Ref. [207]; and by Kameda et *al.* [202] via the study of isomeric γ-decays of fission fragments at 345 MeV/u ^{238}U at the RIKEN Nishina Center RI Beam Factory using BigRIPS.
The purpose of both experiments was to investigate the isomeric states present in the region. They revealed the presence of an isomeric γ-ray transition around ~77 keV in the ^{97}Rb nucleus.

ILL experiment The identification of the transition at 76.5 keV has been done via the analysis of single events from Germanium detectors and also by applying time gates. The identification of the transition was possible thanks to the presence in the time gated spectra of the 68.2 keV transition found in our present experiment (coincidence analysis).

The 76.5 keV transition is found decaying from an isomeric state with an half life of around ~5.1(3) μs. Due to its low energy, the transition is strongly converted. The conversion electron coefficients were determined using Si(Li) detectors. The isomeric transition can be assumed decaying to the ground state.

According to the self-consistent HFB calculation of Rodriguez-Guzman et *al.*, see Ref. [75], see Fig. 2.17, based on the Gogny EDF (Energy Density Functional) DS1 parametrization, the ground state should be based on the $3/2^+[431]$ orbital with prolate deformation. Moreover, the calculations predicted an oblate excited state based on the $3/2^-[312]$ orbital, but at higher energy (~0.5 MeV).

Preliminary quasiparticle-rotor-model (QRPM) calculations have been realized on the specific case of the 76.5 keV isomeric transition by the same collaboration, see Ref. [207]. They corroborate the hypothetic filling of the $3/2^-[312]$.

RIKEN experiment The study of isomeric decays from fission fragments confirmed the presence of an isomeric transition, found at 77.1 keV with an half-life of $6.33^{+0.37}_{-0.34}$ μs. They interpreted the 77.1 keV as decaying to the ground state of ^{97}Rb nucleus. In this case, the corresponding isomeric state is understood as a shape isomer, coming from the competition between deformed and spherical configurations resulting in a shape coexistence.
They tentatively assigned the spin and parity to $5/2^-$ according to the I^π assignment of the ^{95}Rb spherical ground state. It fits the picture described in the physics motivations, where from nucleus-to-nucleus on the onset of deformation, one observed the presence of the different shape configuration moving up/down in energy.
Moreover, such state would confer an E1 characteristic to the transition with hindered B(E1), supporting self consistently the $5/2^-$ assignment ($f_{5/2}$ shell).

Unknown nature Two different assignments, deformed and spherical, have been assumed for the nuclear state associated to the 77 keV transition. Taking into account the very low energy difference between the ground and isomeric states in ^{97}Rb it is very difficult to compare their structure in any theoretical calculations. The nature of this isomer might be clarified, e.g. with moments measurements which could provide

1. between the proposal and the experiment

information both on its intrinsic structure (magnetic dipole moment) and its deformation (electric quadrupole moment).

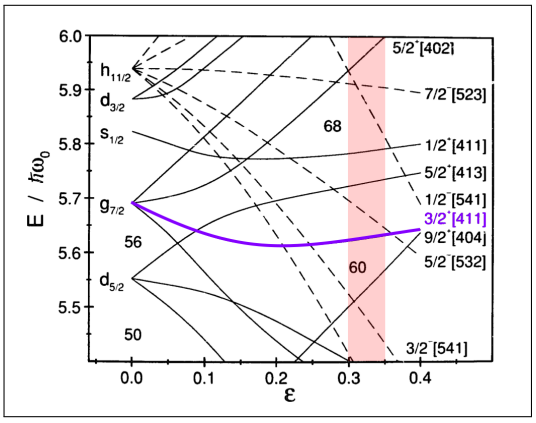

(a) For neutrons in the N=60 region . The energies were calculated using the potential parameters $\kappa = 0.066$ and $\mu = 0.35$.

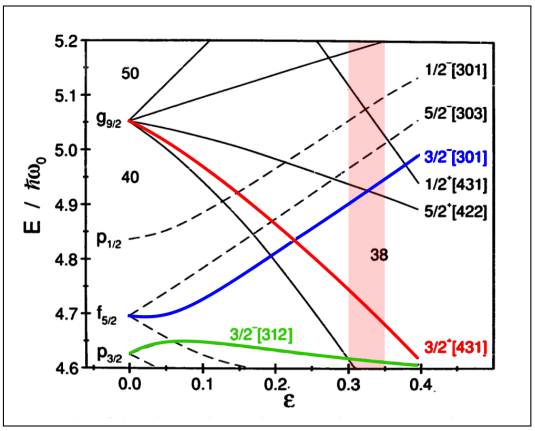

(b) For protons in the Z=40 region. The energies were calculated using the potential parameters κ =0.07 and μ =0.40.

Figure 6.13: Expanded portion of the Nilsson diagrams for neutrons (a) and protons (b). The different orbital of interest have been colored. The pink band corresponds to the intrinsic quadrupole moment measured, see Ref. [77]. Modified picture from Ref. [35, 44].

6.3.2 Shape change

As mentioned, the shape changes for a new deformed configuration. It has been expected that the $3/2^+[431]$ orbital from the $\pi g_{9/2}$ orbit and the $3/2^-[312]$ orbital from the $\pi p_{3/2}$ orbit can correspond to the ground state configuration according to the laser spectroscopic measurements [77]. The present data gave new insight to perform further calculations.

In order to assign in a consistent way the configuration observed for the ground state rotational band in the ^{97}Rb nucleus, the branching ratios were used to deduce the $|g_K - g_R|$ values. It can be obtained from the formula, see Ref. [25, 35] :

$$\left|\frac{(g_K - g_R)}{Q_0}\right| = 0.934 E_\gamma |\delta|^{-1} [(I-1)(I+1)]^{-\frac{1}{2}} \quad \text{in } [e \cdot b]^{-1} \tag{6.1}$$

where: E_γ is the energy in MeV of the γ-ray transition between the nuclear states of respective spin I and (I-1); $|\delta^2|$ is the E2/M1 mixing ratio of the transition, which is found from the branching ratio (R) as:

$$R_I = \frac{Y_\gamma}{Y_{\gamma'}} = 2K^2(2I-1)\left(\frac{E_\gamma}{E_{\gamma'}}\right)^5 \left(1+\delta^{-2}\right)[(I+1)(I-1+K)(I-1-K)]^{-1} \tag{6.2}$$

where: E_γ,Y_γ are respectively the energy in MeV and yield of the transition between the nuclear states of respective spin I and (I-1); $E_{\gamma'}$,$Y_{\gamma'}$ are respectively the energy in MeV and yield of the transition between the nuclear states of respective spin I and (I-2).

$$\frac{B(M1; I \to (I-1))}{B(E2; I \to (I-2))} = \frac{12}{5}\left(\frac{g_K - g_R}{Q_0}\right)^2 K^2 \left(\frac{< IK10|(I-1)K >}{< IK20|(I-2)K >}\right)^2 \quad \text{in } \left[\frac{\mu_N^2}{e^2 fm^2}\right] \tag{6.3}$$

The ratios B(M1)/B(E2) can be derived form the experimental branching ratios obtained from the analysis, see Eq. 6.3.

The experimental values of the different parameters describing the nuclear structure of the ^{97}Rb nucleus are summarized in the Tab. 6.18.

6.3.3 Comparison with theory

Quasi-particle + Rotor Model The calculations performed on the ^{97}Rb by G. Simpson [208] with a quasiparticle + rotor model are presented on the Fig. 6.14. The correct level spacing between the different

nuclear states has been well reproduced for a $3/2^+[431]$-like configuration by "adjusting" the deformation and the Coriolis force. The B(E2) transition strengths and branching ratios constitute also minimization parameters of the theoretical models, which have to reproduce the level spacing and the transition strengths at the same time.

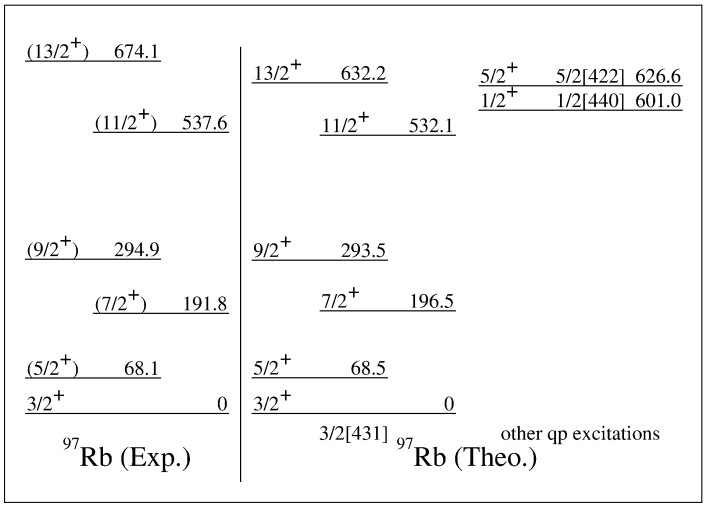

Figure 6.14: Quasi-particle + Rotor calculations performed by G. Simpson [208]. The calculations assumes a rigid rotor.

According to those calculations, one cannot exclude that the state corresponding to the 275 keV transition is based on the $1/2^+[440]$ orbital.

Independent Quasi-particle Model Mean Field calculations on ^{97}Rb isotope have been performed by Filip Kondev [209] on the specific case of the ^{97}Rb nucleus. A Wood-Saxon potential with a "universal" parametrization, as described by P. Moller et *al.* [95], has been used with the BCS model. Some basical concepts of such model are shown in Appendix. A 207.
The deformed band structure observed in the ^{97}Rb isotopes spectra for $N \geqslant 60$ led us to assume the possibility to use the rigid rotor approximation as a plausible hypothesis. The ratios B(M1)/B(E2) can be derived form the experimental branching ratios obtained from the analysis, see Eq. 6.3. Due to the rigid rotor assumption, a specific value for g_R is used. In the calculation, g_R has been considered as fixed (rigid rotor).

As expected the $|g_K - g_R|$ value stay constant in our case, see Tab. 6.19 because the treated nuclear states are inside the same ground state band, implying that they have the same g_K (and $g_R \approx 0.7\frac{Z}{A}$ is fixed).

The theoretical calculations are in good agreement with the $3/2^+[431]$ orbital. At the same time, they exclude the $3/2^-[312]$ orbital possibility. The branching ratios related to the $3/2^+[431]$ orbital are of the same order of magnitude than the experimental values, and in the same order of intensities. The states related to the 7/2 and 11/2 spins respect the same behavior than in the experimental values, however they deviate slightly more than the other. This difference could come from the perturbation applied by the Coriolis force, explaining the deviations of the mixing ratios and the $|g_K - g_R|$ values.
The ground state bands of the ^{97,99}Rb isotopes are expected to exhibit similar rotation and moment of inertia. The dynamic moment of inertia ($\mathcal{J}_2$) is defined as:

$$\mathcal{J}_2 = \left(\frac{d^2E}{d^2I_x}\right)^{-1} \approx 2\hbar\frac{\Delta I_x}{\Delta E_\gamma} \tag{6.4}$$

where E_γ is the energy of the transition between the nuclear states of spin (I+1) and (I-1), which is proportional to the rotational frequency, and the total aligned angular moment $I_x = \sqrt{\left(I+\frac{1}{2}\right)^2 - K^2}$. The moment of inertia ($\mathcal{J}$) is represented as a function of the nuclear spin I on the Fig.6.15(a). The total aligned angular moment (I_x) is plotted as a function of the rotational frequency on the Fig.6.15(b). The slope of the latest curve is the dynamic moment of inertia.

K,I	R_I	B(M1)/B(E2)	$\|g_K - g_R\|$	$\|\delta\|$
3/2, 7/2	0.065±0.003	$1.46^{+0.065}_{-0.068}$	$0.95^{+0.09}_{-0.09}$	$0.105^{+0.002}_{-0.002}$
3/2, 9/2	0.26±0.010	$1.48^{+0.053}_{-0.056}$	$1.11^{+0.10}_{-0.10}$	$0.057^{+0.001}_{-0.001}$
3/2,11/2	0.27±0.04	$0.88^{+1.1}_{-1.5}$	$0.91^{+0.14}_{-0.12}$	$0.042^{+0.003}_{-0.003}$
3/2,13/2	1.34±0.41	$1.59^{+0.42}_{-0.56}$	$1.26^{+0.31}_{-0.25}$	$0.046^{+0.008}_{-0.006}$

Table 6.18: Experimental values obtained for the ^{97}Rb isotope. The branching ratios, B(M1)/B(E2) ratios, $|g_K - g_R|$ and $|\delta|$ values are summarized for each nuclear state.

Q_0= 2.90 g_R = 0.30 K=3/2 g_K=1.71 3/2$^+$[431]				
K,I	R_I	B(M1)/B(E2)	$\|g_K - g_R\|$	$\|\delta\|$
3/2, 7/2	0.03	3.19	1.41	0.071
3/2, 9/2	0.16	2.38	1.41	0.045
3/2,11/2	0.11	2.13	1.41	0.086
3/2,13/2	1.07	2.00	1.41	0.041

Q_0= 2.90 g_R = 0.30 K=3/2 g_K=0.25 3/2$^-$[312]				
K,I	R_I	B(M1)/B(E2)	$\|g_K - g_R\|$	$\|\delta\|$
3/2, 7/2	4.76	0.004	0.050	2.0
3/2, 9/2	48.7	0.003	0.050	1.3
3/2,11/2	13.1	0.003	0.050	2.4
3/2,13/2	365	0.003	0.050	1.2

Table 6.19: Results obtained for the low-lying states of the ^{97}Rb isotope from the Mean Field calculations of F. Kondev [209]. The calculations have been performed for the 3/2$^-$[312] and 3/2$^+$[431] orbital, see Fig. 6.13. The g_K values are fixed according to he configuration, see text for details.

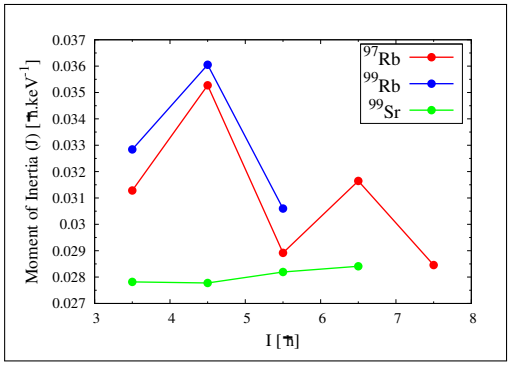

(a) Moment of inertia $\mathcal{J}$ as a function of the nuclear spin (I).

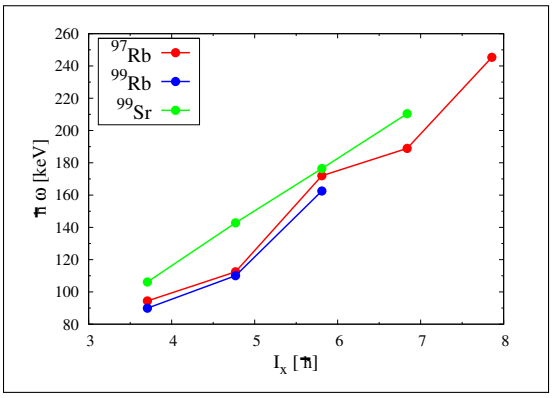

(b) Total aligned angular moment as a function of the rotational frequency for the ground state bands of the ^{97,99}Rb isotopes.

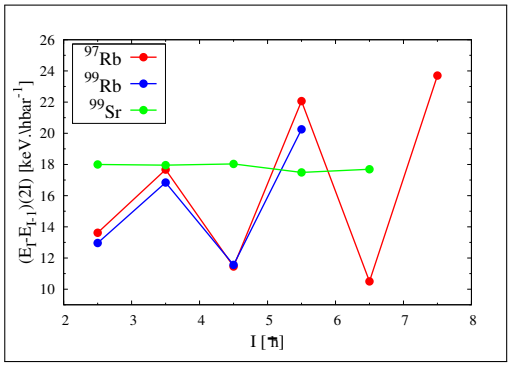

(c) Rotational constant as a function of the spin for the ground state bands of the ^{97,99}Rb isotopes.

Figure 6.15: Experimental moment of inertia, rotational constant and total aligned moment for ^{97,99}Rb and ^{99}Sr.

The presence of staggering effect is highlighted in the Fig. 6.15(c) where the rotational constant is plotted as a function of the spin. The cascade transition energy divided by twice the initial spin give the rotational constant $A = \frac{\hbar^2}{2I}$. The moment of inertia is almost constant with just a trace of signature splitting. The

presence of the signature splitting can be explained by the presence of an important Coriolis force or a perturbation applied by a band with another K quantum number, such as K=1/2.

6.4 Decay products

Considering the half-live of the ^{97,99}Rb and due to the technique employed to deliver the beam, the ^{97,99}Sr decays products represented an important portion of the beam and their Coulomb excitation occurred, see Chap. 4 on page 73. The low-lying excited structures of the latter have been already investigated by several experiments. Representative level schemes of the ^{97,99}Sr isotopes, including the low-lying nuclear states found experimentally, are shown on the Fig. 2.9(a) for ^{97}Sr and Fig. 6.16 for ^{99}Sr.

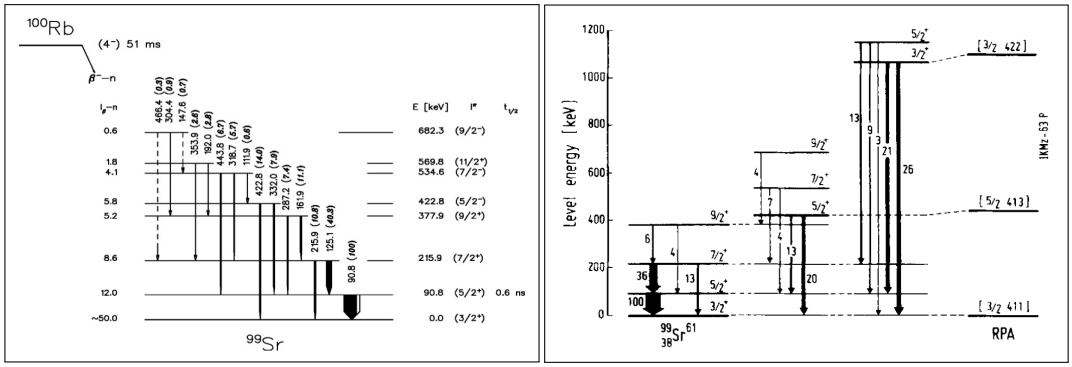

(a) Partial decay scheme of ^{100}Rb to ^{99}Sr.

(b) Band structures in ^{99}Sr.

Figure 6.16: Level schemes of ^{99}Sr. (a) Partial decay scheme of ^{100}Rb to ^{99}Sr. (b) γ-transitions and their relative intensities are given, together with the Nilsson configurations of the band heads deduced from shell model calculations in the RPA.
Figures modified and based on the studies of Lhersonneau et *al.* [210] and Pfeiffer et *al.* [42], see Ref. [211] for the complete level scheme.

According to the *"Table of Isotopes"* of R.B. Firestone [180], a $3/2^+$ spin has been assigned to the ground state of the ^{99}Sr nucleus. This assignment is claimed due to the observed yields from the ^{99}Rb β-decay [42] feeding the ^{99}Sr states of the rotational ground state band. The β-branch from the expected $\pi 3/2^+[431]$ ground state of the ^{99}Rb nucleus to the ^{99}Sr g.s. has a $\log(ft) \sim 5.0$; and the β-branch from the ^{99}Sr g.s. to the $\pi 5/2^+[422]$ ^{99}Y g.s. has a $\log(ft) \sim 5.2$. The latter β-branches led to consider the related transition as β-allowed. In such way, the two ground states should have the same parity and spins with $I_f = I_i \pm 0, 1$. The possible g.s. with negative parity are thus excluded. The different configurations in the region which could fit the ^{99}Sr case are the $\nu 3/2^+[411]$ and the $\nu 5/2^+[413]$ orbitals, see the Nilsson diagram Fig. 6.13. The $\nu 5/2^+[413]$ orbital is placed higher in energy and thus unfavored. Consequently, the spin/parity of the ^{99}Sr ground state has been assigned to $3/2^+$ of the $\nu 3/2^+[411]$ orbital. It has been confirmed by shell model calculations, see Ref. [42]. Moreover, the steady assignment of the $3/2^+$ from the $\pi 3/2^+[431]$ orbital to the ^{99}Rb g.s. is in agreement with the ^{99}Sr assignment in a self consistent way.

The transitions identified for the ^{97}Sr were already known and not any other structure has been observed. On top of the single particle spectra observed in the present Coulomb excitation, deformed configurations similar to the neighboring nuclei have been uncovered by previous studies. For example, the rotational band proposed with a K=3/2, $\nu 3/2^-[541]$ configuration is found at 644.5 keV in the ^{97}Sr and at 614.5 keV in the ^{99}Zr.

The ^{99}Sr rotational ground state band configuration has been also observed higher in energy in the ^{101}Sr isotope at 271.2 keV, see Fig. 6.17.
The 422 keV and 230 keV transition have been placed in the rotational g.s. band. It has been observed in single spectra and coincidence matrices as respectively on top of the 378.0 keV and 570.4 keV levels of the rotational band. However, they are mainly observed in coincidence with strong transitions, such as the 90 keV transition.
The observed 422 keV transition can possibly correspond to the 422.8 keV state in the ^{99}Sr (direct decay to the g.s.). However, the appearance of the 230.5 keV transition in the single spectra and γ-γ matrices led to

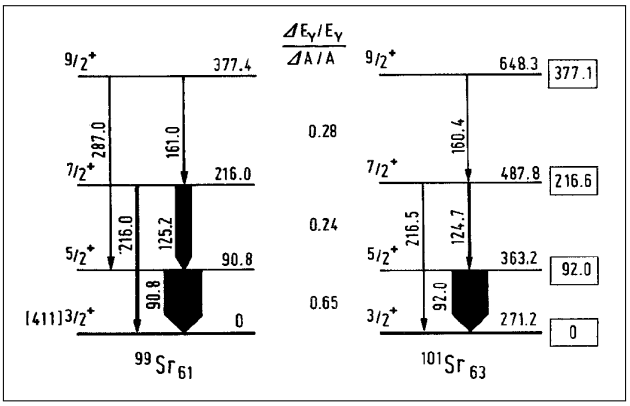

Figure 6.17: Very similar bands built on the $\nu 3/2^+[411]$ orbital in ^{99}Sr and ^{101}Sr. Level energies in ^{101}Sr are indicated relative to the band head at 271.2 keV. From Ref. [212].

envisage the hypothesis that they belong to the ground state rotational band.
The systematics of the rotational frequency (ω), moment of inertia ($\mathcal{J}$) and aligned angular momentum (I_x) in the ^{99}Sr case are in good agreement with this assumption, following the trend observed for lower excited energies.

7 Summary and Conclusions

The present work demonstrates the possibility to study in details the nuclear structure of very neutron-rich nuclei using γ-ray spectroscopy. The present results concern the neutron rich rubidium isotopes in the A$\sim$100 mass region, where nuclei exhibit strong deformation in their ground states adding one neutron around N$\sim$60. If one takes the proton point of view, adding just one proton to the N=60 isotones the nuclei pass from spherical-like shape to well deformed.

Rotational bands in the newly excited ^{97,99}Rb isotopes and ^{99}Sr nucleus confirmed the presence of deformation for N$\geqslant$60. Moreover, the scenario of a rapid shape transition at the onset of deformation is also validated. These nuclei exhibit the characteristics of good rotors up to the highest observed spins.

The particle-rotor model constitutes a appropriated tool to interpret the level scheme as rotational bands for nuclei with N$\geqslant$60. The experimental values have been compared to theoretical quasi-particle models which both merge on the steady assignment of the $3/2^+[431]$ orbital as the ground state configuration of the ^{97}Rb. The strong similarities observed in the rotational frequency, moment of inertia and total aligned angular moment between the ^{97}Rb and ^{99}Rb isotopes led to assign the same configuration for the ^{99}Rb ground state.

Two possible new transitions on top of the ^{99}Sr nucleus have been observed. Their introduction in the ^{99}Sr level scheme is in adequacy with the systematics observed in terms of rotational frequency, moment of inertia and total aligned angular moment.

8 Outlooks and Perspectives

A Coulomb excitation experiment realized with a ^{196}Pt target is still under investigation for the ^{99}Rb beam and could lead to a direct normalization of the matrix elements using the low γ-ray energy of the ^{196}Pt first excited state. It remains difficult to disentangle the part of the target excitation due to the ^{99}Rb nucleus. The restriction of beam time with this target enforced to collect a low statistics. From this normalization, one could deduce the absolute normalization of all the matrix elements, convoluting the results from the relative intensities obtained with the ^{60}Ni and the absolute normalization obtained with the ^{196}Pt target.

It would be interesting to evaluate the de-orientation effect for the different probed nuclei by adding the magnetic dipole moment in the calculation. In a first time using the approximation $g = g_R \approx \frac{Z}{A}$ and after with the g-factor found from the experimental data.

For the ^{97}Rb, the isomeric state ($\sim$75 keV) and the state corresponding to the 275 keV would be introduce in the GOSIA minimization in a close future, in order to evaluate their impact. Moreover, moments measurements could be envisage to gain significant information in terms of intrinsic structure and deformation. In addition, it would help to firmly constrain the matrix elements.

Polarized beam The Coulomb excitation technique constituting already a powerful tool for nuclear structure study could be improved by using nuclear spin polarized beam. One can envisage the possible effects of such polarization in the angular distributions which would help for example to determine the transition nature (M1, E2, ...).
A project supported by CERN envisaged the use of the Tilted Foils Technique (TFT) in order to operate such polarization. It constituted the original thesis project of my doctoral studies. The experimental setup and preliminary results are briefly discussed in the following.

Part II

Investigation of Nuclear Spin Polarization with the Tilted Foils Technique

Introduction

In our studies, we try to investigate the nuclear properties in order to understand the interaction which binds the protons and neutrons inside the nucleus. Our experiments aim to measure the basic nuclear properties such as the lifetime, the decay, the moments and the spins. The knowledge of those properties give new insight on the nuclear structure and the strong nuclear force binding the nucleus. They are used to derive new information and interpretations from different nuclear models.

The intrinsic angular momentum, or usually called spin, characterizes directly the nature of the particle. It is submitted to the same laws governing the quantum momentums such as the orbital angular momentum.

The control of the spin population of nuclei is of great interest to probe the nuclear structure. Nuclear spin-polarized Radioactive Isotope Beams (RIBs) represent a powerful tool to study the nuclear structure and electromagnetic properties of materials with β-NMR (Nuclear Magnetic Resonance) and γ-ray spectroscopy. As example of experimental methods using oriented beams, one can cite the Time Differential Perturbed Angular Distribution (TDPAD) used to measure the magnetic dipole and electric quadrupole moments of microsecond isomeric states.
The possibility to obtain nuclear spin-polarized ensembles has already been investigated for many decades with different methods, e.g. the Low Temperature Nuclear Orientation (LTNO). Concerning specifically the polarization of RIBs, two main techniques are used nowadays: the optical pumping employed in ISOL facilities, and the projectile-fragmentation reaction method used at the In-Flight facilities. The optical pumping technique is not suitable for any RIBs far from stability and any chemical elements. The projectile-fragmentation can produce polarization only in a specific beam energy range.
The tilted foils technique offers the possibility to use short lived radioactive beams by polarizing the nuclei in-flight. Already investigated in the past, new interests for this technique arose since the recent use of RIBs far from the β-stability valley.

One proposes to investigate the possibility to nuclear spin-polarize RIBs using the specific Tilted Foils Technique (TFT) at the CERN-ISOLDE facility. The nuclear polarization project at CERN started many year ago with the High Voltage Platform (HV Platform); in the present study, one uses post-accelerated beams from REX-ISOLDE. The REX-ISOLDE setup offers the possibility to post-accelerate polarized beams, but also the possibility to investigate several charge states and beam energies.

The polarization project can be separated in three different parts. The first part consists to investigate the effect of polarized beams in reactions. A Coulomb excitation of ^{21}Ne has been realized with a mobile tilted foils setup, in order to look for an asymmetric feature in the angular distributions of scattered particles. Its analysis has been reported by my colleague H.T. Törnqvist in his licentiate thesis and in the following Ref. [213, 214]. At the origins of the project, the Coulomb excitation experiment presented in the previous part was envisaged to be performed with polarized beam using the mobile tilted foils setup.
The second part, corresponding to the present work, consists to study the impact of the different parameters of the TFT used to obtain a high degree of polarization. In order to measure the spin polarization, the β-NMR technique has been employed. An important phase of development preceded the first experiment. The main part of our work consisted to design a TFT polarizer and a β-NMR setup as well as the development of the related electronic system and acquisition system.
The last part consists to investigate the possibility to post-accelerate polarized beam keeping a high degree of polarization, see Ref. [215, 216].

The preliminary results of the commissioning experiment with a ^{8}Li beam realized in July 2012 will be presented and discussed.

Chapter 1

Physics Motivation

A manner to increase our knowledge on the atomic nucleus, is to control one or several of its properties. Among the properties of the nuclear matter under extreme conditions, the nuclear spin represents a crucial parameter.

The control over the nuclear spin-oriented ensemble (non-uniform population of states) is beneficial to improve the sensitivity of several experimental methods. In a statistical point of view, the introduction of oriented spins in collection of nuclei, reactions or decay channels reduces the number of degrees of freedom . It can allow the experimentalist to access to otherwise inaccessible observables.
As an example, we already envisaged to determine the spin/parity of the nuclear states populated in the Coulomb excitation of Rb isotopes with a polarized beam.

Several techniques already exist to produce ensembles of spin-oriented nuclei. The orientation can be obtained from reaction mechanisms where the studied nuclear state is produced, or, from the interaction of the ensemble of nuclei with its environment after the production of the nuclear states.

The oldest technique employed to produce polarized ensembles is the Low Temperature Nuclear Orientation (LTNO), see Ref. [217]. The nuclei are usually implanted in a ferromagnetic host at very low temperature of around few mK, and a strong magnetic field of around few T is applied on the nuclei ensemble, orienting the spins in the preferential direction of the field. At this temperature, the nuclear spins follows the Boltzmann distribution with different population of the magnetic sub-states. The amount of polarization resulting from this technique varies in the range of around 10% to ~ 100%.strong magnetic field the nuclei are usually implanted in a ferromagnetic host placed at very low temperature of around few mK. At this temperature, the nuclear spins follow the Boltzmann distribution creating different population of the magnetic sub-states.

Another renowned technique is the optical pumping, see Ref. [218]. It can be used to polarize an ensemble of nuclei. The process consists to apply several absorption of polarized photons and spontaneous emissions of photons on the atomic cloud. This process can be performed by using circularly polarized laser light. For an appropriate atomic scheme of the related nucleus, the atomic spins can be oriented. By hyperfine interaction the atomic orientation is transfered to the nucleus.

Among the different reactions used experimentally, the projectile-fragmentation reaction produces directly a certain magnetic sub-states distribution. The projectile impinges the target with a beam energy of around few MeV/u and produce fragments based on the initial projectile, plus abrazed nucleons. K. Asahi [219, 220] and H. Okuno [221] demonstrated experimentally that for a small angle respect to the primary beam direction, the fragment can be polarized. This in-flight technique can reach a level of polarization of ~10-15% at most.

According to the envisaged experimental study, the appropriate polarization technique has to be chosen. The mentioned polarization techniques used today benefits of high degree of polarization; however, they are restricted due to the final beam energy, lifetimes or chemical nature.

A project has been established at the CERN-ISOLDE facility [222] in order to evaluate the possibility to use the tilted foils technique to polarize RIBs.
It consists to spin polarize the ion beam, passing through thin foils tilted at an oblique angle with respect to the beam direction. The initially obtained atomic polarization is transferred to the nucleus by hyperfine interaction. This technique does not depend on the chemical nature of the element. Short lived nuclei can be polarized in-flight without any need to be stopped in a catcher. It opens up the possibility to post-accelerate

such polarized RIB. The range of polarizable nuclei is assumed wide due to the only restrictions of the method to have nucleus with atomic/nuclear spins different from zero and a low beam energy (~ few tens or hundreds of keV/u).
Imagined as a compact setup, it can be easily introduced in existing beam-lines. This technique offers an easy control of the polarization direction, which can be changed at any time. The degree of polarization increases with the number of foils used. It also increases as a function of the tilt angle between the beam axis and the axis normal to the foil. It saturates as a function of the atomic spin and number of foils. However, the method is not as efficient as the others with a maximum of around 10% of polarization observed up to now.

The tilted foils technique is deemed to polarize beams, nevertheless, the mechanisms governing the polarization process and their related parameters need to be investigated in order to understand and control it. Afterward it would be simpler to adapt the technique to a specific studied nucleus. For this purpose, one developed a β-NMR setup to observe and measure the polarization of radioactive beam.

Chapter 2

Generalities

1 Polarization and alignment

1.1 Angular distribution of radiation from an oriented nuclei ensemble

The emission of the γ-rays and β-particle is determined by the spin direction (θ, ϕ). The general angular distribution of radiation emitted from an oriented state of spin I_i is found as, see Ref. [217, 223]:

$$W(\theta,\phi) = \sqrt{4\pi}\sqrt{2I_i+1}\sum_{k,n}\frac{\rho_n^k * (I_i)A_k Y_{kn}(\theta,\phi)}{\sqrt{2k+1}} \tag{2.1}$$

with ρ_n^k the statistical tensor and $Y_{kn}(\theta,\phi)$ the spherical harmonics. The statistical tensor is derived from the density matrix and is defined as:

$$\rho_n^k = \sqrt{2k+1}\sum_{m,m'}(-1)^{I_i+m'}\begin{pmatrix} I_i & I_i & k \\ -m' & m & n \end{pmatrix} <I_i m|\rho|I_i m'> \tag{2.2}$$

The statistical tensor is directly linked with the orientation parameters $(B_k(I))$, for axially symmetric ensemble, as:

$$\rho_n^k(I_i) = \frac{1}{\sqrt{2I_i+1}} B_k(I_i)\delta_{n0} \tag{2.3}$$

For axially symmetric oriented state [1], the components of the angular distribution for $n \neq 0$ are null, see Ref.[223]. Thus, the diagonal matrix elements of the statistical tensor corresponds to the population of nuclear magnetic sub-states, noted $p(m)$ with $\sum_m p(m) = 1$. Then, according to the Eq. 2.1 and 2.3 one obtains:

$$W(\theta,\phi) = \sum_k B_k(I_i)A_k P_k(\cos\theta) \tag{2.4}$$

where $P_k(\cos\theta)$ are the Legendre polynomials.

1.2 Orientation in space for axially symmetric states

An ensemble of nuclei can be qualified as isotropic, polarized or aligned depending on the space orientation of the nuclear spins. Those terms are used to describe the distribution of the m-states as:

$$\begin{aligned} \text{isotropic distribution} &: p(m) = \frac{1}{2I+1} \text{ for all m; } B_k = 0 \text{ and } k \neq 0 \\ \text{polarization} &: p(m) \neq p(-m);\ B_k \neq 0 \text{ for odd k} \\ \text{alignment} &: p(m) = p(-m);\ B_k = 0 \text{ for odd k} \end{aligned} \tag{2.5}$$

where B_k is the orientation parameter, see Ref. [217]. The different types of orientation are illustrated on the Fig. 2.1

The β-decays is a manifestation of the weak interaction and due to the parity violation of the latter, thus, the β-decays are sensitive to the polarization of nuclei ensemble. The γ-rays distribution is symmetrical with respect to $\theta = \pi/2$ [2], thus the latter are in general only sensitive to the alignment of nuclear ensemble.

1. the z-axis is chosen as the symmetry axis
2. We reminds that θ is the angle between the polarization direction and the emission of the β- γ-ray

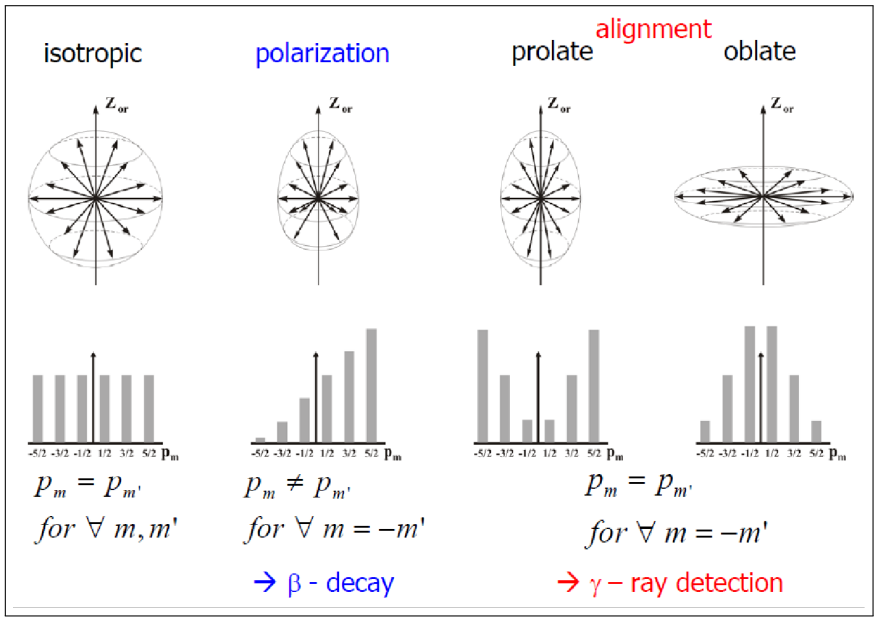

Figure 2.1: Isotropic, aligned and polarized distributions, see Ref. [224].

1.3 β-decay in Oriented Nuclear Ensemble

In order to describe the behavior of β-decay in oriented nuclear ensemble, the weak interaction is considered as of pure V-A interaction type with full violation of parity conservation and it respects the time reversal invariance [3], see Ref. [225].

1.3.1 Allowed β-decay

The electron and neutrino do not carry orbital momentum in allowed β-decay, thus their spins add up either to 0 (Fermi) or 1 (Gamov-Teller). The selection rules are found to be:

$$I_i - I_f = 0, \pm 1 \qquad and \qquad \pi_i = \pi_f \tag{2.6}$$

– If $I_f = I_i = 0$, one cannot observe any anisotropy due to the only contribution of the Fermi matrix element in the decay.

– If $I_f - I_i = \pm 1$, the Gamow-Teller matrix element is the only contributor and the angular distributions are found to be:

$$W_{\beta^\pm}(\theta) = 1 + A_1(\beta^\pm) B_1(I) \cos\theta \tag{2.7}$$

where the β-decay angular distribution coefficients are defined as:

$$A_1(\beta^\pm) = \begin{cases} \mp \dfrac{v}{c} \sqrt{\dfrac{I_i + 1}{3I_i}} & \text{for} \quad I_f = I_i - 1 \\ \pm \dfrac{v}{c} \sqrt{\dfrac{I_i}{3(I_i + 1)}} & \text{for} \quad I_f = I_i + 1 \end{cases} \tag{2.8}$$

– If $I_f = I_i \neq 0$ mixed Fermi - Gamov-Teller decay can occur. The mixing ratio defined as:

$$y = \frac{C_V <1>}{C_A <\sigma>} \tag{2.9}$$

where <1> is the Fermi (vector) matrix element and $<\sigma>$ is the Gamow-Teller (axial vector) matrix element. The angular distribution becomes:

$$W_{\beta^\pm}(\theta) = 1 + \frac{v/c}{1 + y^2} \left\{ \frac{\mp 1}{\sqrt{3I(I+1)}} + \frac{2}{\sqrt{3}} y \right\} B_1(I) \cos\theta \tag{2.10}$$

3. In those conditions, one finds $C^{(\prime)}_{A,V} = C^{(\prime)}_{A,V}{}^*$

1.3.2 First-forbidden β-decay

In first-forbidden β-decay, six different matrix elements contribute to the decay due to the orbital angular momentum (L=1) carried away. The selection rules are found as:

$$I_i - I_f = 0, \pm 1, \pm 2 \qquad and \qquad \pi_i = -\pi_f \tag{2.11}$$

In this case, the maximum angular momentum is $J = \frac{3}{2}$ and the angular distribution functions have six different coefficients $A_1(\beta^{\pm})$, $A_2(\beta^{\pm})$ and $A_3(\beta^{\pm})$. The $A_1(\beta^{\pm})$ and $A_3(\beta^{\pm})$ coefficients are associated with parity non-conserving terms. The $A_2(\beta^{\pm})$ is associated to terms deriving from the orbital angular momentum L=1 carried away by the β-particle. The different coefficients can be found in the Ref. [225].

2 Tilted Foils Polarization Process

The beam passing through a thin foil experience electron exchange inside the material. During its pass, one consider that the atomic and nuclear spins are completely decoupled. At the exit of the thin foil, the ion exhibits a important atomic polarization which is transferred in-flight to the nucleus via hyperfine interaction, see Ref. [226].

2.1 Atomic Polarization

The mechanisms responsible of the atomic spin polarization of ions passing through a foil are not fully identified and are still under investigation. One will give some explanations using a "macroscopic" treatment of the mechanisms, which corresponds to the most common picture employed to describe this phenomenon.

The degree of atomic polarization increases with the tilt angle (α) between the beam axis ($\vec{k_i}$) and the axis ($\vec{n}$) normal to the foil surface, see Fig. 2.2. The direction of polarization ($\hat{P}_J$) corresponds to the unit vector of the vectorial product of the normal axis ($\vec{n}$) and the beam direction ($\vec{k_i}$). The polarization direction can be easily changed by turning the foils along the beam axis , which would modify the normal axis direction of the foil surface, see Ref. [227].
At the exit surface of the foil, the electronic states of the outgoing ions are polarized due to the asymmetry of charge created by the tilt angle.

Another explanation has been provided by S. Momota et *al.* [228] and M. Lindroos [229]. The beam passing through a thin foil is submitted to interaction inside the foil with cylindrical symmetry respect to the beam axis (z-axis). During its pass through the foil, the ion is submitted to electron exchange and the atomic spin is completely decoupled to the nuclear spin. The ion exits the foil with a cylindrical electron cloud (aligned ions). At the exit of the tilted foil, a torque is produced between the positively charge ion and the electrons in the foil, see Fig 2.2. This torque can modify the atomic spin projection and thus polarize an ensemble of ions. In other terms, due to the angle the cylindrical symmetry is broken and a different field is felt in +z than in -z, resulting in the shift of the electron cloud mass center. Then the asymmetric charge distribution at the foil surface can polarize the atoms, see Ref. [228].

The atomic polarization depends highly on the tilt angle and it has been proven experimentally that the maximum of atomic polarization is obtained for the largest angles.
In this scenario the quality of the foil surface is potentially important. The presence of defects could create statistically more perpendicular surfaces with respect to the beam direction; and thus it would have a direct impact on the polarization efficiency.

2.2 Transfer of atomic polarization to the nucleus

After the foil, the outgoing ion has its atomic spin polarized. The transfer from atomic to nuclear polarization occurs in-flight in vacuum via hyperfine interaction. In the following, one denotes $\vec{J}$ the atomic spin, $\vec{I}$ the nuclear spin and $\vec{F}$ the total spin ($\vec{F} = \vec{I} + \vec{J}$). F is a good quantum number, resulting from the coupling of the atomic and nuclear spins.
The atomic polarization creates a hyperfine field in which the nuclear spin precess as well as the atomic spin.

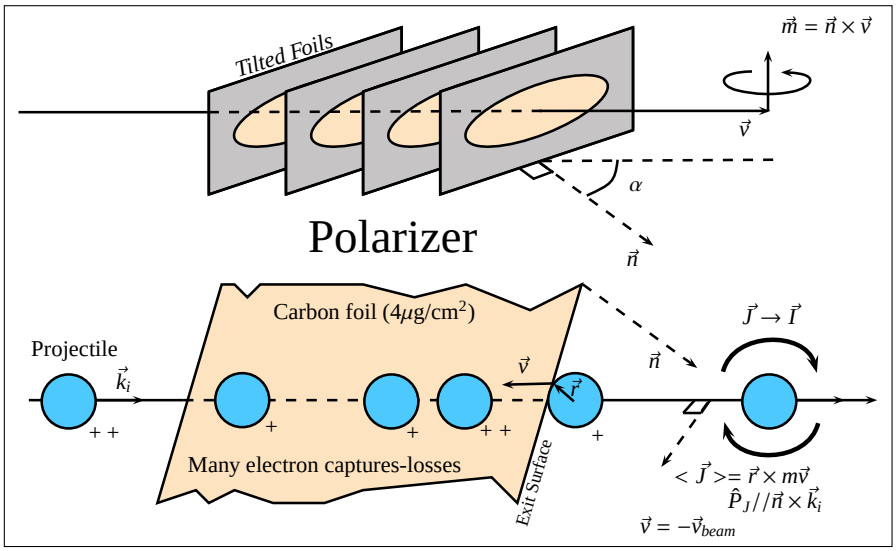

Figure 2.2: Polarization process. (top) The polarization direction is the same as the vectorial product of the axis normal to the foil surface and the beam velocity. α denotes the tilt angle. $\vec{n}$ is the outgoing surface normal. (bottom) Interaction of the outgoing ion with the foil surface. See text for more details, see Ref. [227, 228].

The total angular momentum is a constant of motion and the atomic polarization can be transferred to the nucleus via hyperfine interaction.
In order to perform the transfer, one needs to let the system precessing a large number of times ($\omega t \gg 1$) in order to make an average of the nuclear spin which has the tendency to point in the direction of $\vec{F}$, see Fig. 2.3. The time scale to generate to transfer the polarization to the nucleus has been estimated of the order of the nanosecond or less from an experimental results where an isomeric state of $T_{1/2} = 26.8$ ns in ^{147}Gd has been successfully polarized up to ~11(2)%, see Ref. [230].

2.3 Multi-foils stack

In order to obtain a high degree of polarization many foils are installed one following the other. The atomic spin will be affected with the next foil on contrary to the nuclear spin which is assumed remaining unaffected (decoupling of the atomic and nuclear spins in the foil). The phenomenon is illustrated by M. Hass et *al.* and G. Goldring and Y. Niv in the following Ref. [231, 232]. The process is repeated for each foil, reducing progressively the angle between the average nuclear spin and the average atomic spin, see Fig. 2.3.

The experimental transfer of polarization can be estimated via the transfer tensor $G_{kk'}^{qq'}(t)$ as described in the Ref. [226], which can be integrated over the time. A detailed quantum theoretical treatment is given in the Ref. [226] and will not be described deeply in this section. However, one can provide the relevant conclusions.
The total polarization transfer realized via N foils is found as $\left(G_{kk'}^{qq'}(t)\right)^N$, if only the atomic spin is interacting with the foils and the nuclear spin is affected by hyperfine interactions, if only the outgoing surface contributes to the atomic polarization (and the reset), orientation with ranks k⩾2 are negligible and $\omega_{FF'}t \gg 1$ ($\omega_{FF'}$ is the quantum angular velocity).

The most suitable beam energies to polarize RIBs are in the range of few keV/u due to the major role of the effective capture and stripping of electrons in the atomic polarization, see Ref. [230, 233].

The degree of nuclear polarization P_I and the saturation of the transfer (occurring when F and I coincide) has been found experimentally as following a classical model, see Ref. [232].
The nuclear polarization after a number of N foils is found to be:

$$P'_I(N) = P'_I(\infty)\left\{1 - \left(1 - \frac{P'_I(1)}{P'_I(\infty)}\right)^N\right\} \tag{2.12}$$

where $P'_I(1)$ is the polarization after one foil which is expressed as the product of the atomic polarization P'_J and the polarization transfer operator $P(I,J)$, thus $P'_I(1) = P'_J P(I,J)$. The polarization transfer operator is

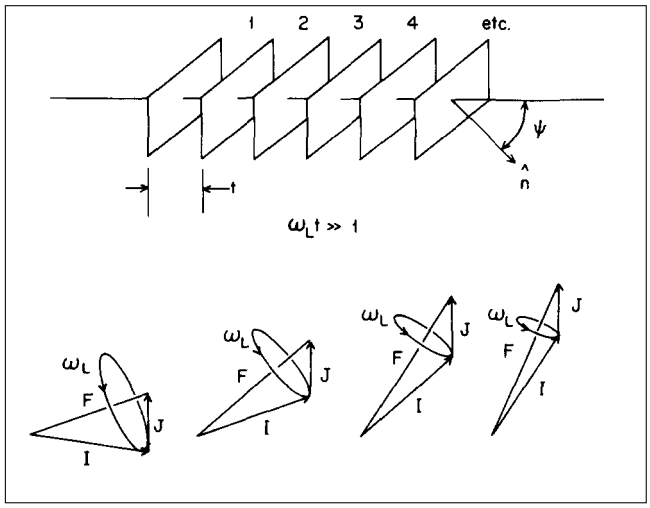

Figure 2.3: Transfer of atomic spin polarization to the nucleus with multi-foils stack. The atomic spin polarization is transferred to the nucleus via hyperfine interactions. If the multi-foils stack respects $\omega t \gg 1$, the atomic polarization is reset at the exit of each foil. The nuclear polarization is assumed remaining unaffected. In this scenario, after a certain number of foils, the nuclear polarization reaches a saturation. From Ref. [230].

defined as:

$$P(I,J) = \frac{1}{4\lambda^4}\left\{2\lambda + (\lambda^2 - 1)\ln\left(\frac{1+\lambda}{1-\lambda}\right)\right\} \qquad with \qquad \lambda = \frac{2IJ}{I^2 + J^2} \tag{2.13}$$

The saturation of polarization is found to be:

$$P'_I(\infty) = \frac{P'_J}{P'_J + (1 - P'_J)/I} \tag{2.14}$$

The usual atomic and nuclear polarization (P_X) can be directly derived from the present expressions as:

$$P'_X = P_X\sqrt{(X+1)/X} \qquad with \qquad X = I, J \tag{2.15}$$

An example of the nuclear polarization function expressed as above is given in Fig. 2.4. The nuclear polarization becomes more sensitive to low number of foils if J increases. The saturation of the degree nuclear polarization decreases as a function of J.

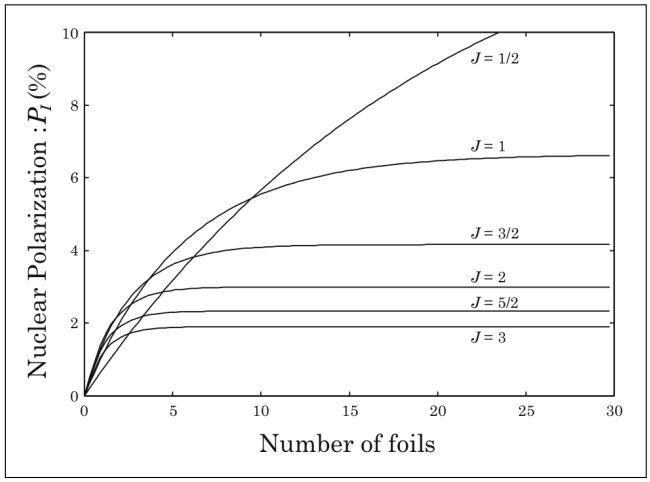

Figure 2.4: Estimated curves of the nuclear polarization form the Eq. 2.12 varying the atomic spin value J assuming a nuclear spin value of I=2 and atomic polarization P_J of 3%. From Ref. [234].

We mentioned the important dependence of the technique on the atomic/nuclear spin, on the tilt angle, on the time dependence (ωt) and on the number of foils; however, there is still a crucial parameter to possibly

control the process: the beam velocity.

H.G. Berry et *al.* [235] and Bendahn et *al.* [236] investigated the energy dependence of the orientation created by the tilted foils technique.
This parameter can possibly have an important impact on the final degree of polarization. The few experimental data does not constitute a sufficient statistics to firmly interpret the tendency. However, it seems that the nuclear spin polarization decreases going higher in energy ($\gtrsim$ 100 keV). Moreover, the last experimental data exhibited for the ^{8}Li by Hirayama et *al.* [234] that the nuclear polarization should be optimum at a lower energy of around 60 − 100 keV.

3 β-NMR and Tilted Foils techniques

3.1 External magnetic field applied on an oriented nuclear ensemble

Let us consider the case of an oriented nuclear ensemble implanted in a cubic crystal. In this case no electric field gradient is induced and thus the magnetic sub-states (m) remain degenerated.
The degeneracy is lifted when we apply a static magnetic field typically of few hundred up to few 10^4 Gauss via an external field, or via an internal hyperfine magnetic field of the host which is typically of around 10-100 Tesla.
In this case the energy difference between nuclear sub-states (m) is given by the Zeemann Hamiltonian:

$$H = -\vec{\mu}.\vec{B} = \hbar\vec{\omega_L}.\vec{I} \tag{2.16}$$

where $\vec{\omega_L} = -\frac{g\mu_N}{\hbar}\vec{B}$ is the Larmor frequency. g is the gyomagnetic factor. If the nuclei ensemble is oriented (z-axis parallel to the magnetic field), the magnetic levels are found proportional to m: $E_m = -\hbar\omega_L m$

3.2 Nuclear Magnetic Resonance

The NMR (Nuclear Magnetic Resonance) technique consists in applying a radio frequency field to spin-polarized nuclei ensemble, immersed in a static magnetic field. If the applied radio-frequency matches the Larmor frequency ($\omega_{rf-applied} = \omega_L$), this can induce transitions ($|\Delta m| = 1$) between the Zeemann splitted magnetic sub-states, causing a mixing or their populations, thus destroying the asymmetry of the angular distribution. A complete demonstration of such observable when the applied radio-frequency matches the Larmor frequency is described theoretically by Matthias et *al.* [237]. More informations can be found on the original paper of the inventors of the technique: Purcell, Torque and Pound [238].

In our case, the NMR technique is used to destroy the polarization created by the tilted foils.

3.3 TFT + β-NMR

A scheme of a typical experimental setup is shown on the Fig. 2.5.

The beam passes through the tilted foils polarizer which can modify the polarization direction by turning the foils around the beam axis. Afterwards, the beam is implanted in a sample host. The host is immersed in an external magnetic field used to preserve the polarization direction (The spins precess around the polarization direction). β-detectors are placed in the polarization direction to evaluate the asymmetry. RF coils are placed perpendicular to the polarization direction in order to apply an RF field, used to destroy the polarization.

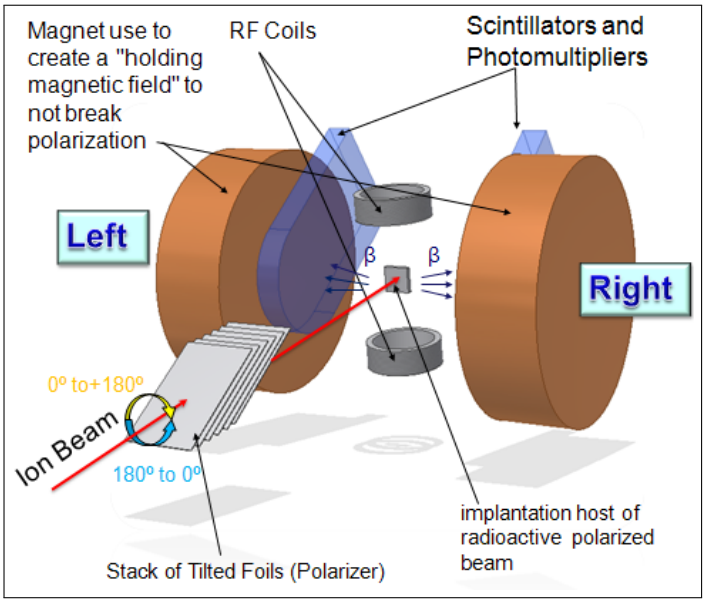

Figure 2.5: β-NMR and TFT setup.

Chapter 3

Experimental Setup and Preliminary Results

1 Introduction

The present chapter describes the experimental setups used to polarize a ^{8}Li radioactive beam at CERN using the TFT. This first test is used as a commissioning to prove the reliability of the present setup. The ^{8}Li radioactive beam has been used by several different polarization techniques. It constitutes an appropriate candidate to compare the potential of each existing technique. Further experiments for different (N,Z) combinations and atomic configurations are already envisaged by the collaboration, see Ref. [239].
One proposed to evaluate the capacity of the tilted foils and β-NMR setups that we respectively installed and developed at the CERN-ISOLDE facility. The β-NMR equipments have been donated by Pr. W.D. Zeitz from the Hahn Meitner Institute of Berlin. The tilted foils setup and all the related electronics have been entirely designed and developed by my colleague H. Törnqvist and myself.

2 Overview of the experiment

The experiment was designed to investigate the use of the tilted foils technique before post acceleration. Before the development of sophisticated setups, commissioning experiments needed to be performed. We would like to evaluate the degree of nuclear spin polarization created with the TFT by measuring the asymmetry in the distribution of β particles.
A scheme of the different setups used to deliver and polarize the RIB is given on Fig. 3.1.

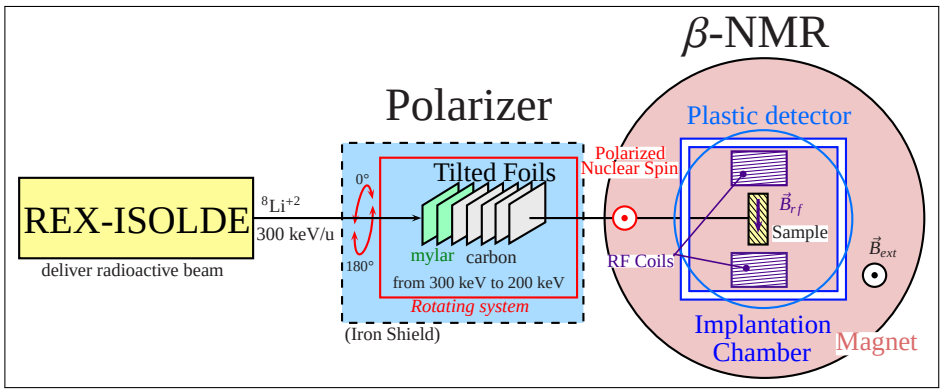

Figure 3.1: Scheme of the experimental setups.

3 Production/Delivery of ^{8}Li radioactive beam

The ^{8}Li beam has been produced via the ISOL technique. After a mass separation with the HRS, the beam has been purified and bunched in REX-TRAP. A charge breeding has been operated with the REX-EBIS. The REX-LINAC was tuned to the lowest accessible energy of 300 keV/u.
The same device has been employed to provide the $^{8}Li^{+2}$ radioactive beam than the Rb radioactive beams.

The REX-ISOLDE setup has been already described in the Subsec. 2.6 on page 83.
After the REX-LINAC, the beam can be sent to several apparatus as, for example, MINIBALL. Our setup is positioned at the second beam-line behind REX-ISOLDE, where many experiments are usually scheduled. In order to perform all of them including ours, a large space between the bender and the tilted foils setup has been added, see Fig. 3.2.

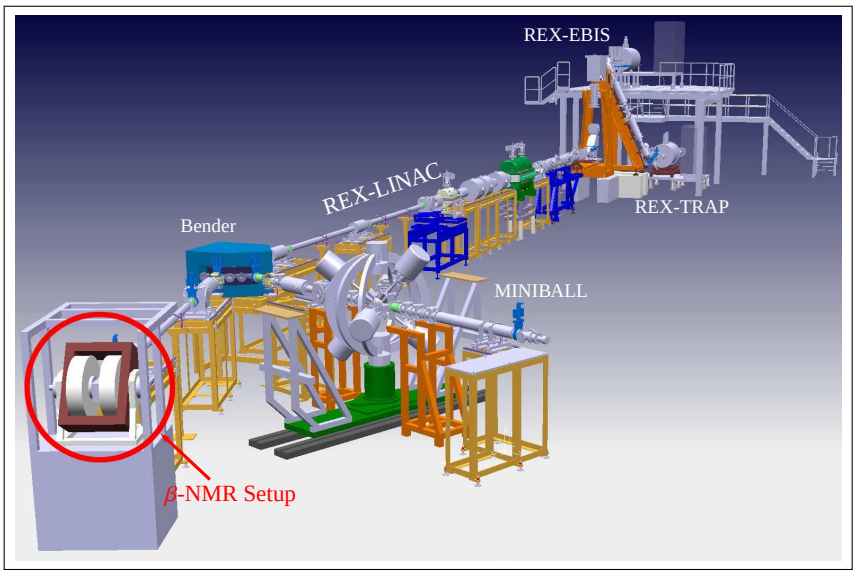

Figure 3.2: Overview of the experimental setups, including the second beam-line of REX-ISOLDE.

Before reaching the tilted foils polarizer, the phase space of the beam is controlled using different sets of triplet and doublet magnets.

4 Tilted Foils Holder and Rotating System

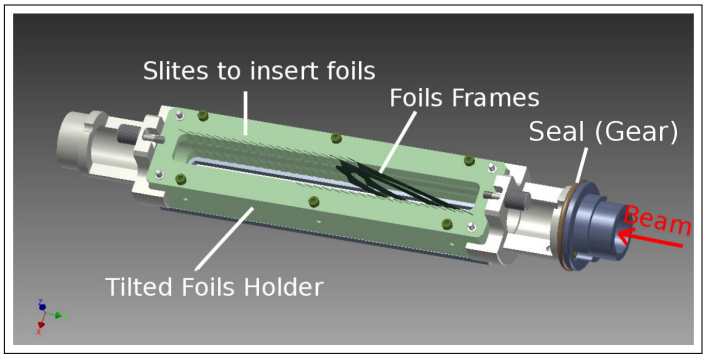

Figure 3.3: Tilted Foils Holder (for a tilted angle of 75°) and Tilting device.

The foils holder can contain up to 20 foils, see Fig. 3.3. In our experiment, we used diamond-like carbon foils of 4 μg/cm^2(~20 nm) manufactured by TU München. A set of three foils holders with different tilt angles (65°, 70°, 75°) have been manufactured by the Weizmann Institute (Rehovot, Israel).
Similar foils than the carbon foils can be used to degrade the beam energy, such as mylar foils.

A stepper motor has been installed to turn at 180° the foils holder in order to flip the polarization direction. The rotating part is turned using a gearing system constituted by a conical part (attached to the stepper motor) in contact with a seal (used as a gear). The reliability of the rotation of the tilted foils holder is insured by a

position detector. A part of the systematical error can be removed by reversing the polarization direction.

The foils chamber has a separate vacuum system in order to pump it independently.

In order to reduce the beam deviation caused by the β-NMR magnet, one decided to install a soft-iron shield around the foils holder. Simulations using the Vector Field Opera software have been performed in order to obtain a good compromise between the beam deviation (due to the β-NMR magnet), the thickness of the soft-iron shield and the available space to mount the setup, see Fig. 3.4.
Several simulation cases are reported in the Tab. 3.1.

$^{A}X^{q}$	Beam energy [kev/u]	B_{ext} [T]	Deviation [mm]
$^{8}Li^{3+}$	300	0.1	+1.5
$^{8}Li^{2+}$	300	0.1	-0.05
$^{27}Na^{7+}$	300	0.1	-0.07

Table 3.1: Results of Opera Simulations for different RIB cases. B_{ext} corresponds to the holding filed applied by the β-NMR magnet. "Deviation" is the beam deviation at the sample position without steering magnet. For all the deviation values presented, the β-NMR magnet has been shifted of 3 mm from the beamline alignment (in the same direction than the deviation).

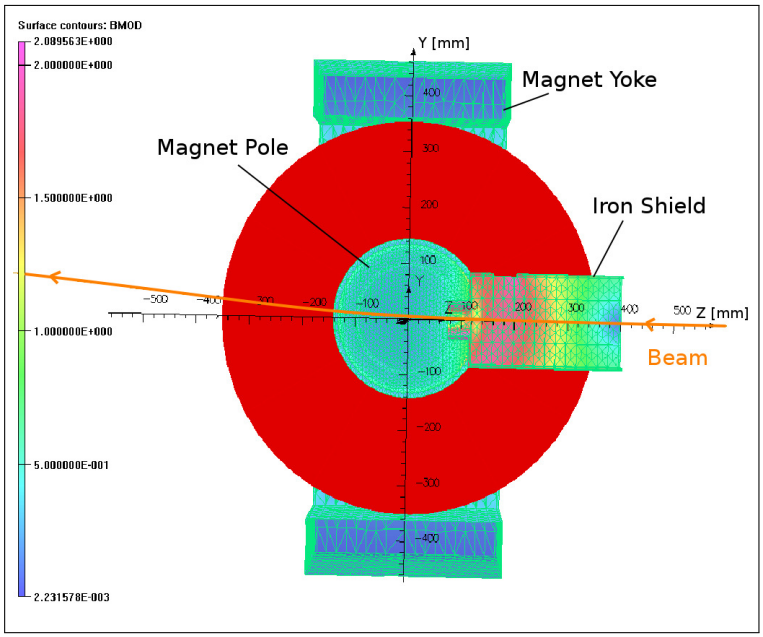

Figure 3.4: Example of opera simulation realized with a $^{8}Li^{3+}$ beam, an holding field of 0.1 T and a beam energy of 300 keV/u.

In order to compensate the resulting deviation, the magnet can be slightly moved in all the directions. Moreover, a steering magnet has been installed just before the foils chamber.

5 β-NMR setup

A global picture of the TFT and β-NMR setups is shown on the Fig. 3.5.

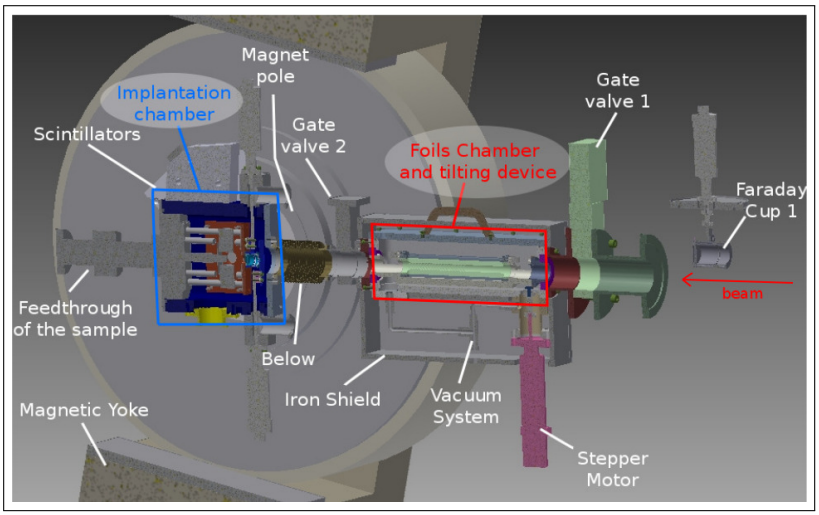

Figure 3.5: β-NMR + TFT setups.

5.1 β-NMR magnet

The β-NMR magnet is used to hold the nuclear spin in a preferential direction. It creates a low external magnetic field sometimes qualified as "holding" field.

5.2 Implantation Chamber

Technical drawings of the implantation chamber are shown on the Fig. 3.6. In order to be sure that the beam is properly implanted in the sample host, several beam diagnostic devices have been introduced: Faraday Cups, collimators for beam and β particles, and an additional detector have been placed on the sample place during the beam transport tests. Each diagnostic elements have been designed in order to fit inside the small space offered by the implantation chamber.

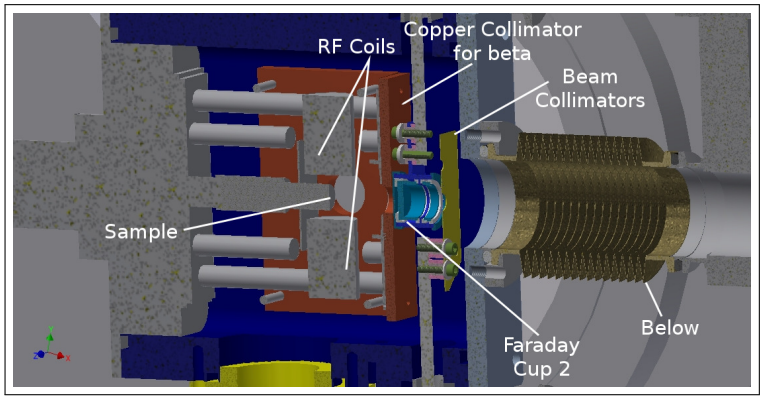

Figure 3.6: Implantation chamber.

A motion feed-through holds and positions the catcher in the center of the chamber corresponding to the center of the detection setups, and also the center of the RF coils, see Fig 3.7.

The RF frequency used to destroy the polarization is applied by RF coils which is controlled by a RF generator and a RF amplifier.
The coils positioned perpendicularly to the polarization direction in a way that the RF field is applied perpendicular to the applied external magnetic field from the β-NMR magnet.

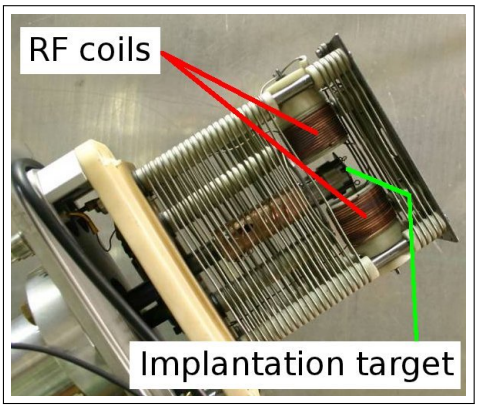

Figure 3.7: RF Coils, feed-through and sample.

In order to reduce the background, the solid angles of the β-detectors have been reduced by adding thick copper collimators. To allow the β-particles to reach the scintillator detectors and insure to keep the vacuum, two opening windows are placed in front of the scintillators in the polarization direction. They are both covered with thin niobium foils to seal the implantation chamber without stopping the β-particles.

5.3 Scintillators

The implantation chamber under vacuum let pass β particle through two niobium foil windows placed in opposite direction respect to the sample. In front of each of them, a pair of ΔE-E detectors (with respective thickness of 2 mm and 10 mm) is used to detect the β particles. The ΔE detector is used to avoid possible γ-ray background and determine more precisely the true coincidence. The implantation chamber is inserted inside a part containing the scintillators (ΔE-E detectors). From this part, light guides have been installed to collect the resulting signal from the detectors. The signal is sent to photo-multipliers, see Fig. 3.8.

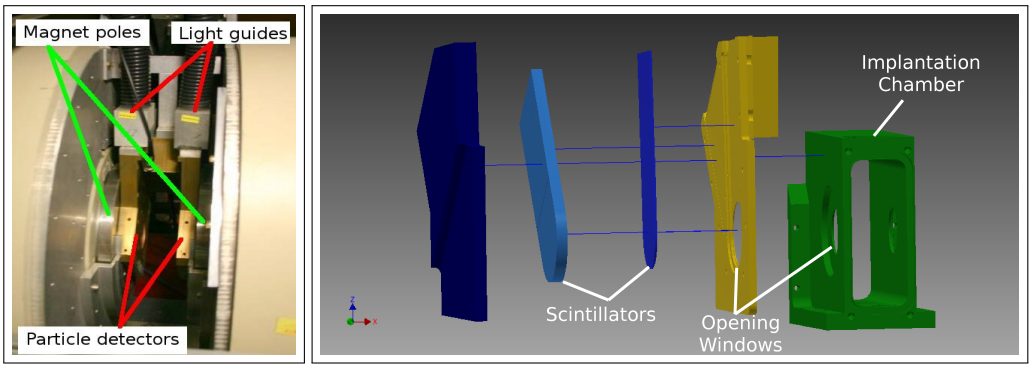

Figure 3.8: Scintillators, light guides and opening windows to detect β-particles.

6 The commissioning experiment

As mentioned above, an experiment using a well known nucleus in β-NMR was requested to validate the reliability of the developed setup. Without this commissioning test, no further investigation is possible.

A radioactive beam of $^{8}Li^{2+}$ has been used. The properties of the ^{8}Li are summarized in the Tab. 3.2. The beam intensities obtained at the entrance of the foil chamber were found around $\sim 4.10^{5}$ pps.

$T_{1/2}$	Q_e	Asym. par.: A	A/q
0.810 ms	13 MeV	-1/3	4

Table 3.2: Physics properties of the ^{8}Li. A: Asymmetry parameter, A/q: mass/charge ratio.

In order to investigate the hypothesis of higher polarization for lower beam energies, the REX-LINAC was set to the lowest accessible beam energy of 300 keV/u. One used mylar foils for slowing down more the beam before the carbon foils. The introduction of the mylar foils reduces the beam energy down to an average energy of 200 keV/u at the entrance of the stack of 10 carbon foils. The foils holder with a tilt angle of 70° has been employed in the latest tests.

Passing through the mylar and carbon foils, the beam is submitted to charge exchange and at the exit of the foils an equilibrium charge state is found. Calculations have been performed to determine the equilibrium charge state at the exit of the foils stack using the LISE++ software package [181], see Ref. [240]. One founds, in our specific case, that the main charge state after the stack of foils would be identical to the incoming beam ($^8Li^{2+}$). It is important to mention that the predictions of the equilibrium charge states for low beam energies are generally not well reproduced by the existing models.

After its polarization, the radioactive beam is implanted into a sample host, chosen with a long spin-lattice relaxation time compared to the decay time of the studied nucleus.
We opted for an implantation crystal of Pt, thanks to its cubic structure and its spin-lattice relaxation time of around ~4.3 s at T=295 K, see Ref. [241] (which is much longer than the lifetime of ^{8}Li nucleus).
In order to preserve the polarization, a holding magnetic field of 0.05 T has been applied by the β-NMR magnet. Moreover, a RF field is applied via Helmholtz coils in order to destroy the polarization and observe the amplitude of the polarization. The corresponding NMR resonance of the ^{8}Li should be found at a frequency of around f_{Larmor}=315 kHz.

7 Preliminary results

7.1 Assymetry and Ratio

The standard parameter to measure the non isotropic emission of non-parity conservation radiation is the asymmetry (ϵ) between 0°and 180°, i.e. between the left and right detectors:

$$A = \frac{L-R}{L+R} = \frac{1-\frac{R}{L}}{1+\frac{R}{L}} = \frac{1-\rho}{1+\rho} \qquad with \qquad \rho = \frac{R}{L} \tag{3.1}$$

where L and R are respectively the number of β particle detected at the left or at the right detectors.

In order to get rid of the detection efficiencies associated to the left and right detectors, a double ratio can be used. In the tilted foils technique one can easily change the polarization direction by turning the foils holder along the beam line axis. Theoretically, the polarization corresponding to a foil at an angle +180° and a foil at -0° would have the same amplitude but opposite signs. Taking into account such consideration one can cancel out the efficiency from the two detectors (in our case, one considers the coincidences occurring in a $\Delta E - E$ pair). The asymmetry is found to be:

$$A' = \frac{1-\rho'}{1+\rho'}, \qquad \text{with} \qquad \rho' = \sqrt{\frac{R(+180°)L(-0°)}{L(+180°)R(-0°)}} \tag{3.2}$$

It is important to note that if the beam is not well aligned , the symmetric configuration is broken. In this condition, the double ratio method can introduce unknown systematic errors.

7.2 Results and Discussion

The iron shield was introduced to reduce the beam deviation created by the external magnetic field of the β-NMR magnet. However, after a certain time without observing some significant asymmetry, one decided to remove it. After removing it, one could find the NMR resonance in a short time. One can reasonably expect that the presence of the iron shield perturbed the preservation of polarization during the flight of the ions between the tilted foils and the implantation host, probably due to the field inhomogeneity.

A scan with a large frequency modulation has been applied around the expected value of the Larmor frequency. An clear asymmetry is observed at around 315 kHz with an amplitude of around ∼1 %, see Fig. 3.9. One could expect that the polarization would increase with few more foils compared to the only 10 we used for this test.

One can express the β-decay angular distribution as:

$$W(\theta) = 1 + AP\beta_e \cos\theta \qquad with \qquad P = \frac{I_z}{I} \tag{3.3}$$

where: A is the asymmetry parameter, $\beta_e = \frac{v_e}{c}$, θ the angle between the polarization and the β-particle.

The convolution of the spin relaxation time (4.3 s) and the half-life (840 ms) reduces the experimentally observed asymmetry of around ∼15%.

One calculated the double ratio using fixed foil orientation, without taking into account the geometrical factor and ignoring the backscattering of β-particles [1], we obtained the lower limit of polarization at around $3.56 \pm 0.29\%$ and $-2.77 \pm 0.27\%$ for the respective angle −70°and +70°, see Fig. 3.9. It is important to note that the degree of polarization is relatively important for such intermediate beam energy.

1. The geometrical factor and the backscattering of β-particles reduces the experimental observed asymmetry.

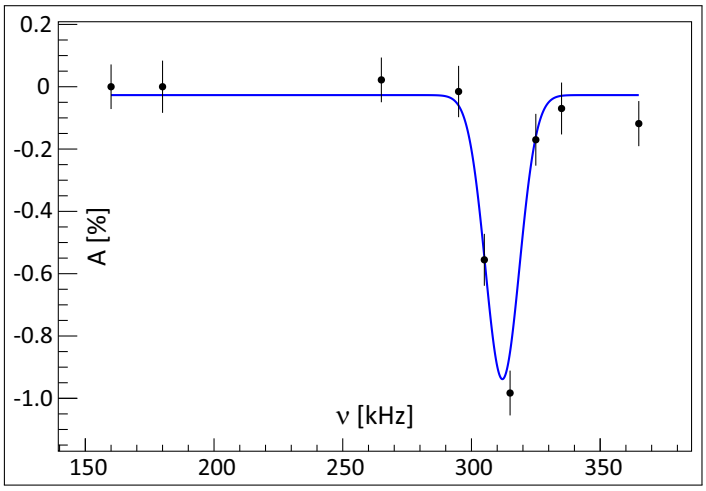

Figure 3.9: Asymmetry vs RF frequency.

JAEA-ISOL experiment In the meantime, Hirayama et *al.* [234] performed a polarization measurement using a ^{8}Li RIB at JAEA-ISOL. The primary targets of ^{13}C or boron nitride were bombarded by a 64 MeV ^{7}Li beam from the TRIAC Tandem. They used an annealed Pt catcher at room temperature, an external magnetic field of B_{ext}=0.05 T. On Contrary to us, they used thin polystyrene foils of around 4.2 μg/cm^2.

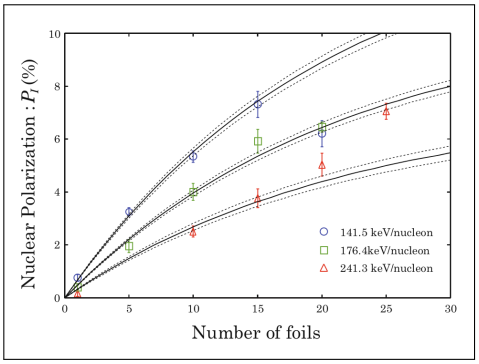

Figure 3.10: Nuclear polarization P_I of the ^{8}Li beam as a function of the number of polystyrene foils measured for incident beam energies of 141.5, 176.4 and 241.3 keV/u. The solid lines are fits with the Eq. 2.12 for nuclear polarization P_I to the data. The dotted lines beside the solid lines indicates the fitting errors. From Ref. [234]

The technique has been used at lower beam energies of 141.5 keV.u, 176.4 keV/u, and 241.3 keV/u. From the dependence of the degree of nuclear spin polarization on the number of foils, see Fig. 3.10, they observed a deviation from the theoretical model. They interpreted it as coming from the possibility to induce atomic polarization from different atomic states.
Indeed, the theoretical models does not take into account the energy dependence of the induced atomic polarization, which assumes that only one atomic state generates the nuclear polarization. Moreover, at the exit of the target, one obtain an equilibrium charge state which depends on the beam energy. In case of highly mixed charge states different atomic states could be dominant and it would contribute to deviate from the model.

They also investigated beam energy and charge state dependence using only one polystyrene foil, see Fig. 3.11. As seen on the Fig. 2.4, the half integer atomic spin value of J=1/2 would favor the polarization. However, the ^{8}Li^{1+} does not have a half integer atomic spin value of J=1/2 and it seems to be the main contribution of the production of nuclear polarization.

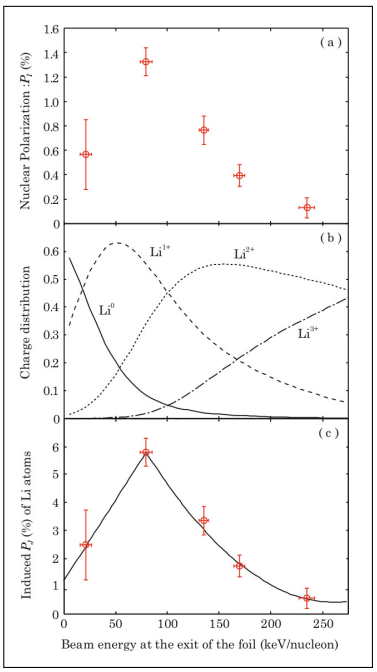

Figure 3.11: (a) Nuclear polarization with a single foil measured as a function of the beam energy at the exit of the foil. energies E_I of 23.8 and 85.3 keV/u were obtained by degrading the initial beam energy of 176.4 keV/u using mylar foils of 3.4 and 1.7 μm, respectively. The energies were measured by SSD (Solid State Detector), except for the data point of lowest energy, which was calculated by the SRIM2008 code. The horizontal error bars show the beam energy spread, which was considered to be the effect of multiple scattering in the foil.
(b) Charge state distribution of Li ions as a function of the beam energy for $^{8}Li^{0,+1,+2,+3}$ ions.
(c) Estimated atomic polarization P_J from Eq. 2.12 for atomic spin J=1/2 and number of foils N=1. the solid line shows the interpolation of the energy dependence of the atomic polarization. From Ref. [234]

Furthermore, in the case of multiple tilted foils, taking into account the energy loss at each foils and the energy-dependence of the atomic polarization as in the Fig. 3.11, the atomic states with J=1 [2] should be responsible of the atomic polarization and thus nuclear polarization, see Fig. 3.12.

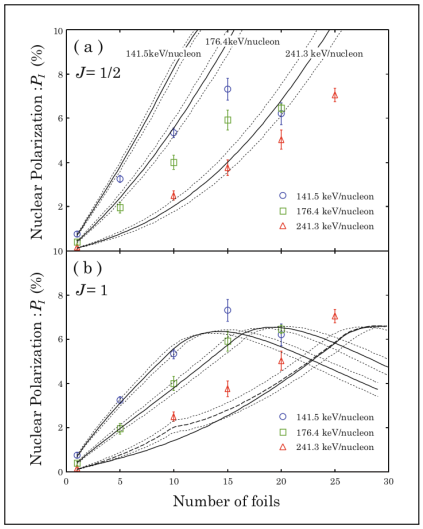

Figure 3.12: Estimation of nuclear polarization considering the energy dependent atomic polarization with the atomic spin values of (a) J=1/2 and (b) J=1. From Ref. [234]

Further studies would be necessary to confirm such feature inducing atomic polarization.

2. The atomic sates with J=1 are $1s2p(^1P_1) \rightarrow 1s^2(^1S_0)$ with τ = 0.04 ns, $1s2p(^3P_1) \rightarrow 1s^2(^1S_0)$ with τ = 55.6 μs and $1s2p(^3P_1) \rightarrow 1s2s(^3S_1)$ with τ = 44 ns.

Summary and Outlooks

The commissioning experiment proved that the present setup at ISOLDE is ready to perform further investigation using the tilted foils technique. A systematic study of the following parameters would be of great importance to understand the underlying process involved in the creation of polarization: the tilt angle, the incident beam energy, the closing of the atomic shell after polarization, the number of foils, the iron shield, the foil degradation, the different atomic state populations.

Further studies by Hirayama et *al.* demonstrated again that lower beam energy and high number of foils a favorable to reach a high degree of atomic polarization and thus by hyperfine interaction higher nuclear polarization.
They also highlighted the possibility of the main contribution in the polarization of the J=1 atomic states, instead of the J=1/2 atomic states.

A next step consisting to post-accelerate nuclear spin-polarized ion beams at ISOLDE would start maybe with the HIE-ISOLDE project. The people in charge of this project envisaged to use a stack of foils earlier in the LINAC in order to obtain polarized radioactive beams.

In a near future, other nuclei would be investigated with the present TFT setup. A proposal to study magnetic moments of isotopes of indium has already been accepted by the CERN Research Board [224].

General Conclusions

The manuscript is arranged in two parts corresponding to two different studies. However, it was envisaged to make them interacting polarizing the Rb beams using the tilted foils technique.

The first part concerned the study of the onset of deformation around A=100, N=60. By adding just one nucleon a sudden development of deformation appears.
The Coulomb excitations of ^{93,95,97,99}Rb isotopes have been realized mainly in order to identify the Nilsson orbital responsible of the development of deformation at N=60 for the Rb isotopic chain. It constitutes complementary experiments from which we obtain new insight on the neutron and proton side. It was the first time, one populated the excited nuclear structure of the ^{97}Rb and ^{99}Rb isotopes. The Coulomb excitation allows a "direct" measurement of the matrix elements. From the experimental yields, one calculated the matrix elements using the GOSIA2 code. One deduced the transition strengths related to those matrix elements.
By comparing the experimental results extracted from the present set of data one concludes that the $\pi 3/2^+[431]$ corresponds to the orbital on which the rotational band of the ^{97}Rb g.s is built.
The observation of similar structures in the ^{97,99}Rb is an implicit proof that the ^{99}Rb rotational band is based on the same $\pi 3/2^+[431]$ orbital.
The Coulomb excitation of the ^{99}Sr nucleus has also been performed due to the beam composition and its half-life. One proposes to enlarge the rotational band structure with one additional states. The corresponding state is in agreement with the rotational and inertia feature observed in the rest of the rotational g.s. band.

The second part is dedicated to the investigation of the tilted foils technique for future use nuclear spin polarized radioactive ion beams. A TFT and a β-NMR setups have been installed at CERN in order to evaluate such possibility a ISOLDE.
The design and the related electronic systems have been performed in order to fit the specific requirement of such setup.
A commissioning experiment realized with ^{8}Li beam gave promising results, and confirmed the reliability of the experimental setup that we developed at CERN-ISOLDE.
In the meantime, studies have been performed by Hirayama et *al.* which highlighted notably the energy-dependence of the atomic polarization and the possible of role of atomic states with different spins in the induction of atomic polarization. In the case of the polarization of ^{8}Li nuclei at low energy (50-150 keV/u), they notably establish the strong possibility of the J=1 atomic states in the polarization to the detriment of the J=1/2 atomic states. Further studies are requested to confirm such behavior.
The collaboration envisaged to use the present TFT setup in the study of the magnetic moments of the neutron-rich odd-even In isotopes at the future HIE-ISOLDE facility.

Appendix A

Formalism and Models

Some additional information concerning the "Anisotropic Modified Harmonic Oscillator" and "Wood-Saxon + BCS" models are provided in the present appendix in order to introduce their related formalism sometimes sometimes used in the cited publications.

1 Anisotropic Modified Harmonic Oscillator and Nilsson Model

Based on the spherical modified oscillator, the anisotropic modified harmonic oscillator introduced the concept of deformed nuclei via the elongation parameter δ, see Ref. [89]. The elongation along the z-axis, x-axis and y-axis can be different. The corresponding single-particle Hamiltonian takes the form:

$$H_{\text{AMHO}} = \underbrace{-\frac{\hbar^2}{2M}\Delta + \frac{1}{2}M\left[\omega_{x_1}^2 x_1^2 + \omega_{y_1}^2 y_1^2 + \omega_{z_1}^2 z_1^2\right]}_{H^0_{\text{AMHO}}} - C\vec{l}\cdot\vec{s} - D\vec{l}^2 \tag{A.1}$$

where, (x_1,y_1,z_1) are the particle coordinates in the body fixed coordinate system. The three different rotational frequencies ω_x^2, ω_y^2, ω_z^2 describe the nuclear deformation. C and D has mentioned above are constant, but they depends on the universal parametrization of κ and μ.

1.1 δ-parametrization

Considering the axially symmetric nuclei, the nuclear shape is represented as an ellipsoid. The axial symmetric nuclei have been described by Nilsson [20], introducing of an elongation parameter δ.

$$\begin{cases} \omega_z^2 &= \omega_0^2(\delta)\left(1 - \frac{4}{3}\delta\right) \\ \omega_\perp^2 &= \omega_0^2(\delta)\left(1 + \frac{2}{3}\delta\right) \end{cases} \tag{A.2}$$

The volume conservation imposes: $\omega_{x_1}\omega_{y_1}\omega_{z_1} = C^{ste}$, thus $\omega_0 = \mathring{\omega}_0\left(1 - \frac{4}{3}^2 - \frac{16}{27}\delta^3\right)^{-\frac{1}{6}}$ with $\mathring{\omega}_0 = 41A^{-\frac{1}{3}}$ MeV ($\omega_0(\delta = 0)$).

Using a dimensionless set of coordinates (x_0,y_0,z_0) the Hamiltonian is separated in a spherical and deformed part:

$$x_0 = \sqrt{m\omega_0}x_1, \quad y_0 = \sqrt{m\omega_0}y_1, \quad z_0 = \sqrt{m\omega_0}z_1 \tag{A.3}$$

and,

$$H^0_{\text{AMHO}} = \mathring{H}_0 + H_{def} \quad \text{, with} \quad \begin{cases} \mathring{H}_0 &= \frac{\omega_0}{2}\left(-\Delta + r^2\right) \\ H_{def} &= \omega_0\delta\frac{4}{3}\sqrt{\frac{\pi}{5}}r^2Y_{20} \end{cases} \tag{A.4}$$

In this representation, $\mathring{H}_0$,l^2,l_z and s_z are diagonal. Moreover the operator $j_z = l_z + s_z$ commutes with H_{AMHO}. The corresponding quantum numbers necessary to define the nuclear states are N (total quanta of the oscillator), l, Λ, Σ, with $K = \Lambda + \Sigma$ and the related parity, see Fig. A.1. The spherical Hamiltonian is found to be:

$$\mathring{H}_0 = |Nl\Lambda\Sigma> = \left(N + \frac{3}{2}\right)\omega_0|Nl\Lambda\Sigma> \tag{A.5}$$

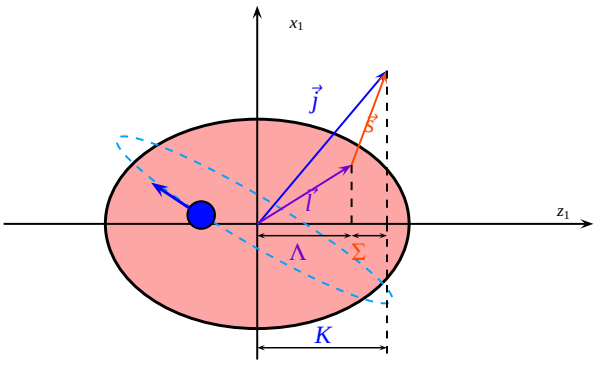

Figure A.1: Coupling of the angular moment $\vec{j} = \vec{l} + \vec{s}$ of the valence nucleons. Ω, Λ and Σ are the respective projections of $\vec{j}$, $\vec{l}$ and $\vec{s}$.

1.2 ϵ-parametrization

The deformation can be expressed in a different manner with the deformation operator ϵ with its frequency $\omega(\epsilon)$:

$$\left\{ \begin{array}{rcl} \omega_z & = & \omega_0(\epsilon)\left(1 - \frac{2}{3}\epsilon\right) \\ \omega_\perp & = & \omega_0(\epsilon)\left(1 + \frac{1}{3}\epsilon\right) \end{array} \right. \tag{A.6}$$

The elongation parameter ϵ is defined by:

$$\left\{ \begin{array}{rcl} \epsilon & = & \delta + \frac{1}{6}\delta^2 + O(\delta^3) \\ \omega_0(\epsilon) & = & \mathring{\omega}_0\left(1 + \frac{1}{9}\epsilon^2 + O(\epsilon^3)\right) \end{array} \right. \tag{A.7}$$

The Hamiltonian H^0_{AMHO} can be diagonalized in a set of coordinates (x_2,y_2,z_3) transforming the ellipsoid shape to a sphere:

$$H^0_{\text{AMHO}} = \mathring{H}_0 + H_{def}, \qquad \text{with} \left\{ \begin{array}{rcl} \mathring{H}_0 & = & \frac{\omega_0(\epsilon)}{2}\left(-\Delta + x_2^2 + y_2^2 + z_2^2\right) \\ H_{def} & = & \frac{\epsilon}{6}\omega_0(\epsilon)\left\{\left(-\frac{\partial^2}{\partial x_2^2} + x_2^2\right) + \left(-\frac{\partial^2}{\partial y_2^2} + y_2^2\right) - 2\left(-\frac{\partial^2}{\partial z_2^2} + z_2^2\right)\right\} \end{array} \right. \tag{A.8}$$

with: $x_2 = x_1\sqrt{m\omega_{x_1}}$, $y_2 = y_1\sqrt{m\omega_{y_1}}$, $z_2 = z_1\sqrt{m\omega_{z_1}}$

1.3 Introduction of κ and μ

The introduction of the dimensionless quantities κ and μ are used to emphazise the diagonalization of $\vec{l}\vec{s}$ and $\vec{l}^2$. They are defined as:

$$\kappa = \frac{C}{2\omega_0}, \quad \mu = \frac{2D}{C} \tag{A.9}$$

A new deformation parameter ξ is associated:

$$\xi = -\frac{\delta}{\kappa}\hat{\omega}_0(\delta) = -\frac{\delta}{\kappa}\left(1 - \frac{4}{3}\delta^2 - \frac{16}{27}\delta^3\right)^{-\frac{1}{6}} \tag{A.10}$$

with: $\hat{\omega}_0 = \frac{\omega_0(\delta)}{\mathring{\omega}_0}$ and the deformation Hamiltonian is related to δ such as:

$$H_{def,\delta} = \delta\omega_0\left(\frac{4}{3}\right)\sqrt{\frac{\pi}{5}}r^2Y_{20} = \kappa\mathring{\omega}_0\xi\left(\frac{4}{3}\sqrt{\frac{\pi}{5}}\right) \tag{A.11}$$

thus,

$$H_{\text{AMHO}} - \hat{H}_0 = -\kappa\mathring{\omega}_0\mathcal{M} \tag{A.12}$$

with: $\mathcal{M} = \xi\left(-\frac{4}{3}\sqrt{\frac{\pi}{5}}\right)r^2 Y_{20} - 2\vec{ls} - \mu\vec{l^2}$

The matrix is diagonalized for different values of the deformation ξ. For low deformation, the set of quantum numbers: K, π, l, j can describe entirely the shape. For high deformation, the set of quantum numbers $K, \pi, N, n_{z_1}, \Lambda$ ($\Lambda = K \pm \frac{1}{2}$). For intermediate deformation, the situation is more complicated and for example K is not a good quantum number [1].

Neglecting the $\vec{ls}$ coupling and $\vec{l^2}$ terms, the energy level of the anisotropic harmonic oscillator is found as:

$$E_0 = \omega_0(\epsilon)\left[\left(N + \frac{3}{2}\right) + \epsilon\frac{n_{x_2} + n_{y_2} - 2n_{z_2}}{3}\right] \tag{A.13}$$

The single particle is described via the set of quantum numbers K^π and the asymptotic quantum numbers $[Nn_{z_1}\Lambda]$.

A additional correction of the anisotropic harmonic oscillator Hamiltonian has been introduced to reproduce in a better way the experimental energy levels [2]:

$$H_{\text{AMHO}} = H^0_{\text{AMHO}} - C\vec{ls} - D\left(\vec{l^2} - < \vec{l^2} >_N\right) \tag{A.14}$$

with: $< \vec{l^2} >_N = \frac{N(N+3)}{2}$, the average value of $< \vec{l^2} >$ taken over each N-shell.
The latter term reproduces the Woods-Saxon radial shape, but the $< \vec{l^2} >_N$ value is subtracted to avoid a global energy compression of the orbits.

2 Wood Saxon + BCS model

The mean field notion allows to treat approximately the nucleus. To reproduce in a better way the behavior and the properties of the nucleus, it is necessary to take into account the pairing correlation ingredient in the problem.
The nucleon are immersed in an anisotropic modified harmonic oscillator potential (similar to Woods-Saxon potential), see Sec.1. With such potential the orbitals ordering reproducing the experimental data are usually roughly reproduced.
The residual nuclear interaction of the pairing strength needs to be taken into account, it allows to couple the nucleons by pairs. In the 1960s, Barden, Cooper and Shrieffer (BCS)[242] introduced a specific formalism in order to describe the supraconductivity phenomenon. To describe the pairing governing the residual interaction, this formalism has been transposed to the nucleus case in order to study its superfluid properties. The corresponding wave function is more sophisticated than for the "AMHO", and the previous single particle states are described with single quasi-particles. A single quasi-particle state is the linear combination of the particle and hole. The Cooper pairs coupling two fermions of the same nature constitute bosons and should respect the Bose-Einstein distribution. Moreover, their bosonic nature confers them a symmetric character.

The BCS wave function describing the nuclear quasi-particle state is found as:

$$| \psi_{BCS} >= \prod_{k>0} P^+_k \, | \, 0 > \tag{A.15}$$

where, $| \, 0 >$ represents the new "vacuum" (vacuum of the coupled particles),$P^+_k = u_k + v_k a^+_k a^+_{\bar{k}}$, v_k represents the probability to occupy the pair $(k, \bar{k})$ and u_k the probability of its none occupation. a^+_k is the creation operator of a particle in a nuclear state k and $a^+_{\bar{k}}$ the creation operator of a particle in the nuclear state $\bar{k}$. The statistics imposes the following relation:

$$v_k^2 + u_k^2 = 1 \tag{A.16}$$

The energy of a "BCS" nuclear state is of the form:

$$E = E_{\text{Wood Saxon}} + E_{Pair}(\Delta) \tag{A.17}$$

1. K is the superposition of spherical states with different l-values
2. It reduced the amount of (κ,μ) pairs needed to reproduces the experimental results.

In the BCS formalism only the average number of particles is conserved :

$$N = \sum_k v_k^2 \tag{A.18}$$

The use of this formalism requests the restoration of the nucleons number.

Annihilation η_k and creation η_k^+ operators for the quasi-particles can also be defined. The Bogoliubov-Valatin transformation allows to create the quasi-particle operators such as :

$$\eta_k \mid \psi_{BCS} >= 0 \tag{A.19}$$

with: $\eta_k = u_k a_k - v_k a_{\bar{k}^+}$
The transformation is canonical and linear, thus the quasi-particle are also fermions, see Ref. [89].

2.1 Pairing correlation

In the Fig.1.6, an oscillation of the odd and even masses is observed in the relative mass [3]. The residual interaction coupling nucleons together is generally treated with a two bodies potential. Usually a seniority force is employed such as:

$$-G_{ij} =< i\bar{i} \mid V \mid j\bar{j} > \tag{A.20}$$

with: $\bar{i}$ is the reversed time state compared to the state i, G_{ij} is constant, and $V = V_0\delta(\vec{r}_i - \vec{r}_j)$. For more information, the *"Theory of complex nuclei"* written by V.G. Soloviev [89].

2.2 Average number of nucleons

To determine the occupation probability for each nuclear state, the number of nucleons is used to constrain the solutions. The minimization of the following expression is the transcription of this constraint:

$$< H_{Wood-Saxon} + V_{Pair} - \lambda_N(N - \bar{N}) - \lambda_Z(Z - \bar{Z}) > \tag{A.21}$$

with: λ_N and λ_Z the Lagrange parameters, called chemical potential [4]. The variational principle is found as:

$$\delta < \psi_{BCS} \mid H_{Wood-Saxon} + V_{Pair} - \lambda_N(N - \bar{N}) - \lambda_Z(Z - \bar{Z}) \mid \psi_{BCS} >= 0 \tag{A.22}$$

which leads to:

$$2\left(E_k^{s.p.} - \lambda u_k v_k - \Delta_k\left(u_k^2 + v_k^2\right)\right) = 0 \tag{A.23}$$

where, the pairing tensor Δ_k is found to be :

$$\Delta_k = \frac{1}{2}\sum_l \frac{G_{lk}\Delta_l}{\sqrt{\left(E_l^{s.p.} - \lambda\right)^2 + \Delta_l}} \tag{A.24}$$

The BCS energy minimization respecting the normalization condition, see Eq.A.16 on the previous page, leads to the occupation probabilities:

$$\begin{cases} u_k^2 &= \frac{1}{2}\left(1 + \frac{E_k^{s.p.} - \lambda}{\sqrt{\left(E_k^{s.p.} - \lambda\right)^2 + \Delta_k^2}}\right) \\ v_k^2 &= \frac{1}{2}\left(1 - \frac{E_k^{s.p.} - \lambda}{\sqrt{\left(E_k^{s.p.} - \lambda\right)^2 + \Delta_k^2}}\right) \end{cases} \tag{A.25}$$

In the "Wood-Saxon" treatment with no pairing, the $v_k = 1$ for $E_k < \lambda$ and all the states lower than the Fermi energy are occupied, the others are completely empty. In the paring case, the occupation probabilities (v_k, u_k) are not null at the Fermi level. The Fermi surface is diffused which corresponds to the fact that a pair can be diffused at $E_k^{s.p.} \pm \Delta$. If all the nucleons are coupled in pairs, only the pairs close to the Fermi level play a role in the pairing effect.

3. Of course the same behavior is present in the S_p, S_n. It explains the fact that usually nuclear spectroscopists use the S_{2n} and S_{2p}, because the pairing is more or less annihilated
4. They are also called Fermi energies

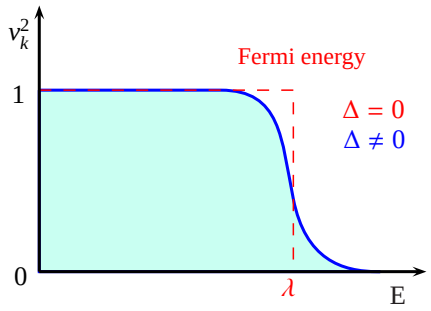

Figure A.2: Variation of the occupation probability v_k^2 in the no pairing case ($\Delta = 0$) and paring case ($\Delta \neq 0$) along the single particle energy. The red curve corresponds to a pure "Wood-Saxon" and the blue curve to a "Wood-Saxon + pairing" treatment.

2.3 Shape constraint

The study of deformation gradient can be operated introducing the quadrupole moments Q_{20} (axial deformation) and Q_{22} (triaxial deformation) in the minimization process. For example, the potential energy surface of the nucleus can be obtain via the minimization expression:

$$\delta < \psi_{BCS} \mid H_{Wood-Saxon} + V_{pair} - \lambda_N(N - \bar{N}) - \lambda_Z(Z - \bar{Z}) - c\left(Q_0 - \bar{Q}_0\right)^2 \mid \psi_{BCS} >= 0 \tag{A.26}$$

with, the quadrupole operators :

$$\begin{cases} Q_{20} &= \sqrt{\dfrac{16\pi}{5}} \sum_{i=1}^{A} r_i^2 Y_{20}(\theta_i, \phi_i) \\ Q_{22} &= \sqrt{\dfrac{4\pi}{5}} \sum_{i=1}^{A} r_i^2 \left(Y_{22}(\theta_i, \phi_i) + Y_{2-2}(\theta_i, \phi_i)\right) \end{cases} \tag{A.27}$$

On contrary, the introduction of the quadrupole moments will constrain the minimization.

2.4 Lipkin-Nogami Method

The Wood Saxon formalism conserves only the average number of nucleons, thus it is necessary to restore the particle number. In order to improve the pairing corrections and restore the particle number the Lipkin-Nogami method can be used. As the BCS formalism, initially present in the solid state physics, the method proposed by H.J. Lipkin, see Ref. [243], has been applied for nuclear physics in 1964 by Y. Nogami *et al.* [244].
Developing to an higher order the minimization expression, see Eq. A.27, the particle number is recovered:

$$\delta < \psi_{BCS} \mid H_{Wood-Saxon} + V_{pair} - \lambda_{N,1}(N - \bar{N}) - \lambda_{Z,1}(Z - \bar{Z}) - \lambda_{N,2}(N^2 - \bar{N}^2) - \lambda_{Z,2}(Z^2 - \bar{Z}^2) - c\left(Q_0 - \bar{Q}_0\right)^2 \mid \psi_{BCS} = 0 \tag{A.28}$$

The deformation can be constraint, for example in a pure rigid rotor hypothesis, via the constraint parameter c. In such way the total energy of the nucleus can be expressed as a function of the quadrupole moment parameter.
And, the quasi-particle and the single particle energies can be obtained by projection.

2.5 Iterative process

The whole minimization process is an iterative process, and, after the determination of the quasi-particle and single particle energies, a new minimization with the obtained parameters is operated.

Appendix B

Experimental details

1 Chemical Properties of Rubidium

Electrochemical Equivalent	3.1888 g/amp-hr
Electron Work Function	2.16 eV
Electronegativity	0.82 (Pauling); 0.89 (Allrod Rochow)
Heat of Fusion	2.192 kJ/mol
Ionization Potential First	4.177 eV
Ionization Second	27.28 eV
Ionization Third	40 eV
Valence Electron Potential (-eV)	9.47
Electron affinity	0.485916(20)

Table B.1: Chemical properties of the rubidium. The different chemical properties have an important impact on production cross sections of the ISOL techniques.

2 MINIBALL angles of the Coulomb excitations

Elem.	θ	ϕ	Clus.	Crys.
core	1.94781	2.36069	0	0
seg. 1	1.82999	2.4867	0	0
seg. 2	1.98574	2.54765	0	0
seg. 3	1.79411	2.32027	0	0
seg. 4	1.901	2.18879	0	0
seg. 5	2.1171	2.41168	0	0
seg. 6	2.06524	2.21509	0	0

Elem.	θ	ϕ	Clus.	Crys.
core	0.978496	0.872915	1	0
seg. 1	1.12744	0.935178	1	0
seg. 2	1.11336	0.761571	1	0
seg. 3	1.79411	1.04949	1	0
seg. 4	0.855891	0.99956	1	0
seg. 5	0.964254	0.674157	1	0
seg. 6	0.825131	0.792863	1	0

Elem.	θ	ϕ	Clus.	Crys.
core	2.26538	2.83439	0	1
seg. 1	2.40748	2.9588	0	1
seg. 2	2.41782	2.70969	0	1
seg. 3	2.25242	3.03898	0	1
seg. 4	2.11493	2.92609	0	1
seg. 5	2.2555	2.6073	0	1
seg. 6	2.10953	2.21509	0	1

Elem.	θ	ϕ	Clus.	Crys.
core	1.21734	0.401228	1	1
seg. 1	1.2368	0.2342	1	1
seg. 2	1.08786	0.288023	1	1
seg. 3	1.35587	0.339691	1	1
seg. 4	1.34473	0.499605	1	1
seg. 5	1.06746	0.476237	1	1
seg. 6	1.20679	0.577814	1	1

Elem.	θ	ϕ	Clus.	Crys.
core	2.43079	2.14331	0	2
seg. 1	2.34453	1.93242	0	2
seg. 2	2.255	2.12019	0	2
seg. 3	2.50991	1.92196	0	2
seg. 4	2.59757	2.17625	0	2
seg. 5	2.3204	2.34037	0	2
seg. 6	2.49296	2.40692	0	2

Elem.	θ	ϕ	Clus.	Crys.
core	0.741844	0.313285	1	2
seg. 1	0.594662	0.408442	1	2
seg. 2	0.721676	0.559725	1	2
seg. 3	0.634975	0.145771	1	2
seg. 4	0.78775	0.0939703	1	2
seg. 5	0.871085	0.455	1	2
seg. 6	0.899181	0.242157	1	2

Table B.2: MINIBALL Ge detector angles.

Elem.	θ	ϕ	Clus.	Crys.
core	1.09574	2.68945	2	0
seg. 1	1.24664	2.649	2	0
seg. 2	1.15035	2.51993	2	0
seg. 3	1.20011	2.80465	2	0
seg. 4	1.05492	2.85999	2	0
seg. 5	0.988927	2.54938	2	0
seg. 6	0.939075	2.73904	2	0
Elem.	θ	ϕ	Clus.	Crys.
core	1.05327	2.15476	2	1
seg. 1	0.987147	1.9896	2	1
seg. 2	0.891547	2.13934	2	1
seg. 3	1.13858	2.01865	2	1
seg. 4	1.20829	2.16706	2	1
seg. 5	0.97036	2.31807	2	1
seg. 6	1.13378	2.31342	2	1
Elem.	θ	ϕ	Clus.	Crys.
core	0.650103	2.48598	2	2
seg. 1	0.608116	2.74087	2	2
seg. 2	0.756589	2.67582	2	2
seg. 3	0.503711	2.52642	2	2
seg. 4	0.569093	2.2535	2	2
seg. 5	0.810188	2.45665	2	2
seg. 6	0.72306	2.25684	2	2

Elem.	θ	ϕ	Clus.	Crys.
core	2.19156	0.843981	3	0
seg. 1	2.31142	0.964259	3	0
seg. 2	2.33624	0.76057	3	0
seg. 3	2.16739	1.01833	3	0
seg. 4	2.05013	0.909051	3	0
seg. 5	2.20105	0.650168	3	0
seg. 6	2.06064	0.739293	3	0
Elem.	θ	ϕ	Clus.	Crys.
core	2.40585	0.293622	3	1
seg. 1	2.35831	0.0838349	3	1
seg. 2	2.25428	0.230884	3	1
seg. 3	2.50577	0.127221	3	1
seg. 4	2.5488	0.37729	3	1
seg. 5	2.28518	0.435268	3	1
seg. 6	2.42991	0.53009	3	1
Elem.	θ	ϕ	Clus.	Crys.
core	1.95389	0.393171	3	2
seg. 1	1.8337	0.491171	3	2
seg. 2	1.96779	0.563589	3	2
seg. 3	1.81917	0.336738	3	2
seg. 4	1.93122	0.23195	3	2
seg. 5	2.09866	0.461848	3	2
seg. 6	2.07517	0.280562	3	2

Table B.3: MINIBALL Ge detector angles.

Elem.	θ	ϕ	Clus.	Crys.
core	2.4948	4.26473	4	0
seg. 1	2.56055	3.99571	4	0
seg. 2	2.39633	4.03538	4	0
seg. 3	2.65326	4.26635	4	0
seg. 4	2.55901	4.53457	4	0
seg. 5	2.31949	4.26359	4	0
seg. 6	2.39502	4.49253	4	0
Elem.	θ	ϕ	Clus.	Crys.
core	2.02968	3.97557	4	1
seg. 1	1.86394	4.00431	4	1
seg. 2	1.95545	4.15126	4	1
seg. 3	1.92791	3.84315	4	1
seg. 4	2.08816	3.79731	4	1
seg. 5	2.13322	4.13792	4	1
seg. 6	2.20358	3.93971	4	1
Elem.	θ	ϕ	Clus.	Crys.
core	2.02805	4.54898	4	2
seg. 1	2.08557	4.72744	4	2
seg. 2	2.20174	4.58612	4	2
seg. 3	1.92556	4.68063	4	2
seg. 4	1.86247	4.51919	4	2
seg. 5	2.1325	4.3875	4	2
seg. 6	1.95481	4.37288	4	2

Elem.	θ	ϕ	Clus.	Crys.
core	1.15791	4.19636	5	0
seg. 1	1.31293	4.13265	5	0
seg. 2	1.1954	4.01153	5	0
seg. 3	1.28147	4.29981	5	0
seg. 4	1.1342	4.37701	5	0
seg. 5	1.02666	4.0684	5	0
seg. 6	0.996902	4.27342	5	0
Elem.	θ	ϕ	Clus.	Crys.
core	1.04668	3.63959	5	1
seg. 1	0.957529	3.47287	5	1
seg. 2	0.872229	3.65051	5	1
seg. 3	1.12126	3.48303	5	1
seg. 4	1.21275	3.63109	5	1
seg. 5	0.977809	3.8275	5	1
seg. 6	1.15192	3.79624	5	1
Elem.	θ	ϕ	Clus.	Crys.
core	0.657955	4.08365	5	2
seg. 1	0.646788	4.35744	5	2
seg. 2	0.794698	4.24803	5	2
seg. 3	0.511434	4.18718	5	2
seg. 4	0.544707	3.86737	5	2
seg. 5	0.82373	4.00754	5	2
seg. 6	0.706518	3.81692	5	2

Table B.4: MINIBALL Ge detector angles.

Elem.	θ	ϕ	Clus.	Crys.
core	1.8958	5.39667	6	0
seg. 1	1.75099	5.44752	6	0
seg. 2	1.85708	5.55884	6	0
seg. 3	1.78555	5.29746	6	0
seg. 4	1.92532	5.23748	6	0
seg. 5	2.01189	5.51312	6	0
seg. 6	2.04581	5.33806	6	0
Elem.	θ	ϕ	Clus.	Crys.
core	1.99536	5.88293	6	1
seg. 1	2.08354	6.0231	6	1
seg. 2	2.15405	5.8658	6	1
seg. 3	1.93242	6.02548	6	1
seg. 4	1.84301	5.89719	6	1
seg. 5	2.05456	5.71925	6	1
seg. 6	1.89627	5.74867	6	1
Elem.	θ	ϕ	Clus.	Crys.
core	2.34767	5.51442	6	2
seg. 1	2.3698	5.29964	6	2
seg. 2	2.22855	5.37355	6	2
seg. 3	2.48656	5.44675	6	2
seg. 4	2.45033	5.68251	6	2
seg. 5	2.19485	5.56956	6	2
seg. 6	2.30148	5.72391	6	2

Elem.	θ	ϕ	Clus.	Crys.
core	1.08885	5.84073	7	0
seg. 1	1.24235	5.83038	7	0
seg. 2	1.16927	5.68716	7	0
seg. 3	1.17182	5.97447	7	0
seg. 4	1.02153	5.99977	7	0
seg. 5	1.00776	5.68218	7	0
seg. 6	0.928841	5.85347	7	0
Elem.	θ	ϕ	Clus.	Crys.
core	1.12963	5.32179	7	1
seg. 1	1.08655	5.15674	7	1
seg. 2	0.974068	5.27682	7	1
seg. 3	1.23127	5.20743	7	1
seg. 4	1.27945	5.35905	7	1
seg. 5	1.02547	5.45899	7	1
seg. 6	1.18522	5.48612	7	1
Elem.	θ	ϕ	Clus.	Crys.
core	0.691007	5.52327	7	2
seg. 1	0.610754	5.74044	7	2
seg. 2	0.763154	5.7392	7	2
seg. 3	0.545766	5.4883	7	2
seg. 4	0.646796	5.28527	7	2
seg. 5	0.849411	5.54954	7	2
seg. 6	0.794609	5.34178	7	2

Table B.5: MINIBALL Ge detector angles.

3 CD Detector Calibration

(^{12}C at 2.83 MeV/u)			(^{16}O at 2.83 MeV/u)			(^{20}Ne at 2.83 MeV/u)			(^{40}Ar at 2.83 MeV/u)		
Strip	E[MeV/u]	E_{tot}	Strip	E[MeV/u]	E_{tot}	Strip	E[MeV/u]	E_{tot}	Strip	E[MeV/u]	E_{tot}
15	2.61	32.52	15	2.54	40.64	15	2.49	49.8	15	2.4	96
14	2.59	31.08	14	2.53	40.48	14	2.48	49.6	14	2.37	94.8
13	2.58	30.96	13	2.52	40.32	13	2.46	49.2	13	2.34	93.6
12	2.57	30.84	12	2.5	40	12	2.44	48.8	12	2.31	92.4
11	2.55	30.6	11	2.48	39.68	11	2.43	48.6	11	2.28	91.2
10	2.54	30.48	10	2.47	39.52	10	2.41	48.2	10	2.25	90
9	2.53	30.36	9	2.45	39.2	9	2.39	47.8	9	2.21	88.4
8	2.51	30.12	8	2.44	39.04	8	2.37	47.4	8	2.18	87.2
7	2.5	30	7	2.42	38.72	7	2.35	47	7	2.15	86
6	2.49	29.88	6	2.4	38.4	6	2.32	46.4	6	2.11	84.4
5	2.47	29.64	5	2.38	38.08	5	2.3	46	5	2.08	83.2
4	2.46	29.52	4	2.37	37.92	4	2.28	45.6	4	2.05	82
3	2.45	29.4	3	2.35	37.6	3	2.27	45.4	3	2.02	80.8
2	2.44	29.28	2	2.34	37.44	2	2.25	45	2	1.99	79.6
1	2.42	29.04	1	2.32	37.12	1	2.23	44.6	1	1.96	78.4
0	2.41	28.92	0	2.3	36.8	0	2.21	44.2	0	1.93	77.2

Table B.6: Calibration: Energies vs θ for the CD annular strips for the scattering on ^{196}Pt.

Bibliography

[1] K. Krane. *Introductory of Nuclear Physics*. Wiley, 2006. 18, 19, 33, 40, 43, 60

[2] W. A. Friedman. *Effect of Exchange and the Pauli Principle on Nucleon - Nucleus Scattering II*. Number 45. Annals of Physics, 1967. p. 265-313. 18

[3] W. Elsasser. Application of Pauli's Principle to Nuclei - Sur le Principe de Pauli dans les Noyaux. *J. de Phys. et Rad.*, 5(625), 1934. 18

[4] E. Rutherford and F. Soddy. Radioactive Change. *Philosophical Magazine and Journal of Sciences*, 5:p. 576–591, 1903. 19

[5] D.L Hill and J.A. Wheeler. Nuclear Constitution and the Interpretation of Fission Phenomena. *Phys. Rev.*, 89(5):1102, Mar. 1953. 20, 21

[6] J.P. Vary. Ab-Initio Nuclear Theory - Progress and Prospects from Quarks to the Cosmos. *Act Physica Polonica B*, 42(3-4), 2011. 21

[7] UNEDF Collaboration. Unified Nuclear Energy Density Functional, November 2012. 22

[8] J. Chadwick. Possible Existence of a Neutron. *Nature*, (129):312, Feb. 1932. 22

[9] C. F. v. Weizsäeker. Zur Theorie der Kernmassen. *Z. Phys.*, 96:431, Jul. 1935. 22

[10] S.G. Nilsson and I. Ragnarsson. *Shape and Shells in Nuclear Structure*. Press Syndicate of the University of Cambridge, 1995. 23, 24, 25, 33, 35, 36, 43

[11] W. D. Myers and W. J. Swiatecki. Nuclear Masses and Deformations. *Nuclear Physics*, 81(1):1 – 60, 1966. 23, 24, 26

[12] W.D. Myers and W.J. Swiatecki. Anomalies in Nuclear Masses - Proceedings of the Lysekil Symposium 1966. *Ark. Fys.*, 36(43):343, 1967. Stockholm, Almqvist Wiksell,. 23

[13] D. Iwanenko and E. Gapon. Zur Bestimmung der isotopenzahl. *Die Naturwissenschaften*, 20:792–793, 1932. 24

[14] M. Goeppert-Mayer. *Nobel Lecture*. Elsevier Publishing Company, Amsterdam, 1972, 1963. 24

[15] R.D. Woods and D.S. Saxon. Diffuse Surface Optical Model for Nucleon-Nuclei Scattering. *Physical Review*, 95:577–578, Jul. 1954. 27

[16] M. Goeppert-Mayer. On Closed Shells in Nuclei. *Phys. Rev.*, 74(235), 1948. 27

[17] M. Goeppert-Mayer. On Closed Shells in Nuclei II. *Phys. Rev.*, 75(1969), 1949. 27

[18] O. Haxel, J. Hans, D. Jensen and H.E. Suess. Concerning the Interpretation of "Magic" Nucleon Numbers in Connection with the Structure of Atomic Nuclei. *Die Naturwissenschaften*, 35(376), 1948. 27

[19] O. Haxel, J. Hans, D. Jensen and H. E. Suess. On the "Magic Numbers" in Nuclear Structure. *Phys. Rev.*, 75:1766–1766, 16 Apr. 1949. 27

[20] S.G. Nilsson. -. *Mat. Fys. Medd. Dan Vid Selsk.*, 29(16), 1955. 28, 31, 205

[21] C. Gustafsson, I.L. Lamm, B. Nilsson and S.G. Nilsson. -. *Ark. Fys.*, 36(613), 1967. 28

[22] T. Bengtsson and I. Ragnarsson. Rotational Bands and Particle-Hole Excitations at Very High Spin. *Nucl. Phys. A*, 436(1):14 – 82, 1985. 29

[23] W. Nazarewicz, J. Dudek, R. Bengtsson, T. Bengtsson and I. Ragnarsson. Microscopic Study of the High-Spin Behavior in Selected A 80 Nuclei. *Nucl. Phys. A*, 435(2):397 – 447, 1985. 29

[24] Peter Möller and J.Rayford Nix. Nuclear Mass Formula with a Yukawa-Plus-Exponential Macroscopic Model and a Folded-Yukawa Single-Particle Potential. *Nucl. Phys. A*, 361(1):117 – 146, 1981. 29

[25] A. Bohr and B. R. Mottelson. *Nuclear Structure*, volume Vol.I Vol. II. W.A. Benjamin, New York, 1969. 31, 32, 34, 59, 68, 70, 168

[26] K. Heyde. *Basic Ideas and Concepts in Nuclear Physics - An Introduction Approach*. Series in Fundamental and Applied Nuclear Physics. IOP Publishing Ltd., third edition edition, 2004. 33, 40, 43, 66, 69

[27] L. Grodzins. The Uniform Behaviour of Electric Quadrupole Transition Probabilities from First 2+ States in Even-Even Nuclei. *Phys. Lett.*, 2(2):88–91, 1962. 34

[28] F.S. Stephens, R.M. Diamond and S.G. Nilsson. A Coupling Scheme Relevant to High Angular Momenta and Intermediate Nuclear Deformations. *Phys. Lett. B*, 44(5):429–432, 1973. 35

[29] F.S. Stephens. Coriolis Effects and Rotation Alignment in Nuclei. *Rev. Mod. Phys.*, 47:43–65, Jan 1975. 35

[30] S.E. Larsson and G. Leander and I. Ragnarsson. Nuclear Core-Quasiparticle Coupling. *Nucl. Phys. A*, 307(2):189–223, 1978. 35

[31] J. Meyer-Ter-Vehn. Collective Model Description of Transitional Odd-A Nuclei: (II). Comparison with Unique Parity States of Nuclei in the $A = 135$ and $A = 190$ Mass Regions. *Nucl. Phys. A*, 249(1):141 – 165, 1975. 35

[32] J. Meyer-Ter-Vehn. Collective Model Description of Transitional Odd-A Nuclei: (I). The Triaxial-Rotor-Plus-Particle Model. *Nucl. Phys. A*, 249(1):111–140, 1975. 35

[33] D.R. Inglis. Particle Derivation of Nuclear Rotation Properties Associated with a Surface Wave. *Phys. Rev.*, 96:1059–1065, Nov 1954. 37

[34] S.A.E. Johansson. Gamma De-Excitation of Fission Fragments (II). Delayed Radiation. *Nuclear Physics*, (64):p. 147–160, 1965. 39

[35] M.A.C. Hotchkis, J.L. Durell, J.B. Fitzgerald, A.S. Mowbray, W.R. Phillips, I. Ahmad, M.P. Carpenter, R.V.F. Janssens, T.L. Khoo, E.F. Moore, L.R. Morss, Ph. Benet and D. Ye. Rotational Bands in the Mass 100 Region. *Nuclear Physics*, A(530):p. 111–134, 1991. 39, 40, 168

[36] E. Cheifetz, R.C. Jared, S.G. Thompson J.B. and Wilhelmy. Experimental Information Concerning Deformation of Neutron Rich Nuclei in the $A \sim 100$ Region. *Phys. Rev. Lett.*, 25:38–43, Jul 1970. 39

[37] R.A. Meyer ed. J. Eberth and K. Sistemich, editors. *Proceedings International Workshop on Nuclear Structure of the Zirconium Region*. Bad Honnef, Springer, Berlin, 1988, 1988. 39

[38] E. Monnand, J.A. Pinston, F. Schussler, B. Pfeiffer, H. Lawin, G. Battistuzzi, K. Shizuma and K. Sistemich. Evidence for a Rotational Band in ^{99}Y. *Zeitschrift für Physik A Atoms and Nuclei*, 306:183–184, 1982. 39

[39] F.K. Wohn, J.C. Hill, R.F. Petry, H. Dejbakhsh, Z. Berant and R.L. Gill. Rotational Structure and Nilsson Orbitals for Highly Deformed Odd-A Nuclei in the $A \sim 100$ Region. *Phys. Rev. Lett.*, 51:873–876, Sep. 1983. 39

[40] K. Shizuma, H. Ahrens, J.P. Bocquet, N. Kaffrell, B.D. Kern, H. Lawin, R.A. Meyer, K. Sistemich, G. Tittel and N. Trautmann. Odd Neutron Nuclei Near A=100: Rotational Bands in ^{103}Mo and ^{105}Mo Populated in the β-decays of ^{103}Nb and ^{105}Nb. *Zeitschrift für Physik A Atoms and Nuclei*, 315:65–75, 1984. 39

[41] T. Seo, H. Lawin, G. Lhersonneau, R.A. Meyer, G. Menzen and K. Sistemich. The Nilsson-Potential Parameters for Neutrons at $A \simeq 100$ and New Deformation Values for ^{103}Mo and ^{105}Mo. *Zeitschrift für Physik A Atoms and Nuclei*, 320:393–398, 1985. 39

[42] B. Pfeiffer, E. Monnand, J.A. Pinston, J. Münzel, P. Möller, J. Krumlinde, W. Ziegert and K.-L. Kratz. Rotational bands in 99Sr. *Zeitschrift für Physik A Atoms and Nuclei*, 317:123–124, 1984. 39, 171, 173

[43] T. Seo, A.-M. Schmitt, H. Ahrens, J.P. Bocquet, N. Kaffrell, H. Lawin, G. Lhersonneau, R.A. Meyer, K. Shizuma, K. Sistemich, G. Tittel and N. Trautmann. Evidence for Rotational Bands in ^{103}Nb. *Zeitschrift für Physik A Atoms and Nuclei*, 315:251–253, 1984. 39

[44] R.A. Meyer, E. Monnand, J.A. Pinston, F. Schussler, I. Ragnarsson, B. Pfeiffer, H. Lawin, G. Lhersonneau, T. Seo and K. Sistemich. Deformation in Odd-Mass Nuclei Near A∼100: One- and Three-Quasiparticle Nilsson States in $^{99}_{39}Y_{60}$. *Nucl. Phys. A*, 439(3):510–534, 1985. 39, 40, 168

[45] R.F. Petry, H. Dejbakhsh, J.C. Hill, F.K. Wohn, M. Shmid and R.L. Gill. Rotational Structure of Highly Deformed ^{99}Y: Decay of ^{99}Sr. *Phys. Rev. C*, 31:621–633, Feb 1985. 39

[46] R.F. Petry, J.D. Goulden, F.K. Wohn, J.C. Hill, R.L. Gill and A. Piotrowski. Decay of ^{101}Sr and the Rotational Structure of ^{101}Y. *Phys. Rev. C*, 37:2704–2721, Jun 1988. 39

[47] N.J. Stone. Table of Nuclear Magnetic Dipole and Electric Quadrupole Moments. *Atomic Data and Nuclear Data Tables*, 90(1):75–176, 2005. 39, 51

[48] A.G. Smith, J.L. Durell, W.R. Phillips, M.A. Jones, M. Leddy, W. Urban, B.J. Varley, I. Ahmad, L.R. Morss, M. Bentaleb, A. Guessous, E. Lubkiewicz, N. Schulz and R. Wyss. Spin-Dependent Triaxial Deformation in Neutron-Rich Mo Isotopes. *Phys. Rev. Lett.*, 77:1711–1714, Aug. 1996. 39

[49] P. Bonche, H. Flocard, P.H. Heenen, S.J. Krieger and M.S. Weiss. Self-Consistent Study of Triaxial Deformations: Application to the Isotopes of Kr, Sr, Zr and Mo. *Nucl. Phys. A*, 443(1):39–63, 1985. 39, 40

[50] H. Hua, C.Y. Wu, D. Cline, A.B. Hayes, R. Teng, R.M. Clark, P. Fallon, A. Görgen, A.O. Macchiavelli and K. Vetter. Triaxiality and the Aligned h_{112} Neutron Orbitals in Neutron-Rich Zr and Mo Isotopes. *Phys. Rev. C*, 69:014317, Jan. 2004. 39

[51] R. Rodrguez-Guzmn, P. Sarriguren, L.M. Robledo and S. Perez-Martin. Charge Radii and Structural Evolution in Sr, Zr and Mo Isotopes. *Phys. Lett. B*, 691(202), 2010. 39, 41, 52, 53

[52] H. Mach, M. Moszyski, R.L. Gill, F.K. Wohn, J.A. Winger, J.C. Hill, G. Molnr and K. Sistemich. Deformation and Shape Coexistence of 0^+ States in ^{98}Sr and ^{100}Zr. *Phys. Lett. B*, 21, 1989. 39, 41

[53] J.A. Pinston, J. Genevey, R. Orlandi, A. Scherillo, G.S. Simpson, I. Tsekhanovich, W. Urban, H. Faust and N. Warr. Shape Coexistence in the Very Neutron-Rich Odd-Odd ^{96}Rb. *Phys. Rev. C*, 71:064327, Jun. 2005. 39, 49

[54] G. Lhersonneau, B. Pfeiffer, K.-L. Kratz, H. Ohm and K. Sistemich. Shape Coexistence in the N=59 Isotone ^{97}Sr. *Zeitschrift für Physik A Atomic Nuclei*, 330:347–348, 1988. 39

[55] W. Urban, J.L. Durell, A.G. Smith, W.R. Phillips, M.A. Jones, B.J. Varley, T. Rzaca-Urban, I. Ahmad, L.R. Morss, M. Bentaleb and N. Schulz. Medium-spin structure of ^{96,97}Sr and ^{98,99}Zr nuclei and the onset of deformation in the $A \sim 100$ region. *Nucl. Phys. A*, 689(3):605–630, 2001. 39, 46, 49

[56] G. Lhersonneau, B. Pfeiffer, K.-L. Kratz, H. Ohm, K. Sistemich, S. Brant and V. Paar. Structure of the N=59 Nucleus ^{97}Sr: Coexistence of Spherical and Deformed States. *Zeitschrift für Physik A Atomic Nuclei*, 337:149–159, 1990. 39, 164

[57] M. Büscher, R.F. Casten, R.L. Gill, R. Schuhmann, J.A. Winger, H. Mach, M. Moszyński and K. Sistemich. Coexistence Features in the Spherical-Deformed $A \cong 100$ Transition Region: Picosecond Lifetime Measurements in ^{97}Sr, ^{97}Y, and ^{97}Zr. *Phys. Rev. C*, 41:1115–1125, Mar 1990. 39

[58] P. Federman and S. Pittel. Towards a Unified Microscopic Description of Nuclear Deformation. *Phys. Lett. B*, 69(4):385–388, 1977. 39, 41, 44, 45

[59] P. Federman and S. Pittel. Unified Shell-Model Description of Nuclear Deformation. *Phys. Rev. C*, 20:820–829, Aug. 1979. 39, 44

[60] A. Etchegoyen, P. Federman and E.G. Vergini. Importance of the Neutron-Proton Interaction for Zr Isotopes. *Phys. Rev. C*, 39:1130–1133, Mar. 1989. 39

[61] A. Faessler, J.E. Galonska, U. Götz and H.C. Pauli. 40

[62] D. Galeriu, D. Bucurescu and M. Ivascu. Nuclear Deformations in the $A \approx 80 - 100$ Region. *Journal of Physics G: Nuclear Physics*, 12(4):329, 1986. 40

[63] A. Kumar and M.R. Gunye. Nuclear Structure of Sr, Zr, and Mo Isotopes. *Phys. Rev. C*, 32:2116–2121, Dec 1985. 40, 45

[64] A. de-Shalit and I. Talmi. *Theoretical Nuclear Physics - Nuclear Structure*, volume Vol. I. John Wiley and Sons, 1974. 40

[65] G. Audi, M. Wang, A.H. Wapstra, F.G. Kondev, M. MacCormick, X. Xu, B. Pfeiffer, X. Sun and J. Blachot. Atomic Mass Data Center. Chinese Physics C, Dec. 2012. 41, 124

[66] S. Naimi. Critical-Point Boundary for the Nuclear Quantum Phase Transition Near A=100 from Mass Measurements of ^{96,97}Kr. *Phys. Rev. Lett.*, 2010. 41

[67] U. Hager, T. Eronen, J. Hakala, A. Jokinen, V.S. Kolhinen, S. Kopecky, I. Moore, A. Nieminen, M. Oinonen, S. Rinta-Antila, J. Szerypo and J. Äystö. First Precision Mass Measurements of Refractory Fission Fragments. *Phys. Rev. Lett.*, 96:042504, Feb 2006. 41

[68] U. Hager, A. Jokinen, V.-V. Elomaa, T. Eronen, J. Hakala, A. Kankainen, S. Rahaman, J. Rissanen, I.D. Moore, S. Rinta-Antila, A. Saastamoinen, T. Sonoda and J. Äystö. Precision Mass Measurements of Neutron-Rich Yttrium and Niobium Isotopes. *Nucl. Phys. A*, 793(1–4):20–39, 2007. 41

[69] S. Rinta-Antila, T. Eronen, V.-V. Elomaa, U. Hager, J. Hakala, A. Jokinen, P. Karvonen, H. Penttilä, J. Rissanen, T. Sonoda, A. Saastamoinen and J. Äystö. Decay Study of Neutron-Rich Zirconium Isotopes Employing a Penning Trap as a Spectroscopy Tool. *The European Physical Journal A*, 31:1–7, 2007. 41

[70] A. Kankainen, L. Batist, S.A. Eliseev, V.-V. Elomaa, T. Eronen, U. Hager, J. Hakala, A. Jokinen, I. Moore, Yu.N. Novikov, H. Penttilä, K. Peräjärvi, A.V. Popov, S. Rahaman, S. Rinta-Antila, P. Ronkanen, A. Saastamoinen, D.M. Seliverstov, T. Sonoda, G.K. Vorobjev and J. Äystö. Mass Measurements of Neutron-Deficient Nuclides Close to A = 80 with a Penning Trap. *The European Physical Journal A - Hadrons and Nuclei*, 29:271–280, 2006. 41

[71] S. Rahaman, U. Hager, V.-V. Elomaa, T. Eronen, J. Hakala, A. Jokinen, A. Kankainen, P. Karvonen, I.D. Moore, H. Penttilä, S. Rinta-Antila, J. Rissanen, A. Saastamoinen, T. Sonoda and J. Äystö. Precise Atomic Masses of Neutron-Rich Br and Rb Nuclei Close to the r-process Path. *The European Physical Journal A*, 32:87–96, 2007. 41

[72] G. Audi, A.H. Wapstra and C. Thibault. The Ame2003 Atomic Mass Evaluation: (II). Tables, Graphs and References. *Nucl. Phys. A*, 729(1):337 – 676, 2003. The 2003 NUBASE and Atomic Mass Evaluations. 41

[73] M. Albers et *al.* Coulomb Excitation on the Neutron Rich Isotopes ^{94,96}Kr. *ARIS Conference*, 2011. 41, 43

[74] R. Rodriguez-Guzman, P. Sarriguren, and L. M. Robledo. Shape Evolution in Yttrium and Niobium Neutron-Rich Isotopes. *Phys. Rev. C*, 82, 2011. 061302(R). 41

[75] R. Rodriguez-Guzman, P. Sarriguren, and L.M. Robledo. Signatures of Shape Transitions in Odd- A Neutron-Rich Rubidium Isotopes. *Phys. Rev. C*, 82, 2010. 061302(R). 41, 52, 53, 167

[76] S. Anghel, G. Cata-Danil and N.V. Zamfir. Structure Features Revealed from the Two Neutron Separation Energies. *Rom. Journ. Phys.*, 54(3-4):p. 301–319, 2009. Bucarest. 42

[77] C. Thibault, F. Touchard, S. Büttdenbach, R. Klapisch, M. de Saint Simon, H.T. Duong, P. Jacquinot, P. Juncar, S. Liberman, P. Pillet, J. Pinard, J.L. Vialle, A. Pesnelle and G. Huber. Hyperfine Structure and Isotope Shift of the D_2 Line of $^{76-98}$Rb and some of their Isomers. *Phys. Rev. C*, 23(6), Jun. 1981. 42, 43, 50, 51, 168

[78] M. Keim, E. Arnold, W. Borchers, U. Georg, A. Klein, R. Neugart, L. Vermeeren, R.E. Silverans and P. Lievens. Laser-Spectroscopy Measurements of $^{72\text{-}96}$Kr Spins, Moments and Charge Radii. *Nucl. Phys. A*, 586(2):p. 219–239, April 1995. 43

[79] F. Buchinger, E.B. Ramsay, E. Arnold, W. Neu, R. Neugart, K. Wendt, R.E. Silverans, P. Lievens, L. Vermeeren, D. Berdichevsky, R. Fleming, D.W.L. Sprung and G. Ulm. Systematics of Nuclear Ground State Properties in $^{78\text{-}100}$Sr by Laser Spectroscopy. *Phys. Rev. C*, 41:2883–2897, Jun 1990. 43

[80] F. Buchinger, E.B. Ramsay, E. Arnold, W. Neu, R. Neugart, K. Wendt, R.E. Silverans, P. Lievens, L. Vermeeren, D. Berdichevsky, R. Fleming, D.W.L. Sprung and G. Ulm. Erratum: Systematics of nuclear ground state properties in $^{78-100}$Sr by laser spectroscopy. *Phys. Rev. C*, 42:2754–2754, Dec 1990. 43

[81] P. Lievens and R.E. Silverans and L. Vermeeren and W. Borchers and W. Neu and R. Neugart and K. Wendt and F. Buchinger and E. Arnold. Nuclear Ground State Properties of ^{99}Sr by Collinear Laser Spectroscopy with Non-Optical Detection. *Phys. Lett. B*, 256(2):141–145, 1991. 43

[82] B. Cheal, M.D. Gardner, M. Avgoulea, J. Billowes, M.L. Bissell, P. Campbell, T. Eronen, K.T. Flanagan, D.H. Forest, J. Huikari, A. Jokinen, B.A. Marsh, I.D. Moore, A. Nieminen, H. Penttilä, S. Rinta-Antila, B. Tordoff G. Tungate and J. Äystö. The Shape Transition in the Neutron-Rich Yttrium Isotopes and Isomers. *Phys. Lett. B*, 645:p. 133–137, 2007. 43

[83] K. Baczynska, J. Billowes, P. Campbell, F.C. Charlwood, B. Cheal, T. Eronen, D.H. Forest, A. Jokinen, T. Kessler, I.D. Moore, M. Rüffer, G. Tungate and J. Äystö. Nuclear Spin Determination of ^{100m}Y by Collinear Laser Spectroscopy of Optically Pumped Ions. *Journal of Physics G: Nuclear and Particle Physics*, 37, Jul. 2010. 43

[84] P. Campbell, H.L. Thayer, J. Billowes, P. Dendooven, K.T. Flanagan, D.H. Forest, J.A.R. Griffith, J. Huikari, A. Jokinen, R. Moore, A. Nieminen, G. Tungate, S. Zemlyanoi and J. Äystö. Laser Spectroscopy of Cooled Zirconium Fission Fragments. *Phys. Rev. Lett.*, 89:082501, Aug. 2002. 43

[85] H.L. Thayer, J. Billowes, P. Campbell, P. Dendooven, K.T. Flanagan, D.H. Forest, J.A.R. Griffith, J. Huikari, A. Jokinen, R. Moore, A. Nieminen, G. Tungate, S. Zemlyanoi and J. Äystö. Collinear Laser Spectroscopy of Radioisotopes of Zirconium. *Journal of Physics G: Nuclear and Particle Physics*, 29:p. 2247–2262, Aug. 2003. 43

[86] B. Cheal, K. Baczynska, J. Billowes, P. Campbell, F.C. Charlwood, T. Eronen, D.H. Forest, A. Jokinen, T. Kessler, I.D. Moore, M. Reponen, S. Rothe, M. Rüffer, A. Saastamoinen, G. Tungate and Äystö. Laser Spectroscopy of Niobium Fission Fragments: First Use of Optical Pumping in an Ion Beam Cooler Buncher. *Physical Review Letters*, 102(222501), Jun. 2009. 43

[87] F.C. Charlwood, K. Baczynska, J. Billowes, P. Campbell, B. Cheal, T. Eronen, D.H. Forest, A. Jokinen, T. Kessler, L.D. Moore, H. Pentill, R. Powis, M. Rüffer, A. Saastamoinen, G. Tungate and J. Äystö. Nuclear Charge Radii of Molybdenum Fission Fragments. *Phys. Lett. B*, 674:p. 23–27, 2009. 43

[88] G. Fricke and K. Heilig. *Nuclear Charge Radii, Landolt-Börnstein - Group Elementary Particles, Nuclei and Atoms, Chap. 20, p. 1.* Springer, Berlin, 2004. 43

[89] V.G. Soloviev. *Theory of Complex Nuclei*. Pergamon Press, 1976. 43, 68, 205, 208

[90] J. Tuli, T. Johnson and B. Singh. XUNDL - Experimental Unevaluated Nuclear Data List, Nov. 2012. Compilation of XUNDL datasets is carried out primarily by the nuclear data groups at McMaster U. (Canada), Argonne National Lab., and Triangle Universities Nuclear Lab. - Coordinator: Balraj Singh hispin@mcmaster.ca. 44

[91] N. Mărginean, D. Bucurescu, C.A. Ur, C. Mihai, L. Corradi, E. Farnea, D. Filipescu, E. Fioretto, D. Ghiţă, B. Guiot, M. Górska, M. Ionescu-Bujor, A. Iordăchescu, D. Jelavić-Malenica, S.M. Lenzi, P. Mason, R. Mărginean, D. Mengoni, G. Montagnoli, D.R. Napoli, S. Pascu, G. Pollarolo, F. Recchia, A.M. Stefanini, R. Silvestri, T. Sava, F. Scarlassara, S. Szilner and N.V. Zamfir. Evolution of Deformation in the Neutron-Rich Krypton Isotopes: The ^{96}Kr Nucleus. *Phys. Rev. C*, 80:021301, Aug. 2009. 43

[92] M. Albers, N. Warr et *al.* Coulomb Excitation of the Exotic Nuclei ^{94}Kr and ^{96}Kr. In *Presentation*, Institut für Kernphysik der Universität zu Köln, Germany, 2012. MINIBALL Workshop 2012. 44

[93] P. Federman and S. Pittel. Hartree-Fock-Bogolyubov Study of Deformation in the Zr-Mo Region. *Phys. Lett. B*, 77(1):29–32, 1978. 44

[94] K. Sistemich Eds. J. Eberth, R.A. Meyer, editor. *Nuclear Structures of the Zirconium Region*, Research Reports in Physics, Bad Honnef, Germany, April 1988. Proc. Int. Workshop on Nuclear Structures of the Zirconium Region, Springer-Verlag. 44, 46

[95] P. Moller, J.R. Nix, W.D. Myers and W.J. Swiatecki. Nuclear Ground-State Masses and Deformations. *Atomic Data and Nuclear Data Tables*, 59(2):185–381, 1995. 45, 169

[96] J.A. Pinston and W. Urban. First Observation of the $\nu\,9/2[404]$ Orbital in the $A \sim 100$ Mass Region. *Eur. Phys. J. A*, 16(11), Jan. 2003. 46

[97] W. Urban. The $\nu\,9/2[404]$ Orbital and the Deformation in the $A \sim 100$ Region. *Eur. Phys. J. A*, 22(241), 2004. 46

[98] Heyde, Kris and Wood, John L. Shape Coexistence in Atomic Nuclei. *Rev. Mod. Phys.*, 83:1467–1521, Nov 2011. 47

[99] S. Hilaire and M. Girod. Large-Scale Mean-Field Calculations from Proton to Neutron Drip Lines using the D1S Gogny Force. *The European Physical Journal A*, 33:237–241, 2007. 48, 49

[100] C.Y. Wu, H. Hua, D. Cline, A.B. Hayes, R. Teng, R.M. Clark, P. Fallon, A. Görgen, A.O. Macchiavelli and K. Vetter. Multifaceted Yrast Structure and the Onset of Deformation in ^{96,97}Sr and ^{98,99}Zr. *Phys. Rev. C*, 70:064312, Dec 2004. 48

[101] G.S. Simpson, J.A. Pinston, D. Balabanski, J. Genevey, G. Georgiev, J. Jolie, D.S. Judson, R. Orlandi, A. Scherillo, I. Tsekhanovich, W. Urban and N. Warr. High-spin μs isomer in ^{98}Zr. *Phys. Rev. C*, 74:064308, Dec 2006. 48

[102] S. Brant, G. Lhersonneau and K. Sistemich. Shape Coexistence in the Odd-Odd Neutron-Rich Nucleus ^{98}Y Studied in the Interacting Boson Model. *Phys. Rev. C*, 69:034327, Mar 2004. 49

[103] G. Georgiev, J.M. Daugas, G. Simpson, D.L. Balabanski, A. Blazhev, D. Bucurescu, S. Das-Gupta, T. Faul, D. Filipescu, E. Fiori, L. Gaudefroy, D. Ghita, M. Hass, K. Hauschild, D. Jenkins, U. Köster, T. Kroel, V. Kumar, G. Lo Bianco, N. Marginean, A. López-Martens, C. Mihai, R. Lozeva, V. Méot, D. Mücher, P. Reiter, O. Roberts, O. Roig, M. Seidlitz, K. Singh, A. Stuchbery, D. Voulot, J. Van de Walle, N. Warr and F. Wenander and A. Wendt. Nuclear Structure Studies of the Neutron-Rich Rubidium Isotopes using Coulomb Excitation. Technical Report CERN-INTC-2009-019. INTC-P-266, CERN, Geneva, Jan 2009. 48, 49, 51, 52

[104] G.S. Simpson. Near-Yrast, Medium Spin, Excited States of ^{91}Rb, ^{93}Rb, ^{95}Rb. *Phys. Rev.*, 82, 2010. 50, 140, 165, 166

[105] K. Sistemich, K. Kawade, H. Lawin, G. Lhersonneau, H. Ohm, U. Paffrath, V. Lopac, S. Brant and V. Paar. Structure of Low-Lying Levels in ^{91}Rb and ^{93}Rb. *Zeitschrift für Physik A Atomic Nuclei*, 325:139–147, 1986. 50

[106] I. Ragnarsson. Some Applications of the Shell Correction Method. Technical report, 4^{th} International Symposium on Future Directions in Studies of Nuclei Far from Stability, Nashville, TN, USA, 10 - 13 Sep. 1979, p. 367-387, 1979. CERN-TH-2765. 50, 51

[107] W. R. Garsington. NuShellX code - Shell Model Calculations, Nov. 2012. 51

[108] P. Semmes and I. Ragnarsson. The Particle plus Triaxial Model: A Users Guide. Nuclear Physics Workshop - Oak Ridge, Aug. 1991. 51

[109] R. Rodriguez-Guzman, P. Sarriguren and L.M. Robledo. Shape Evolution in Yttrium and Niobium Neutron-Rich Isotopes. *Phys. Rev. C*, 83(044307), 2011. 52, 53

[110] P.-G. Reinhard and E.W. Otten. Transition to Deformed Shapes as a Nuclear Jahn-Teller Effect. *Nucl. Phys. A*, 420(2):173–192, 1984. 53

[111] H.A. Jahn and E. Teller. Stability of Polyatomic Molecules in Degenerate Electronic States. I. Orbital Degeneracy. *Proceedings of the Royal Society of London. Series A - Mathematical and Physical Sciences*, 161(905):220–235, 1937. 53

[112] I. Stefanescu, G. Georgiev, F. Ames, J. Äystö, D.L. Balabanski, G. Bollen, P.A. Butler, J. Cederkäll, N. Champault, T. Davinson, A. De Maesschalck, P. Delahaye, J. Eberth, D. Fedorov, V.N. Fedosseev, L.M. Fraile, S. Franchoo, K. Gladnishki, D. Habs, K. Heyde, M. Huyse, O. Ivanov, J. Iwanicki, J. Jolie, B. Jonson, Th. Kröll, R. Krücken, O. Kester, U. Köster, A. Lagoyannis, L. Liljeby, G. Lo Bianco, B.A. Marsh, O. Niedermaier, T. Nilsson, M. Oinonen, G. Pascovici, P. Reiter, A. Saltarelli, H. Scheit, D. Schwalm, T. Sieber, N. Smirnova, J. Van de Walle, P. Van Duppen, S. Zemlyanoi, N. Warr, D. Weisshaar and F. Wenander. Coulomb Excitation of ^{68,70}Cu: First Use of Postaccelerated Isomeric Beams. *Phys. Rev. Lett.*, 98:122701, Mar 2007. 54

[113] K. Alder and A. Winther. *Electromagnetic Excitation - Theory of Coulomb Excitation with Heavy Ions*. North-Holland Publishing compagny, Amsterdam-Oxford, 1975. 55, 59, 60, 62, 64, 65, 114, 128

[114] L.C. Biedenharn and P.J. Brussaard. *Coulomb Excitation*. Clarendon Press, Oxford, 1965. 55

[115] B. Mottelson. reprinted. In *Intern. Phys. Conf.* [245], page p. 11. 55

[116] K.A. Ter-Martirosyan. Excitation of Nuclei by the Coulomb Field of Charged Particles - English translation. In *Zhurnal Eksperimental noi i Teoreticheskoi Fiziki (Journal of Experimental and Theoretical Physics)* [245]. 55

[117] T. Huus and C. Zupancic. -. *Mat. Fys. Medd. Dan. Vid. Selsk.*, 28(1), 1953. 55

[118] L.D. Landau and E.M. Lifshitz. *The Classical Theory of Fields*. Pergamon Press, Oxford, 1962. p. 193. 59

[119] A.R. Edmonds. *Angular Momentum in Quantum Mechanics*. Princeton University Press, 1957. 60

[120] Alder, K. and Bohr, A. and Huus, T. and Mottelson, B. and Winther, A. Study of Nuclear Structure by Electromagnetic Excitation with Accelerated Ions. *Rev. Mod. Phys.*, 28:471, Oct 1956. 65

[121] G. Breit and J.P. Lazarus. Effects of Finite Amplitude in Coulomb Excitation. *Phys. Rev.*, 100:942–943, Nov 1955. 66

[122] J. de Boer and J. Eichler. *The Reorientation Effect*, volume 1. Advances in Nuclear Physics, Michel Baranger and Erich Vogt, 1968. 66

[123] G. Breit, R.L. Gluckstern and J.E. Russell. Reorientation Effect in Coulomb Excitation. *Phys. Rev.*, 103(3):727–738, Aug. 1956. 66

[124] Bosch, F. and Spehl, H. Asymptotic Attenuation Coefficients in Random Perturbations of Angular Correlations. *Zeitschrift für Physik A Atoms and Nuclei*, 280:329–339, 1977. 66, 130

[125] R. Brenn, H. Spehl, A. Weckherlin, H.A. Doubt and G. Middelkoop. Nuclear deorientation for heavy ions recoiling in vacuum and low pressure gas. *Zeitschrift für Physik A Atoms and Nuclei*, 281:219–227, 1977. 66, 130

[126] D.W.L. Sprung, S.G. Lie, M. Vallières and P. Quentin. 68

[127] S. Perries, D. Samsoen, J. Meyer, M. Meyer. and P. Quentin. Collective Gyromagnetic Ratios and the Structure of Odd Superdeformed $A = 190$ Nuclei. *Phys. Rev. C*, 55:1797–1804, Apr 1997. 68

[128] A. Bohr and B. R. Mottelson. *Nuclear Structure*, volume Vol. I Vol.II. W.A. Benjamin, New York, 1975. 70

[129] P. Van Duppen. *Lecture Notes of Physics - Isotope Separation On Line and Post Acceleration*, volume 700. Springer-Verlag Berlin Heidelberg, 2006. 74, 77

[130] M. Gaelens *et al.* High Efficiency Release Targets for Radioactive Ion Beams - A Different Approach. In *Proceedings of 15th International Conference on the Application of Accelerators in Research and Industry (CAARI98)*, volume AIP CP475, page p. 302, Denton, Texas, USA, 1999. 74

[131] J. Benlliure. *Lecture Notes of Physics - Spallation Reactions in Applied and Fundamental Research*, volume 700. Springer-Verlag Berlin Heidelberg, 2006. 75

[132] Armbruster. Measurement of a Complete Set of Nuclides, Cross Sections, and Kinetic Energies in Spallation of ^{238}U 1 A GeV With Protons. *Phys. Rev. Lett.*, 93, 2004. 75

[133] J. Chaumont. *Contribution à l'Etude de la Fission par Spectrométrie de Masse en Ligne.* PhD thesis, Faculté des Sciences d'Orsay - Université de Paris, 1970. 77, 79

[134] A. Fick. Über Diffusion. *Ann. Physik*, (170):p. 59, 1885. 77

[135] L. Maunoury. *Production de Faisceaux d'Ions radioactifs Multichargés pour SPIRAL: Etudes et Réalisation du Premier Ensemble Cible-Source*. Ganil t 98 01, thesis of Caen University, 1998. 77

[136] F. Landré-Pellemoine. *Production de Faisceaux d'Ions Radioactifs par la Méthode ISOL pour SPIRAL.* PhD thesis, Caen University, 2001. 77

[137] M. Fujioka et al. Diffusion of Radio-isotopes from Solids in the Form of Foils, Fibers and Particles. *Nuclear Instruments and Methods in Physics Research*, 186:409–412, 1981. 77

[138] R. Kirchner. On the Release and Ionization Efficiency of Catcher-Ion-Source Systems in Isotope Separation On-Line. *Nuclear Instruments and Methods in Physics Research B*, 70:186–199, 1992. 78

[139] J.H. de Boer. The Dynamical Character of Adsorption. *Clarendon Press Oxford*, 1969. 78

[140] L.C. Carraz *et al.* Fast Release of Nuclear Reaction Products from Refractory Matrices. *Nuclear Instruments and Methods*, 148:217–230, 1978. 78

[141] G.D. Alton *et al.* Studies of Release Properties of ISOL - Target Materials using Ion Implantation. *Nuclear Instruments and Methods in Physics Research B*, 66:492–502, 1992. 78

[142] V.I. Mishin, V.N. Fedoseyev, H.-J. Kluge, V.S. Letokhov, H.L. Ravn, F. Scheerer, Y. Shirakabe, S. Sundell and O. Tengblad. Chemically Selective Laser Ion-Source for the CERN-ISOLDE On-Line Mass Separator Facility. *Nuclear Instruments and Methods in Physics Research Section B: Beam Interactions with Materials and Atoms*, 73(4):550–560, 1993. 78

[143] RILIS Collaboration. RILIS, Jun. 2012. 78

[144] V.S. Letokhov. *Laser Photo Ionization Spectroscopy*. Academic Press, 1987. 78

[145] G.S. Hurst and M.G. Payne. *Principles and Applications of Resonance Ionization Spectroscopy*. Hilger, 1988. 78

[146] R. Kirchner. Progress in Ion Source Development for On-Line Separators. *Nuclear Instruments and Methods in Physics Research*, 186(1–2):275–293, 1981. 79

[147] O. Kofoed-Hansen and K.O. Nielsen. Short-Lived Krypton Isotopes and Their Daughter Substances. *Phys. Rev.*, 82:96–97, Apr 1951. 80

[148] D. Darquennes, P. Decrock, Th. Delbar, W. Galster, M. Huyse, Y. Jongen, M. Lacroix, P. Leleux, I. Licot, E. Liénard, P. Lipnik, M. Loiselet, G. Ryckewaert, Kitwanga Sindano Wa, P. Van Duppen, J. Vanhorenbeeck, J. Vervier, and S. Zaremba. Production of Intense Radioactive Ion Beams Using Two Accelerators. *Phys. Rev. C*, 42:R804–R806, Sep 1990. 80

[149] P. Decrock, Th. Delbar, P. Duhamel, W. Galster, M. Huyse, P. Leleux, I. Licot, E. Liénard, P. Lipnik, M. Loiselet, C. Michotte, G. Ryckewaert, P. Van Duppen, J. Vanhorenbeeck, J. Vervier. Determination of the $^{13}N(p,\gamma)^{14}O$ Reaction Cross Section Using a ^{13}N Radioactive Ion Beam. *Phys. Rev. Lett.*, 67:808–811, Aug. 1991. 80

[150] P. Van Duppen, P. Decrock, M. Huyse, Th. Delbar, W. Galster, P. Leleux, I. Licot, E. Liénard, P. Lipnik, M. Loiselet, C. Michotte, G. Ryckewaert, J. Vervier, P. Duhamel and J. Vanhorenbeeck. Production, Acceleration and Use of Radioactive Ion Beams at Louvain-la-Neuve. *Nuclear Instruments and Methods in Physics Research Section B: Beam Interactions with Materials and Atoms*, 70(1–4):393 – 397, 1992. 80

[151] SPIRAL2 Collaboration. SPIRAL2, Jun. 2012. 80

[152] M.G. Saint-Laurent. SPIRAL Phase II, European RTT. Report GANIL R 01 03, GANIL, Sept. 2001. 80

[153] Project Leader: Yorick Blumenfeld EURISOL Collaboration. EURISOL Design Study, Jun. 2012. 80

[154] The EURISOL report. Technical report, 2003. 80

[155] Canada's National Laboratory for Particle and Nuclear Physics. ISAC2, Jun. 2012. 80

[156] D. Habs and P. Van Duppen. Proposal to the ISOLDE Committee - Radioactive Beam Experiments at ISOLDE: Coulomb Excitation and Neutron Transfer Reactions of Exotic Nuclei. Isc/p68, European Organization for Nuclear Research, 14.11.1994. 80

[157] M. Lindroos and T. Nilsson. HIE-ISOLDE: the technical options. Technical Report CERN-2006-013, CERN, 2006. 80

[158] CERN. The HIE-ISOLDE Project, Jul. 2012. 80

[159] ISOLDE Group. History, Jun. 2012. 80

[160] ISOLDE Group. ISOLDE Website, Sept. 2012. 82, 83

[161] D. Habs *et al.* Proposal to the ISOLDE Committee: "Radioactive Beam EXperiment at ISOLDE". Technical report, CERN, 1994. 83

[162] REX-ISOLDE Collaboration (https://isolde.web.cern.ch/ISOLDE/REX-ISOLDE/collaboration.html). Radioactive Beam EXperiment at ISOLDE , January 2012. 84, 86

[163] F. Ames, G. Bollen, P. Delahaye, O. Forstner, G. Huber, O. Kester, K. Reisinger and P. Schmidt. Cooling of Radioactive Ions with the Penning Trap REXTRAP. *Nuclear Instruments and Methods in Physics Research Section A: Accelerators, Spectrometers, Detectors and Associated Equipment*, 538(1–3):17–32, 2005. 83

[164] F. Wenander, J. Cederkäll, J. Björn, L. Liljeby, G. Nyman, K.-G. Rensfelt, Ö. Skeppstedt and B. Wolf. REXEBIS, Design and Initial Commissioning Results. *AIP Conference Proceedings*, 572(1):59–73, 2001. 86

[165] J.L. Biarrotte. Cavités Accélératrices RF. In *Ecole IN2P3 accélérateurs*, La Londe les Maures, Sept. 2009. 86

[166] O. Kester, T. Sieber, S. Emhofer, F. Ames, K. Reisinger, P. Reiter, P.G. Thirolf, R. Lutter, D. Habs, B.H. Wolf, G. Huber, P. Schmidt, A.N. Ostrowski, R. von Hahn, R. Repnow, J. Fitting, M. Lauer, H. Scheit, D. Schwalm, H. Podlech, A. Schempp, U. Ratzinger, O. Forstner, F. Wenander, J. Cederkäll, T. Nilsson, M. Lindroos, H. Fynbo, S. Franchoo, U. Bergmann, M. Oinonen, J. Äystö, P. Van Den Bergh, P. Van Duppen,M. Huyse, N. Warr, D. Weisshaar, J. Eberth, B. Jonson, G. Nyman, M. Pantea, H. Simon, G. Shrieder, A. Richter, O. Tengblad, T. Davinson, P.J. Woods, G. Bollen, L. Weissmann, L. Liljeby and K.G. Rensfelt. Accelerated Radioactive Beams from REX-ISOLDE. *Nuclear Instruments and Methods in Physics Research Section B: Beam Interactions with Materials and Atoms*, 204(0):20–30, 2003. 14^{th} International Conference on Electromagnetic Isotope Separators and Techniques Related to their Applications. 87

[167] R. Lutter, O. Schaile, K. Shöeffel K. Steinberger and C. Broude. MARABOU - MBS and ROOT Based Online/Offline utility, Feb. 2012. 88, 101

[168] NNDC Brookhaven National Laboratory Jag Tuli, Tim Johnson et *al.* Evaluated Nuclear Structure Data File (ENSDF) Retrieval - ENSDF is compiled by the International Network of Nuclear Structure and Decay Data Evaluators , Jun. 2012. 88, 140

[169] CERN. Media Archive (http://mediaarchive.cern.ch/MediaArchive/Photo/Public/2002/0204022/0204022$_0$6/), January 2006. 91

[170] Silena International. Model 7710 Quad Bias Supply, May 2012. 92

[171] S.L. Thomas, T. Davinson and A.C. Shotter. A Modular Amplifier System for the Readout of Silicon Strip Detectors. *Nuclear Instruments and Methods in Physics Research Section A: Accelerators, Spectrometers, Detectors and Associated Equipment*, 288(1):212 – 218, 1990. Proceedings of the Fifth European Symposium on Semiconductors Detectors. 93

[172] Mesytec Detector Readout. MADC-32: Fast 32 channel peak sensing , May 2011. 93

[173] Pierre Delahaye and Fredrik Wenander. Contaminants in the beam , October 2010. 97, 125

[174] Hans Bethe. Zur Theorie des Durchgangs schneller Korpuskularstrahlen durch Materie. *Annalen der Physik*, 397(3):325–400, 1930. 98

[175] N. Warr. MINIBALL Ionization Chamber. Technical report, CERN, 2010. 98

[176] F. Rademakers, P. Canal, B. Bellenot, O. Couet, A. Naumann, G. Ganis, M. Tadel, L. Moneta, V. Vasilev, A. Gheata, P. Russo and R. Brun *et al.* ROOT - An Object Oriented Framework For Large Scale Data Analysis, Nov. 2012. 101

[177] G.F. Knoll. *Radiation Detection and Measurement*. Wiley, New York, 2002. 103, 104

[178] Klein, O. and Nishina, T. Über die Streuung von Strahlung durch freie Elektronen nach der neuen relativistischen Quantendynamik von Dirac. *Zeitschrift für Physik*, 52:853–868, 1929. 103

[179] M.J. Berger, J.H. Hubbell, S.M. Seltzer, J. Chang, J.S. Coursey, R. Sukumar, D.S. Zucker, and K. Olsen. XCOM: Photon Cross Sections Database, Dec. 2011. 104

[180] R.B. Firestone and L.P. Ekström. Table of Radioactive Isotopes. LBNL Isotopes Project - LUNDS Universitet, Jan. 2004. 104, 171

[181] LISE Group. LISE++ Package, Jul. 2012. 109, 114, 195

[182] W.W. Wilcke, J.R. Birkelund, H.J. Wollersheim, A.D. Hoover, J.R. Huizenga, W.U. Schröder and L.E. Tubbs. Reaction Parameters for Heavy-Ion Collisions. *Atomic Data and Nuclear Data Tables*, 25(5-6):389–619, 1980. 113, 114

[183] O. Niedermaier. *Low Energy Coulomb Excitation of the Neutron-Rich Mg Isotopes ^{30}Mg and ^{32}Mg*. PhD thesis, MPI Heidelberg, 2005. 114

[184] F.W.N. Boer, H.J. Wollersheim, H. Emling, H. Grein, E. Grosse, W. Spreng, G. Eckert, Th.W. Elze, K. Stelzer and Ch. Lauterbach. Nucleon transfer reactions to rotational states induced by ^{206,208}pb projectiles. *Zeitschrift für Physik A Atomic Nuclei*, 325:457–466, 1986. 114

[185] R. Bass. *Nuclear Reactions with Heavy Ions*. Springer-Verlag, new york edition, 1980. 114

[186] J.F. Ziegler. *SRIM User's Manual*. 115, 116

[187] J. F. Ziegler. The Stopping and Range of Ions in Matter, Aug. 2012. 115, 116

[188] MINIBALL Workshop and Users Meeting 2012, editors. *Coulomb Excitation of the Highly Deformed ^{98}Sr: State of the Art of Beam Manipulation*, Koeln, Mar. 2012. Universität zu Köln - Institut für Kernphysik. 119

[189] F. Wenander. Rb Radioactive Beams. Technical report, CERN, 2009. 121

[190] GOSIA collaboration. GOSIA, Dec. 2012. 128

[191] C.Y. Wu, T. Czosnyska and D. Cline. Gosia Users Manual UR-NSRL-305 (1991). *Bull. Amer. Phys. Soc.*, 28(745), 1983. 128

[192] D. Cline, T. Czosnyska and C.Y. Wu. *GOSIA User's Manual*. 128, 131

[193] D Cline. Nuclear shapes studied by coulomb excitation. *Annual Review of Nuclear and Particle Science*, 36(1):683–716, 1986. 128

[194] H. Ferentz and N. Rosenzweig. *α, β and γ-ray Spectroscopy*. Amsterdam, 1965. 129

[195] A. Abragam, and R.V. Pound. Influence of Electric and Magnetic Fields on Angular Correlations. *Phys. Rev.*, 92:943–962, Nov 1953. 129

[196] T. Kibédi, T.W. Burrows, M.B. Trzhaskovskaya, P.M. Davidson, and Jr.C.W. Nestor. BrIcc v2.3S Conversion Coefficient Calculator, 21 Dec. 2011. 130, 138, 139, 144, 145, 150, 151, 152, 160, 161, 162

[197] T. Kibédi, T.W. Burrows, M.B. Trzhaskovskaya, P.M. Davidson and Jr.C.W. Nestor. Evaluation of Theoretical Conversion Coefficients using BrIcc. *Nuclear Instruments and Methods in Physics Research Section A: Accelerators, Spectrometers, Detectors and Associated Equipment*, 589(2):202–229, 2008. 130

[198] A.E. Kavka, C. Fahlander, A. Bäcklin, D. Cline, T. Czosnyka, R.M. Diamond, D. Disdier, W.J. Kernan, L. Kraus, I. Linck, N. Schulz, J. Srebrny, F.S. Stephens, L.E. Svensson, B. Varnestig, E.G. Vogt and C.Y. Wu. Coulomb Excitation of $^{76,80,82}Se$. *Nucl. Phys. A*, 593(2):177–211, 1995. 131

[199] J.J. Ressler, J.A. Caggiano, C.J. Francy, P.N. Peplowski, J.M. Allmond, C.W. Beausang, L.A. Bernstein, D.L. Bleuel, J.T. Burke, P. Fallon, A.A. Hecht, D.V. Jordan, S.R. Lesher, M.A. McMahan, T.S. Palmer, L. Phair, N.D. Scielzo, P.G. Swearingen, G.A. Warren and M. Wiedeking. Fission Fragment Isomers Populated via ^{6}Li +^{232} Th. *Phys. Rev. C*, 81:014301, Jan 2010. 135

[200] J.W. Grüter, K. Sistemich, P. Armbruster, J. Eidens and H. Lawin. Identification of μs-Isomers among Primary Fission Products. *Phys. Lett. B*, 33(7):474–476, 1970. 135

[201] Coral M. Baglin. Nuclear Data Sheets for A = 93. *Nuclear Data Sheets*, 80(1):1–156, 1997. 135

[202] D. Kameda, T. Kubo, T. Ohnishi, K. Kusaka, A. Yoshida, K. Yoshida, M. Ohtake, N. Fukuda, H. Takeda, K. Tanaka, N. Inabe, Y. Yanagisawa, Y. Gono, H. Watanabe, H. Otsu, H. Baba, T. Ichihara, Y. Yamaguchi, M. Takechi, S. Nishimura, H. Ueno, A. Yoshimi, H. Sakurai, T. Motobayashi, T. Nakao, Y. Mizoi, M. Matsushita, K. Ieki, N. Kobayashi, K. Tanaka, Y. Kawada, N. Tanaka, S. Deguchi, Y. Satou, Y. Kondo, T. Nakamura, K. Yoshinaga, C. Ishii, H. Yoshii, Y. Miyashita, N. Uematsu, Y. Shiraki, T. Sumikama, J. Chiba, E. Ideguchi, A. Saito, T. Yamaguchi, I. Hachiuma, T. Suzuki, T. Moriguchi, A. Ozawa, T. Ohtsubo, M.A. Famiano, H. Geissel, A.S. Nettleton, O.B. Tarasov, D. Bazin, B.M. Sherrill, S.L. Manikonda and J.A Nolen. Observation of New Microsecond Isomers among Fission Products from In-Flight Fission of 345 MeV/nucleon ^{238}U. *Phys. Rev. C*, 86:054319, Nov 2012. 154, 167

[203] R.F. Casten. *Nuclear Structure from a Simple Perspective*. Oxford U.P, 1990. 165

[204] Otsuka, Takaharu, Fujimoto, Rintaro, Utsuno, Yutaka, Brown, B. Alex, Honma, Michio, Mizusaki and Takahiro. Magic Numbers in Exotic Nuclei and Spin-Isospin Properties of the *NN* Interaction. *Phys. Rev. Lett.*, 87:082502, Aug. 2001. 165

[205] Otsuka, Takaharu and Suzuki, Toshio and Fujimoto, Rintaro and Grawe, Hubert and Akaishi, Yoshinori. Evolution of Nuclear Shells due to the Tensor Force. *Phys. Rev. Lett.*, 95:232502, Nov 2005. 165

[206] C. Folden, A.S. Nettleton, A.M. Amthor, T.N. Ginter, M. Hausmann, T. Kubo, W. Loveland, S.L. Manikonda, D.J. Morrissey, T. Nakao, M. Portillo, B.M. Sherrill, G.A. Souliotis, B.F. Strong, H. Takeda and O.B. Tarasov. New Neutron-Rich Microsecond Isomers Observed among Fission Products of ^{238}U at 80 MeV/nucleon. *Phys. Rev. C*, 79:064318, Jun 2009. 165

[207] M. Rudigier, A. Blazhev, J.-M. Regis, N. Warr, J. Jolie, C. Fransen, M. Hackstein, M. Pfeiffer, W. Rother, T. Thomas, G. Simpson, M. Ramdhane, U. Köster, T. Materna, W. Urban and J.-M. Daugas. First Observation of Isomeric State in ^{97}Rb. DPG Spring Meeting of the Divisions - Hadronic and Nuclear Physics - Physics Education, Mar. 2012. Mainz 2012 Conference. 167

[208] G. Simpson. QRPM Calculations on ^{97}Rb. private communication, 2012. 169

[209] F. Kondev. Calculations on ^{97}Rb with a Woods-Saxon + BCS Model. private communication, 2012. 169, 171

[210] G. Lhersonneau, B. Pfeiffer, H. Gabelmann and K.-L. Kratz. Identical Transitions in the Strongly Deformed ^{99}Sr and ^{100}Sr. *Phys. Rev. C*, 63(054302), 2001. 173

[211] NNDC Brookhaven National Laboratory Ag Tuli, T. Johnson et *al.* ENSDF - ^{99}Sr Level Scheme, Nov. 2012. 173

[212] G. Lhersonneau, H. Gabelmann, B. Pfeiffer and K.-L. Kratz. Structure of the Highly Deformed Nucleus $^{101}Sr_{63}$ and Evidence for Identical K=3/2 Bands. *Zeitschrift für Physik A Hadrons and Nuclei*, 352:293–301, 1995. 173

[213] H. Törnqvist, C. Sotty, G. Georgiev, M. Hass, A. Herlert, M. Kowalska, T. Nilsson, J. Pakarinen and F Wenander. Implementation and Evaluation of Tilted Foils Polarization at REX-ISOLDE. *Physica Scripta*, 2012(T150):014040, 2012. 177

[214] H.T. Törnqvist. Tilted Foils Nuclear Spin Polarization and Measurement with Coulomb Excitation. Master's thesis, Departement of Fundamental Physics - Chalmers University of Technology, SE-412 96 Gothenburg, Sweden, 2012. 177

[215] E.G. Myers, A.J. Mendez, K.W. Kemper, P.L. Kerr, E.L. Reber and B.G. Schmidt. Transport of Polarized Ions Through a Tandem-Superconducting-Linac Heavy-Ion Accelerator. *Nuclear Instruments and Methods in Physics Research Section A: Accelerators, Spectrometers, Detectors and Associated Equipment*, 334(2–3):271–282, 1993. 177

[216] G. Georgiev, M. Hass, D.L. Balabanski, E. Fiori, A. Gottberg, A. Herlert, L. Hemmingsen, K. Johnston, M. Lindroos, J. Ljungvall, T. Nilsson, J. Pakarinen, K. Riisager, C. Sotty, M. Stachura, H.T. Törnqvist, J. Van de Walle, D. Voulot, F. Wenander and W.D. Zeitz. Post-Accelerated Polarized Beams at the REX-LINAC. Technical Report CERN-INTC-2010-058. INTC-I-124, CERN, Geneva, May 2010. 177

[217] H. Postma and N.J. Stone. *Low Temperature Nuclear Orientation*. Elsevier Science Publishing Co., Inc., 52 Vanderbilt Avenue, New York, NY 10017, Jan. 1986. 179, 181

[218] C. Cohen-Tannoudji. *Théorie Quantique du Cycle de Pompage Optique. Vérification Expérimentale des Nouveaux Effets Prévus*. PhD thesis, Université Paris - LSH-ENS - Laboratoire de Spectroscopie Hertzienne de l'ENS, 1962. 179

[219] K. Asahi, M. Ishihara, N. Inabe, T. Ichihara, T. Kubo, M. Adachi, H. Takanashi, M. Kouguchi, M. Fukuda, D. Mikolas, D.J. Morrissey, D. Beaumel, T. Shimoda, H. Miyatake and N. Takahashi. New Aspect of Intermediate Energy Heavy Ion Reactions. Large Spin Polarization of Fragments. *Phys. Lett. B*, 251(4):488–492, 1990. 179

[220] K. Asahi, H. Okuno, H.Ueno, H. Sato, J. Kura, T. Kubo, T. Nakamura, N. Inabe, A. Yoshida, Y. Ohkubo, M. Adachi, T. Ichihara, M. Ishihara, T. Shimoda, H. Miyatake, N. Takahashi, D. Beaumel, D.J. Morrissey and W.-D. Schmidt-Ott. Spin-Oriented Projectile Fragments: The First Application to g-factor Measurements. *Hyperfine Interactions*, 75:101–108, 1992. 179

[221] H. Okuno, K. Asahi, H. Ueno, H. Sato, M. Adachi and others. Polarization in Projectile Fragmentation and g-factor Measurements for Neutron Rich Nuclei. *Hyperfine Int.*, 1992. 179

[222] G. Georgiev, M. Hass, A. Herlert, D.L. Balabanski, E. Fiori, A. Gustafsson, L. Hemmingsen, P. Imielski, K. Johnston, M. Lindroos, R. Lozeva, K. Riisager, M. Stachura, J. Van de Walle, D. Voulot, F. Wenander and W.D. Zeitz. Tilted-Foils Polarization at REX-ISOLDE. Technical Report CERN-INTC-2009-015. INTC-I-083, CERN, Geneva, Jan 2009. 179

[223] K. Krane. *Low Temperature Nuclear Orientation - Chapter 2 - Nuclear Orientation Formalism*. Elsevier Science Publishing Co., Inc., 52 Vanderbilt Avenue, New York, NY 10017, Jan. 1986. 181

[224] G. Georgiev, D.T. Yordanov, D.L. Balabanski, V. Fedosseev, M. Hass, Y. Hirayama, N. Imai, M. Kowalska, A. Kusoglu, J. Ljungvall, B. Marsh, T. Nilsson, S. Rothe, C. Sotty, A.E. Stuchbery, H.T. Törnqvist, F. Wenander. Nuclear Moment Studies in the Odd-Mass In Isotopes up to N=82 using the Tilted Foils Technique. Technical Report CERN-INTC-2012-059. INTC-P-360, CERN, Geneva, Oct 2012. 182, 201

[225] L. Vanneste. *Low Temperature Nuclear Orientation - Chapter 3 - Alpha- and Beta-Emission from Oriented Nuclei*. Elsevier Science Publishing Co., Inc., 52 Vanderbilt Avenue, New York, NY 10017, Jan. 1986. 182, 183

[226] H.G. Berry and M. Hass. Beam-Foil Spectroscopy. *Annual Review of Nuclear and Particle Science*, 32(1):1–34, 1982. 183, 184

[227] N.H. Tolk, L.C. Feldman, J.S. Kraus, J.C. Tully, M. Hass, Y. Niv, G.M. Temmer. Role of Surface Interactions in Beam-Foil Excited-State Formation. *Phys. Rev. Lett.*, 47:487–490, Aug. 1981. 183, 184

[228] S. Momota, Y. Nojiri, M. Fukuda, K. Matsuta and T. Minamisono. Mechanism of Polarization Production by Means of the Tilted-Foil Technique Studied Using Beta-Radioactive Nuclei. *Hyperfine Interactions*, 141-142:513–548, 2002. 183, 184

[229] M. Lindroos. *Decay Properties and Hyperfine Interactions in Oriented α-, β- and γ-emitting nuclei*. PhD thesis, Chalmers University of Technology, Göteborg, Sweden, 1993. 183

[230] G. Goldring, M. Hass and E. Dafni. The Tilted-Multifoil Hyperfine Interaction and Nuclear Spectroscopy. *Hyperfine Interactions*, 33:19–35, 1987. 184, 185

[231] M. Hass, E. Dafni, H.H. Bertschat, C. Broude, F.D. Davidovsky, G. Goldring and P.M.S. Lesser. Nuclear Polarization of High-Spin Levels and the Sign of the Quadrupole Moment of ^{54}Fe(10+). *Nucl. Phys. A*, 414(2):316–332, 1984. 184

[232] G. Goldring and Y. Niv. Nuclear Polarization Generated in Multi Tilted-Foil Arrays. *Hyperfine Interactions*, 21:209–218, 1985. 184, 185

[233] Y. Nojiri. Tilted Foil Technique Applied to β-NMR Studies. *Hyperfine Interactions*, 100:23–36, 1996. 185

[234] Y. Hirayama, M. Mihara, Y.X. Watanabe, S.C. Jeong, H. Miyatake, S. Momota, T. Hashimoto, N. Imai, K. Matsuta, H. Ishiyama, S. Ichikawa, T. Ishii, T. Izumikawa, I. Katayama, H. Kawakami, H. Kawamura, I. Nishinaka, K. Nishio, H. Makii, S. Mitsuoka, A. Osa, Y. Otokawa, and T.K. Sato. Tilted-Foil Technique for Producing a Spin-Polarized Radioactive Isotope Beam. *The European Physical Journal A*, 48:1–10, 2012. 186, 197, 198

[235] H.G. Berry, S.N. Bhardwaj, L.J. Curtis and R.M. Schectman. Orientation and Alignment of Atoms by Beam-Foil Excitation. *Phys. Lett. A*, 50(1):59–60, 1974. 186

[236] J. Bendahán, C. Broude, M. Hass, E. Dafni, G. Goldring, J. Gerl, D. Habs, W. Körten and D. Schwalm. Heavy ion beam polarization produced by the multi-tilted-foil interaction. *Zeitschrift für Physik A Atomic Nuclei*, 331:343–346, 1988. 186

[237] E. Matthias, B. Olsen, D.A. Shirley, J.E. Templeton and R.M. Steffen. Theory of Nuclear Magnetic Resonance Detected by Nuclear Radiations. *Phys. Rev. A*, 4:1626–1658, Oct 1971. 187

[238] E.M. Purcell, H.C. Torrey and R.V. Pound. Resonance Absorption by Nuclear Magnetic Moments in a Solid. *Phys. Rev.*, 69:37–38, Jan 1946. 187

[239] G. Georgiev, D.T. Yordanov, D.L. Balabanski, V. Fedosseev, M. Hass, Y. Hirayama, N. Imai, M. Kowalska, A. Kusoglu, J. Ljungvall, B. Marsh, T. Nilsson, S. Rothe, C. Sotty, A.E. Stuchbery, H. Törnqvist and F. Wenander. Nuclear Moment Studies in the Odd-Mass In isotopes up to N=82 using the Tilted Foils Technique. Technical Report CERN-INTC-2012-059. INTC-P-360, CERN, Geneva, Oct. 2012. 189

[240] K. Shima and N. Kuno and M. Yamanouchi and H. Tawara. Equilibrium Charge Fractions of Ions of Z = 4–92 Emerging from a Carbon Foil. *Atomic Data and Nuclear Data Tables*, 51(2):173 – 241, 1992. 195

[241] O. Ofer, K.H. Chow, I. Fan, M. Egilmez, T.J. Parolin, M.D. Hossain, J. Jung, Z. Salman, R.F. Kiefl, C.D.P. Levy, G. Morris, M.R. Pearson, H. Saadaoui, Q. Song, D. Wang and W.A. MacFarlane. β-NMR study of Isolated ^{8}Li^{+} in the Enhanced Paramagnet Platinum. *Phys. Rev. B*, 86:064419, Aug. 2012. 195

[242] J. Bardeen, L.N. Cooper and J.R. Schrieffer. Theory of Superconductivity. *Phys. Rev.*, 108:1175–1204, Dec 1957. 207

[243] H.J. Lipkin. Collective Motion in Many-Particle Systems: Part 1. The Violation of Conservation Laws. *Annals of Physics*, 9(2):272–291, 1960. 209

[244] Nogami, Yukihisa. Improved Superconductivity Approximation for the Pairing Interaction in Nuclei. *Phys. Rev.*, 134:B313–B321, Apr 1964. 209

[245] K. Alder and A. Winther. *Coulomb Excitation*. Academic Press, New York, 1966. 221